MICROCOPY RESOLUTION TEST CHART
NATIONAL BUREAU OF STANDARDS-1963-A

CALCULATION OF TRAILING-EDGE, STERN AND WAKE FLOWS BY A TIME-MARCHING SOLUTION OF THE PARTIALLY-PARABOLIC EQUATIONS

by

H. C. Chen and V. C. Patel

IIHR Report No. 285
Iowa Institute of Hydraulic Research
The University of Iowa
Iowa City, Iowa   52242

April 1985

CALCULATION OF TRAILING-EDGE, STERN AND WAKE FLOWS BY A TIME-MARCHING SOLUTION OF THE PARTIALLY-PARABOLIC EQUATIONS

by

H. C. Chen and V. C. Patel

AD A 156 673

REPORT DOCUMENTATION PAGE

| 1. REPORT NUMBER IIHR Report No. 285	2. GOVT ACCESSION NO.	3. RECIPIENT'S CATALOG NUMBER
4. TITLE (and Subtitle) Calculation of Trailing-Edge, Stern and Wake Flows by a Time-Marching Solution of the Partially-Parabolic Equations		5. TYPE OF REPORT & PERIOD COVERED Technical Report Nov. 1982-Apr 1985
		6. PERFORMING ORG. REPORT NUMBER IIHR Report No. 285
7. AUTHOR(s) H.C. Chen and V.C. Patel		8. CONTRACT OR GRANT NUMBER(s) N00014-83-K-0136 N00014-81-K-0200
9. PERFORMING ORGANIZATION NAME AND ADDRESS Iowa Institute of Hydraulic Research The University of Iowa Iowa City, Iowa 52242		10. PROGRAM ELEMENT, PROJECT, TASK AREA & WORK UNIT NUMBERS NR 655-002
11. CONTROLLING OFFICE NAME AND ADDRESS Office of Naval Research DTNSRDC 800 N Quincy St Bethesda Arlington, VA 22217 MD 20084		12. REPORT DATE April 1985
		13. NUMBER OF PAGES 240
14. MONITORING AGENCY NAME & ADDRESS(if different from Controlling Office) Office of Naval Research 536 S Clark Street Chicago, IL 60605		15. SECURITY CLASS. (of this report) Unclassified
		15a. DECLASSIFICATION/DOWNGRADING SCHEDULE

16. DISTRIBUTION STATEMENT (of this Report)

Approved for Public Release; Distribution Unlimited

17. DISTRIBUTION STATEMENT (of the abstract entered in Block 20, if different from Report)

19. KEY WORDS (Continue on reverse side if necessary and identify by block number)

Thick 3D Boundary Layer; Stern Flow, Wake, Partially-Parabolic Equations; Turbulence Models; Body-Fitted Coordinates; Computational Fluid Dynamics.

20. ABSTRACT (Continue on reverse side if necessary and identify by block number)
   This report describes in detail a computational method for the solution of the partially-parabolic (or semi-elliptic or parabolized) Reynolds-averaged Navier-Stokes equations for the calculation of external flow around ship-like three-dimensional bodies. Among the main features of the method are the following. Numerically-generated body-fitted coordinates are used to facilitate applications to a wide variety of shapes. The convective-transport equations are discretized using the finite-analytic scheme which employs analytic solutions of the locally-linearized equations. A time-marching algorithm is employed to enable future

extentions to be made to handle unsteady and fully-elliptic problems. A two-step global pressure-correction algorithm has been developed to accelerate convergence. The method can be used with large solution domains in order to capture the viscous-inviscid interaction so that iterative matching between separate viscous-flow and potential-flow solutions is not necessary. For turbulent flows, the well known k-ε model is used, but with a more convenient and realistic treatment of the flow close to solid walls.

The generality and flexibility of the method are demonstrated by applications to several two-dimensional, axisymmetric and three-dimensional flows.

TABLE OF CONTENTS

ABSTRACT

This report describes in detail a computational method for the solution of the partially-parabolic (or semi-elliptic or parabolized) Reynolds-averaged Navier-Stokes equations for the calculation of external flow around ship-like three-dimensional bodies. Among the main features of the method are the following. Numerically-generated body-fitted coordinates are used to facilitate applications to a wide variety of shapes. The convective-transport equations are discretized using the finite-analytic scheme which employs analytic solutions of the locally-linearized equations. A time-marching algorithm is employed to enable future extensions to be made to handle unsteady and fully-elliptic problems. A two-step global pressure-correction algorithm has been developed to accelerate convergence. The method can be used with large solution domains in order to capture the viscous-inviscid interaction so that iterative matching between separate viscous-flow and potential-flow solutions is not necessary. For turbulent flows, the well known k-ε model is used, but with a more convenient and realistic treatment of the flow close to solid walls.

The generality and flexibility of the method are demonstrated by applications to several two-dimensional, axisymmetric and three-dimensional flows.

ACKNOWLEDGEMENTS

LIST OF SYMBOLS

Alphabetical Symbols

A, B — convection coefficients in the linearized convective-transport equation (IV-24)

$A_\phi, B_\phi, D_\phi, E_\phi$ — convection coefficients in the transport equation for ϕ ($\equiv U, V, W, k, \epsilon$)

A_i, A^i — covariant and contravariant components of a vector $\underset{\sim}{A}$ in general curvilinear coordinates ξ^i

$A_{i,j}, A^i_{,j}$ — covariant derivatives of A_i and A^i

a, b, c — convection coefficients in linearized grid-generation equations

$\underset{\sim}{a}_i, \underset{\sim}{a}^i$ — covariant and contravariant base vectors in the general curvilinear coordinates ξ^i

a^j_i — jth component of $\underset{\sim}{a}_i$

$a_\phi, b_\phi, c_\phi, d_\phi$ — constants in transport equations (III-16)

a_d, a_u, etc. — finite-analytic coefficients for pressure and pressure-correction equations

b^* — half-width of wake defined in Fig. 22

$\underset{\sim}{b}^i$ — $\underset{\sim}{a}_j \times \underset{\sim}{a}_k$, defined in equation (A-34)

b^i_j — jth component of $\underset{\sim}{b}^i$

c_d, c_n, c_e	finite-analytic coefficients for pressure and pressure-correction equations
C_F	$\tau_w / \frac{1}{2} \rho U_e^2$, friction coefficient in Clauser plots
C_f	$\tau_w / \frac{1}{2} \rho U_o^2$, friction coefficient in Fig. 16 (turbulent flow)
C_τ	$\sqrt{Re}\ \tau_w / \rho U_o^2$, friction coefficient in Fig. 13 (laminar flow)
C_{nb}	finite analytic coefficient for transport equations (nb = P, EC, NE, etc.)
C_p	$2p$, pressure coefficient normalized by $\frac{1}{2}\rho U_o^2$
$C_\mu, C_{\epsilon 1}, C_{\epsilon 2}$	turbulence-model constants
D_1	partial mass source term defined in equation (IV-34a)
$\hat{D}$	source function in pressure equation (IV-35)
D^*	mass source term in pressure-correction equation (IV-39)
d_d, d_n, etc.	finite-analytic coefficients for pressure and pressure-correction equations
E_2	series summation term in equation (IV-6)
$E_i, E^i, E(i)$	covariant, contravariant and physical components of a vector $\underset{\sim}{A}$ in orthogonal coordinates x^i

$\underline{e}_i$, $\underline{e}^i$ covariant and contravariant base vectors in orthogonal coordinates x^i

F   geometric coefficients in distorted polar coordinates

F^2,F_A,F_B,F_C grid-control functions in η- direction

f^i grid-control functions in equations (III-19) and (III-20)

G   (1)   turbulence generation term in equation (III-9)

    (2)   geometric coefficient in distorted polar coordinates

g   (1)   geometric coefficient in equation (III-30)

    (2)   source function in linearized transport equations (III-57) and (IV-22)

g_{ij} metric tensor in the general curvilinear coordinates ξ^i

g^{ij} conjugate metric tensor in the general curvilinear coordinates ξ^i

h   grid size in equation (IV-24b) for finite-analytic local element

h_i metric coefficients or scale factors in orthogonal coordinate x^i

h_{ij} metric tensor in orthogonal coordinates x^i

h^{ij} conjugate metric tensor in the orthogonal coordinates x^i

J Jacobian

k (1)   dimensionless turbulent kinetic-energy, normalized by U_o^2

                 (2)   grid size in equation (IV-24b) for finite-analytic local element

k_{ij} curvature parameters in orthogonal coordinates

$\overline{k}_{32}$ geometric coefficient in equation (III-47b) in distorted polar coordinates

L length scale (plate or body length)

N distance measured in the direction normal to the body cross-section

n distance measured in the direction normal to the wall

$\underset{\sim}{n}^i$ unit vectors normal to the coordinate lines

p dimensionless pressure, normalized by ρU_o^2

p^* guessed (imperfect) pressure field

p' $p-p^*$, pressure-correction

$\underset{\sim}{q}$ dimensionless total velocity vector, normalized by U_o

q magnitude of $\underset{\sim}{q}$

q^ξ, q^η, q^ζ dimensionless component velocities along ξ, η, ζ directions, respectively

R radius

R_O body radius

R_{max} maximum body radius

Re Reynolds number

R_{eff} effective Reynolds number in equation (III-10)

r R/L, dimensionless radius

r_n, r_s dimensionless inner and outer boundaries in distorted polar coordinates

$\underset{\sim}{r}$ position vector

S_ϕ, s_ϕ source functions for transport quantities $\phi (\equiv U, V, W, k, \varepsilon)$

t dimensionless time, normalized by L/U_O

U, V, W dimensionless velocity components, normalized by U_O

U^*, V^*, W^* velocities obtained from guessed (imperfect) pressure field p^*

$\tilde{U}, \tilde{V}, \tilde{W}$ pseudovelocities in equation (IV-31)

$\hat{U}, \hat{V}, \hat{W}$ modified pseudovelocities in equation (IV-33)

U_O	constant free-stream (reference) velocity
U_e	edge velocity in Clauser plots
U_c	centerline velocity normalized by U_O
$\underset{\sim}{U}$	velocity vector
$U(i)$	physical components of $\underset{\sim}{U}$
U_τ	$(\tau_w/\rho U_O^2)^{1/2}$, normalized friction (wall shear) velocity
$\overline{u^2}$, $\overline{uv}$, etc.	dimensionless Reynolds stresses, normalized by U_O^2
U_δ	velocity at the edge of boundary layer (Fig. 22)
W_O, W_O^*	velocity defects in Fig. 22
X, Y, Z	Cartesian coordinates
x, y, z	dimensionless Cartesian coordinates
x^i	dimensionless orthogonal coordinates ($i=1,2,3$)
x, r, θ	dimensionless cylindrical-polar coordinates
y^+	dimensionless distance measured in the direction normal to the wall

Greek Symbols

α	angle betwwen $\underset{\sim}{\tau}_\eta$ and $\underset{\sim}{n}^\eta$

α_{ij}	curvature parameters in orthogonal coordinates x^i
Γ^i_{jk}	Christoffel symbols in equation (A-45)
δ	boundary-layer thickness
δ^j_i	Kronecker delta
ε	rate of turbulent energy dissipation, normalized by U_o^3/L
$\varepsilon_{\ell mn}$	permutation symbol
κ	von Karman constant
λ_m	eigenvalues
ν	kinematic viscosity
ν_t	turbulent eddy-viscosity
ξ, η, ζ	transformed (general curvilinear) coordinates
ξ^i	general curvilinear coordinates (i=1,2,3)
η^*, ζ^*	transformed coordinates in linearized convective-transport equations (IV-24)
π	=3.141592653589793
θ	(1) angle in cylindrical-polar coordinates
	(2) momentum thickness
ρ	density

$\sigma_k, \sigma_\varepsilon$	turbulence model constants
τ	time increment
τ_w	wall shear stress
$\underset{\sim}{\tau}_i$	unit vectors tangent to the coordinate lines ($i = \xi, \eta, \zeta$)
ϕ	transport quantities (U, V, W, k, ε)
ψ	$\pi/2$
∇	gradient
∇^2	Laplacian
Δ	difference
Δ_p	dimensionless pressure gradient
Δ_τ	dimensionless stress gradient

Subscripts

EC,NE	east-central, north-east (similarly for WC,SC,NW,etc.)
d,u,e,w,n,s	downstream, upstream, east, west, north and south control surfaces
nb	neighboring nodal points

p	interior node for numerical cells
x,r,θ,t	first derivatives with respect to x,r,θ and t
$xx,rr,\theta\theta$	second derivatives with respect to x,r,θ
ξ,η,ζ	first derivatives with respect to ξ,η,ζ
$\xi\xi,\eta\eta,\zeta\zeta$	second derivatives with respect to ξ,η,ζ
ϕ	transport quantities ($\phi \equiv U,V,W,k,\epsilon$)

Superscripts

d,e,etc.	downstream, east, etc., control surfaces
n,n-1	n^{th} and $(n-1)^{th}$ time step
ϕ	transport quantities ($\equiv U,V,W,k,\epsilon$)

CALCULATION OF TRAILING-EDGE, STERN AND WAKE FLOWS
BY A TIME-MARCHING SOLUTION OF THE PARTIALLY-PARABOLIC EQUATIONS

I. INTRODUCTION

Numerical solutions of the complete Navier-Stokes equations for laminar flow, and the corresponding Reynolds-averaged equations for turbulent flow, have received a great deal of attention in recent years since, in principle, they describe flows with any level of complexity, the only uncertainty being that introduced by the turbulence model employed to effect closure of the Reynolds equations. Indeed, solutions using a variety of finite-difference, finite-element and hybrid schemes are becoming quite common for flows involving simple two-dimensional and axisymmetric geometries or some other simplifying features. For example, many more solutions have been obtained for internal flows in which the boundary conditions are easier to specify. Due to the explosion of the literature in this branch of computational fluid mechanics it is not surprising that an authoritative review of the state-of-the-art has not yet appeared. No such review is intended here. However, it is of interest to note here that considerable confusion abounds in the terminology used in the literature, particularly with regard to the use of the term "Navier-Stokes". In addition to the complete Reynolds-averaged equations for turbulent flow, it is often associated, rather loosely and incorrectly, with equations in which further approximations are made. This distinction, or the lack of it, is particularly evident in solution methods which claim to address three-dimensional external flows. If the correct definition is insisted upon, then there exist a very few solutions of the Navier-Stokes equations or the Reynolds-averaged equations in three-dimensional external flows. Methods which appear to have this capability are those of Briley and McDonald (1977),

Spradley, Stalnaker and Ratliff (1981), and Hankey, Graham and Shang (1982) for laminar flow, and Shang et al. (1980, 1983) and Spalding (1981) for turbulent flow.

As the power of modern computers continues its dramatic increase and the costs continue to decrease, many problems of practical interest, which invariably involve complex three-dimensional geometries, will, in the long run, become tractable through the solutions of the complete equations. The rapid progress being made in another branch of computational fluid mechanics, namely the numerical generation of computational grids for arbitrary bodies, will undoubtedly facilitate such applications. However, the ultimate success in the prediction of turbulent flows will be determined, in large measure, by future progress in the area of turbulence modeling. For example, comparisons made at the 1980-81 Stanford Conferences (Kline, Cantwell and Lilley, 1983) for simple flows involving separation indicated that the solutions of the Reynolds-averaged Navier-Stokes equations show considerable dependence on the turbulence model used. Thus, the modeling of turbulence remains the major source of uncertainty. Another major obstacle to progress in the treatment of complex three-dimensional flows is the difficulty (and expense) of obtaining comprehensive and reliable data which can be used to validate the solutions.

The primary difficulty in the solution of the full Navier-Stokes equations is that they are elliptic and consequently the solution must be found simultaneously in all three spatial directions. The computer-storage requirements and the computational effort can be greatly reduced, however, by the use of equations whose complexity lies somewhere between that of the Navier-Stokes and the boundary-layer equations. Two different approaches have been followed in the formulation of such "higher-order" equations: one seeking to simplify the Navier-Stokes equations by discarding certain terms and the other to generalize the first-order boundary-layer equations by introducing additional terms.

2

Although the two approaches lead to the same equations in the limit, intermediate equations representing different levels of approximations have been used, and appropriate solution procedures developed, for the description of restricted classes of flows.

For general three-dimensional flows, we can distinguish at least three levels of approximations between the classical boundary-layer equations and the complete Navier-Stokes equations. A set of second-order boundary-layer equations can be deduced by formally retaining the second-order terms in the familiar order-of-magnitude analysis (Nash and Patel, 1972). These equations contain additional terms involving the surface curvatures and the variations of the coordinate metrics in the direction normal to the surface which are neglected in the first-order equations. However, the approximations inherent in such an analysis restrict the resulting equations to shear layers developing parallel to continuously curved surfaces. A greater degree of generality is embodied in the somewhat inappropriately named 'thin-layer' or 'thin-layer Navier-Stokes' equations, in which all viscous and turbulent transport terms other than those in the direction normal to the surface are neglected. The difference between these and the second-order equations lies in the retention of the convective terms in the normal direction. It is clear that both are restricted to flows in which cross-stream diffusion parallel to the surface is negligible and therefore do not apply, for example, to the flow in a streamwise corner. The next level of generality, beyond which lie the complete equations, is achieved by the so-called partially-parabolic (or 'parabolized Navier-Stokes', or 'semi-elliptic Navier-Stokes') equations, in which only the longitudinal transport due to viscosity and turbulence is neglected.

All three sets of equations share a common simplification, namely the destruction of the ellipticity of the Navier-Stokes equations in the longitudinal direction. This enables the solu-

tions to be marched in the downstream direction, from some initial plane, provided of course there is no recirculation or reverse flow in that direction. Physically, these approximations differ from those in first-order boundary-layer theory insofar as the pressure is regarded as an unknown and provides the mechanism for the propagation of information from downstream. If the downstream effects are weak, as in thin boundary layers and in fully-developed flows in straight ducts of arbitrary cross-section, then the problem is truly parabolic and a single downstream-marching solution suffices. If they are not, as in the flow over the stern and in the near wake of a ship, several sweeps are necessary to obtain the solution. Methods utilizing the more general equations differ in the order in which the continuity and momentum equations are solved and in the manner in which the pressure is updated in each sweep.

It should be noted that the thin-layer and partially-parabolic equations are identical in two-dimensional and axisymmetric flows due to the absence of transverse diffusion. The substantial simplification introduced by two dimensionality has led to the development of several different numerical methods for the solution of these equations. Some of these will be discussed later.

In three-dimensional flows, the thin-layer approximations were introduced by Baldwin and Lomax (1978) to treat a class of flows in high-speed aerodynamics. The most recent applications are those of Pulliam and Steger (1980), Hung (1980) and Chien and Hsieh (1983) for laminar flow, and Pulliam and Lomax (1979), Deiwert (1981) and Hung and Chaussee (1981) for turbulent flow. These approximations were introduced primarily to reduce the computational effort involved in the solution of the complete Navier-Stokes equations and, as pointed out by Hung and Chaussee, the thin-layer solutions for supersonic flow past bodies at incidence agree with those of the Navier-Stokes equations. Thin-layer equations have also been used, quite independently, in ship

hydrodynamics. However, they have been obtained by an entirely different route, namely by the generalization of the boundary-layer equations to account for the thick boundary-layer effects over ship sterns. The equations used by Soejima (1983) and Odabasi and Davies (1983), and the corresponding higher-order momentum-integral equations of Nagamatsu (1980) and Larsson and Chang (1980), belong in this latter category. Although the underlying assumptions are similar, and lead to identical equations for incompressible flow, the solution methodology has also developed along different lines since the supersonic-flow applications in aerodynamics are viewed from a Navier-Stokes perspective whereas those in ship hydrodynamics continue to be viewed from a boundary-layer perspective. While the former have been quite successful, the latter have met with only limited success, presumably because extensions of solution procedures developed for thin boundary layers may not be the most appropriate for the more general equations. A major difference between the two approaches lies in the manner in which the important upstream influence of the pressure field is treated.

As noted earlier, the partially-parabolic equations differ from the thin-layer equations in that terms in viscous and turbulent transport of momentum in the transverse direction parallel to the surface are retained. Apart from the problem of modeling the additional Reynolds stresses, there is no difference in the mathematical properties of the two sets of equations, and therefore, essentially the same numerical techniques can be used for their solution. The partially-parabolic approximations were first introduced by Pratap and Spalding (1976), to describe flows in which there is a predominant flow direction (along which the diffusion is neglected and there is no recirculation) but significant pressure effects propagate upstream. The retention of the transverse diffusion terms enables the treatment of a much wider class of three-dimensional flows of practical interest, e.g. the flow in curved ducts of arbitrary cross-section, the flow in a

5

streamwise corner (wing-fuselage or hull-appendage junctions), the flow over the stern and in the wake of ship, and the flow over slender bodies at incidence.

The solution of the partially-parabolic equations in three-dimensional external flows is the subject of the present report. This report describes the development of a numerical method which incorporates several novel features designed to improve the accuracy of the solutions and the ease of application to a wide range of flows of practical interest. The types of flows which can be treated by the partially-parabolic equations are described in the next section along with the general features of the new method. Subsequent sections are concerned with the transformation of the equations into curvilinear body-fitted coordinate systems, the numerical generation of the coordinates and the novel finite-analytic method used to solve the equations. The report concludes with the presentation of some solutions in two-dimensional, axisymmetric, and three-dimensional flows which demonstrate the performance and capabilities of the method.

II. PARTIALLY-PARABOLIC FLOWS

As a representative example of high Reynolds-number flow on a three-dimensional body, we consider the flow around a ship hull. Experiments and calculations indicate that first-order boundary-layer equations adequately describe the flow over a large part of the hull if phenomena associated with the free surface are excluded. The assumptions embodied in boundary-layer theory begin to breakdown gradually over the stern, in a region which is typically 10 to 20 percent of the ship length. The experimental information pertaining to the evolution of the flow over the stern and in the near wake has been reviewed by Patel (1982). Among the features which differentiate the stern flow from the boundary-layer flow over the hull are (a) a rapid thickening of the viscous layer, (b) variation of pressure across the layer, implying a strong viscous-inviscid interaction, (c) the development of a large longitudinal vorticity component which may or may not lead to a free-vortex type of separation, and (d) a general reduction in the level of turbulence. The wake of the ship evolves gradually from this flow and also shows basically the same features. An important observation that also emerges from the experiments is that there is usually no region of flow reversal in the direction of ship motion. The flow features noted above are precisely those which can be addressed by the partially-parabolic equations. In particular, these equations can be used to describe the flow in the region between the thin boundary layer upstream and the wake far downstream of the hull.

Extensive regions of thick boundary layers, strong viscous-inviscid interaction and longitudinal vortex formation are also observed on bodies of revolution at incidence (see, for example, Patel and Baek, 1983). For boat-tailed bodies at small to moderate incidences, longitudinal flow reversal may be absent and again the partially-parabolic approximations can be used to describe the development of the vortices on the body and in the wake.

7

In axisymmetric flow, the longitudinal vortices are of course absent, but measurements in the thick boundary layer over the tail and in the near wake of five different bodies (Patel et al., 1974; Patel and Lee, 1977; Huang et al., 1979, 1980) indicate all of the remaining features of the flow over a ship stern. As in the three-dimensional examples, the boundary layer thickens as a result of the convergence of the streamlines in planes parallel to the surface (or due to the decrease in the cross-sectional area of the body) and leads to strong viscous-inviscid interaction. Here again, the partially-parabolic (or the identical thin-layer) equations can be employed to extend the boundary-layer solutions into the wake. Many different methods have been developed for this simple class of flows (see Nakayama et al., 1976; Dyne, 1978; Geller, 1979; Dietz, 1980; Hoffman, 1980, 1982; Huang et al., 1980; Muraoka, 1980; Zhou, 1982; Hogan, 1983; Markatos, 1984). All except the last four of these employ the classical iterative approach to account for the viscous-inviscid interaction.

Two-dimensional external flows in which the partially-parabolic approximations may be applied are those involving a confluence of two or more shear layers. Practical examples are the flow at the trailing edge and in the wake of an airfoil in the absence of separation, the interaction between wakes and boundary layers as on multi-component airfoils and downstream of wing-body junctions, and the initial regions of jets, wall jets and mixing layers. The near wake of a flat plate represents the limiting case and the simplest example insofar as the viscous-inviscid interaction is weak and confined to a very small region close to the trailing edge. Two-dimensional trailing-edge and near-wake flows have been treated by a variety of methods, including numerical solutions of the full Navier-Stokes or Reynolds equations (Hah and Lakshminarayana, 1982; Horstman, 1983; Adair et al., 1983), solutions of the partially-parabolic equations (Rubin and Reddy, 1983), and methods which couple the external inviscid

8

flow to the boundary layer and wake flow through successive iterations (Le Balleur, 1983; Bradshaw et al., 1983; Vatsa and Verdon, 1983). McDonald and Briley (1983) have reviewed the recent developments in the latter area and the extensions of such techniques to treat flows with small regions of separation using the so-called inverse boundary-layer calculations.

The method to be presented here is concerned with the solution of the partially-parabolic Reynolds-averaged equations for three-dimensional flows of an incompressible fluid. Although our primary interest lies in the flow over ship sterns, with all the complicating factors noted above, the method will be used also for the solution of some two-dimensional and axisymmetric flows in order to evaluate its detailed performance.

Previous solutions of the partially-parabolic equations in three-dimensional external flows are quite limited. Abdelmeguid et al. (1979) presented the first application to ship hulls and Markatos et al. (1980), Muraoka (1980, 1982), Tzabiras and Loukakis (1983) and Tzabiras (1983) have pursued it further. As is the case with many other applications in internal flows, all of these use essentially the same numerical scheme, based on the work of Patankar and Spalding (1972), and the k-ε model of turbulence with standard wall functions. A brief review of these references is useful to indicate the present status of the subject and also to point out the major features of the new method.

II.1 The Partially-Parabolic Approximations

Strictly speaking, the partially-parabolic approximations are physically most realistic only if the diffusion in the direction of the local mean streamline is neglected. In all previous calculations, however, the partially-parabolic equations have been derived by neglecting the stress gradients in a primary, predominant-flow direction which is chosen a priori, usually the free-stream direction or the direction of ship motion. Obviously, significant errors may arise in regions where the

9

local flow is not in the primary direction, e.g. close to a curved surface or where the secondary motion is not weak. If the choice of the primary direction is postponed until a suitable coordinate system is selected, some of the terms implicitly neglected in the previous work can be retained without altering the partially-parabolic nature of the equations. This is discussed in Section III.3.

II.2 The Coordinate System

In all previous solutions for ship hulls, the Reynolds equations are first written in the cylindrical polar coordinates (x,r,θ), with x in the direction of ship motion. After neglecting the x-derivatives of the stresses, these are then transformed such that the hull surface becomes one of the coordinate surfaces. Abdelmeguid and Muraoka employed analytical transformations which led to a nonorthogonal distorted polar coordinate system in the (r,θ) plane, while Tzabiras and Loukakis employed conformal-transformation techniques to generate orthogonal coordinates in this plane. In both cases, the coordinate lines in the (x,r) planes are r orthogonal. The improved results obtained by the latter authors have been attributed to this difference in the coordinates.

Recently, Cheng and Patel (1983) have suggested the use of numerically-generated body-fitted coordinates for ship flow calculations. Their method has been extended in the present work to a more general class of coordinate systems, and the numerical procedure for the calculation of the coordinates has been simplified and made more efficient. The basic theory is discussed in Section III.1 and some examples are presented in Section IV.1. This general and flexible grid-generation method facilitates the evaluation of the influence of coordinate systems on the numerical solutions and also enables the method to be employed for other shapes.

II.3 Turbulence Model

As in the previous studies, the present method employs the standard two-equation k-ε turbulence model and uses wall functions to avoid integration of the equations through the sublayer. One of the objectives of the research is to evaluate the efficacy of this method, and the role of the turbulence model, in general, in the flow over trailing edges and ship sterns. This can be accomplished by detailed comparisons with experimental data only after confirming the accuracy and reliability of the numerical solution procedures. Although the turbulence model equations are given in Section III, specific comments concerning the boundary conditions and the evaluation of the model are postponed to the discussion of the results for particular cases.

II.4 Solution Domain and Boundary Conditions

In practical applications of the partially-parabolic equations, the upstream boundary of the solution domain is placed at a station where the boundary layer is thin and can be calculated by first-order theory. The location of downstream boundary should be "far enough" from the body such that the local flow is parabolic, i.e. no influence propagates upstream from there. Some of the earlier solutions were obtained with the downstream boundaries located in the near wake, and therefore contain an unknown influence. The coordinates and the numerical methods used here enable the downstream boundary to be placed several body-lengths downstream without a large penalty in computer time.

The extent of the solution domain normal to the body is usually taken to be of the order of the thickness of the viscous flow and the conditions at this outer boundary are specified from potential-flow solutions. In view of the interaction between the viscous and invisid flows, several iterations are required to obtain a converged solution. While this procedure is commonly employed in two-dimensional and axisymmetric flows, previous solutions for three-dimensional flows have been obtained without any iteration, i.e. by simply specifying the external conditions

11

from the potential flow. Although usual methods of displacement-thickness or equivalent surface singularities can be used to account for the influence of the viscous flow on the external flow, the computation times have thus far proved to be quite prohibitive for fully three-dimensional interactive solutions.

One of the important features of the present method is that the external boundary of the computation domain is placed at a large enough distance from the body so that uniform-flow conditions can be imposed there. This captures the entire zone of viscous-inviscid interaction and avoids the need for potential-flow and iterative solutions altogether. As we shall see from the examples presented later on, this particular feature is made possible by coordinate stretching and the properties of the "finite-analytic" numerical method that is employed.

II.5 Numerical Scheme

For two-dimensional and axisymmetric problems, different numerical schemes have been used to solve the partially-parabolic equations. The methods also differ in the manner in which the pressure field is calculated to allow for the upstream propagation of information. This has usually involved several sweeps through the computation domain marching from the upstream to the downstream boundaries. In the few applications to three-dimensional external flows mentioned earlier, the implicit finite-volume numerical scheme of Patankar and Spalding (1972) has been used together with the SIMPLE algorithm of Patankar (1980) for pressure correction due to the ready availability of commercial computer programs. In these calculations, an initial pressure field is obtained from the potential-flow solution and the pressure is corrected in successive sweeps of the viscous solution. Pratap (1975) and others have noted a rather slow rate of convergence. Use of this pressure-correction procedure in our preliminary studies led to an oscillatory pressure field which lasted for several hundred sweeps. It was therefore found necessary to adopt alternative methods.

The present numerical scheme has three distinctive features. First, it employs the recently-developed finite-analytic numerical scheme (Chen et al., 1982) which is quite different from the conventional finite-difference and finite-element methods. In fact, it can be viewed as a combination of the two approaches. It uses analytical solutions of the locally-linearized convective transport equations for each numerical cell in the computation domain and combines them to obtain the global solution by conventional methods. Secondly, the pressure correction is obtained by a two-step procedure which uses a modified *version of the SIMPLER algorithm*. This improves the convergence properties of the overall solution. Thirdly, the method is formulated for the more general unsteady three-dimensional problem. While this leads to a small increase in computer-storage requirements, it facilitates the management of information and enables future extensions to unsteady and fully-elliptic flows. For steady flows, the converged solution is also obtained by time marching but, in this case, time serves as an iteration parameter. Details of the numerical scheme are discussed in Section IV.

III. EQUATIONS AND COORDINATE SYSTEMS

Since most of the applications presented in this report are associated with external flows past axisymmetric and three-dimensional bodies, such as ship forms, it is convenient to choose cylindrical polar coordinates as the basic coordinate system in the physical domain. Formulations starting with other basic coordinate systems can be derived in a similar manner (see Appendix I).

Consider the equations of motion in cylindrical coordinates (x, r, θ) for unsteady, three-dimensional, incompressible flows. The exact Reynolds-averaged equations of continuity and momentum of the mean flow in dimensionless form are,

$$\frac{\partial U}{\partial x} + \frac{1}{r} \frac{\partial}{\partial r} (rV) + \frac{1}{r} \frac{\partial W}{\partial \theta} = 0 \tag{III-1}$$

$$\frac{\partial U}{\partial t} + U \frac{\partial U}{\partial x} + V \frac{\partial U}{\partial r} + \frac{W}{r} \frac{\partial U}{\partial \theta} + \frac{\partial}{\partial x} (p + \overline{uu}) + \frac{\partial}{\partial r} (\overline{uv})$$
$$+ \frac{1}{r} \frac{\partial}{\partial \theta} (\overline{uw}) + \frac{\overline{uv}}{r} - \frac{1}{Re} \nabla^2 U = 0 \tag{III-2}$$

$$\frac{\partial V}{\partial t} + U \frac{\partial V}{\partial x} + V \frac{\partial V}{\partial r} + \frac{W}{r} \frac{\partial V}{\partial \theta} - \frac{W^2}{r} + \frac{\partial}{\partial x} (\overline{uv}) + \frac{\partial}{\partial r} (p + \overline{vv})$$
$$+ \frac{1}{r} \frac{\partial}{\partial \theta} (\overline{uw}) + \frac{\overline{vv}}{r} - \frac{\overline{ww}}{r} - \frac{1}{Re} (\nabla^2 V - \frac{2}{r^2} \frac{\partial W}{\partial \theta} - \frac{V}{r^2}) = 0 \tag{III-3}$$

$$\frac{\partial W}{\partial t} + U \frac{\partial W}{\partial x} + V \frac{\partial W}{\partial r} + \frac{W}{r} \frac{\partial W}{\partial \theta} + \frac{WV}{r} + \frac{\partial}{\partial x} (\overline{uw}) + \frac{\partial}{\partial r} (\overline{vw})$$
$$+ \frac{1}{r} \frac{\partial}{\partial \theta} (p + \overline{ww}) + 2 \frac{\overline{vw}}{r} - \frac{1}{Re} (\nabla^2 W + \frac{2}{r^2} \frac{\partial V}{\partial \theta} - \frac{W}{r^2}) = 0 \tag{III-4}$$

with $\nabla^2 = \frac{\partial^2}{\partial x^2} + \frac{\partial^2}{\partial r^2} + \frac{1}{r} \frac{\partial}{\partial r} + \frac{1}{r^2} \frac{\partial^2}{\partial \theta^2}$

11

where $x = \frac{X}{L}$, $r = \frac{R}{L}$, θ are the dimensionless coordinates normalized by a characteristic length L, and t is the time normalized by L/U_O. U, V, W are, respectively, the longitudinal, radial and circumferential components of mean velocity normalized by the characteristic velocity U_O. p is the pressure normalized by ρU_O^2. $Re = \frac{U_O L}{\nu}$ is the Reynolds number defined in terms of U_O, L and molecular kinematic viscosity ν. The barred quantities $\overline{uu}$, $\overline{uv}$, etc. are the Reynolds stresses, normalized by U_O^2.

In the present study, the two-equation k-ε turbulence model is used to model the Reynolds stresses. Each Reynolds stress is related to the corresponding mean rate of strain by an isotropic eddy viscosity ν_t as follows:

$$- \overline{uv} = \nu_t \left(\frac{\partial U}{\partial r} + \frac{\partial V}{\partial x} \right)$$

$$- \overline{uw} = \nu_t \left(\frac{\partial W}{\partial x} + \frac{1}{r} \frac{\partial U}{\partial \theta} \right)$$

$$- \overline{vw} = \nu_t \left(\frac{1}{r} \frac{\partial V}{\partial \theta} + \frac{\partial W}{\partial r} - \frac{W}{r} \right) \qquad (III-5)$$

$$- \overline{uu} = \nu_t \left(2 \frac{\partial U}{\partial x} \right) - \frac{2}{3} k$$

$$- \overline{vv} = \nu_t \left(2 \frac{\partial V}{\partial r} \right) - \frac{2}{3} k$$

$$- \overline{ww} = \nu_t \left(\frac{2}{r} \frac{\partial W}{\partial \theta} + 2 \frac{V}{r} \right) - \frac{2}{3} k$$

The eddy viscosity is related to the dimensionless turbulent kinetic energy k, and its rate of dissipation ε, by

$$\nu_t = c_\mu \frac{k^2}{\varepsilon} \qquad (III-6)$$

where c_μ (=0.09) is a constant, and k and ε are governed by the convective transport equations

15

$$\frac{\partial k}{\partial t} + U \frac{\partial k}{\partial x} + V \frac{\partial k}{\partial r} + \frac{W}{r} \frac{\partial k}{\partial \theta} = \frac{\partial}{\partial x} \left(\frac{1}{\sigma_k R_{eff}} \frac{\partial k}{\partial x} \right)$$

$$+ \frac{1}{r} \frac{\partial}{\partial r} \left(\frac{1}{\sigma_k R_{eff}} r \frac{\partial k}{\partial r} \right) + \frac{1}{r^2} \frac{\partial}{\partial \theta} \left(\frac{1}{\sigma_k R_{eff}} \frac{\partial k}{\partial \theta} \right) + G - \varepsilon \qquad (III-7)$$

$$\frac{\partial \varepsilon}{\partial t} + U \frac{\partial \varepsilon}{\partial x} + V \frac{\partial \varepsilon}{\partial r} + \frac{W}{r} \frac{\partial \varepsilon}{\partial \theta} = \frac{\partial}{\partial x} \left(\frac{1}{\sigma_\varepsilon R_{eff}} \frac{\partial \varepsilon}{\partial x} \right)$$

$$+ \frac{1}{r} \frac{\partial}{\partial r} \left(\frac{1}{\sigma_\varepsilon R_{eff}} r \frac{\partial \varepsilon}{\partial r} \right) + \frac{1}{r^2} \frac{\partial}{\partial \theta} \left(\frac{1}{\sigma_\varepsilon R_{eff}} \frac{\partial \varepsilon}{\partial \theta} \right)$$

$$+ C_{\varepsilon 1} \frac{\varepsilon}{k} G - C_{\varepsilon 2} \frac{\varepsilon^2}{k} \qquad (III-8)$$

where G is the turbulence generation term:

$$G = \nu_t \left\{ 2 \left[\left(\frac{\partial U}{\partial x} \right)^2 + \left(\frac{\partial V}{\partial r} \right)^2 + \left(\frac{1}{r} \frac{\partial W}{\partial \theta} + \frac{V}{r} \right)^2 \right] + \left(\frac{1}{r} \frac{\partial U}{\partial \theta} + \frac{\partial W}{\partial x} \right)^2 \right.$$

$$\left. + \left(\frac{\partial V}{\partial x} + \frac{\partial U}{\partial r} \right)^2 + \left(\frac{1}{r} \frac{\partial V}{\partial \theta} + \frac{\partial W}{\partial r} - \frac{W}{r} \right)^2 \right\} \qquad (III-9)$$

The effective Reynolds number, R_{eff}, is defined as

$$\frac{1}{R_{eff}} = \frac{1}{Re} + \nu_t = \frac{1}{Re} + C_\mu \frac{k^2}{\varepsilon} \qquad (III-10)$$

The constants in these equations were taken as $C_\mu = 0.09$, $C_{\varepsilon 1} = 1.44$, $C_{\varepsilon 2} = 1.92$, $\sigma_k = 1.0$, and $\sigma_\varepsilon = 1.3$. We note again that ν_t, k, and ε are all made dimensionless by the characteristic velocity and length scales U_0 and L, respectively.

Using equations (III-5, III-6 and III-10), the momentum equations (III-2) through (III-4) and the turbulence-model equations (III-7) and (III-8) are transformed to

$$\frac{\partial U}{\partial t} + \left(U - 2 \frac{\partial \nu_t}{\partial x} \right) \frac{\partial U}{\partial x} + \left(V - \frac{\partial \nu_t}{\partial r} \right) \frac{\partial U}{\partial r} + \left(W - \frac{1}{r} \frac{\partial \nu_t}{\partial \theta} \right) \frac{1}{r} \frac{\partial U}{\partial \theta}$$

$$+ \frac{\partial p}{\partial x} + \frac{2}{3} \frac{\partial k}{\partial x} - \frac{\partial \nu_t}{\partial r} \frac{\partial V}{\partial x} - \frac{1}{r} \frac{\partial \nu_t}{\partial \theta} \frac{\partial W}{\partial x} - \frac{1}{R_{eff}} \nabla^2 U = 0 \qquad (III-11)$$

16

$$\frac{\partial V}{\partial t} + (U - \frac{\partial \nu_t}{\partial x}) \frac{\partial V}{\partial x} + (V - 2 \frac{\partial \nu_t}{\partial r}) \frac{\partial V}{\partial r} + (W - \frac{1}{r} \frac{\partial \nu_t}{\partial \theta}) \frac{1}{r} \frac{\partial V}{\partial \theta}$$

$$+ \frac{\partial p}{\partial r} + \frac{2}{3} \frac{\partial k}{\partial r} - \frac{\partial \nu_t}{\partial x} \frac{\partial U}{\partial r} - \frac{1}{r} \frac{\partial \nu_t}{\partial \theta} (\frac{\partial W}{\partial r} - \frac{W}{r}) - \frac{W^2}{r}$$

$$- \frac{1}{R_{eff}} (\nabla^2 V - \frac{2}{r^2} \frac{\partial W}{\partial \theta} - \frac{V}{r^2}) = 0 \qquad (III-12)$$

$$\frac{\partial W}{\partial t} + (U - \frac{\partial \nu_t}{\partial x}) \frac{\partial W}{\partial x} + (V - \frac{\partial \nu_t}{\partial r}) \frac{\partial W}{\partial r} + (W - \frac{2}{r} \frac{\partial \nu_t}{\partial \theta}) \frac{1}{r} \frac{\partial W}{\partial \theta}$$

$$+ \frac{1}{r} \frac{\partial p}{\partial \theta} + \frac{WV}{r} + \frac{2}{3} \frac{1}{r} \frac{\partial k}{\partial \theta} - \frac{\partial \nu_t}{\partial x} (\frac{1}{r} \frac{\partial U}{\partial \theta}) - \frac{\partial \nu_t}{\partial r} (\frac{1}{r} \frac{\partial V}{\partial \theta} - \frac{W}{r})$$

$$- \frac{1}{r} \frac{\partial \nu_t}{\partial \theta} (\frac{2V}{r}) - \frac{1}{R_{eff}} (\nabla^2 W + \frac{2}{r^2} \frac{\partial V}{\partial \theta} - \frac{W}{r^2}) = 0 \qquad (III-13)$$

$$\frac{\partial k}{\partial t} + (U - \frac{1}{\sigma_k} \frac{\partial \nu_t}{\partial x}) \frac{\partial k}{\partial x} + (V - \frac{1}{\sigma_k} \frac{\partial \nu_t}{\partial r}) \frac{\partial k}{\partial r} + (W - \frac{1}{\sigma_k r} \frac{\partial \nu_t}{\partial \theta}) \frac{1}{r} \frac{\partial k}{\partial \theta}$$

$$- \frac{1}{\sigma_k R_{eff}} \nabla^2 k - G + \epsilon = 0 \qquad (III-14)$$

$$\frac{\partial \epsilon}{\partial t} + (U - \frac{1}{\sigma_\epsilon} \frac{\partial \nu_t}{\partial x}) \frac{\partial \epsilon}{\partial x} + (V - \frac{1}{\sigma_\epsilon} \frac{\partial \nu_t}{\partial r}) \frac{\partial \epsilon}{\partial r} + (W - \frac{1}{\sigma_\epsilon r} \frac{\partial \nu_t}{\partial \theta}) \frac{1}{r} \frac{\partial \epsilon}{\partial \theta}$$

$$- \frac{1}{\sigma_\epsilon R_{eff}} \nabla^2 \epsilon - C_{\epsilon 1} \frac{\epsilon}{k} G + C_{\epsilon 2} \frac{\epsilon^2}{k} = 0 \qquad (III-15)$$

It is convenient to rewrite the governing transport equations (III-11) through (III-15) in the following general form

$$\nabla^2 \phi = R_{eff} [(a_\phi U - b_\phi \nu_{t,x}) \phi_x + (a_\phi V - c_\phi \nu_{t,r}) \phi_r +$$

$$(a_\phi W - d_\phi \frac{1}{r} \nu_{t,\theta}) (\frac{1}{r} \phi_\theta) + a_\phi \phi_t] + s_\phi \qquad (III-16)$$

where ϕ may represent any one of the convective transport quantities: U, V, W, k or ϵ, and the subscripts x,r,θ denote derivatives. The corresponding coefficients a_ϕ, b_ϕ, c_ϕ and d_ϕ are

17

$$a_U = 1, \quad b_U = 2, \quad c_U = 1, \quad d_U = 1$$

$$a_V = 1, \quad b_V = 1, \quad c_V = 2, \quad d_V = 1$$

$$a_W = 1, \quad b_W = 1, \quad c_W = 1, \quad d_W = 2 \qquad \text{(III-17)}$$

$$a_k = \sigma_k, \quad b_k = 1, \quad c_k = 1, \quad d_k = 1$$

$$a_\varepsilon = \sigma_\varepsilon, \quad b_\varepsilon = 1, \quad c_\varepsilon = 1, \quad d_\varepsilon = 1$$

and the source functions s_ϕ for U, V, W, k and ε are, respectively,

$$s_U = R_{eff} \left[p_x + \frac{2}{3} k_x - \nu_{t,r} V_x - \left(\frac{1}{r} \nu_{t,\theta} \right) W_x \right] \qquad \text{(III-18a)}$$

$$s_V = R_{eff} \left[p_r + \frac{2}{3} k_r - \nu_{t,x} U_r - \left(\frac{1}{r} \nu_{t,\theta} \right) \left(W_r - \frac{W}{r} \right) - \frac{W^2}{r} \right]$$

$$+ \frac{2}{r^2} W_\theta + \frac{V}{r^2} \qquad \text{(III-18b)}$$

$$s_W = R_{eff} \left[\frac{1}{r} p_\theta + \frac{2}{3} \frac{1}{r} k_\theta + \frac{WV}{r} - \nu_{t,x} \left(\frac{1}{r} U_\theta \right) - \nu_{t,r} \left(\frac{1}{r} V_\theta - \frac{W}{r} \right) \right.$$

$$\left. - \left(\frac{1}{r} \nu_{t,\theta} \right) \left(\frac{2V}{r} \right) \right] - \frac{2}{r^2} V_\theta + \frac{W}{r^2} \qquad \text{(III-18c)}$$

$$s_k = - \sigma_k R_{eff} \, (G - \varepsilon) \qquad \text{(III-18d)}$$

$$s_\varepsilon = - \sigma_\varepsilon R_{eff} \left(C_{\varepsilon 1} \frac{\varepsilon}{k} G - C_{\varepsilon 2} \frac{\varepsilon^2}{k} \right) \qquad \text{(III-18e)}$$

Equations (III-11) through (III-15) are coupled, nonlinear, partial differential equations and, together with the continuity equation (III-1), are sufficient, in principle, to solve for the six unknowns p, U, V, W, k and ε when proper initial and boundary conditions are specified. It should be noted that these are

18

still the complete elliptic equations and no approximations have been made other than those inherent in the turbulence model.

III.1 Body-Fitted Coordinates

For most practical applications, the geometry of the body is usually quite complex and the cylindrical or other basic orthogonal coordinates are not the most convenient ones to use. It is therefore desirable to introduce analytic or numerical coordinate transformations, which facilitate the applications of the boundary conditions and also simplify the computational domain in the transformed plane.

As mentioned earlier, two types of coordinate systems, namely a distorted polar coordinate system obtained by analytic transformation and that based on conformal-transformation at each section, have been employed in previous investigations associated with ship hulls. From the limited calculations performed with these, it appears that the solutions are greatly dependent upon the choice of coordinates since all have used essentially the same equations, turbulence model and numerical method. Therefore, it is important to investigate other coordinates, and techniques for coordinate generation, so that accurate and efficient flow calculations can be performed. Here we shall follow the increasingly popular method of numerical grid generation, as suggested recently by Cheng and Patel (1983), since it offers the advantages of generality and flexibility and, most importantly, transforms the computation domain into a simple rectangular region with equal grid spacing.

In the numerical grid-generation technique, we seek a coordinate system for the numerical analysis of the flow in the domain D shown in Fig. 1. This domain is bounded by an arbitrary hull surface S, the ship centerplane C, the free surface or water plane W, the upstream and downstream sections A and B, respectively, and an external boundary Σ. Section A may be located at a hull section where the boundary layer is thin, and B may be

19

placed at a section in the far wake. The choice of the external boundary Σ is arbitrary. The basic idea of a boundary-conforming curvilinear system is to find a transformation such that the curvilinear boundary surfaces of the physical domain D in cylindrical or in any other basic orthogonal coordinate system, say (x^1, x^2, x^3), are transformed into boundaries of a simple rectangular domain in the computational space (ξ, η, ζ) shown in Fig. 2.

With the values of the curvilinear coordinates specified on the boundaries of D, it then remains to generate the values of these coordinates in the interior of D. This is a boundary-value problem in the physical field with the curvilinear coordinates (ξ, η, ζ) as dependent variables and the orthogonal coordinates (x^1, x^2, x^3) as the independent variables, with boundary conditions specified on the curved boundaries. Thus, a system of elliptic partial differential equations can be used to generate the coordinates since the field solution of such a system is determined entirely by the boundary conditions. However, the elliptic system must be chosen such that it precludes the occurrence of extrema in the interior of the domain and assures a one-to-one mapping between the physical and the transformed planes.

For the general three-dimensional but simply-connected domain of interest here, a set of Poisson equations of the form

$$\nabla^2 \xi = f^1(\xi, \eta, \zeta)$$
$$\nabla^2 \eta = f^2(\xi, \eta, \zeta) \tag{III-19}$$
$$\nabla^2 \zeta = f^3(\xi, \eta, \zeta)$$

or simply

$$\nabla^2 \xi^i = f^i, \qquad i = 1, 2, 3 \tag{III-20}$$

with $\xi^1 = \xi$, $\xi^2 = \eta$, $\xi^3 = \zeta$

may be taken as the basic coordinate generating system. Here, ∇^2 is the Laplacian operator in orthogonal coordinates x^i. The nonhomogeneous source functions f^i may be assigned appropriate values to yield the desired concentration of coordinate surfaces. The choice of these functions for specific applications will be discussed later in Section V. Equation (III-20) is subject to either Dirichlet or Neumann boundary conditions on the boundary surfaces, which are surfaces of constant ξ^i.

Since it is very desirable to perform all numerical computations in the transformed (ξ, η, ζ) plane with equal grid spacing, i.e. $\Delta\xi = \Delta\eta = \Delta\zeta = 1$, equation (III-20) is cumbersome to use. It is more convenient to invert it and solve for the orthogonal coordinates. In other words, the dependent and independent variables are interchanged so that the orthogonal coordinates (x^1, x^2, x^3) in the physical plane become the dependent variables, with the curvilinear coordinates (ξ, η, ζ) as the independent variables. The boundary-value problem in the transformed field then involves generating the values of the orthogonal coordinates $x^i = x^i$ (ξ, η, ζ) in the interior from the specified boundary values of x^i on the rectangular boundary surfaces of the transformed field. Since the boundaries in the transformed plane are all rectangular (constant ξ, η, or ζ plane), these computations are carried out on a cubic grid regardless of the shape of the physical boundaries.

In obtaining the inverse transformation of equation (III-20), several general relations between the physical (x^1, x^2, x^3) and the transformed (ξ, η, ζ) coordinates are required. The basic expressions may be found in many reference books, for example Aris (1971) and Lass (1975), although some of the relations are not explicitly given. For the sake of completeness, therefore, some important relations are given in Appendix I with specific reference to the transformation between any orthogonal coordinates (x^1, x^2, x^3) and general coordinates (ξ^1, ξ^2, ξ^3) = (ξ, η, ζ). The latter are not necessarily orthogonal. With these transformation formulae, equations (III-20) become:

$$\nabla^2 x^1 = \frac{1}{h_1 h_2 h_3} \frac{\partial}{\partial x^1} \left(\frac{h_2 h_3}{h_1} \right)$$

$$\nabla^2 x^2 = \frac{1}{h_1 h_2 h_3} \frac{\partial}{\partial x^2} \left(\frac{h_1 h_3}{h_2} \right) \qquad \text{(III-21)}$$

$$\nabla^2 x^3 = \frac{1}{h_1 h_2 h_3} \frac{\partial}{\partial x^3} \left(\frac{h_1 h_2}{h_3} \right)$$

where

$$\nabla^2 = g^{11} \frac{\partial^2}{\partial \xi^2} + g^{22} \frac{\partial^2}{\partial \eta^2} + g^{33} \frac{\partial^2}{\partial \zeta^2} + 2g^{12} \frac{\partial^2}{\partial \xi \partial \eta} + 2g^{13} \frac{\partial^2}{\partial \xi \partial \zeta}$$

$$+ 2 g^{23} \frac{\partial^2}{\partial \eta \partial \zeta} + f^1 \frac{\partial}{\partial \xi} + f^2 \frac{\partial}{\partial \eta} + f^3 \frac{\partial}{\partial \zeta} \qquad \text{(III-21a)}$$

h_i are the metric coefficients in the chosen orthogonal coordi-
nates x^i, and g^{ij} is the conjugate metric tensor in the trans-
formed coordinates ξ^i ($= \xi, \eta, \zeta$). Note that, for the cylindrical
polar coordinates (x, r, θ) chosen here, the metrices h_i are (1,
1, r), respectively.

Equations (III-21) can be solved numerically in the trans-
formed domain (ξ, η, ζ) when proper boundary conditions are spec-
ified on all boundary surfaces (i.e. constant ξ, η and ζ). If
$f^1 = f^2 = f^3 = 0$, the transformation is said to be
homeomorphic. In general, however, non-zero values may be as-
signed to these functions to exercise control over the grid dis-
tribution. Solutions of Equations (III-21) to obtain numerical
grids for particular shapes are presented in Section V.

III.2 The Reynolds Equations in Transformed Coordinates

In the previous section, the numerical grid-generation tech-
nique based on a coordinate transformation from an orthogonal
curvilinear system to a general curvilinear system was out-
lined. It then remains to transform the governing equations of
motion to the transformed plane. Although it is possible to
transform both the independent (x^1, x^2, x^3, t) and the dependent

$(U, V, W, k, \varepsilon)$ variables to the (ξ, η, ζ) coordinates, we will consider only the tranformation of the independent variables, leaving the velocity components U, V, W in the original (x^1, x^2, x^3) coordinates in the physical plane. This approach makes it possible to retain a certain amount of physical intuition in the approximations to be made later.

As mentioned earlier, the cylindrical polar coordinates (x, r, θ) appear to be most convenient for the description of the flow field around axisymmetric bodies and ship forms. Thus, in this study, equations (III-1) and (III-11) through (III-15) will be used as the basic equations in the physical plane to derive the equations in the transformed domain (ξ, η, ζ). Transformed equations resulting from other basic orthogonal coordinates, which may be useful in other applications, are given in Appendix I.

Using the general expression of the gradient, divergence and Laplacian given in Appendix I, equations (III-11) through (III-15) for unsteady three-dimensional flow can be transformed to the following form

$$g^{11}\phi_{\xi\xi} + g^{22}\phi_{\eta\eta} + g^{33}\phi_{\zeta\zeta} + 2g^{12}\phi_{\xi\eta} + 2g^{13}\phi_{\xi\zeta} + 2g^{23}\phi_{\eta\zeta}$$

$$+ f^1\phi_\xi + f^2\phi_\eta + f^3\phi_\zeta = \frac{R_{eff}}{J}\ [\alpha^1_\phi(b^1_1\phi_\xi + b^2_1\phi_\eta + b^3_1\phi_\zeta)$$

$$+ \alpha^2_\phi\ (b^1_2\ \phi_\xi + b^2_2\ \phi_\eta + b^3_2\ \phi_\zeta) + \alpha^3_\phi(b^1_3\ \phi_\xi + b^2_3\phi_\eta + b^3_3\phi_\zeta)]$$

$$+ a_\phi\ R_{eff}\ \phi_t + s_\phi \qquad\qquad\qquad (III-22)$$

where

$$\alpha^1_\phi = a_\phi U - \frac{b_\phi}{J}\ (b^1_1\ \nu_{t,\xi} + b^2_1\ \nu_{t,\eta} + b^3_1\ \nu_{t,\zeta})$$

$$\alpha^2_\phi = a_\phi V - \frac{c_\phi}{J}\ (b^1_2\ \nu_{t,\xi} + b^2_2\ \nu_{t,\eta} + b^3_2\ \nu_{t,\zeta}) \qquad (III-23)$$

$$\alpha^3_\phi = a_\phi W - \frac{d_\phi}{J}\ (b^1_3\ \nu_{t,\xi} + b^2_3\ \nu_{t,\eta} + b^3_3\ \nu_{t,\zeta})$$

and a_ϕ, b_ϕ c_ϕ and d_ϕ are as defined in equation (III-17). Hereafter, the subscripts (ξ, η, ζ) on ϕ $(=U, V, W, k, \epsilon)$ and ν_t denote derivatives.

Equation (III-22) is identical with equation (A-84) in Appendix I. It can be rearranged into a general convective-transport equation of the form

$$g^{11}\phi_{\xi\xi} + g^{22}\phi_{\eta\eta} + g^{33}\phi_{\zeta\zeta} = 2A_\phi\phi_\zeta + 2B_\phi\phi_\eta + D_\phi\phi_\xi + E_\phi\phi_t + S_\phi \qquad \text{(III-24)}$$

where

$$2A_\phi = \frac{R_{eff}}{J}(b_1^3\alpha_\phi^1 + b_2^3\alpha_\phi^2 + b_3^3\alpha_\phi^3) - f^3 \qquad \text{(III-25a)}$$

$$2B_\phi = \frac{R_{eff}}{J}(b_1^2\alpha_\phi^1 + b_2^2\alpha_\phi^2 + b_3^2\alpha_\phi^3) - f^2 \qquad \text{(III-25b)}$$

$$D_\phi = \frac{R_{eff}}{J}(b_1^1\alpha_\phi^1 + b_2^1\alpha_\phi^2 + b_3^1\alpha_\phi^3) - f^1 \qquad \text{(III-25c)}$$

$$E_\phi = a_\phi R_{eff} \qquad \text{(III-25d)}$$

$$S_\phi = s_\phi - 2(g^{12}\phi_{\xi\eta} + g^{13}\phi_{\xi\zeta} + g^{23}\phi_{\eta\zeta}) \qquad \text{(III-25e)}$$

and the source functions s_ϕ are defined in equations (A-85a) through (A-85f) in the transformed plane. For the cylindrical polar coordinates (x, r, θ) chosen here, the only nonzero k_{ij} and α_{ij} are $k_{32} = \frac{1}{r}$, $\alpha_{22} = \alpha_{33} = -\frac{1}{r^2}$. Therefore, the source functions are greatly simplified:

$$s_U = R_{eff}\left[\frac{1}{J}(b_1^1 p_\xi + b_1^2 p_\eta + b_1^3 p_\zeta) + \frac{2}{3J}(b_1^1 k_\xi + b_1^2 k_\eta + b_1^3 k_\zeta)\right.$$

$$- \frac{1}{J^2}(b_2^1 \nu_{t,\xi} + b_2^2 \nu_{t,\eta} + b_2^3 \nu_{t,\zeta})(b_1^1 V_\xi + b_1^2 V_\eta + b_1^3 V_\zeta)$$

$$- \frac{1}{J^2}(b_3^1 \nu_{t,\xi} + b_3^2 \nu_{t,\eta} + b_3^3 \nu_{t,\zeta})(b_1^1 W_\xi + b_1^2 W_\eta$$

$$\left. + b_1^3 W_\zeta)\right] \qquad \text{(III-26a)}$$

$$s_V = R_{eff} \left\{ - \frac{W^2}{r} + \frac{1}{J} (b_2^1 p_\xi + b_2^2 p_\eta + b_2^3 p_\zeta) + \frac{2}{3J} (b_2^1 k_\xi + b_2^2 k_\eta + b_2^3 k_\zeta) \right.$$

$$- \frac{1}{J^2} (b_1^1 \nu_{t,\xi} + b_1^2 \nu_{t,\eta} + b_1^3 \nu_{t,\zeta})(b_2^1 U_\xi + b_2^2 U_\eta + b_2^3 U_\zeta)$$

$$- \frac{1}{J} (b_3^1 \nu_{t,\xi} + b_3^2 \nu_{t,\eta} + b_3^3 \nu_{t,\zeta})\left[\frac{1}{J} (b_2^1 W_\xi + b_2^2 W_\eta \right.$$

$$\left. \left. + b_2^3 W_\zeta) - \frac{W}{r} \right] \right\} + \frac{2}{rJ} (b_3^1 W_\xi + b_3^2 W_\eta + b_3^3 W_\zeta) + \frac{V}{r^2} \qquad (III\text{-}26b)$$

$$s_W = R_{eff} \left\{ \frac{WV}{r} + \frac{1}{J} (b_3^1 p_\xi + b_3^2 p_\eta + b_3^3 p_\zeta) + \frac{2}{3J} (b_3^1 k_\xi + b_3^2 k_\eta + b_3^3 k_\zeta) \right.$$

$$- \frac{1}{J^2} (b_1^1 \nu_{t,\xi} + b_1^2 \nu_{t,\eta} + b_1^3 \nu_{t,\zeta})(b_3^1 U_\xi + b_3^2 U_\eta + b_3^3 U_\zeta)$$

$$- \frac{1}{J} (b_2^1 \nu_{t,\xi} + b_2^2 \nu_{t,\eta} + b_2^3 \nu_{t,\zeta})\left[\frac{1}{J} (b_3^1 V_\xi + b_3^2 V_\eta + b_3^3 V_\zeta) - \frac{W}{r} \right.$$

$$\left. \left. - \frac{2V}{rJ} (b_3^1 \nu_{t,\xi} + b_3^2 \nu_{t,\eta} + b_3^3 \nu_{t,\zeta}) \right\} - \frac{2}{rJ} (b_3^1 V_\xi + b_3^2 V_\eta + b_3^3 V_\zeta) \right.$$

$$+ \frac{W}{r^2} \qquad (III\text{-}26c)$$

$$s_k = - \sigma_k R_{eff}(G - \varepsilon) \qquad (III\text{-}26d)$$

$$s_\varepsilon = - \sigma_\varepsilon R_{eff} \left(C_{\varepsilon 1} \frac{\varepsilon}{k} G - C_{\varepsilon 2} \frac{\varepsilon^2}{k} \right) \qquad (III\text{-}26e)$$

with

$$G = \nu_t \left\{ \frac{2}{J^2} (b_1^1 U_\xi + b_1^2 U_\eta + b_1^3 U_\zeta)^2 + \frac{2}{J^2} (b_2^1 V_\xi + b_2^2 V_\eta + b_2^3 V_\zeta)^2 \right.$$

$$+ 2 \left[\frac{1}{J} (b_3^1 W_\xi + b_3^2 W_\eta + b_3^3 W_\zeta) + \frac{V}{r} \right]^2$$

$$+ \frac{1}{J^2} (b_1^1 V_\xi + b_1^2 V_\eta + b_1^3 V_\zeta + b_2^1 U_\xi + b_2^2 U_\eta + b_2^3 U_\zeta)^2$$

$$+ \frac{1}{J^2} (b_1^1 W_\xi + b_1^2 W_\eta + b_1^3 W_\zeta + b_3^1 U_\xi + b_3^2 U_\eta + b_3^3 U_\zeta)^2$$

$$\left. + \left[\frac{1}{J} (b_2^1 W_\xi + b_2^2 W_\eta + b_2^3 W_\zeta + b_3^1 V_\xi + b_3^2 V_\eta + b_3^3 V_\zeta) - \frac{W}{r} \right]^2 \right\} \quad (III\text{-}26f)$$

The radius r, the geometric coefficents b_i^j and g^{ij}, and the Jacobian J which appear in the above equations are functions of the coordinates only. When either analytic or numerical transformations are employed to generate the grid distributions, $r = r(\xi, \eta, \zeta)$ is known in the transformed plane. The geometric coefficients b_i^j and g^{ij} for the present transformation are obtained from equations (A-35), (A-40), and (A-42) with $(x^1, x^2, x^3) = (x, r, \theta)$ and $(h_1, h_2, h_3) = (1, 1, r)$, i.e.

$$(b_i^j) = \begin{pmatrix} b_1^1 & b_2^1 & b_3^1 \\ b_1^2 & b_2^2 & b_3^2 \\ b_1^3 & b_2^3 & b_3^3 \end{pmatrix} = \begin{pmatrix} r(r_\eta \theta_\zeta - r_\zeta \theta_\eta) & r(x_\zeta \theta_\eta - x_\eta \theta_\zeta) & x_\eta r_\zeta - x_\zeta r_\eta \\ r(r_\zeta \theta_\xi - r_\xi \theta_\zeta) & r(x_\xi \theta_\zeta - x_\zeta \theta_\xi) & x_\zeta r_\xi - x_\xi r_\zeta \\ r(r_\xi \theta_\eta - r_\eta \theta_\xi) & r(x_\eta \theta_\xi - x_\xi \theta_\eta) & x_\xi r_\eta - x_\eta r_\xi \end{pmatrix}$$

$$(III\text{-}27)$$

and

$$gg^{11} = g_{22} g_{33} - g_{23}^2$$
$$gg^{22} = g_{11} g_{33} - g_{13}^2$$
$$gg^{33} = g_{11} g_{22} - g_{12}^2$$
$$gg^{12} = gg^{21} = g_{13} g_{23} - g_{12}g_{33} \qquad (III\text{-}28)$$
$$gg^{13} = gg^{31} = g_{12} g_{23} - g_{13}g_{22}$$
$$gg^{23} = gg^{32} = g_{12} g_{13} - g_{23}g_{11}$$

where

$$g_{11} = x_\xi^2 + r_\xi^2 + r^2\theta_\xi^2$$

$$g_{22} = x_\eta^2 + r_\eta^2 + r^2\theta_\eta^2$$

$$g_{33} = x_\zeta^2 + r_\zeta^2 + r^2\theta_\zeta^2 \tag{III-29}$$

$$g_{12} = g_{21} = x_\xi x_\eta + r_\xi r_\eta + r^2\theta_\xi\theta_\eta$$

$$g_{13} = g_{31} = x_\xi x_\zeta + r_\xi r_\zeta + r^2\theta_\xi\theta_\zeta$$

$$g_{23} = g_{32} = x_\eta x_\zeta + r_\eta r_\zeta + r^2\theta_\eta\theta_\zeta$$

and

$$g = g_{11}\,g_{22}\,g_{23} + 2g_{12}\,g_{13}\,g_{23} - (g_{23})^2\,g_{11} - (g_{13})^2\,g_{22} - (g_{12})^2\,g_{33} \tag{III-30}$$

is the determinant of the metric tensor g_{ij}. Also, the Jacobian can be expressed as

$$J = \sqrt{g} = \begin{vmatrix} x_\xi & x_\eta & x_\zeta \\ r_\xi & r_\eta & r_\zeta \\ r\theta_\xi & r\theta_\eta & r\theta_\zeta \end{vmatrix} \tag{III-31}$$

It should be remarked here that equation (III.24) is still fully elliptic in space and (U, V, W) represent the velocity components in the physical cylindrical polar coordinates (x, r, θ). Equations (III-24) through (III-26), together with the equation of continuity, i.e.

$$(b_1^1 U + b_2^1 V + b_3^1 W)_\xi + (b_1^2 U + b_2^2 V + b_3^2 W)_\eta$$

$$+ (b_1^3 U + b_2^3 V + b_3^3 W)_\zeta = 0 \tag{III-32}$$

(see equation A-66) are the Reynolds-averaged Navier-Stokes equations for unsteady, three-dimensional flows.

Before considering the partially-parabolic approximations it is useful to write down the full Reynolds equations for two special cases, namely axisymmetric flow, which illustrates the simplifications that arise, and three-dimensional flow in the distorted cylindrical polar coordinate system which has been used by some previous investigators.

(i) Axisymmetric flow

In this case, $U_\zeta = V_\zeta = k_\zeta = \varepsilon_\zeta = p_\zeta = x_\zeta = r_\zeta = \theta_\xi = \theta_\eta = 0$ and $\theta_\zeta = 1$. Therefore, equation (III-24) reduces to

$$g^{11}\phi_{\xi\xi} + g^{22}\phi_{\eta\eta} = 2B_\phi\phi_\eta + D_\phi\phi_\xi + E_\phi\phi_t + S_\phi \qquad \text{(III-33)}$$

with

$$2B_\phi = \frac{R_{eff}}{J}(b_1^2\alpha_\phi^1 + b_2^2\alpha_\phi^2) - f^2 \qquad \text{(III-34a)}$$

$$D_\phi = \frac{R_{eff}}{J}(b_1^1\alpha_\phi^1 + b_2^1\alpha_\phi^2) - f^1 \qquad \text{(III-34b)}$$

$$E_\phi = a_\phi R_{eff} \qquad \text{(III-34c)}$$

$$S_\phi = s_\phi - 2g^{12}\phi_{\xi\eta} \qquad \text{(III-34d)}$$

where

$$\alpha_\phi^1 = a_\phi U - \frac{b_\phi}{J}(b_1^1\nu_{t,\xi} + b_1^2\nu_{t,\eta})$$

$$\alpha_\phi^2 = a_\phi V - \frac{c_\phi}{J}(b_2^1\nu_{t,\xi} + b_2^2\nu_{t,\eta})$$

Also, the source functions s_ϕ are

$$s_U = R_{eff} \left[\frac{1}{J} (b_1^1 p_\xi + b_1^2 p_\eta) + \frac{2}{3J} (b_1^1 k_\xi + b_1^2 k_\eta) \right.$$

$$\left. - \frac{1}{J^2} (b_2^1 \nu_{t,\xi} + b_2^2 \nu_{t,\eta}) (b_1^1 V_\xi + b_1^2 V_\eta) \right] \qquad (III-35a)$$

$$s_V = R_{eff} \left[\frac{1}{J} (b_2^1 p_\xi + b_2^2 p_\eta) + \frac{2}{3J} (b_2^1 k_\xi + b_2^2 k_\eta) \right.$$

$$\left. - \frac{1}{J^2} (b_1^1 \nu_{t,\xi} + b_1^2 \nu_{t,\eta}) (b_2^1 U_\xi + b_2^2 U_\eta) \right] + \frac{V}{r^2} \qquad (III-35b)$$

$$s_k = - \sigma_k R_{eff} (G - \epsilon) \qquad (III-35c)$$

$$s_\epsilon = - \sigma_\epsilon R_{eff} \left(c_{\epsilon 1} \frac{\epsilon}{k} G - c_{\epsilon 2} \frac{\epsilon^2}{k} \right) \qquad (III-35d)$$

with

$$G = \nu_t \left\{ \frac{2}{J^2} (b_1^1 U_\xi + b_1^2 U_\eta)^2 + \frac{2}{J^2} (b_2^1 V_\xi + b_2^2 V_\eta)^2 + 2\left(\frac{V}{r}\right)^2 \right.$$

$$\left. + \frac{1}{J^2} (b_1^1 V_\xi + b_1^2 V_\eta + b_2^1 U_\xi + b_2^2 U_\eta)^2 \right\} \qquad (III-35e)$$

The coefficients b_i^j and g^{ij} in the above equations can be obtained easily from equations (III-27) through (III-31) by noting that $\theta_\xi = \theta_\eta = 0$ and $\theta_\zeta = 1$, and are therefore given by

$$b_1^1 = r r_\eta \; ; \; b_2^1 = - r x_\eta ; \; b_1^2 = - r r_\xi ; \; b_2^2 = r x_\xi \qquad (III-36)$$

$$g g^{11} = r^2 (x_\eta^2 + r_\eta^2)$$

$$g g^{12} = g g^{21} = - r^2 (x_\xi x_\eta + r_\xi r_\eta) \qquad (III-37)$$

$$g g^{22} = r^2 (x_\xi^2 + r_\xi^2)$$

and the Jacobian is

$$J = \sqrt{g} = r (x_\xi r_\eta - x_\eta r_\xi) \qquad (III-38)$$

These equations are used later to calculate the flow in the
thick axisymmetric boundary layer over the tail, and in the near
wake, of bodies of revolution for which extensive data are
available.

(ii) Equations in Distorted Cylindrical Polar Coordinates

The distorted coordinates employed by Abdelmeguid et al.
(1979) and Muraoka (1980, 1982) correspond to the analytical
transformations

$$\xi = x$$

$$\eta = \frac{r - r_s}{r_n - r_s} = \frac{r - r_s}{\Delta} \qquad \text{(III-39)}$$

$$\zeta = \theta/\psi$$

where x is measured along the direction of ship motion, r_n and r_s
represent the radial distances to the preselected outer and inner
(hull) boundaries, respectively, and $\psi = \pi/2$ is the extent of the
domain in the circumferential direction, i.e., from the waterline
to the keel.   Thus, η and ζ vary between 0 and 1, and boundary
conditions are applied along $\eta = 0, 1$ and $\zeta = 0, 1$.

When the abbreviations

$$\Delta = r_n - r_s$$

$$F = \frac{\partial r_s}{\partial x} + \eta \frac{\partial \Delta}{\partial x} \qquad \text{(III-40)}$$

$$G = \frac{1}{r} \left(\frac{\partial r_s}{\partial \theta} + \eta \frac{\partial \Delta}{\partial \theta} \right)$$

$$h_3 = r\psi = (r_s + \eta\Delta) \psi$$

are introduced, the coefficients a_i^ℓ and b_i^ℓ in the transformed
plane can be written, by equations (A-33) and (III-27),

$$(a_i{}^\ell) = \begin{pmatrix} a_1^1 & a_2^1 & a_3^1 \\ a_1^2 & a_2^2 & a_3^2 \\ a_1^3 & a_2^3 & a_3^3 \end{pmatrix} = \begin{pmatrix} 1 & 0 & 0 \\ F & \Delta & h_3 G \\ 0 & 0 & h_3 \end{pmatrix} \qquad \text{(III-41)}$$

$$(b_\ell{}^i) = \begin{pmatrix} b_1^1 & b_2^1 & b_3^1 \\ b_1^2 & b_2^2 & b_3^2 \\ b_1^3 & b_2^3 & b_3^3 \end{pmatrix} = \begin{pmatrix} h_3\Delta & 0 & 0 \\ -h_3 F & h_3 & -h_3 G \\ 0 & 0 & \Delta \end{pmatrix}$$

where b_ℓ^i is the cofactor of a_i^ℓ, such that $a_i^\ell b_\ell^i = J\delta_i^j$, and the Jacobian J is defined by

$$J = \det (a_i{}^\ell) = h_3 \Delta \qquad \text{(III-43)}$$

The metric tensor g_{ij} is given by

$$g_{ij} = \sum_{\ell=1}^{3} a_i{}^\ell a_j{}^\ell$$

or

$$(g_{ij}) = \begin{pmatrix} g_{11} & g_{12} & g_{13} \\ g_{12} & g_{22} & g_{23} \\ g_{13} & g_{23} & g_{33} \end{pmatrix} = \begin{pmatrix} 1+F^2 & F\Delta & h_3 FG \\ F\Delta & \Delta^2 & h_3\Delta G \\ h_3 FG & h_3\Delta G & h_3(1+G^2) \end{pmatrix} \qquad \text{(III-44)}$$

with

$$g = \det (g_{ij}) = J^2 = h_3^2 \Delta^2 \qquad \text{(III-45)}$$

and the conjugate metric tensor g^{ij} is

31

$$(g^{ij}) = (g_{ij})^{-1} = \begin{pmatrix} g^{11} & g^{12} & g^{13} \\ g^{12} & g^{22} & g^{23} \\ g^{13} & g^{23} & g^{33} \end{pmatrix} = \begin{pmatrix} 1 & -\dfrac{F}{\Delta} & 0 \\ -\dfrac{F}{\Delta} & \dfrac{1+F^2+G^2}{\Delta^2} & -\dfrac{G}{h_3\Delta} \\ 0 & -\dfrac{G}{h_3\Delta} & \dfrac{1}{h_3^2} \end{pmatrix} \qquad \text{(III-46)}$$

Also, the functions f^1, f^2 and f^3 are respectively,

$$f^1 = \nabla^2 \xi = \xi_{xx} + \xi_{rr} - \frac{1}{r}\xi_r + \frac{1}{r^2}\xi_{\theta\theta} = 0 \qquad \text{(III-47a)}$$

$$f^2 = \nabla^2 \eta = \eta_{xx} + \eta_{rr} + \frac{1}{r}\eta_r + \frac{1}{r^2}\eta_{\theta\theta}$$

$$= \frac{\partial}{\partial x}\left(-\frac{F}{\Delta}\right) + \frac{1}{r\Delta} + \frac{1}{r}\frac{\partial}{\partial\theta}\left(-\frac{G}{\Delta}\right)$$

$$= \frac{1}{\Delta}\left(\frac{1}{r} - \frac{\partial F}{\partial x} - \frac{1}{r}\frac{\partial G}{\partial\theta} + \frac{F}{\Delta^2}\frac{\partial\Delta}{\partial x} + \frac{G}{\Delta^2}\frac{1}{r}\frac{\partial\Delta}{\partial\theta}\right) \equiv \frac{1}{\Delta}\bar{k}_{32} \qquad \text{(III-47b)}$$

$$f^3 = \nabla^2 \zeta = \zeta_{xx} + \zeta_{rr} + \frac{1}{r}\zeta_r + \frac{1}{r^2}\zeta_{\theta\theta} = 0 \qquad \text{(III-47c)}$$

Therefore, the governing equations in these coordinates can be written

$$(h_3\Delta U)_\xi + \left[h_3(V - FU - GW)\right]_\eta + (\Delta W)_\zeta = 0 \qquad \text{(III-48)}$$

and

$$\phi_{\xi\xi} + (1 + F^2 + G^2)\frac{1}{\Delta^2}\phi_{\eta\eta} + \frac{1}{h_3^2}\phi_{\zeta\zeta} = 2A_\phi \phi_\zeta + 2B_\phi \phi_\eta$$

$$+ D_\phi \phi_\xi + E_\phi \phi_t + S_\phi \qquad \text{(III-49)}$$

where

$$2A_\phi = \frac{R_{eff}}{h_3\Delta}(\Delta\alpha_\phi^3) = \frac{R_{eff}}{h_3}\left[a_\phi W - d_\phi\left(\frac{1}{h_3}v_{t,\zeta} - \frac{G}{\Delta}v_{t,\eta}\right)\right] \qquad \text{(III-50a)}$$

$$2B_\phi = \frac{R_{eff}}{h_3 \Delta} (- h_3 F \alpha_\phi^1 + h_3 \alpha_\phi^2 - h_3 G \alpha_\phi^3) - f^2$$

$$= \frac{1}{\Delta} [R_{eff} (\alpha_\phi^2 - F \alpha_\phi^1 - G \alpha_\phi^3) - \overline{k}_{32}]$$

$$= \frac{1}{\Delta} \{R_{eff} [a_\phi (V - FU - GW) + b_\phi F \nu_{t,\xi} + d_\phi \frac{G}{h_3} \nu_{t,\zeta}$$

$$- (c_\phi + F^2 b_\phi + G^2 d_\phi) \frac{1}{\Delta} \nu_{t,n}] - \overline{k}_{32}\} \tag{III-50b}$$

$$D_\phi = \frac{R_{eff}}{h_3 \Delta} (h_3 \Delta \alpha_\phi^1) = R_{eff} (a_\phi U - b_\phi \nu_{t,\xi} + b_\phi \frac{F}{\Delta} \nu_{t,n}) \tag{III-50c}$$

$$E_\phi = a_\phi R_{eff} \tag{III-50d}$$

$$S_\phi = s_\phi - \frac{2F}{\Delta} \phi_{\xi n} - \frac{2G}{h_3 \Delta} \phi_{n\zeta} \tag{III-50e}$$

and

$$s_U = R_{eff} [p_\xi - \frac{F}{\Delta} p_n + \frac{2}{3} (k_\xi - \frac{F}{\Delta} k_n) - (\frac{1}{\Delta} \nu_{t,n})(V_\xi - \frac{F}{\Delta} V_n)$$

$$- (\frac{1}{h_3} \nu_{t,\zeta} - \frac{G}{\Delta} \nu_{t,n})(W_\xi - \frac{F}{\Delta} W_n)] \tag{III-51a}$$

$$s_V = R_{eff} [\frac{1}{\Delta} p_n + \frac{2}{3\Delta} k_n - (\nu_{t,\xi} - \frac{F}{\Delta} \nu_{t,n})(\frac{1}{\Delta} U_n)$$

$$- (\frac{1}{h_3} \nu_{t,\zeta} - \frac{G}{\Delta} \nu_{t,n})(\frac{1}{\Delta} W_n - \frac{W}{r}) - \frac{W^2}{r}] + \frac{2}{r} (\frac{1}{h_3} W_\zeta - \frac{G}{\Delta} W_n)$$

$$+ \frac{V}{r^2} \tag{III-51b}$$

$$s_W = R_{eff} [\frac{WV}{r} + \frac{1}{h_3} p_\zeta - \frac{G}{\Delta} p_n + \frac{2}{3} (\frac{1}{h_3} k_\zeta - \frac{G}{\Delta} k_n)$$

$$- (\nu_{t,\xi} - \frac{F}{\Delta} \nu_{t,n})(\frac{1}{h_3} U_\zeta - \frac{G}{\Delta} U_n) - (\frac{1}{\Delta} \nu_{t,n})(\frac{1}{h_3} V_\zeta - \frac{G}{\Delta} V_n - \frac{W}{r})$$

$$- (\frac{1}{h_3} \nu_{t,\zeta} - \frac{G}{\Delta} \nu_{t,n})(\frac{2V}{r})] - \frac{2}{r} (\frac{1}{h_3} V_\zeta - \frac{G}{\Delta} V_n) + \frac{W}{r^2} \tag{III-51c}$$

$$s_k = - \sigma_k R_{eff} (G - \epsilon) \tag{III-51d}$$

$$s_\epsilon = - \sigma_\epsilon R_{eff} (C_{\epsilon 1} \frac{\epsilon}{k} G - C_{\epsilon 2} \frac{\epsilon^2}{k}) \tag{III-51e}$$

33

with

$$G = \nu_t \{ 2(U_\xi - \frac{F}{\Delta} U_\eta)^2 + 2(\frac{1}{\Delta} V_\eta)^2 + 2(\frac{1}{h_3} W_\zeta - \frac{G}{\Delta} W_\eta + \frac{V}{r})^2$$

$$+ (\frac{1}{h_3} U_\zeta - \frac{G}{\Delta} U_\eta + W_\xi - \frac{F}{\Delta} W_\eta)^2 + (V_\xi - \frac{F}{\Delta} V_\eta + \frac{1}{\Delta} U_\eta)^2$$

$$+ (\frac{1}{h_3} V_\zeta - \frac{G}{\Delta} V_\eta + \frac{1}{\Delta} W_\eta - \frac{W}{r})^2 \} \qquad (III-51f)$$

When the partially-parabolic assumptions, discussed later, are made by neglecting the stress gradients along the direction of ship motion x, the above equations reduce to those employed in Abdelmeguid et al. (1979) and Muraoka (1980, 1982).

Thus, the general equations (III-24) and (III-32) can be used with analytic as well as numerical coordinate transformations. When other analytic or numerical coordinate transformations are considered, one needs only to replace the three sets of coefficients b_ℓ^i, g^{ij} and f^i. The subsequent solution procedure remains exactly the same. This demonstrates the generality and flexibility of the present approach in setting up the governing equations and coordinates.

III.3 The Partially-Parabolic Equations

As discussed in Section II, the partially-parabolic approximations are based on the physical assumption that longitudinal diffusion due to viscosity and turbulence may be neglected in a certain class of flows at high Reynolds numbers. Noting that in most flows of practical interest, and in particular on ship sterns, the direction of the mean streamlines may vary significantly from point to point, the most appropriate coordinate system which captures the spirit of the partially-parabolic approximations is the intrinsic or streamline coordinate system. While such a system has been used recently in the simpler case of axisymmetric flows (Zhou, 1982; Hogan, 1983), it is not a very practical one for three-dimensional flows. In

most previous applications of partially-parabolic equations, diffusion has been neglected in some preselected primary or predominant flow direction, e.g. in the direction of ship motion. Thus, all x-derivatives of the viscous and turbulent stresses are dropped in the Reynolds equations (III-2) through (III-4) prior to a coordinate transformation. Obviously, significant errors may arise in regions where the direction of the local flow deviates appreciably from the selected primary-flow direction. In addition, the omission of ϕ_{xx} is not sufficient to render the equations partially-parabolic in the transformed domain unless a particular type of coordinate system, in which $\xi = \xi(x)$, is selected. This can be seen clearly from the following. Since

$$\phi_x = \xi_x \phi_\xi + \eta_x \phi_\eta + \zeta_x \phi_\zeta$$

$$\phi_y = \xi_y \phi_\xi + \eta_y \phi_\eta + \zeta_y \phi_\zeta \qquad (III-52)$$

$$\phi_z = \xi_z \phi_\xi + \eta_z \phi_\eta + \zeta_z \phi_\zeta$$

and

$$\phi_{xx} = \xi_x^2 \phi_{\xi\xi} + \eta_x^2 \phi_{\eta\eta} + \zeta_x^2 \phi_{\zeta\zeta} + 2\xi_x \eta_x \phi_{\xi\eta} + 2\xi_x \zeta_x \phi_{\xi\zeta} + 2\eta_x \zeta_x \phi_{\eta\zeta}$$

$$+ \xi_{xx} \phi_\xi + \eta_{xx} \phi_\eta + \zeta_{xx} \phi_\zeta$$

$$\phi_{yy} = \xi_y^2 \phi_{\xi\xi} + \eta_y^2 \phi_{\eta\eta} + \zeta_y^2 \phi_{\zeta\zeta} + 2\xi_y \eta_y \phi_{\xi\eta} + 2\xi_y \zeta_y \phi_{\xi\zeta} + 2\eta_y \zeta_y \phi_{\eta\zeta}$$

$$+ \xi_{yy} \phi_\xi + \eta_{yy} \phi_\eta + \zeta_{yy} \phi_\zeta$$

$$\phi_{zz} = \xi_z^2 \phi_{\xi\xi} + \eta_z^2 \phi_{\eta\eta} + \zeta_z^2 \phi_{\zeta\zeta} + 2\xi_z \eta_z \phi_{\xi\eta} + 2\xi_z \zeta_z \phi_{\xi\zeta} + 2\eta_z \zeta_z \phi_{\eta\zeta}$$

$$+ \xi_{zz} \phi_\xi + \eta_{zz} \phi_\eta + \zeta_{zz} \phi_\zeta \qquad (III-53)$$

the viscous diffusion terms $\mu \nabla^2 \phi$ become

$$\mu \nabla^2 \phi = \mu(\phi_{xx} + \phi_{yy} + \phi_{zz})$$

$$= \mu(g^{11}\phi_{\xi\xi} + g^{22}\phi_{\eta\eta} + g^{33}\phi_{\zeta\zeta} + 2g^{12}\phi_{\xi\eta} + 2g^{13}\phi_{\xi\zeta} + 2g^{23}\phi_{\eta\zeta}$$

$$+ f^1\phi_\xi + f^2\phi_\eta + f^3\phi_\zeta)$$

with

$$g^{11} = x_\xi^2 + y_\xi^2 + z_\xi^2, \text{ etc.} \tag{III-54}$$

Therefore, the omission of ϕ_{xx} does not strictly imply that $g^{11} = 0$. In order to render the transformed equations partially-parabolic, one must select $\xi = \xi(x)$, i.e., $\xi_y = \xi_z = 0$, so that there is no contribution of ϕ_{yy} and ϕ_{zz} to $\phi_{\xi\xi}$. In other words, additional approximations must be made, explicitly or implicitly, to render the transformed equations partially-parabolic if a general coordinate transformation $\xi = \xi(x,y,z)$ is to be used.

In the present work, an alternative approach is employed by introducing the partially-parabolic approximations after transforming the fully-elliptic Reynolds equations into the body-fitted coordinates. Mathematically, equations (III-24) can be rendered partially-parabolic by simply neglecting the terms involving the second derivatives with respect to ξ, the marching direction, to obtain

$$g^{22}\phi_{\eta\eta} + g^{33}\phi_{\zeta\zeta} = 2A_\phi\phi_\zeta + 2B_\phi\phi_\eta + D_\phi\phi_\xi + E_\phi\phi_t + S_\phi \tag{III-55}$$

Where, all coefficients remain the same as defined earlier. Note that all first derivatives in the $\xi-$ direction arising out of the diffusive terms and coordinate transformations are retained in these coefficients. These approximations do not strictly imply that the physical diffusion in the $\xi-$ direction is neglected, as the following shows.

From Equation (III-54), we note that, even for laminar flows, $\mu g^{11} \phi_{\xi\xi}$ does not represent the physical diffusion in the ξ- direction unless $g^{12}=g^{13}=0$ and $f^1=0$. The former requires an orthogonal coordinate system (ξ,η,ζ) in the transformed plane, while the latter places a restriction on the grid distribution. The interpretation of $\phi_{\xi\xi}$ becomes even more difficult when turbulent flows are considered. For example, the molecular and turbulent diffusion of x-momentum in the x-direction in (x,y,z) or (x,r,θ) coordinates, using equation (III-5), is simply

$$\frac{\partial}{\partial x}\left[2\nu\frac{\partial U}{\partial x} - \overline{uu}\right] = 2(\nu + \nu_t)\frac{\partial^2 U}{\partial x^2} + 2\frac{\partial \nu_t}{\partial x}\frac{\partial U}{\partial x} - \frac{2}{3}\frac{\partial k}{\partial x}$$

In our general notation, this is

$$= \frac{2}{R_{eff}}\phi_{xx} + 2\nu_{t,x}\phi_x - \frac{2}{3}k_x; \qquad \phi \equiv U \qquad\qquad \text{(III-56)}$$

Mathematically, it is necessary to neglect only the first term to render the x-momentum equation parabolic in the x-direction. The second term can be retained and treated in the same manner as the convective term $U\phi_x$ in the equations while the third can be absorbed into the source terms.

Whether the present approach represents an improvement over the convectional one remains to be determined by actual solutions. Nevertheless, two important features of this approach are noteworthy. First, invoking the partially-parabolic approximations in the body-fitted coordinates, in which ξ is taken along the body, and along an external streamline far from the body, ensures that diffusion is neglected in a direction roughly coincident with the local streamlines in the solution domain. Secondly, the omission of the fewest terms in the complete Reynolds equations facilitates the future extension of the solution procedure to the fully-elliptic equations. In fact, one may simply retain $\phi_{\xi\xi}$ in the source functions S_ϕ and estimate their contributions from the solution at a previous time step or

iteration. This is then a fully-elliptic formulation with upwind differencing for first derivatives with respect to ξ.

In order to illustrate the physical significance of the partially-parabolic approximations in general, it is instructive to consider the following linear one-dimensional elliptic transport equation with constant positive convective coefficient A and source function g

$$\phi_{xx} = 2A\phi_x + g \qquad (III-57)$$

subjected to the boundary conditions

$$\phi(-h) = \phi_U \; ; \; \phi(h) = \phi_D$$

where the subscripts U and D denote upstream and downstream, respectively. The analytic solution of equation (III-57), when evaluated at the center node P of the interval $-h < x < h$, gives

$$\phi_P = \left(\frac{e^{Ah}}{e^{Ah} + e^{-Ah}}\right) \phi_U + \left(\frac{e^{-Ah}}{e^{Ah} + e^{-Ah}}\right) \phi_D - \left(\frac{h \tanh Ah}{2A}\right) g \qquad (III-58)$$

This indicates that the influence from downstream decreases rapidly as the convective coefficient 2A (or the cell Reynolds number) becomes large. Furthermore, the derivative at point P can also be obtained analytically as

$$\phi_x \Big|_P = \frac{2A(\phi_D - \phi_U) + 2gh}{e^{2Ah} - e^{-2Ah}} - \frac{g}{2A} \qquad (III-59)$$

For large convective coefficients, this simply reduces to

$$\phi_x \Big|_P = -\frac{g}{2A} \qquad (III-60)$$

in agreement with equation (III-57) with $\phi_{xx} = 0$.

Thus, with the present partially-parabolic approximations ($\phi_{\xi\xi} = 0$), the ξ- derivatives associated with the convective

terms (ϕ_ξ, $\nu_{t,\xi}$) can be evaluated using backward or upwind differences, i.e.,

$$\phi_\xi \Big|_P = \frac{\phi_P - \phi_U}{h} \qquad (III-61)$$

This is also supported by the analytic solution of the model equation since, from equation (III-58),

$$\frac{\phi_P - \phi_U}{h} = \frac{e^{-Ah}}{e^{Ah} + e^{-Ah}} \frac{\phi_D - \phi_U}{h} - \frac{\tanh Ah}{2A} g$$

$$\simeq -\frac{g}{2A} \qquad (III-62)$$

for large A, in agreement with the asymptotic behavior noted above.

Note that the convective coefficient A in equations (III-57) and (III-60) may contain $\nu_{t,x}$ and f^1, in addition to U, for turbulent flows in general coordinates. Therefore, the second term in equation (III-56) should be retained for consistency although ϕ_{xx} is no longer the physical diffusion.

With the ξ- derivatives in the general transport equations (III-55) evaluated by upwind differences, it is possible to solve them by a numerical technique marching in the ξ- direction, provided the pressure gradients in the source terms S_ϕ ($\phi \equiv$ U, V, W) are known. The pressure is obtained, in turn, by requiring the velocity field to satisfy the continuity equation (III-32).

39

IV. NUMERICAL SOLUTION PROCEDURES

In this section we consider the numerical techniques for grid generation and the solution of the partially-parabolic equations (III-55)

$$g^{22}\phi_{\eta\eta} + g^{33}\phi_{\zeta\zeta} = 2A_\phi\phi_\zeta + 2B_\phi\phi_\eta + D_\phi\phi_\xi + E_\phi\phi_t + S_\phi \qquad (IV-1)$$

and the equation of continuity (III-32)

$$(b_1^1 U + b_2^1 V + b_3^1 W)_\xi + (b_1^2 U + b_2^2 V + b_3^2 W)_\eta$$

$$+ (b_1^3 U + b_2^3 V + b_3^3 W)_\zeta = 0 \qquad (IV-2)$$

Details of the numerical method used in grid generation, together with some examples, are presented in Section IV.1. The finite-analytic numerical method of Chen and Chen (1982, 1984), developed initially for elliptic equations, is then revised and extended to solve the five transport equations (IV-1) for ϕ = U,V,W,k and ε with a guessed pressure field. This is described in Section IV.2. The continuity equation is used to obtain equations which enable the determination of the pressure and pressure-correction fields from the velocity field. This procedure is described in Section IV.3. The treatment of the boundary conditions is described in Section IV.4, and the overall numerical solution algorithm is then outlined in Section IV.5.

IV.1. Grid Generation

As described in Section III.1, a general curvilinear co-ordinate system can be constructed by numerically solving equations (III-21), i.e.,

$$\nabla^2 x^1 = \frac{1}{h_1 h_2 h_3} \frac{\partial}{\partial x^1} \left(\frac{h_2 h_3}{h_1}\right)$$

$$\nabla^2 x^2 = \frac{1}{h_1 h_2 h_3} \frac{\partial}{\partial x^2} \left(\frac{h_1 h_3}{h_2}\right) \qquad \text{(IV-3)}$$

$$\nabla^2 x^3 = \frac{1}{h_1 h_2 h_3} \frac{\partial}{\partial x^3} \left(\frac{h_1 h_2}{h_3}\right)$$

where

$$\nabla^2 = g^{11} \frac{\partial^2}{\partial \xi^2} + g^{22} \frac{\partial^2}{\partial \eta^2} + g^{33} \frac{\partial^2}{\partial \zeta^2} + 2g^{12} \frac{\partial^2}{\partial \xi \partial \eta} + 2g^{13} \frac{\partial^2}{\partial \xi \partial \zeta} + 2g^{23} \frac{\partial^2}{\partial \eta \partial \zeta}$$

$$+ f^1 \frac{\partial}{\partial \xi} + f^2 \frac{\partial}{\partial \eta} + f^3 \frac{\partial}{\partial \zeta} \qquad \text{(IV-3a)}$$

h_i are the metric coefficients in the chosen orthogonal coordinates x^i and g^{ij} is the conjugate metric tensor in the transformed coordinates (ξ, η, ζ). The control functions f^i can be chosen to generate the desired grid concentration. Note that the orthogonal coordinates x^i in the physical plane can be selected arbitrarily. The equations for two cases are given below.

(i) Cartesian Coordinates in the Physical Plane

When Cartesian coordinates are used to describe the three-dimensional computational domain, a body-fitted grid system can be generated from equation (IV-3) with $(x^1, x^2, x^3) = (x, y, z)$ and $(h^1, h^2, h^3) = (1, 1, 1)$, i.e.,

$$g^{11} x_{\xi\xi} + g^{22} x_{\eta\eta} + g^{33} x_{\zeta\zeta} + 2g^{12} x_{\xi\eta} + 2g^{13} x_{\xi\zeta}$$

$$+ 2g^{23} x_{\eta\zeta} + f^1 x_\xi + f^2 x_\eta + f^3 x_\zeta = 0$$

$$g^{11}y_{\xi\xi} + g^{22}y_{\eta\eta} + g^{33}y_{\zeta\zeta} + 2g^{12}y_{\xi\eta} + 2g^{13}y_{\xi\zeta}$$

$$+ 2g^{23}y_{\eta\zeta} + f^{1}y_{\xi} + f^{2}y_{\eta} + f^{3}y_{\zeta} = 0 \qquad (IV-4)$$

$$g^{11}z_{\xi\xi} + g^{22}z_{\eta\eta} + g^{33}z_{\zeta\zeta} + 2g^{12}z_{\xi\eta} + 2g^{13}z_{\xi\zeta}$$

$$+ 2g^{23}z_{\eta\zeta} + f^{1}z_{\xi} + f^{2}z_{\eta} + f^{3}z_{\zeta} = 0$$

where

$$g^{1i} = \frac{1}{g}(g_{mj}g_{nk} - g_{mk}g_{nj}), \quad \text{with cyclic } (i,j,k) \text{ and } (l,m,n),$$

$$g_{11} = x_{\xi}^2 + y_{\xi}^2 + z_{\xi}^2$$

$$g_{22} = x_{\eta}^2 + y_{\eta}^2 + z_{\eta}^2$$

$$g_{33} = x_{\zeta}^2 + y_{\zeta}^2 + z_{\zeta}^2$$

$$g_{12} = g_{21} = x_{\xi}x_{\eta} + y_{\xi}y_{\eta} + z_{\xi}z_{\eta} \qquad (IV-5)$$

$$g_{13} = g_{31} = x_{\xi}x_{\zeta} + y_{\xi}y_{\zeta} + z_{\xi}z_{\zeta}$$

$$g_{23} = g_{32} = x_{\eta}x_{\zeta} + y_{\eta}y_{\zeta} + z_{\eta}z_{\zeta}$$

$$g = J^2 = g_{11}g_{22}g_{33} + 2g_{12}g_{13}g_{23} - (g_{23})^2 g_{11}$$

$$- (g_{13})^2 g_{22} - (g_{12})^2 g_{33}$$

For a two-dimensional flow field in the xy-plane, the governing equations (IV-4) can be simplified by letting $\zeta = z$, so that we have

$$g^{11}x_{\xi\xi} + g^{22}x_{\eta\eta} + 2g^{12}x_{\xi\eta} + f^1x_\xi + f^2x_\eta = 0$$

$$g^{11}y_{\xi\xi} + g^{22}y_{\eta\eta} + 2g^{12}y_{\xi\eta} + f^1y_\xi + f^2y_\eta = 0$$

(IV-6)

with

$$gg^{11} = g_{22} = x_\eta^2 + y_\eta^2$$

$$gg^{12} = -g_{12} = -(x_\xi x_\eta + y_\xi y_\eta)$$

(IV-7)

$$gg^{22} = g_{11} = x_\xi^2 + y_\xi^2$$

$$g = J^2 = (x_\xi y_\eta - x_\eta y_\xi)^2$$

(ii) Cylindrical Polar Coordinates in the Physical Plane

For applications related to axisymmetric bodies and ship forms, it is more convenient to use the cylindrical polar coordinates instead of the Cartesian coordinates. The governing equations for this transformation are obtained by letting $(x^1, x^2, x^3) = (x, r, \theta)$ and $(h_1, h_2, h_3) = (1, 1, r)$ in equation (IV-3), i.e.,

$$g^{11}x_{\xi\xi} + g^{22}x_{\eta\eta} + g^{33}x_{\zeta\zeta} + 2g^{12}x_{\xi\eta} + 2g^{13}x_{\xi\zeta}$$

$$+ 2g^{23}x_{\eta\zeta} + f^1x_\xi + f^2x_\eta + f^3x_\zeta = 0$$

$$g^{11}r_{\xi\xi} + g^{22}r_{\eta\eta} + g^{33}r_{\zeta\zeta} + 2g^{12}r_{\xi\eta} + 2g^{13}r_{\xi\zeta}$$

$$+ 2g^{23}r_{\eta\zeta} + f^1r_\xi + f^2r_\eta + f^3r_\zeta = \frac{1}{r}$$

(IV-8)

$$g^{11}\theta_{\xi\xi} + g^{22}\theta_{\eta\eta} + g^{33}\theta_{\zeta\zeta} + 2g^{12}\theta_{\xi\eta} + 2g^{13}\theta_{\xi\zeta}$$

$$+ 2g^{23}\theta_{\eta\zeta} + f^1\theta_\xi + f^2\theta_\eta + f^3\theta_\zeta = 0$$

where g^{ij} are given by equations (III-28) through (III-31).

For axisymmetric flows, we set $\zeta = \theta$ in equations (IV-8), so that

$$g^{11}x_{\xi\xi} + g^{22}x_{\eta\eta} + 2g^{12}x_{\xi\eta} + f^1x_\xi + f^2x_\eta = 0$$

$$g^{11}r_{\xi\xi} + g^{22}r_{\eta\eta} + 2g^{12}r_{\xi\eta} + f^1r_\xi + f^2r_\eta = \frac{1}{r}$$

<div style="text-align:right">(IV-9)</div>

where g^{ij} are given in equations (III-37) through (III-38) as:

$$gg^{11} = r^2 g_{22} = r^2(x_\eta^2 + r_\eta^2)$$

$$gg^{12} = -r^2 g_{12} = -r^2(x_\xi x_\eta + r_\xi r_\eta)$$

$$gg^{22} = r^2 g_{11} = r^2(x_\xi^2 + r_\xi^2)$$

<div style="text-align:right">(IV-10)</div>

$$g = J^2 = r^2(x_\xi r_\eta - x_\eta r_\xi)^2$$

(iii) Choice of Coordinates and Numerical Solutions

The above equations can be solved numerically in the transformed domain ξ^i when appropriate grid-control functions f^i are selected and proper boundary conditions are specified on all boundary surfaces. Depending upon the particular application, equations (IV-4) or (IV-8) have been used previously to generate various body-fitted coordinates. A review of these algorithms has been made recently by Thompson, Warsi and Mastin (1982). The present formulation provides greater flexibility and generality in the selection of the coordinate systems in the physical plane.

44

Insofar as the problem of grid generation is concerned, the choice of the basic orthogonal coordinate system used to describe the boundaries of the computation domain in the physical plane is a matter of convenience. For example, the flow on an axisymmetric body is best described in cylindrical polar coordinates although a three-dimensional formulation with Cartesian coordinates can also be employed. If the boundaries in the physical plane are all straight, it may be more convenient to start with the Cartesian coordinates. For three-dimensional bodies, such as ship hulls, both the Cartesian and the cylindrical-polar coordinates can be used. If the equations of motion are transformed completely so that the velocity components are in the direction of the transformed coordinates, the choice of the orthogonal coordinates used in the physical plane is immaterial. However, if only a partial transformation is used, with the velocity components left in the basic orthogonal system, as in the present formulation, then the choice of the basic coordinate system becomes important and is dictated by the numerical algorithm used to solve the flow equations. The problem is illustrated in Fig. 3, which shows a numerically-generated grid for a ship section. It is clear that the use of Cartesian components which do not rotate with the η, ζ coordinates will lead to serious, and perhaps insurmountable, numerical difficulties. On the other hand, since the velocity components in polar coordinates rotate with the η, ζ directions, the numerical problems are avoided. Although, as noted above, the need for an a priori choice of the basic coordinates in the physical plane for each class of problems can be avoided by a complete transformation of the equations into the numerical cocordinates, the additional computer storage required for practical three-dimensional flows appears to be prohibitive at the present time, and the authors are not aware of successful solutions using such coordinates. However, the partial transformations used here enable solutions to be obtained in a cost-effective manner with modest-size computers.

For applications to axisymmetric bodies and elongated three-dimensional bodies with one or more planes of symmetry, such as airplane fuselages and ship forms, it is convenient to construct coordinates such that axial cross-sections of the body form one set of coordinate surfaces, i.e. to select $\xi(x)$, where x is measured along the body axis. This results in some simplification of the equations of motion and also facilitates the specification of the computation domain and boundary conditions. Other advantages include the possibility of constructing orthogonal or nearly-orthogonal coordinates in the cross-sectional planes, a continuous evolution of the coordinates from the tail of the body into the wake, and the ease of interpretation of the results. An obvious disadvantage of using generalized coordinates, which is often overlooked, is that considerable interpolation in the computed results may be required in order to make comparisons with experimental data obtained in a convenient, and usually orthogonal, laboratory coordinate system.

The present coordinate-generation method is illustrated by means of two examples, namely an axisymmetric body and an elongated ship-like body whose cross-sections are everywhere elliptic with an axis ratio of 3:1. In both cases the flow region of interest is the thick boundary layer over the stern and its evolution into the wake.

To generate the coordinates for an axisymmetric body (Afterbody 5 of Huang et al., 1980), the constant-ξ stations are chosen to be the constant-x planes (i.e., the transverse sections). The first station, $\xi = 1$, is located at $X = 0.6L$ while the last station, $\xi = 60$, is located in the far wake at $X = 13.20L$, where L is the body length and x is the axial distance from the nose. In the radial direction, the outer boundary is cylindrical and is placed at $R = 0.3137L$, which corresponds to $\eta = 19$ in the transformed domain. Under this arrangement, equations (IV-9) reduce to

$$g^{11}r_{\xi\xi} + g^{22}r_{\eta\eta} + 2g^{12}r_{\xi\eta} + f^1 r_\xi + f^2 r_\eta = \frac{1}{r} \qquad \text{(IV-11)}$$

with

$$f^1 = - g^{11} \frac{x_{\xi\xi}}{x_\xi} \qquad \text{(IV-12)}$$

The control function f^1 is therefore determined by the desired distribution of the axial stations. With f^1 specified, equation (IV-11) yields the distribution of points in the radial direction, $r(\xi,\eta)$. To obtain the desired grid distribution in this direction, the control function f^2 is prescribed by

$$f^2(\xi,\eta) = \frac{1}{rr_\eta} + F^2(\xi,\eta) \qquad \text{(IV-13)}$$

with

$$F^2(\xi,\eta) = \begin{cases} F_A(\eta) & \xi < \xi_A \\ F_C(\xi,\eta) & \xi_A < \xi < \xi_B \\ F_B(\eta) & \xi > \xi_B \end{cases} \qquad \text{(IV-13a)}$$

where $\xi_A = 15$, $\xi_B = 42$, and F_A and F_B are determined by the node distributions at the initial and final stations as

$$F_A(\eta) = - g^{22} \frac{r_{\eta\eta}}{r_\eta} \Bigg|_{\xi=1} \qquad \text{(IV-13b)}$$

$$F_B(\eta) = - g^{22} \frac{r_{\eta\eta}}{r_\eta} \Bigg|_{\xi=60} \qquad \text{(IV-13c)}$$

and F_C is given by a linear combination of F_A and F_B:

$$F_C(\xi,\eta) = [(\xi_B-\xi)F_A(\eta) + (\xi-\xi_A)F_B(\eta)]/(\xi_B-\xi_A) \qquad \text{(IV-13d)}$$

Note that equation (IV-11), together with the f^2 defined in equation (IV-13), reduces to the following homogeneous equation

47

$$g^{11}r_{\xi\xi} + g^{22}r_{\eta\eta} + 2g^{12}r_{\xi\eta} + f^1 r_\xi + F^2 r_\eta = 0 \qquad \text{(IV-14)}$$

which is equivalent to the two-dimensional formulation in Cartesian coordinates (x,r) with control functions f^1 and F^2. Therefore, the same grid distributions can be generated in both the cylindrical and Cartesian coordinates if the control function f^2 is replaced by F^2 in the latter formulation.

Equation (IV-14), with the control functions specified by equations (IV-12) and (IV-13), can be solved by any convenient numerical method. Here, we have used two different finite-difference techniques, namely, a central-difference scheme and an exponential scheme.

In the central-difference scheme, the discretized form of equation (IV-14) can be written

$$
\begin{aligned}
r_{\xi,\eta} = &\{ (g^{11} + 0.5f^1)_{\xi,\eta} r_{\xi+1,\eta} + (g^{11} - 0.5f^1)_{\xi,\eta} r_{\xi-1,\eta} \\
&+ (g^{22} + 0.5F^2)_{\xi,\eta} r_{\xi,\eta+1} + (g^{22} - 0.5F^2)_{\xi,\eta} r_{\xi,\eta-1} \\
&+ 0.5 g^{12}_{\xi,\eta} (r_{\xi+1,\eta+1} + r_{\xi-1,\eta-1} - r_{\xi-1,\eta+1} - r_{\xi+1,\eta-1}) \} \\
&/ [2(g^{11} + g^{22})_{\xi,\eta}] \qquad \text{(IV-15)}
\end{aligned}
$$

with $2 < \xi < 59$, $2 < \eta < 18$. With the Neumann conditions specified at the boundaries, this system of algebraic equations was solved by an SOR algorithm with an over-relaxation factor of 1.8. The results are shown in Fig. 4 by the dotted lines. The boundary-fitted coordinates thus obtained evolve smoothly from the body into the wake, and give the desired grid distribution in the thick boundary layer region over the tail of the body.

We note that, with nonzero f^1 and F^2, equation (IV-14) is, in fact, a convective-transport equation with convective velocities or cell Reynolds numbers $-f^1/g^{11}$ and $-F^2/g^{22}$ in the

transformed plane. It is well known that a negative $F^2(\xi,\eta)$ value (i.e., positive convective velocity) will result in an upwind bias from smaller constant-η lines, and therefore pull the grid lines toward the body surface. On the other hand, a positive F^2 value results in the expansion of grid lines near the body surface. For large values of the cell Reynolds numbers (i.e., $|f^1/g^{11}|$ or $|F^2/g^{22}| > 2$), the central-difference scheme becomes inaccurate and unstable due to the negative coefficients (i.e., $(g^{11} + 0.5f^1) < 0$ or $(g^{22} + 0.5F^2) < 0$) appearing in the discretized equation (IV-15).

In order to avoid the instability of the central-difference scheme and improve the accuracy, the exponential scheme of Spalding (1972) was also employed to provide an automatic upwind shift. With this scheme, the governing equation (IV-14) can be written as

$$(2g^{11}a \coth a + 2g^{22}b \coth b)_{\xi,\eta} r_{\xi,\eta}$$

$$= (2g^{11}a \operatorname{csch} a)_{\xi,\eta}(e^{-a}r_{\xi+1,\eta} + e^{a}r_{\xi-1,\eta})$$

$$+ (2g^{22}b \operatorname{csch} b)_{\xi,\eta}(e^{-b}r_{\xi,\eta+1} + e^{b}r_{\xi,\eta-1})$$

$$+ 2g^{12}_{\xi,\eta} (r_{\xi+1,\eta+1} + r_{\xi-1,\eta-1} - r_{\xi-1,\eta+1} - r_{\xi+1,\eta-1}) \qquad \text{(IV-16)}$$

with

$$2a = - \left.\frac{f^1}{g^{11}}\right|_{\xi,\eta} = \left.\frac{x_{\xi\xi}}{x_{\xi}}\right|_{\xi=\text{constant}} \qquad \text{(IV-16a)}$$

$$2b = - \left.\frac{F^2}{g^{22}}\right|_{\xi,\eta} \qquad \text{(IV-16b)}$$

49

The above system of algebraic equations was solved by the tri-diagonal-matrix algorithm with an over-relaxation factor of 1.8. The coordinates thus obtained are shown by the solid lines in Fig. 4.

It can be seen that the coordinate lines obtained by both schemes agree quite well everywhere. However, the discrepancy will increase when larger values of $F^2(\xi,\eta)$ are used. Note that the central-difference scheme yields consistently lower values due to the stronger upwind influence from smaller constant-η lines. This eventually leads to the occurrence of a minimum in the interior of the domain as the values of F^2 become large. On the other hand, the exponential scheme assures a one-to-one mapping between the physical and transformed planes since all influence coefficients in equation (IV-16) are positive.

In order to demonstrate the grid-generation technique for a three-dimensional body, we consider the 3:1 elliptic body of Huang et al. (1983). In this example, the outer boundary is a cylindrical surface of radius R = 0.8137L, which corresponds to η = 19 in the transformed plane. The constant-ξ stations are again chosen to be the constant-x planes, with the initial (ξ=1) and final (ξ=60) stations located at X = 0.5L and X = 16.25L, respectively. In the circumferential direction, seven stations are used, with ζ=2 and 6 corresponding to θ = 0° and 90°, respectively. The symmetry conditions at θ = 0° and 90° are, respectively.

$$r(\xi,\eta,1) = r(\xi,\eta,3), \quad \theta(\xi,\eta,1) = -\theta(\xi,\eta,3) \quad \text{at } \theta = 0$$

$$\text{(IV-17)}$$

$$r(\xi,\eta,7) = r(\xi,\eta,5), \quad \theta(\xi,\eta,7) = \pi-\theta(\xi,\eta,5) \quad \text{at } \theta = \frac{\pi}{2}$$

Under this arrangement, equations (IV-8) become

$$g^{11}r_{\xi\xi} + g^{22}r_{\eta\eta} + g^{33}r_{\zeta\zeta} + 2g^{12}r_{\xi\eta} + 2g^{13}r_{\xi\zeta} + 2g^{23}r_{\eta\zeta}$$

$$+ f^1 r_\xi + f^2 r_\eta + f^3 r_\zeta = \frac{1}{r} \tag{IV-18}$$

$$g^{11}\theta_{\xi\xi} + g^{22}\theta_{\eta\eta} + g^{33}\theta_{\zeta\zeta} + 2g^{12}\theta_{\xi\eta} + 2g^{13}\theta_{\xi\zeta} + 2g^{23}\theta_{\eta\zeta}$$

$$+ f^1\theta_\xi + f^2\theta_\eta + f^3\theta_\zeta = 0$$

The control functions f^1 and f^2 defined by equations (IV-12) and (IV-13) are again employed here, while $f^3(\zeta)$ is determined by the circumferential grid distribution on the outer boundary as

$$f^3(\zeta) = -g^{33}\left.\frac{\theta_{\zeta\zeta}}{\theta_\zeta}\right|_{\xi=1,\eta=19} \tag{IV-19}$$

In order to facilitate the use of wall functions in the turbulence model, Neumann boundary conditions are specified on all boundaries; i.e., $\eta = 1,19$; $\zeta = 2,6$; of the contant-ξ stations to ensure local orthogonality of these coordinates. Equations (IV-18) are then solved by a finite-difference method.

Because the central-difference scheme used in the previous example indicated a lack of convergence for large f^1, f^2 and/or f^3, only the exponential scheme described above was employed here. After some manipulation, the discretized equations become

$$(2g^{11}a \coth a + 2g^{22}b \coth b + 2g^{33}c \coth c)_{\xi,\eta,\zeta}\phi_{\xi,\eta,\zeta}$$

$$= (2g^{11}a \operatorname{csch} a)_{\xi,\eta,\zeta}(e^{-a}\phi_{\xi+1,\eta,\zeta} + e^a\phi_{\xi-1,\eta,\zeta})$$

$$+ (2g^{22}b \operatorname{csch} b)_{\xi,\eta,\zeta}(e^{-b}\phi_{\xi,\eta+1,\zeta} + e^b\phi_{\xi,\eta-1,\zeta})$$

$$+ (2g^{33}c \operatorname{csch} c)_{\xi,\eta,\zeta}(e^{-c}\phi_{\xi,\eta,\zeta+1} + e^c\phi_{\xi,\eta,\zeta-1})$$

$$+ 2g^{12}_{\xi,\eta,\zeta}(\phi_{\xi+1,\eta+1,\zeta} + \phi_{\xi-1,\eta-1,\zeta} - \phi_{\xi+1,\eta-1,\zeta}$$

$$- \phi_{\xi-1,n+1,\zeta}) + 2g^{13}_{\xi,n,\zeta}(\phi_{\xi+1,n,\zeta+1} + \phi_{\xi-1,n,\zeta-1}$$

$$- \phi_{\xi+1,n,\zeta-1} - \phi_{\xi-1,n,\zeta+1}) + 2g^{23}_{\xi,n,\zeta}(\phi_{\xi,n+1,\zeta+1}$$

$$+ \phi_{\xi,n-1,\zeta-1} - \phi_{\xi,n+1,\zeta-1} - \phi_{\xi,n-1,\zeta+1}) \qquad (IV-20)$$

where ϕ represents either r or θ, and

$$2a = -\left.\frac{f^1}{g^{11}}\right|_{\xi,n,\zeta} = \left.\frac{x_{\xi\xi}}{x_\xi}\right|_{\xi= constant} \qquad (IV-20a)$$

$$2b = \begin{cases} -\left.\dfrac{F^2}{g^{22}}\right|_{\xi,n,\zeta} = \begin{cases} F_A(n) & \xi < \xi_A \\ F_C(\xi,n) & \xi_A < \xi < \xi_B \\ F_B(n) & \xi > \xi_B \end{cases} & \text{for } \phi \equiv r \\[2em] = -\left.\dfrac{f^2}{g^{22}}\right|_{\xi,n,\zeta} & \text{for } \phi \equiv \theta \end{cases} \qquad (IV-20b)$$

$$2c = -\left.\frac{f^3}{g^{33}}\right|_{\xi,n,\zeta} = \left.\frac{\theta_{\zeta\zeta}}{\theta_\zeta}\right|_{\xi=1,\ n=19} \qquad (IV-20c)$$

with

$$F_A(n) = \left.\frac{r_{nn}}{r_n}\right|_{\xi=1,\ \zeta=6}$$

$$F_B(n) = \left.\frac{r_{nn}}{r_n}\right|_{\xi=60,\ \zeta=6}$$

$$F_C(\xi,n) = [(\xi_B-\xi)F_A + (\xi-\xi_A)F_B]/(\xi_B-\xi_A)$$

Note that the control functions F^2 and f^3 can be, in general, functions of ξ, n and ζ, although simpler expressions are used here. For more complicated geometries, the control functions may be determined by the node distributions on all boundary surfaces

and an interpolation between them. Detailed discussions regarding the selection of control functions can be found in, among others, Thompson (1982) and Thompson, Warsi and Mastin (1982).

With the Neumann boundary conditions specified on all boundaries of the constant-ξ stations, equations (IV-20) were solved by the tridiagonal-matrix algorithm with an over-relaxation factor of 1.4. The coordinates thus obtained are nearly orthogonal at each cross-section, and also provide the desired expansion in the thick boundary layer region over the tail. Figure 5 shows several views of the coordinates in the stern region.

In the present study, the control functions f^i were either specified beforehand or evaluated numerically from the prescribed distributions of boundary nodes. In most applications, the geometric coefficients g_{ij}, g^{ij} and b_i^j were evaluated using central-difference formulae. However, more accurate exponential expressions, derived from the local analytic solutions, can be employed to evaluate these geometric coefficients when the grid expansion ratios become large. Note that coordinate systems generated by central-difference and exponential schemes will, in general, give different geometric coefficients even if the same control functions are employed.

Since the geometric coefficients and the control functions appear in the continuity and the convective-transport equations, numerical errors arising from the grid-generation technique are not entirely decoupled from errors in the flow calculations. In order to reduce this error propagation, the coordinates generated by the exponential scheme were adopted in all calculations presented here.

If other grid-generation techniques, such as conformal transformations, are employed to generate the coordinates, it is still possible to use the convective-transport equations (IV-1)

derived earlier, provided the control functions f^i are evaluated numerically from equation (A-57), i.e.,

$$f^i = \frac{1}{J} \frac{\partial}{\partial \xi^j} (Jg^{ij}) \qquad\qquad (IV-21)$$

In this fashion, numerical errors in the flow calculations can be decoupled from those introduced by the grid-generation technique. However, the use of equation (A-57) for f^i, which involves second derivatives of the coordinates, may result in significant numerical errors in the fluid-flow calculations. Therefore, the control functions used here were read directly from the grid-generation routines, rather than evaluating them numerically from equation (A-57).

IV.2 Finite-Analytic Method for the Transport Equations

Because of the absence of the term $\phi_{\xi\xi}$ in the convective transport equations (IV-1), these equations are parabolic in the ξ- direction but remain elliptic in the $\eta\zeta$ plane. In order to correctly predict the elliptic nature of the flow at each cross-section, the finite-analytic method of Chen and Chen (1982, 1984), has been revised and extended to solve the present partially-parabolic transport equations. The solution procedure is described in the following.

In the finite-analytic approach, equations (IV-1) in each rectangular numerical element, $\Delta\xi = \Delta\eta = \Delta\zeta = 1$, are locally linearized as

$$g_p^{22} \phi_{\eta\eta} + g_p^{33} \phi_{\zeta\zeta} = 2(A_\phi)_p \phi_\zeta + 2(B_\phi)_p \phi_\eta + g \qquad (IV-22)$$

with

$$g = (D_\phi)_p(\phi_p - \phi_U) + \frac{(E_\phi)_p}{\tau}(\phi_p - \phi_p^{n-1}) + (S_\phi)_p \qquad (IV-22a)$$

where the subscript P denotes the center node P of the element shown in Fig. 6 and τ is the time increment. Thus, the time- and ξ- derivatives are approximated by backward-difference formulae, subscript U denoting the upstream nodal value, and superscript (n-1) denoting the value at the previous time step. If we introduce the coordinate-stretching functions

$$\eta^* = \frac{\eta}{\sqrt{g_P^{22}}} \quad , \quad \zeta^* = \frac{\zeta}{\sqrt{g_P^{33}}} \tag{IV-23}$$

equation (IV-22) reduces to the standard two-dimensional convective-transport equation described in Chen & Chen (1982, 1984), i.e.,

$$\phi_{\zeta^*\zeta^*} + \phi_{\eta^*\eta^*} = 2A\phi_{\zeta^*} + 2B\phi_{\eta^*} + g \tag{IV-24}$$

with

$$A = \frac{(A_\phi)_P}{\sqrt{g_P^{33}}} \quad , \quad B = \frac{(B_\phi)_P}{\sqrt{g_P^{22}}} \tag{IV-24a}$$

for a local element with dimensions

$$\Delta\xi = 1$$

$$\Delta\eta^* = k = \frac{1}{\sqrt{g_P^{22}}} \tag{IV-24b}$$

$$\Delta\zeta^* = h = \frac{1}{\sqrt{g_P^{33}}}$$

By specifying a combination of exponential and linear boundary functions, which are derived from the natural solutions of the governing equations, on all four boundaries $\eta^* = \pm k$ and $\zeta^* = \pm h$ of each local element, i.e.,

$$\phi(k, \zeta^*) = a_N(e^{2A\zeta^*} - 1) + b_N\zeta^* + c_N \tag{IV-25a}$$

$$\phi(-k, \zeta^*) = a_S(e^{2A\zeta^*} - 1) + b_S\zeta^* + c_S \tag{IV-25b}$$

$$\phi(\eta^*, h) = a_E(e^{2B\eta^*} - 1) + b_E\eta^* + c_E \tag{IV-25c}$$

$$\phi(\eta^*, -h) = a_W(e^{2B\eta^*} - 1) + b_W\eta^* + c_W \tag{IV-25d}$$

where a, b and c are constants, equation (IV-24) can be solved analytically for each element by the method of separation of variables or any other analytic technique. Details of the solution procedures are described in Chen & Chen (1982, 1984). When the local analytic solution thus derived is evaluated at the central node P of the element, the following nine-point finite-analytic algebraic equation is obtained.

$$\phi_P = C_{NE}\phi_{NE} + C_{NW}\phi_{NW} + C_{SE}\phi_{SE} + C_{SW}\phi_{SW} + C_{EC}\phi_{EC} + C_{WC}\phi_{WC}$$

$$+ C_{NC}\phi_{NC} + C_{SC}\phi_{SC} - C_{S3} \tag{IV-26}$$

where

$$C_{SC} = \left(\frac{e^{Bk}}{2\cosh Bk}\right) P_A$$

$$C_{NC} = e^{-2Bk}C_{SC}$$

$$C_{WC} = \left(\frac{e^{Ah}}{2\cosh Ah}\right) P_B$$

$$C_{EC} = e^{-2Ah}C_{WC}$$

$$C_{SW} = \left(\frac{e^{Ah+Bk}}{4\cosh Ah\cosh Bk}\right)(1 - P_A - P_B)$$

$$C_{SE} = e^{-2Ah}C_{SW}$$

$$C_{NW} = e^{-2Bk}C_{SW}$$

$$C_{NE} = e^{-2Ah-2Bk}C_{SW}$$

$$C_P = \frac{h\ \tanh\ Ah}{2A}\ (1-P_A) = \frac{k\ \tanh\ Bk}{2B}\ (1-P_B)$$

$$P_A = 4E_2\ Ah\ \cosh\ Ah\ \cosh\ Bk\ \coth\ Ah$$

$$P_B = 1 + \frac{Bh\ \coth\ Bk}{Ak\ \coth\ Ah}\ (P_A - 1)$$

and

$$E_2 = \sum_{m=1}^{\infty} \frac{-\ (-1)^m(\lambda_m h)}{[(Ah)^2 + (\lambda_m h)^2]^2 \cosh\ \sqrt{A^2 + B^2 + \lambda_m^2}\ k}$$

$$\lambda_m h = (m - \frac{1}{2})\ \pi$$

The above coefficients are simple rearrangements of those given in Chen & Chen, but are more convenient for efficient numerical calculations. Note that some of them are interrelated as follows:

$$C_{NC} + C_{SC} = P_A$$

$$C_{EC} + C_{WC} = P_B \hspace{3cm} (IV-27)$$

$$C_{NE} + C_{NW} + C_{SE} + C_{SW} = 1 - P_A - P_B$$

Since both P_A and P_B are positive and $(P_A + P_B) < 1$, the finite-analytic coefficients are always positive. Also, the exponents in these coefficients provide a gradual upwind bias as the cell Reynolds numbers $|2Ah|$ and/or $|2Bh|$ increase. Thus, the behavior of the convective-diffusion equation is properly captured and false numerical diffusion is minimized due to the inclusion of all corner points. For large cell Reynolds numbers, the series

summation in E_2 can be avoided by considering the asymptotic expressions of P_A and P_B based on the theory of characteristics, i.e.,

$$|Ak| > |Bh| : P_A = 0, \quad P_B = 1 - |Bh/Ak|$$

$$|Ak| < |Bh| : P_B = 0, \quad P_A = 1 - |Ak/Bh| \qquad (IV-28)$$

Since the downstream influence is negligible at large cell Reynolds numbers, the above approximations do not introduce a significant error in the solution, but the computing time is greatly reduced.

By substituting the nonhomogeneous term g from equation (IV-22a) into equation (IV-26), an eleven-point finite-analytic formula for unsteady, three-dimensional, partially-parabolic equations can be obtained in the form

$$\phi_P = \frac{1}{1 + C_P[(D_\phi)_P + \frac{(E_\phi)_P}{\tau}]} \{ C_{NE}\phi_{NE} + C_{NW}\phi_{NW} + C_{SE}\phi_{SE} + C_{SW}\phi_{SW}$$

$$+ C_{EC}\phi_{EC} + C_{WC}\phi_{WC} + C_{NC}\phi_{NC} + C_{SC}\phi_{SC} + (D_\phi)_P C_P \phi_U$$

$$+ \frac{(E_\phi)_P}{\tau} C_P \phi_P^{n-1} - C_P(S_\phi)_P \} \qquad (IV-29)$$

or

$$\phi_P = \frac{1}{1 + C_P[(D_\phi)_P + \frac{(E_\phi)_P}{\tau}]} \{ \sum_1^8 C_{nb}^\phi \phi_{nb} + (D_\phi)_P C_P \phi_U + \frac{(E_\phi)_P}{\tau} C_P \phi_P^{n-1}$$

$$- C_P(S_\phi)_P \} \qquad (IV-29a)$$

where the subscript nb denotes neighboring nodes (NE:northeast, NW:northwest, etc).

It is seen that ϕ_P depends upon all the eight neighboring nodal values in the $\eta-\zeta$ plane as well as the values at the upstream node U and the value at the previous time step $(n-1)$. Since the finite-analytic coefficients are all positive, the ellipticity of the flow in each cross-section is represented accurately. Note that ϕ_P is not directly dependent upon the downstream nodal value ϕ_D. This parabolic feature enables us to employ a marching procedure along the ξ- direction as well as in time. However, the flow is not truly parabolic in the ξ-direction since the longitudinal pressure gradient P_ξ, which appears in the source functions, introduces the downstream influence of the elliptic pressure field. Due to this indirect pressure transmission, several sweeps in the ξ- direction are needed to obtain a fully-converged pressure and velocity field.

Since equations (IV-29) are implicit, both in space and time, at the current station of calculation, their assembly for all elements results in a set of simultaneous algebraic equations. These equations are solved by the tridiagonal-matrix algorithm. Since it is not necessary to obtain a fully-converged intermediate solution for steady flows, only six line-by-line internal iterations are used during each global sweep. Furthermore, the finite-analytic coefficients appearing in equations (IV-29) are not updated during these internal iterations for economy of computation time.

IV.3 Solution of the Continuity Equation, and Pressure and Velocity Corrections

If the pressure is known a priori, equations (IV-29) can be employed directly to solve the five partially-parabolic convective-diffusion equations (IV-1) for U,V,W,k and ϵ . However, in most practical applications, the pressure is not known and must be determined by requiring the velocity field to satisfy the equation of continuity. Since a direct method for the simultaneous solution of all six equations is not feasible with

present computer capacity, it is necessary to convert the equation of continuity into an algorithm for the calculation of the pressure field appearing in the momentum equations. In this study, the SIMPLER algorithm of Patankar (1980) has been modified and extended to update the pressure field. Details of this algorithm are outlined in the following.

In the present algorithm, the staggered-grid system introduced by Harlow and Welch (1965) in their MAC method is adopted. Figure 6(b) shows the locations of the nodes for U,V,W, and P in the staggered grid. The turbulence quantities k and ε are evaluated at the pressure nodes. The dashed lines represent the control volume faces, and the pressure is calculated at the center of the control volume. For convenience U_d, V_n, W_e and P_P in Fig. 6(b) are assigned the same index, i.e., they are denoted by $U_{\xi\eta\zeta}$, $V_{\xi\eta\zeta}$, $W_{\xi\eta\zeta}$ and $P_{\xi\eta\zeta}$, respectively. It should be recalled here that the velocity components U,V, and W remain in the longitudinal, radial and circumferential directions. In other words, they are, in general, neither perpendicular to the control surfaces nor in the direction of the coordinate lines. However, due to the choice of the cylindrical polar coordinates in the physical plane, the velocity components do not become parallel to the control surfaces.

In the staggered grid, the eleven-point finite-analytic formulae (equation (IV-29)) for the momentum equations yield the velocity components

$$U_d = \frac{1}{1+C_d(D_U+\frac{E_U}{\tau})_d} \left\{ \sum_1^8 C_{nb}^d U_{nb} + C_d[(D_U)_d U_u + \frac{(E_U)_d}{\tau} U_d^{n-1} - (S_U)_d] \right\}$$

$$V_n = \frac{1}{1+C_n(D_V+\frac{E_V}{\tau})_n} \left\{ \sum_1^8 C_{nb}^n V_{nb} + C_n[(D_V)_n V_u + \frac{(E_V)_n}{\tau} V_n^{n-1} - (S_V)_n] \right\}$$

60

$$W_e = \frac{1}{1+C_e(D_W+\frac{E_W}{\tau})_e} \{ \sum_1^8 C_{nb}^e W_{nb} + C_e [(D_W)_e W_u + \frac{(E_W)_e}{\tau} W_e^{n-1} - (S_W)_e] \}$$

(IV-30)

where C_d, C_n and C_e are the finite-analytic coefficients C_p evaluated at the staggered velocity nodes d, n and e in Fig. 6. Note that the above equations contain the pressure-gradient terms inside the source functions. An equation for this unknown pressure field may be obtained as follows.

If we decompose the actual velocity field (U,V,W) in the momentum equations (IV-30) into a pseudovelocity field $(\tilde{U}, \tilde{V}, \tilde{W})$ plus the pressure gradient terms contained in the source functions, i.e.,

$$U_d = \tilde{U}_d - \frac{C_d}{1+C_d(D_U+\frac{E_U}{\tau})_d} \{ \frac{Reff}{J} (b_1^1 p_\xi + b_1^2 p_\eta + b_1^3 p_\zeta) \}_d$$

$$V_n = \tilde{V}_n - \frac{C_n}{1+C_n(D_V+\frac{E_V}{\tau})_n} \{ \frac{Reff}{J} (b_2^1 p_\xi + b_2^2 p_\eta + b_2^3 p_\zeta) \}_n \qquad \text{(IV-31)}$$

$$W_e = \tilde{W}_e - \frac{C_e}{1+C_e(D_W+\frac{E_W}{\tau})_e} \{ \frac{Reff}{J} (b_3^1 p_\xi + b_3^2 p_\eta + b_3^3 p_\zeta) \}_e$$

so that the pseudovelocities contain no pressure terms, then an equation for pressure can be derived by requiring the velocity field to satisfy the discretized equation of continuity (IV-2), i.e.

61

$$(b_1^1 U + b_2^1 V + b_3^1 W)_d - (b_1^1 U + b_2^1 V + b_3^1 W)_u + (b_1^2 U + b_2^2 V + b_3^2 W)_n$$

$$- (b_1^2 U + b_2^2 V + b_3^2 W)_s + (b_1^3 U + b_2^3 V + b_3^3 W)_e - (b_1^3 U + b_2^3 V + b_3^3 W)_w = 0$$

$$(IV-32)$$

The resulting pressure equation will contain many pressure nodes (see Muraoka (1979), for example) if nonorthogonal coordinates are employed. It is therefore desirable to simplify the algorithm by introducing modified pseudovelocities ($\hat{U}$, $\hat{V}$, $\hat{W}$) by decomposing the velocity components as follows:

$$U_d = \hat{U}_d - d_d(p_D - p_P)$$

$$V_n = \hat{V}_n - d_n(p_{NC} - p_P) \qquad (IV-33)$$

$$W_e = \hat{W}_e - d_e(p_{EC} - p_P)$$

where

$$d_d = \frac{(\text{Reff } b_1^1)_d C_d}{J_d[1 + C_d(D_U + \frac{E_U}{\tau})_d]}$$

$$d_n = \frac{(\text{Reff } b_2^2)_n C_n}{J_n[1 + C_n(D_V + \frac{E_V}{\tau})_n]} \qquad (IV-33a)$$

$$d_e = \frac{(\text{Reff } b_3^3)_e C_e}{J_e[1 + C_e(D_W + \frac{E_W}{\tau})_e]}$$

The modified pseudovelocities ($\hat{U}$, $\hat{V}$, $\hat{W}$) defined above still contain part of the pressure-gradient terms if the coordinate

system is nonorthogonal (i.e., $b_i^j \neq 0$ for $i \neq j$, see equation IV-31). These pressure-gradient terms can be evaluated from the pressure field known at the previous time step or iteration without losing any accuracy or generality. If we require the velocity field to satisfy the equation of continuity (IV-32), a simpler pressure equation can be derived in terms of the modified pseudovelocities $(\hat{U}, \hat{V}, \hat{W})$. Note that eighteen velocity components are involved in the equation of continuity (IV-32) for each small control volume. However, due to the staggered grid system employed here, only six of these, namely, U_d, U_u, V_n, V_s, W_e, and W_w, can be obtained directly from the governing equations (IV-30). It is, therefore, necessary to approximate the remaining twelve by interpolations. A simple linear interpolation is used here to evaluate these values from the velocity field known at the previous time step or iteration, so that the continuity equation becomes

$$(b_1^1 U)_d - (b_1^1 U)_u + (b_2^2 V)_n - (b_2^2 V)_s + (b_3^3 W)_e - (b_3^3 W)_w + D_1 = 0 \qquad (IV-34)$$

where

$$D_1 = (b_2^1 V + b_3^1 W)_d - (b_2^1 V + b_3^1 W)_u + (b_1^2 U + b_3^2 W)_n - (b_1^2 U + b_3^2 W)_s$$

$$+ (b_1^3 U + b_2^3 V)_e - (b_1^3 U + b_2^3 V)_w \qquad (IV-34a)$$

is the mass source obtained from the velocity field at the previous time step or sweep. An equation for pressure is then derived by substituting equations (IV-33) into (IV-34), i.e.,

$$a_P p_P = a_d p_D + a_u p_U + a_n p_{NC} + a_s p_{SC} + a_e p_{EC} + a_w p_{WC} - \hat{D} \qquad (IV-35)$$

where

$$a_d = (b_1^1)_d \, d_d$$

63

$$a_u = (b_1^1)_u \, d_u$$

$$a_n = (b_2^2)_n \, d_n$$

$$a_s = (b_2^2)_s \, d_s \qquad\qquad (IV-35a)$$

$$a_e = (b_3^3)_e \, d_e$$

$$a_w = (b_3^3)_w \, d_w$$

$$a_P = a_d + a_u + a_e + a_w + a_n + a_s$$

and

$$\hat{D} = (b_1^1 \, \hat{U})_d - (b_1^1 \, \hat{U})_u + (b_2^2 \, \hat{V})_n - (b_2^2 \, \hat{V})_s + (b_3^3 \, \hat{W})_e - (b_3^3 \, \hat{W})_w - D_1$$

$$(IV-35b)$$

The modified pseudovelocities $(\hat{U}, \hat{V}, \hat{W})$ contain the neighboring nodal values of velocity, source functions, and part of the pressure-gradient terms. All of them can be evaluated from the information known at the previous time step or iteration. Therefore, apart from the interpolations for D_1, the pressure equation (IV-35) is still an exact algebraic representation of the equation of continuity (IV-2). In this fashion, the pressure field can be obtained directly from an estimated velocity field, and the slow convergence usually encountered in the SIMPLE algorithm is avoided.

Although the guessed pressure field can be updated directly by equation (IV-35), in practical applications the new pressure field may produce a velocity field which does not satisfy the equation of continuity. An iterative procedure is therefore required to correct this erroneous velocity field to achieve more rapid convergence. In this study, a velocity-correction formula,

similar to that used in the SIMPLE algorithm, is derived in terms of the pressure-corrections.

If we denote the imperfect velocity field resulting from an imperfect pressure field p* by (U*, V*, W*), then the discretized momentum equations (IV-33) can be written as

$$U_d^* = \hat{U}_d^* - d_e(p_D^* - p_P^*)$$

$$V_n^* = \hat{V}_n^* - d_n(p_{NC}^* - p_P^*) \qquad\qquad (IV-36)$$

$$W_e^* = \hat{W}_e^* - d_e(p_{EC}^* - p_P^*)$$

In order to improve the guessed pressure field, such that (U*, V*, W*) will eventually satisfy the equation of continuity, one needs to know how the velocity components respond to a change in the pressure field. Such a relation can be obtained by subtracting equation (IV-36) from equation (IV-33), i.e.,

$$U_d - U_d^* = (\hat{U}_d - \hat{U}_d^*) - d_d(p_D' - p_P')$$

$$V_n - V_n^* = (\hat{V}_n - \hat{V}_n^*) - d_n(p_{NC}' - p_P') \qquad\qquad (IV-37)$$

$$W_e - W_e^* = (\hat{W}_e - \hat{W}_e^*) - d_e(p_{EC}' - p_P')$$

where $p' = p - p^*$ is the pressure correction, and U-U*, V-V* and W-W* are the corresponding velocity corrections. If we require the velocity field to satisfy the equation of continuity (IV-34), an equation for the pressure correction p' can be derived. However, due to the implicit nature of the velocity corrections arising from the pseudovelocities, the resulting pressure correction equation would involve the pressure-corrections at all grid points. It is not necessary to retain such a complicated formulation because both the pressure- and velocity-corrections are zero in the final converged solution. Since both the

pressure- and velocity-corrections become trivial when the solution converges, it is possible to omit that part of the velocity-corrections, $\hat{U} - \hat{U}^*$, $\hat{V} - \hat{V}^*$ and $\hat{W} - \hat{W}^*$, which represents the indirect influence of velocity-corrections. With this approximation, the velocity-corrections are expressed explicitly in terms of the pressure-corrections as

$$U_d = U_d^* - d_d(p_D' - p_P')$$

$$V_n = V_n^* - d_n(p_{NC}' - p_P') \qquad\qquad (IV-38)$$

$$W_e = W_e^* - d_e(p_{EC}' - p_P')$$

By requiring the velocity field to satisfy the equation of continuity (IV-30), a pressure-correction equation is then obtained in the form

$$a_p p_P' = a_d p_D' + a_u p_U' + a_n p_{NC}' + a_s p_{SC}' + a_e p_{EC}' + a_w p_{WC}' - D^* \qquad (IV-39)$$

with

$$D^* = (b_1^1 U^*)_d - (b_1^1 U^*)_u + (b_2^2 V^*)_n - (b_2^2 V^*)_s + (b_3^3 W^*)_e - (b_3^3 W^*)_w - D_1$$

$$(IV-39a)$$

where the coefficients a_P, a_d, etc. are as defined in equation (IV-35a). Note that the pressure-correction equation is similar to the pressure equation (IV-35). Although, unlike the pressure equation, the pressure-correction equation is not exact, the approximations made will influence only the rate of convergence but not the final converged solution.

It should be remarked here that both the pressure and pressure-correction equations are elliptic. In other words, the downstream pressure p_D and pressure-correction p_D' will affect the

pressure, and thus the velocity field, upstream. In practical applications to partially-parabolic flows, one may treat the downstream pressure p_D as a known quantity with $p_D' = 0$, so that a marching, instead of an iterative process, can be employed for the calculation of the transport quantities. The pressure field is then updated by repeating the marching process from upstream to downstream for several sweeps until the converged pressure and velocity fields are obtained.

In the present study, the systems of algebraic equations formed by the assembly of the pressure and the pressure-correction equations, (IV-35) and (IV-39), respectively, are solved by the tridiagonal-matrix algorithm with six line-by-line internal iterations. The finite-analytic coefficients a_p, a_d, etc., were updated in each upstream to downstream global sweep, but remained the same during the internal iterations.

IV.4 Boundary Conditions

With the partially-parabolic assumptions, the transport equations for $\phi \equiv U,V,W,k$ and ε become parabolic in the predominant-flow direction ξ, but remain elliptic in the cross-sectional $\eta\zeta$- plane. Due to the latter feature, it is necessary to specify the boundary conditions on all boundaries of each $\eta\zeta$-plane. On the other hand, the parabolic behavior in the ξ-direction enables us to employ a marching technique without specifying the downstream boundary conditions for ϕ. For the fully-elliptic pressure field, one must specify, either explicitly or implicitly, the boundary conditions on all boundaries including the downstream exit plane, so that the upstream transmission of pressure information is properly represented. In other words, one needs to specify only the pressure datum in one numerical cell if all velocity components are prescribed on the boundary surfaces. Alternatively, when the pressure is prescribed on part of the boundary surfaces, then inflow or outflow must be permitted there to avoid overspecification of the boundary conditions.

The appropriate boundary conditions for ship-like bodies are as follows.

(1) Initial or Upstream Section ($\xi = 1$)

The distribution of the velocity components (U,V,W) and the turbulence quantities (k,ε) are prescribed at this section either from detailed thin boundary-layer calculations or from simple flat-plate correlations. Boundary conditions for pressure and pressure-correction are not required in the present staggered-grid arrangement since the pressure is implicitly determined by the specification of the velocity components. Also, since the velocity components are known, there are no corrections to be made, i.e. $(\hat{U},\hat{V},\hat{W})_u = (U^*,V^*,W^*)_u = (U,V,W)_u$.

(2) Exit or Downstream Plane

The exit plane is located in the wake far downstream from the stern, and the zero pressure-gradient ($p_\xi = 0$) condition is specified there. Due to the parabolicity of the transport equations, exit conditions for $\phi = U,V,W,k,\varepsilon$ are not required.

(3) Body Surface ($\eta = 1$)

For laminar flow, the numerical solutions are carried out upto the solid surface where the usual no-slip conditions, $U=V=W=0$, are imposed.

For turbulent flows, a modified "wall-function" approach (Chen, Yoon and Yu (1982)) is employed to avoid the use of low-Reynold-number turbulence models and a large number of grid points to resolve the large gradients in the near-wall region. The boundary conditions are determined in the logarithmic layer by using the universal law-of-the-wall in the form

$$\frac{q}{U_\tau} = \frac{1}{\kappa} \left\{ \ln \left[\frac{4}{\Delta_\tau} \frac{(1 + \Delta_\tau y^+)^{1/2} - 1}{(1 + \Delta_\tau y^+)^{1/2} + 1} \right] + 2[(1 + \Delta_\tau y^+)^{1/2} - 1] \right\}$$

$$+ B + 3.7 \Delta_p \qquad\qquad (IV-40)$$

where U_τ is the friction velocity defined by $U_\tau = \sqrt{\tau_w / \rho U_o^2}$, $y^+ = \text{Re } U_\tau y$ is the dimensionless distance measured in the direction normal to the surface, $\nabla_p = \nabla p / \text{Re} U_\tau^3$ is the dimensionless pressure gradient, Δ_τ is the dimensionless shear-stress gradient and is assumed to be $1/2 \nabla_p$, q is the magnitude of the velocity, $\kappa = 0.42$ is the von Karman constant and B = 5.45. In the present study, it is assumed that at least two points (n = 2 and 3 in Fig. 7) are located in the logarithmic region. This avoids the need for a separate Couette-flow type analysis for the flow between the wall and the first near-wall mesh point which has been used in almost all previous applications of wall functions.

In the present procedure, a value for U_τ is assumed and the boundary conditions at n = 2 are determined from the logarithmic law and the assumptions of local equilibrium, i.e.,

$$\frac{q_2}{U_\tau} = \frac{1}{\kappa} \left\{ \ln \left[\frac{4}{\Delta_\tau} \frac{(1 + \Delta_\tau y_2^+)^{1/2} - 1}{(1 + \Delta_\tau y_2^+)^{1/2} + 1} \right] + 2[(1 + \Delta_\tau y_2^+)^{1/2} - 1] \right\}$$

$$+ B + 3.7 \Delta_p \qquad\qquad (IV-41a)$$

$$k_2 = \frac{U_\tau^2}{\sqrt{c_\mu}} \qquad\qquad (IV-41b)$$

$$\varepsilon_2 = \frac{U_\tau^3}{\kappa y_2} \qquad\qquad (IV-41c)$$

The numerical solution then provides the velocity at $n = 3$ and U_τ is updated by requiring this velocity to satisfy the logarithmic law, i.e., by solving

$$\frac{q_3}{U_\tau} = \frac{1}{\kappa} \left\{ \ln \left[\frac{4}{\Delta_\tau} \frac{(1 + \Delta_\tau y_3^+)^{1/2} - 1}{(1 + \Delta_\tau Y_3^+)^{1/2} + 1} \right] + 2[(1 + \Delta_\tau y_3^+)^{1/2} - 1] \right\}$$

$$+ B + 3.7 \Delta_p \qquad\qquad (IV-42)$$

by a root-finding technique. Thus, an iterative procedure is used to satisfy the wall boundary conditions in the case of turbulent flow, and to determine U_τ. Typically, five iterations are required to obtain satisfactory convergence. In the present study, the pressure-gradient correction is used only in regions of adverse pressure gradients.

By anchoring the solution at two near-wall mesh points on the logarithmic law, the present wall-function approach removes much of the sensitivity of the numerical solution to the location of the first mesh point which has been observed in previous treatments. The procedure is quite straightforward for two-dimensional and axisymmetric flows. For three-dimensional flows, however, an additional assumption concerning the direction of the velocity vector is required to determine the individual components (U,V,W) because the logarithmic law gives only the velocity magnitude. The velocity components (U,V,W) occurring in the governing equations are related to the components (q^ξ, q^η, q^ζ) along the body-fitted coordinates (Fig. 8) by

$$q = (U,V,W) = q^\xi \underset{\sim}{\tau}_\xi + q^\eta \underset{\sim}{\tau}_\eta + q^\zeta \underset{\sim}{\tau}_\zeta \qquad\qquad (IV-43)$$

where, from equation (A-10a),

$$\underset{\sim}{\tau}_{\xi} = \frac{1}{\sqrt{g_{11}}} (x_{\xi}, r_{\xi}, r\theta_{\xi})$$

$$\underset{\sim}{\tau}_{\eta} = \frac{1}{\sqrt{g_{22}}} (x_{\eta}, r_{\eta}, r\theta_{\eta}) \qquad (IV-44)$$

$$\underset{\sim}{\tau}_{\zeta} = \frac{1}{\sqrt{g_{33}}} (x_{\zeta}, r_{\zeta}, r\theta_{\zeta})$$

Thus,

$$U = \frac{x_{\xi}}{\sqrt{g_{11}}} q^{\xi} + \frac{x_{\eta}}{\sqrt{g_{22}}} q^{\eta} + \frac{x_{\zeta}}{\sqrt{g_{33}}} q^{\zeta}$$

$$V = \frac{r_{\xi}}{\sqrt{g_{11}}} q^{\xi} + \frac{r_{\eta}}{\sqrt{g_{22}}} q^{\eta} + \frac{r_{\zeta}}{\sqrt{g_{33}}} q^{\zeta} \qquad (IV-45)$$

$$W = \frac{r\theta_{\xi}}{\sqrt{g_{11}}} q^{\xi} + \frac{r\theta_{\eta}}{\sqrt{g_{22}}} q^{\eta} + \frac{r\theta_{\zeta}}{\sqrt{g_{33}}} q^{\zeta}$$

and the inverse relations are

$$q^{\xi} = \frac{\sqrt{g_{11}}}{J} (b_1^1 U + b_2^1 V + b_3^1 W)$$

$$q^{\eta} = \frac{\sqrt{g_{22}}}{J} (b_1^2 U + b_2^2 V + b_3^2 W) \qquad (IV-46)$$

$$q^{\zeta} = \frac{\sqrt{g_{33}}}{J} (b_1^3 U + b_2^3 V + b_3^3 W)$$

Now, we impose the contraint that q_2 is parallel to the wall and therefore require $q_2^{\eta} = 0$ with the geometric coefficients determined at $\eta = 1$. It is further assumed that there is no rotation of the velocity vector between $\eta = 2$ and $\eta = 3$ in the plane parallel to the surface, i.e.

71

$$\frac{q_2^{\xi}}{q_3^{\xi}} = \frac{q_2^{\zeta}}{q_3^{\zeta}} = \frac{q_2}{q_3} \qquad\qquad (IV\text{-}47)$$

With an assumed U_{τ}, and therefore q_2, equation (IV-47) gives q_2^{ξ} and q_2^{ζ}, and with $q_2^{\eta} = 0$, equation (IV-45) gives the components (U_2, V_2, W_2) required as the boundary conditions in the numerical solution. In turn, this solution gives (U_3, V_3, W_3) and hence q_3, and a new value of U_{τ} from equation (IV-42), new values of q_3^{ξ} and q_3^{ζ} from equation (IV-46), and finally q_2^{ξ} and q_2^{ζ} from equation (IV-47) which provide the updated boundary conditions. This procedure is iterated to convergence.

It should also be noted that in evaluating the distance y normal to the wall, required in the law of the wall, it is necessary to determine the direction cosine between $\underset{\sim}{\tau}_{\eta}$ and $\underset{\sim}{n}^{\eta}$. This is given by

$$\cos \alpha = \underset{\sim}{\tau}_{\eta} \cdot \underset{\sim}{n}^{\eta} = \frac{b_1^2 x_{\eta} + b_2^2 r_{\eta} + b_3^2 r\theta_{\eta}}{\sqrt{g g_{22} g^{22}}} \qquad\qquad (IV\text{-}48)$$

with all the geometric coefficients evaluated at $\eta = 1$.

(4) Outer Boundary

In order to avoid separate viscous and inviscid calculations, and matching between them, the outer boundary is placed at a large distance from the body where the flow is assumed to be uniform. The boundary conditions then become

$$U = 1, \qquad W = 0, \qquad \frac{\partial k}{\partial \eta} = \frac{\partial \varepsilon}{\partial \eta} = 0, \qquad p = 0 \qquad\qquad (IV\text{-}49)$$

The radial outflow V at the outer boundary is not specified but is determined by the solution.

(5) Symmetry Planes

On the ship centerplane and on the undisturbed free surface or waterplane, symmetry conditions for transport quantities, i.e.,

$$W = 0, \qquad \frac{\partial U}{\partial \zeta} = \frac{\partial V}{\partial \zeta} = \frac{\partial k}{\partial \zeta} = \frac{\partial \epsilon}{\partial \zeta} = 0 \qquad (IV-50)$$

are enforced.

(6) Wake Centerline

For axisymmetric bodies, the boundary conditions at the wake centerline $r = 0$ ($\eta = 1$) are specified by

$$V = W = 0, \qquad \frac{\partial U}{\partial \eta} = \frac{\partial k}{\partial \eta} = \frac{\partial \epsilon}{\partial \eta} = 0 \qquad (IV-51)$$

For three-dimensional bodies, the above zero-gradient conditions are no longer adequate since the variations of U, k and ϵ in the circumferential direction, in general, result in multiple values at $r = 0$. In order to avoid this problem, we exclude the wake centerline in the solutions and apply the zero-gradient boundary conditions on the surface $\eta = 2$.

(7) Initial Conditions (t = 0)

For the steady-flow calculations considered here, the initial conditions for the transport quantities $\phi \equiv U, V, W, k, \epsilon$ are taken directly from the values known at the immediately up-stream station during the first sweep and the pressure is assumed to be zero throughout the flow field. Although it is possible to assume more realistic initial conditions and thus accelerate the convergence of the solution, these rather crude initial conditions have been used not only to simplify the use of the method but also to demonstrate its versatility.

IV.5 The Overall Solution Algorithm

The solution algorithm presented below differs from that outlined in Chen and Patel (1984) in the way the pressure is updated. In the previous procedure, the pressure field was obtained station by station by solving the momentum and pressure equations simultaneously during the marching process. While this gave quite satisfactory results, it allowed only one upstream-to-downstream sweep for the pressure field in each global sweep, and therefore the pressure influence propagated only one station upstream per global sweep. The number of sweeps required to achieve convergence with this procedure was typically of the order of the number of streamwise stations employed in the calculations.

In order to improve the rate of convergence, a new global pressure-iteration technique is employed here to bring the downstream pressure influence immediately to the whole solution domain. The new solution algorithm requires only a simple rearrangement of the solution procedures of Chen and Patel (1984) and a slight increase of computer storage for pressure coefficients. In the new global pressure-iteration scheme, the momentum equations are solved using the old pressure field during each global sweep. After the sweep for the transport quantities is completed, the pressure field is solved elliptically with several global iterations just as in fully-elliptic problems. These iterations can be performed from downstream to upstream so that the downstream pressure influence propagates all the way to the inlet station even in the first global sweep. In this fashion, the number of global sweeps required to achieve the same level of convergence as before is reduced by a factor of two or more, while the computation time for each global sweep remains about the same. Hence, the overall computation time is greatly reduced.

For transient problems, where the initial and boundary conditions are properly specified as functions of time, the overall numerical solution procedure may be summarized as follows:

(1) Construct the body-fitted coordinate system for the given body shape and solution domain, and calculate the geometric coefficients b_i^j, g^{ij}, J, etc. from equations (IV-27) to (IV-31).

(2) Specify the initial conditions for the velocity and turbulence fields. Set $p = 0$ everywhere initially.

(3) Specify the velocity and turbulence profiles at the first station $\xi = 1$ (these may be time dependent).

(4) Calculate the finite-analytic coefficients for pressure, pressure-correction and momentum equations at the downstream station. Store only the finite-analytic coefficients a_d, a_n and a_e for the pressure equation.

(5) Solve the momentum equations (IV-29) based on the updated pressure field to obtain the starred velocity field (U^*, V^*, W^*). This system of algebraic equations is solved by a tridiagonal matrix algorithm.

(6) Calculate the mass source D^*, and solve the pressure correction equation (IV-39) by tridiagonal matrix algorithm.

(7) Correct the velocity field using the velocity-correction formulae (IV-38), but do not correct the pressure field.

(8) Calculate the pseudovelocities ($\hat{U}$, $\hat{V}$, $\hat{W}$) in terms of the velocity field from equation (IV-33). Store only $\hat{D}$ for later use.

(9) Solve equations (IV-29) for turbulence quantities ($\phi = k, \varepsilon$) by tridiagonal-matrix algorithm.

(10) March to the next downstream station and repeat steps (3) to (9).

(11) After reaching the last downstream station, solve the pressure equation (IV-35) by tridiagnonal matrix algorithm. Several iterations from downstream to upstream are employed to update the three-dimensional elliptic pressure field.

(12) Repeat steps (3) to (11) for several sweeps until both the pressure and velocity fields have converged within a specified tolerance.

(13)   Return to step (2) for the next time step.

(14)   Stop if the steady-state solution is achieved, or if time exceeds the maximum time period assigned.   For steady-flow calculations, one may relax the convergence criterion in step (12) and use a larger time increment for the intermediate solutions.

In the present study, only one sweep was used in step (12) for each time step.   Also, as noted earlier, instead of specifying the initial conditions for velocity and turbulence profiles everywhere at t = 0, one may specify only the profiles at the first station ξ = 1.   The downstream profiles are then taken from the immediate upstream station (i.e., $\phi_P = \phi_U$ at t = 0) during the first global sweep.

V. SOME EXAMPLE SOLUTIONS

The numerical method described in Section IV has been employed to calculate a variety of two-dimensional, axisymmetric and three-dimensional flows. Here, we shall present only a few representative examples which illustrate the capability of the method and indicate areas which require further study.

V.1 Two-Dimensional Flow on a Flat Plate

This is by far the simplest example of flows which involve the evolution of a wake from a boundary layer because the viscous-inviscid interaction at the trailing edge is weak, the flow is two-dimensional, and Cartesian coordinates can be used in the physical plane. Nevertheless, it provides a useful test of the grid-generation technique, the numerical method, and the turbulence model.

(i) Laminar Flow

The laminar flow over the trailing edge of a flat plate has been the subject of numerous previous investigations using a variety of methods. Among these are numerical solutions of the full Navier-Stokes equations (Janssen, 1958; Dennis and Dunwoody, 1966) for relatively low Reynolds numbers, numerical solutions of the triple-deck equations of Stewartson (1969) and Messiter (1970) which apply at very large Reynolds numbers (Jobe and Burggraf, 1974; Melnik and Chow, 1975; Veldman, 1975), numerical solutions of the partially-parabolic equations (Rubin and Reddy, 1983; Saint-Victor and Cousteix, 1984), and solutions employing viscous-inviscid interaction techniques in which the boundary-layer equations are coupled with the external inviscid stream (Veldman, 1979, 1981; Davis and Werle, 1981). A thorough review of the similarities and differences among the various approaches and their results is beyond the scope of the present paper. However, the results of the present method will be compared with some representative solutions obtained earlier.

77

We select Cartesian coordinates (x,y) in the physical plane, with the origin at the leading edge. With distances normalized by the plate length L, $x = 0$ and 1 correspond to the leading and trailing edges, respectively, and y is normal to the plate. A nonuniform rectangular grid was generated using the technique described in Section IV.1 with $x = x(\xi)$ and $y = y(n)$. With this rather simple coordinate transformation, equations (IV-6) simplify to

$$g^{11} x_{\xi\xi} + f^1 x_\xi = 0$$

$$g^{22} y_{nn} + f^2 y_n = 0$$

(V-1)

If the required grid distribution in the physical space is chosen a priori, then the control functions can be determined from

$$f^1 = - g^{11} \frac{x_{\xi\xi}}{x_\xi}$$

$$f^2 = - g^{22} \frac{y_{nn}}{y_n}$$

(V-2)

Alternatively, one may prescribe the control functions and solve equations (V-1) for the coordinates (x,y). For the calculations presented here, the latter approach is adopted to ensure a smooth variation of the coordinates and the control functions. The particular functions used are

$$\frac{f^1}{2g^{11}} = \begin{cases} A_1 & 0 < z_1 < 1/2 \\ A_1 \sin \pi z_1 & 1/2 < z_1 < 2 \\ A_2 \sin \pi z_2 & 0 < z_2 < 3/2 \\ - A_2 & z_2 > 3/2 \end{cases}$$

(V-3)

and $\dfrac{f^2}{2g^{22}} = - A_3$

where $z_1 = \dfrac{\xi - 1}{\xi_1 - 1}$, $z_2 = \dfrac{\xi - 2\xi_1 + 1}{\xi_2 - 2\xi_1 + 1}$

ξ_1 and ξ_2 correspond to the leading and trailing edges, respectively, and A_1, A_2 and A_3 are positive constants which can be selected to yield the desired grid concentration around $x = 0$, 1 and $y = 0$.

If we further assume that the grid-control functions remain constant within each numerical cell shown in Fig. 9, equations (V-1) can be solved analytically to obtain

$$x_P = \frac{e^a x_U + e^{-a} x_D}{e^a + e^{-a}}$$

$$y_P = \frac{e^b y_S + e^{-b} y_N}{e^b + e^{-b}} \qquad\qquad (V-4)$$

where

$$a = - \left. \frac{f^1}{2g^{11}} \right|_P , \qquad b = - \left. \frac{f^2}{2g^{22}} \right|_P$$

Equations (V-4) constitute a set of simultaneous algebraic equations which can be solved by the tridiagonal-matrix algorithm. The first derivatives of the coordinates, which appear in the geometric coefficients, g^{ij}, b_i^j , etc., can then be obtained readily from

$$\left. x_\xi \right|_P = \frac{2a}{e^{2a} - e^{-2a}} (x_D - x_U)$$

$$\left. y_\eta \right|_P = \frac{2b}{e^{2b} - e^{-2b}} (y_N - y_S) \qquad\qquad (V-5)$$

The numerical grid shown in Fig. 10 was generated with $A_1 = 0.3$, $A_2 = 0.2$, $A_3 = 0.4$, and $\xi = 1$ at $x = -1.385$, $\xi = 19$ ($= \xi_1$) at $x = 0$, $\xi = 49$ ($= \xi_2$) at $x = 1$, $\xi = 64$ at $x = 3.339$, $\eta = 2$ at $y = 0$ and $\eta = 16$ at $y = 12$. Thus, a 64 x 15 mesh covers the physical region that

extends from a distance 1.385 L upstream of the leading edge to 2.339 L downstream of the trailing edge, and 12 L normal to the plate, with the grid concentrated in the neighborhood of the leading and trailing edges and the plate. The domain can be readily extended in all directions by the addition of only a few extra nodes.

The present method has been employed with different grid distributions and mesh sizes, and different locations of the upstream, downstream and outer boundaries to study their influence on the solution. These will be discussed in a separate paper. For the present purposes it suffices to present and compare solutions obtained with grid distributions and solution domains similar to those employed by others. Thus, we shall concentrate on the flow over the trailing edge and employ only a portion of the grid described above.

As in some previous studies, the partially-parabolic equations have been solved for a plate Reynolds number $U_o L/\nu = 10^5$ in the domain $0.4819 < x < 1.473$, $0 < y < 0.2196$ (i.e. $37 < \xi < 60$, $2 < n < 11$), which corresponds roughly to the recent calculations of Saint-Victor and Cousteix. At the upstream station, the streamwise component of velocity U is specified by the Blasius solution and the streamwise gradient of the normal component, V_x, is set equal to zero. All other boundary conditions are prescribed as discussed in Section IV.4.

Figure 11 shows the pressure distribution on the plate and along the wake centerline calculated at different time steps (or global iterations), starting with an initially zero pressure throughout. It is seen that the solution converges monotonically in about 20 steps, the convergence being more rapid over the plate than in the wake. The rapid monotonic convergence of the solution is believed to be due to the two-step, global pressure-correction procedure described in Section IV.3. Solutions with some previous algorithms have led to an oscillatory behavior of pressure, requiring several hundred iterations for acceptable convergence.

The important features of the present solution are shown in Figs. 12, 13 and 14, along with the interacting boundary-layer calculations of Veldman (1979), the triple-deck results of Melnik and Chow (1975) and the partially-parabolic calculations of Saint-Victor and Cousteix (1984). Although all four solutions are qualitatively similar, a closer examination reveals several interesting differences.

First, we consider the flow on the plate (x < 1). It is seen that the triple-deck calculations predict a lower pressure than that calculated by the other methods over the middle of the plate. This is due to the fact that the triple-deck solutions are obtained with the Blasius solution prescribed at an asymptotically large distance upstream of the trailing edge, whereas the other three methods specify the initial conditions at x ~ 0.5. In other words, for the Reynolds number of 10^5 considered here, the triple-deck results suggest that the influence of the trailing edge penetrates further upstream. In fact, other calculations performed with the present method with initial conditions closer to the leading edge (typically x = 0.18) lead to results in much better agreement with the triple-deck solutions, and considerably reduce the difference between the present solutions and those of Veldman, and Saint-Victor and Cousteix, at the trailing edge. The latter authors also commented on the influence of the location of the outer boundary of the solution domain on the upstream pressure distribution. The present method also indicated such a sensitivity. The wall shear-stress coefficient ($C_\tau = \sqrt{Re}\ \tau_w / \rho U_o^2$) shown in Fig. 13 indicates somewhat better agreement in the results of all methods except that the present solution predicts higher values close to the trailing edge, as might be expected from the larger favorable pressure gradient calculated by this method.

Turning next to the flow in the near wake, it is seen that the pressure distribution obtained with the present method agrees rather well with that of Saint-Victor and Cousteix, but both

81
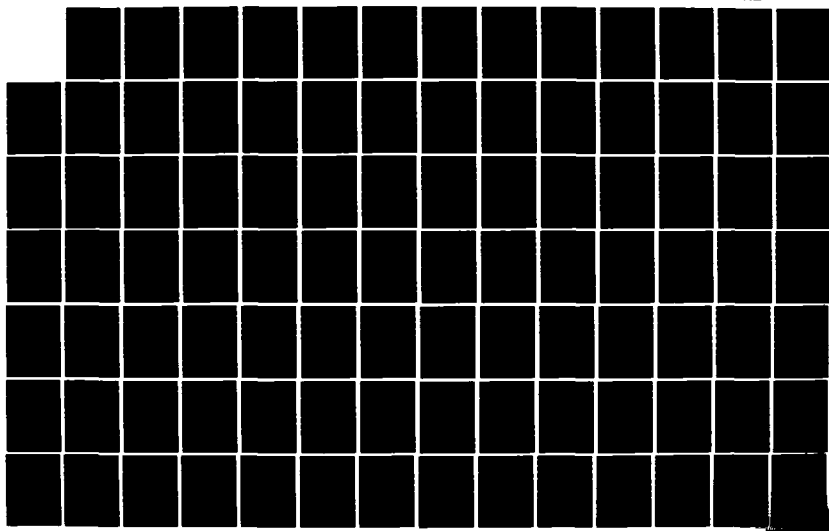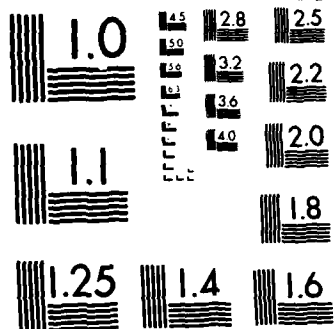
MICROCOPY RESOLUTION TEST CHART

NATIONAL BUREAU OF STANDARDS-1963-A

predict higher pressures than the triple-deck and interacting boundary-layer theories. On the other hand, the velocity variation along the wake centerline (Fig. 14) shows quite different trends. Here, the solutions of Saint-Victor and Cousteix agree with those of Veldman, the present calculation predicts higher velocities, while the triple-deck solution diverges from all others. The latter feature is obviously due to the fact that the triple-deck solution is matched downstream with the $x^{1/3}$ Goldstein near-wake rather than the $x^{1/2}$ parabolic asymptotic wake. The remaining solutions reproduce the parabolic characteristic due to the downstream boundary condition $p_x = 0$ imposed. However, the reasons for the disagreement in wake velocities inspite of the agreement in the pressure distributions of the present method and that of Saint-Victor and Cousteix, and for the disagreement in the pressure distribution inspite of the agreement in the wake velocity of the methods of Veldman and Saint-Victor and Cousteix, are not clear. Calculations performed with the present method by moving the downstream and outer boundaries further away from the plate ($x = 3.34$ and $y = 12.0$, respectively) bring the predicted wake pressure distribution into better agreement with the triple-deck and Veldman solutions but the wake velocity distribution remains unaffected. This leads us to conclude that the solutions of the partially-parabolic equations, both present and past, are sensitive to the location of the solution boundaries and agreement with the triple-deck solution can be secured only by employing a large enough solution domain. These aspects will be discussed in a separate report.

(ii) Turbulent flow

The calculations for the turbulent flow over the trailing edge of a flat plate presented below correspond to the experiments of Ramaprian, Patel and Sastry (1981). If X and Y are coordinates measured along and normal to the plate with X = 0 being the trailing edge, L (= 1.829 m) is the length of the

plate, and U_O (= 22 m/s) is the freestream velocity, the calculations correspond to a Reynolds number $U_O L/\nu = 1.6 \times 10^6$.

In order to obtain the desired grid concentration in the neighborhood of the trailing edge and the plate, the numerical grid-generation technique was again employed but with ξ_1 and ξ_2 corresponding to the initial station in the boundary layer at X/L = - 0.6, and the trailing edge X = 0, respectively. The grid used here corresponds to A_1=0.20, A_2=0.12 and A_3=0.25; with $\xi = \xi_1$=7 at X=-0.6 L, $\xi = \xi_2$ =31 at X=0, ξ =63 at X=8.57 L, η =1 at Y=0 and η =15 at Y=L. In other words, a 57 x 15 mesh is used to cover a physical region of - 1097 mm < X < 15680 mm (-0.6 <X/L <8.57; 7 < ξ <63) and 0 <Y < 1829 mm (0 < Y/L < 1.0; 1 < η < 15). Standard flat-plate boundary-layer profiles were specified at the upstream station.

Since we are interested only in the steady-state solution, a very large time increment, τ = 100, was used with only one global sweep per time step. The convergence histories of several quantities of particular interest are shown in Figs. 15 through 18 at nine different time steps corresponding to sweep numbers 1, 10, 20, 30, 40, 50, 60, 80, and 100. It can be seen that all quantities converge monotonically in about 30 sweeps although the calculations were continued for 100 sweeps or time steps.

Figure 15 shows the pressure distribution on the plate and along the wake centerline. It is seen that a sharp reduction followed by a rapid increase of pressure is predicted near the trailing edge as a result of the sudden change from the no-slip boundary condition on the plate to the zero-shear-stress condition along the wake centerline. Comparison of Fig. 15 with the corresponding case for laminar flow, Fig. 12, indicates that the viscous-inviscid interaction in turbulent flow is stronger, as measured by the pressure changes, but confined to a smaller region around the trailing edge. The wall shear stress coefficient ($C_f = \tau_w / \frac{1}{2} \rho U_O^2$), shown in Fig. 16, decreases continously toward the trailing edge during the first parabolic sweep under

83

zero initial pressure field. However, subsequent iterations lead to an increase near the trailing edge as in the laminar case. The higher shear stress indicates an acceleration of the fluid inside the boundary layer ahead of the trailing edge and is associated with the favorable pressure gradient in this region. It is interesting to note that both the turbulent kinetic energy (k) and the rate of turbulent energy dissipation (ε), and therefore the centerline eddy viscosity shown in Fig. 18, decrease considerably during the time-marching process. This is obviously related to the decrease of velocity gradients in the normal direction as the solution converges. When convergence is achieved, the eddy viscosity $(\nu_t = C_\mu k^2/\varepsilon)$ along the wake centerline increases rapidly with distance from the trailing edge and reaches an essentially constant value of $\nu_t/U_oL = 1.74 \times 10^{-4}$ beyond X > 6000 mm (i.e., X/L > 3.3). The significance of this result is discussed later on.

The principal results of the calculations in the near wake region are compared with experimental data, which extended only upto X = 610 mm, in Figs. 19, 20 and 21. The level of agreement between the calculation, and experiments with respect to the increase of centerline velocity (Fig. 19), mean-velocity profiles (Fig. 20), and turbulent kinetic-energy distributions (Fig. 21) is comparable with that achieved by Patel and Scheuerer (1982), who solved the boundary-layer equations using the same turbulence model but a different numerical method. Computationally, the two methods differ in the number of grid points required to resolve the large gradients in the near wake. The solutions of Patel and Scheuerer were obtained with 60 points across the wake and some 800 streamwise steps in the region 0 < X < 610 mm whereas the present solutions, as noted above, employed 57 x 15 grid nodes over a much larger domain. In fact, as shown in Fig. 21, only 8 points in the y-direction are needed to resolve the boundary layer and the near half-wake, whose thickness is of the order of 50 mm. The remaining 7 points cover the inviscid domain with the

outer boundary located at $Y = L = 1829$ mm. This difference between the nodes required in the two numerical schemes is attributed largely to the use of the finite-analytic scheme in the present method.

Physically, the two methods are also different. The use of the boundary-layer equations neglects the viscous-inviscid interaction at the trailing edge while the partially-parabolic equations take it into account. In the application of boundary-layer equations to the flow on a flat plate, it is assumed that the pressure is uniform (equal to zero, say) everywhere and, therefore, the velocity outside the boundary layer and wake is constant and equal to the freestream velocity U_O. In the partially-parabolic solutions the pressure is set equal to zero only at very large distances from the plate and, associated with the predicted pressure distribution on the plate and along the wake centerline, shown in Fig. 15, is a weak but nonzero pressure field everywhere. In the inviscid nonturbulent flow outside the boundary layer and wake, this results in velocities greater than U_O, i.e., an "overshoot" in the velocity profiles. Although the overshoots are quite small in magnitude, the maximum being of the order of 0.007 U_O in the present case (these are barely visible in traditional plots like Fig. 20), and decrease to zero with distance from the trailing edge in all directions, they are of considerable significance in the interpretation of the results in the far wake and in comparisons with the so-called asymptotic laws.

The overshoot in the velocity profiles mentioned above immediately lead to problems in the definition of parameters used in the traditional analysis of asymptotic wakes. These are illustrated in Fig. 22. The assumption of constant velocity outside the wake, adopted in boundary-layer theory and assumed in experiments, yields the usual definitions of the centerline velocity defect W_O ($= U_O - U_c$) and wake half-width b ($= Y$ where $W/W_O = 1/2$). These are shown in Fig. 22(a). However, if the

pressure, and therefore the velocity, varies in the normal direction outside the wake, then the physically most meaningful definitions are those shown in Fig. 22(b). In this case the velocity defect is the difference between the actual velocity and the inviscid-flow velocity extrapolated into the wake. Note that it is this velocity defect which is related to the drag coefficient of the plate. The determination of the so-defined deficit from a numerical solution is not a straightforward matter because, as we have already noted, the overshoot is small in absolute terms but not small in comparison with the velocity defect which decreases with downstream distance and is a difference between two large quantities. In view of these difficulties, we shall adopt the conventional definitions even in the presence of an overshoot and use the velocity defect W_O^* (= U_O - U_C), and the corresponding half-width b^*, as shown in Fig. 22(c). These have the advantages that they can be determined precisely, can be used to assess certain asymptotic features of the solutions, and also enable a comparison to be made between the calculations and experimental data processed with the same definitions.

Figures 23 and 24 show the calculated velocity and Reynolds shear-stress profiles at several stations far downstream of the trailing edge (X > 2.3 L) in the usual defect forms, i.e., using W_O^* and b^* as the characteristic velocity and length scales, respectively. The velocity overshoot in the outer flow is clearly evident in Fig. 23 and amounts to about 12 percent of the centerline defect. Consistant with the eddy-viscosity assumption and the velocity overshoot, there is also a region of very small negative stress, but the stress reduces to practically zero at $Y/b^* \sim 1.2$. A particularly noteworthy feature is that the velocity profiles become self-similar somewhat earlier than the Reynold-stress profiles, with similarity in both beyond about 6000 mm (i.e. X > 3.3 L, approximately). This coincides roughly with the region beyond which the wake-centerline eddy viscosity became

constant (see Fig. 18). Such a similarity is to be expected on theoretical grounds because the partially-parabolic equations also reduce to the asymptotic, small-defect wake equations which are usually obtained from the boundary-layer equations. Ramparian, Patel and Sastry (1982) reviewed the available flat-plate wake data and concluded that the asymptotic behavior is realized with respect to the mean velocity and turbulence at a distance of the order of 350θ from the trailing edge, θ being the wake momentum thickness. The value of 3.3 L quoted above for the present calculations corresponds to about 770θ and, therefore, the present solutions indicate a somewhat slower approach to the asymptotic state.

Perhaps the most surprising result to emerge from the present calculations is the asymptotic value of the eddy viscosity in the far wake. The calculated value of $v_t/U_oL = 1.74 \times 10^{-4}$, quoted earlier (see Fig. 18), corresponds to $v_t/U_o\theta = 0.04$, which is somewhat higher than 0.035 ($\pm$ 0.001) deduced by Patel and Scheuerer (1982) from the data of Pot (1979) in the range $400 < X/\theta < 1000$. This difference is also observed in the maximum Reynolds stress: the calculated maximum of $- \overline{uv}/W_o^{*2}$ being 0.054 while the measurements of Pot indicate 0.050. These results are surprising because the extensive calculations of Patel and Scheuerer, who used boundary-layer equations but the same turbulence model, led to much smaller values of the eddy-viscosity (0.024) and maximum shear stress (0.034). This substantial underprediction was attributed by Patel and Scheuerer to a deficiency of the k-ϵ turbulence model. The present calculations, however, suggest that the disagreement between the experiments and calculations based on the boundary-layer equations may not be entirely due to the turbulence model. Rather, the variation of pressure and the normal-stress terms which are incorporated in the partially-parabolic equations but neglected in the boundary-layer equations may be responsible for the differences. The uncertainties in the definitions of the velocity

and length scales used in the asymptotic analysis may also contribute to the observed differences. Needless to say, the resolution of these rather perplexing differences is quite important in order to assess the generality of the turbulence model. Additional calculations and more detailed comparisons are obviously needed. These are in progress.

In conclusion, we note that the partially-parabolic method successfully predicts all of the features of laminar and turbulent flows over a flat plate. Inspite of the relative simplicity of this two-dimensional problem, it has provided an opportunity to test several basic components of the method by comparing the present results with those obtained by others with quite different methods.

V.2 Thick Axisymmetric Boundary Layer and Wake

Calculations using the present method have been made for five different bodies for which detailed experimental data are available. We shall, however, present the results for only two cases, namely the models with Afterbody 5 and Afterbody 1 tested by Huang et al. (1980, 1979). The former is of particular interest since the stern contains a point of inflextion and leads to quite dramatic changes in the surface pressure distribution. The latter is included here becasue it is the axisymmetric parent model of a family of three-dimensional bodies of elliptic cross-sections to be discussed later.

The calculations for Afterbody 5 were performed with 60 stations in the domain $0.60 \leq X/L \leq 13.20$, where X is measured along the axis of the body from the nose and L (= 9.55 ft) is the body length, and 19 points between the body and the external boundary at R/L = 0.8137, R being the radial distance from the body axis. A partial view of the body-fitted coordinates is shown in Fig. 4. The use of coordinate-stretching functions in the longitudinal and radial directions ensures that the grid points are closely spaced inside the viscous region and near the stern.

These calculations were started by specifying the grid geo-
metry, and the velocity and turbulence-parameter profiles in the
boundary layer at the upstream station, and assuming that a con-
stant ambient pressure, i.e. p = 0, prevails throughout the solu-
tion domain. For simplicity, flat-plate boundary-layer profiles
were used at the upstream station X = 0.6 L, where the boundary
layer is thin. The numerical solutions were then obtained using
the time-marching technique with a time increment of $\tau = 1.0$.

Since the influence on the transport quantities from down-
stream comes solely from the elliptic pressure field, a converged
solution is obtained only when the pressure field converges. It
is therefore very important to examine first the convergence
history of the pressure field. Fig. 25 shows the pressure dis-
tribution, C_p = 2p, on the body surface and along the wake
centerline calculated at different time steps or global sweeps.
It is seen that the solution converges monotonically and a
"steady-state" or converged solution is obtained after about 30
time steps or global sweeps. The converged solution is in fairly
good agreement with the data.

Fig. 26 shows the variation of pressure across the boundary
layer and in the external flow, as a function of the distance
from surface, $(R - R_o)$, where R_o is the local radius of the body,
all the way to the external boundary of the solution domain,
where C_p = 0 is specified. Here again the agreement with the
available experimental data is quite satisfactory, considering
the difficulties of accurately measuring pressure in such an
environment. Note that uniform ambient pressure is recovered
beyond a distance of about 0.35 L, from the body surface, and
consequently we conclude that the region of viscous-inviscid
interaction in this case extends to about 0.35L or 4 maximum body
diameters. Since the domain of the present calculations extends
well beyond this, the viscous-inviscid interaction is completely
captured without separate viscous-flow and potential-flow
calculations, and iterative matching between them.

Detailed comparisons between the calculated and experimental profiles of the axial (U) and radial (V) components of mean velocity, normalized by U_O, shown in Fig. 27 indicate that the boundary-layer thickness is correctly predicted. We also note that both components of velocity continue to vary outside the boundary layer in conformity with the calculated variation of pressure in the inviscid flow. The velocity profiles, and the profiles of turbulent kinetic-energy shown in Fig. 28, are also in good agreement with the experimental data except in the wall region near the tail (X/L > 0.95, say), where the boundary layer becomes thick. The larger values of mean velocity in the wall region of the thick boundary layer are presumably related to an over-estimation of the eddy-viscosity by the basic k-ε model. The wall-shear velocity U_t is also over-predicted over the last 10 percent of the body length (Fig. 29). In view of the observed disagreement, the measured velocity distributions were reanalyzed using the method of Clauser to determine the wall shear stress (see Fig. 30). As shown in Fig. 29, however, the difference between these and the Preston-tube values quoted by the experimenters is too small to account for the disagreement between the calculations and data over the tail region. In the upstream thin boundary-layer region, the present calculations also predict somewhat higher values of U_τ. This may be due to the use of the simple 1/7 - power law velocity profile at the initial station and possibly an insufficient grid resolution.

The calculations for the second axisymmetric body, namely Afterbody 1 (L=10.06 ft), were performed with 60 stations in the domain 0.50 < X/L < 16.25, and 19 points between the body and the external boundary at R/L = 0.8137. The coordinates for this case are shown in Fig. 31. These indicate somewhat milder curvature changes in the longitudinal direction compared to those for the Afterbody 5. The same initial conditions as for Afterbody 5 were specified at the upstream station X = 0.5L, and a time increment τ = 1.0 was used again.

The principal results of the calculations for Afterbody 1 are shown in Figs. 32 through 36. As can be seen from Figs. 32 and 35, the solution again converges in less than 30 global sweeps. The converged surface pressure distribution shown in Fig. 32 is in excellent agreement with the experimental data. The pressure along the wake centerline (X/L > 1.0), however, decays somewhat faster than the data in the near wake and becomes slightly negative before gradually recovering to the uniform ambient pressure in the far wake. The detailed pressure variations in the radial direction shown in Fig. 33, are also in good agreement with the data. Note that the pressure changes are relatively mild compared with the greater changes observed on Afterbody 5 (Fig. 26). This is obviously due to the smoother curvature variations in the present case. It is also interesting to note that the uniform ambient pressure is again recovered in the outer region, and the viscous-inviscid interaction is restricted to radial distances of the order of 0.35L from the body surface and wake centerline.

Detailed comparisons between the calculated and experimental mean-velocity profiles and turbulent kinetic-energy distributions are shown in Figs. 34 and 35, respectively. It is seen that the boundary layer thickness and half-width of the wake are correctly predicted. The axial (U) and radial (V) components of velocity in the stern and near wake region are also in very good agreement with the corresponding data. The calculated turbulent kinetic-energy distributions, however, are somewhat larger in the thick boundary layer region. As expected from the velocity distributions, the wall-shear velocity shown in Fig. 36 is in fairly good agreement with the data even in the thick boundary layer region near the tail. Here again, the experimental values obtained by Preston tubes agreed reasonably well with those determined from the Clauser plots (Fig. 37).

A comparison between the calculations for Afterbody 1 and Afterbody 5 indicates that quite satisfactory results are ob-

tained in both cases. However, some discrepancies are observed near the tail of Afterbody 5, which contains an inflexion point in the longitudinal profile and leads to rather larger adverse pressure gradients. The differences in the boundary-layer behavior in the tail region of the two bodies are also apparent from the Clauser plots shown in Figs. 30 and 37. It is seen from Fig. 37 that, under the moderate pressure gradients on Afterbody 1, the velocity profiles indicate larger regions of logarithmic behavior. On the other hand, the Clauser plots for Afterbody 5 shown in Fig. 30 indicate significant departures from the law of wall and greater scatter. The basic k-ε turbulence model employed here does not include any corrections for transverse or longitudinal curvatures, but a pressure-gradient correction has been employed in the wall functions. The results indicate that the latter may not be entirely satisfactory in strong pressure gradients. Also, the somewhat larger turbulent kinetic-energy levels predicted in the thick boundary layer region of Afterbody 5 suggest that some modifications may be required in the turbulence model.

Results similar to those presented here have also been obtained by a variety of other methods, ranging from interacting boundary-layer analysis (Patel and Lee, 1977; Lee, 1978; Huang, Santelli and Belt, 1979; Dietz, 1980; Hoffman, 1980), through partially-parabolic solutions (Muraoka, 1980; Hoffman, 1980; Hogan, 1983), to a fully-elliptic solution (Zhou, 1982). Unfortunately, only Huang et al. and Hogan have presented calculations for the two bodies considered here. Somewhat improved velocity profiles for Afterbody 5 were obtained by both in the wall regions by incorporating an empirical correction in the turbulence models.

A particularly noteworthy feature of the present solutions is the behavior of the pressure distribution close to the tail. Figures 25 and 32 indicate a region of pressure decrease followed by an increase over the extreme tail and then a monotonic decease

in the near wake. In the interacting boundary-layer solutions of Huang et al., on the other hand, the calculated pressure decreases continuously at the tail. We believe that the features predicted by the present method are genuine and are associated with the rapid changes in the geometry near the tail as well as the upstream influence of the complex pressure interaction in the tail region. Note that such a pressure behavior is also predicted by the present and previous calculations for even the simplest case of the trailing edge of a flat-plate (Figs. 11 and 15).

Finally, it should be remarked that the present calculations for Afterbody 1 and Afterbody 5, as well as those for three other bodies, for which extensive data are available in the thick boundary layer, extend to quite large distances ($\sim$ 15L) into the far wake. A critical examination of all the results will provide information not only on the performance of the turbulence model in the presence of strong lateral and longitudinal surface curvatures over the tail region but also on the flow in the near and far axisymmetric wakes, for which the available experimental data is rather limited.

V.3 Three-Dimensional Flow Over the Stern and in the Wake of Ship-Like Bodies

Huang, Groves and Belt (1983, 1984) and Groves, Belt and Huang (1982) have reported extensive measurements in the stern boundary layer of two ship-like bodies whose cross-sections are elliptic, with axes ratio 3:1 and 2:1. These bodies have the same lengths and cross-sectional area distributions as the parent axisymmetric (1:1 axes-ratio) Afterbody 1. We shall present some aspects of the calculations performed with the present method for these bodies.

The three-dimensional calculations for both bodies were performed with 60 stations in the longitudinal direction between

0.5 < X/L < 16.25. Of these, 40 are placed in the boundary-layer region 0.5 < X/L < 1 to capture the flow features associated with the rapid changes in body curvatures in the longitudinal and circumferential directions. The remaining 20 stations are located in the wake upto X/L = 16.25. Two nonuniform grid nets of 19 x 7 and 19 x 12 mesh points, respectively, are used at each cross-section, the outer boundary being a cylindrical surface of constant radius R = 0.8137L. Some views of the numerically-generated coordinates for the 3:1 body with (60, 19, 7) mesh points in the (ξ, η, ζ) directions were shown in Fig. 5. Similar coordinates were used for the second body. For this case, calculations were also performed with the finer (60, 19, 12) mesh to study the grid-dependence of the solutions.

The solutions were started by specifying the velocity and turbulence-parameter profiles at the upstream station where the boundary layer is thin and a constant ambient pressure was again assumed throughout the solution domain. For simplicity, flat-plate boundary-layer profiles with constant boundary-layer thickness around the girth were specified at the upstream station, although more appropriate initial conditions can be obtained from three-dimensional thin boundary-layer solutions. The unsteady marching technique is again employed with large time increments of $\tau = 1.0$ and 0.5 for the coarse and fine mesh calculations, respectively. Plane of symmetry boundary conditions were specified at $\theta = 0^0$ ($\zeta = 2$) and $\theta = 0^0$ ($\zeta = N$) as follows:

Along $\theta = 0(\zeta=2)$:

$$r(\xi, \eta, 1) = r(\xi, \eta, 3)$$
$$\theta(\xi, \eta, 1) = \theta(\xi, \eta, 3)$$
$$\phi(\xi, \eta, 1) = \phi(\xi, \eta, 3), \quad \phi \equiv U, V, k, \varepsilon, p$$
$$W(\xi, \eta, 1) = -W((\xi, \eta, 2)$$

and, along $\theta=90^0(\zeta=N)$:

$$r(\xi,\eta,N+1) = r(\xi,\eta,N-1)$$
$$\theta(\xi,\eta,N+1) = \pi-\theta(\xi,\eta,N-1)$$
$$\phi(\xi,\eta,N+1) = \phi(\xi,\eta,N-1), \quad \phi \equiv U,V,k,\epsilon,p$$
$$W(\xi,\eta,N) = - W(\xi,\eta,N-1)$$

where N=6 and 11 for the coarse and fine meshes, respectively.

Figures 38 and 39 show the convergence histories of the wall and wake-centerline pressure distributions, C_p = 2p and the friction velocity, U_τ , respectively, along θ = 90° for the 3:1 elliptic body. It can be seen that both converged monotonically in about 30 time steps or global sweeps. The converged pressure distributions along θ = 0° and 90°, shown in Fig. 40, are in fairly good agreement with the data. As in the previous two examples, significant pressure variations are again observed in the tail region.

Although there is no data available for direct comparison, the pressure distributions across the boundary layer and in the external flow are shown in Fig. 41 at several streamwise stations. It is seen that the uniform ambient pressure is recovered in the outer region, and the viscous-inviscid interaction, which is confined to radial distances of the order of 0.4L, is again captured. This is particularly encouraging considering the practical difficulties of matching separate viscous and inviscid solutions for three-dimensional thick boundary layers and wakes.

Figure 42 shows the calculated and experimental wall pressure distributions around the girth at several streamwise stations. Higher wall pressures are observed along θ = 90° as a result of more rapid curvature changes along that line. The calculations, however, predict a somewhat stronger three-dimensional effect as evidenced by the larger girthwise variation of pressure. It is somewhat surprising to note that larger discre-

pancies, in fact, are observed along $\theta = 0°$ where the boundary layer remains relatively thin throughout the stern region. It is also interesting to note that the potential-flow calculations, provided by Huang of the DTNSRDC (David W. Taylor Naval Ship Research and Development Center), also predict lower wall pressures along $\theta = 0°$, as shown in Fig. 43. A comparison between the potential-flow solutions and the present calculations indicates that the viscous-inviscid interaction is confined largely to the vicinity of $\theta = 90°$ where the boundary layer thickness is large. The large transverse and longitudinal inviscid pressure gradients around $\theta = 90°$ also suggest that conventional boundary-layer calculations based on the potential-flow pressure distribution will be in error, and may predict premature separation, in this region.

Figure 44 shows the distributions of the two nonzero components (U,V) of mean velocity within the boundary layer and in the wake in the two planes of symmetry. It should be emphasized that this is a close-up view of the viscous region since the solution domain extends well into the external inviscid flow field. The calculations are seen to be in good agreement with the measurements, which extend only upto $X/L = 0.954$. In fact, the level of agreement is comparable to that achieved in the axisymmetric flow on Afterbody 1 (Fig. 34). It is interesting to observe the evolution of the three-dimensionality of the flow over the stern. The boundary-layer thickness is nearly constant around the girth at $X/L = 0.719$ but the thickness along $\theta = 90°$ is almost three times that along $\theta = 0°$ by $X/L = 0.954$. Although no data are available in the wake, the calculations indicate that the three-dimensionality of the wake persists for quite large distances downstream. However, due to turbulent diffusion in the circumferential direction, the solutions eventually lead to an axisymmetric far wake. Also, we note that conventional boundary-layer calculations performed by Huang, Groves and Belt (1983) and Patel, Sarda and Shahshahan (1983) for this body breakdown around

96

X/L = 0.93 due to the thickening of the boundary layer, whereas the present method does not encounter such a difficulty and continues smoothly into the wake.

Figure 45 shows the turbulent kinetic-energy distributions along $\theta = 0°$ and $90°$ at several streamwise locations. Since not all normal Reynolds-stress components were measured on the planes of symmetry, the calculated turbulent kinetic-energy distributions along $\theta = 0°$ and $\theta = 90°$ are compared with the measurements at $\theta = 67°$ and $\theta = 87°$, respectively. It is seen that the agreement between the calculations and experiments, in general, is quite good except at $\theta = 90°$ and $X/L = 0.934$, where the experiments indicate a sudden increase of turbulent kinetic-energy, while the calculations predict a continuous decrease of maximum turbulent kinetic-energy, and a continuous thickening of boundary layer toward the tail. The disagreement between the calculated and measured kinetic-energy distributions in the outer part of the thick boundary layer along $\theta = 90°$ is also noteworthy since it may be related to a deficiency of the turbulence model.

Finally, the wall shear stresses along $\theta = 0°$ and $\theta = 90°$, which were not measured in this experiment, were determined from Clauser plots of the measured velocity profiles as shown in Fig. 46. In Fig. 47, the calculated wall-shear velocities are compared with those obtained from the Clauser plots. It is seen that the calculations predict the overall features observed in the experiments but the values are somewhat higher. It is also interesting to note that the present calculations predict a higher shear stress along $\theta = 90°$ in the thin boundary layer region upto $X/L = 0.7$ even though a constant shear stress was specified around the girth at the upstream station. This behavior is also evident from the Clauser plots of the measured velocity profiles at $X/L = 0.719$.

For the 2:1 axes-ratio body, the calculations were performed using both the coarse (60x19x7) and the finer (60x19x12) grid. Figure 48 shows the calculated and experimental pressure distri-

97

butions on the wall and along the centerline of the wake on the two planes of symmetry. It is seen that both grids give essentially the same results which are in good agreement with the data. Note that the pressure distributions show a behavior very similar to those obtained for the 3:1 body (Fig. 40) and the axisymmetric Afterbody 1 (Fig. 32).

The pressure distributions across the boundary layer and in the external inviscid flow are compared with the experimental data in Fig. 49. The agreement between the calculations and measurements, in general, is good within the boundary layer. However, the calculated pressures recover slowly to the uniform ambient pressure in the outer region, while the measurements indicate an unrealistically abrupt return to zero pressure just outside the boundary layer. This is particularly evident from the close-up views of the pressure distributions shown in Fig. 50. The measurements extend only upto a normal distance of the order of 10 inches, and indicate rather large normal pressure gradients at the outermost measurement station. This is in sharp contrast with the measurements on the axisymmetric Afterbody 1 (Fig. 33) which clearly indicated a much larger region of normal pressure variation and a gradual approach to the ambient pressure. In fact, the calculations for all three bodies (1:1, 2:1 and 3:1) indicate about the same extent of viscous-inviscid interaction, and therefore the disagreement seen in Figs. 49 and 50 outside the boundary layer is most likely due to systematic errors in the measurement of the rather small pressure changes. It should be remarked here also that the measured wall pressures appear to be inconsistent with the pressures measured in the flow field. In particular, the wall pressures at $X/L = 0.858$ and 0.894 along $\theta = 90°$ are considerably lower than those measured very close to the wall (see Fig. 50b). It is also of interest to note that the present calculations predict a decrease of pressure in the near-wall region along $\theta = 0°$ upto $X/L = 0.95$, whereas the experiments indicate a continuous increase toward the body

98

surface in the tail region. If these differences are taken into account, the general level of agreement between the calculations and experiments is actually much better than that indicated by the wall pressure distribution shown in Fig. 48.

For further understanding of the three-dimensional pressure field, the calculated and experimental wall pressures around the girth are shown in Fig. 51. The calculations are in fairly good agreement with data and show a behavior very similar to that observed on the 3:1 body, except that the girthwise pressure changes are somewhat smaller, as expected. It should be remarked, however, that considerable scattering of the data is seen near $\theta = 90°$ while the calculations predict a smooth variation toward the symmetry plane. Nevertheless, the overall agreement in the pressure distributions is quite satisfactory.

Detailed comparisons of the calculated velocity profiles with the experimental data are shown in Figs. 52 and 53 for the coarse and finer grid calculations, respectively. Both calculations are in good agreement with the corresponding data in the boundary-layer region $(X/L < 1)$, but the calculations with the finer gird predict a somewhat stronger three-dimensionality in the far wake, presumably due to the better resolution of travsverse gradients near $\theta = 0°$. The evolution of the three-dimensionality of the flow over the stern is again well predicted.

Figure 54 shows a comparison between the calculated wall-shear velocities along $\theta = 0°$ and $90°$ and those measured by Huang et al. using Preston tubes. It is seen that the calculations exhibit the same trends as the experimental data, but the calculated values are much higher. This is particularly surprising in view of the fact that the calculated velocity profiles are in fairly good agreement with the data. In order to resolve this apparent discrepancy, the experimental velocity profiles were again analyzed using Clauser plots, which are shown in Fig. 55. The wall-shear velocities determined in this manner

99

are shown in Fig. 56. These are in much better agreement with the calculations.

In Fig. 57, the calculated turbulent kinetic-energy distributions are compared with the experimental data at several streamwise stations. In the thick boundary layer region, the calculated energy levels are comparable with those obtained for the 3:1 body, but are much higher than the data on the 2:1 body. This is somewhat surprising in view of the good agreement observed in the previous case (see Fig. 45).

It is instructive to compare the calculations and measurements at a fixed streamwise station, $X/L = 0.934$ say, common to all three bodies of the same family. In the axisymmetric case, Fig. 35 shows that the maximum measured value of k is of the order of 2.9×10^{-3} and this compares favorably with the calculated values. On the 2:1 and 3:1 bodies (Figs. 57 and 45, respectively) the maximum measured values in the relatively thin boundary layer along the flatter surface at $\theta = 0°$ are 3.4×10^{-3} and 4.0×10^{-3}, and the corresponding calculations indicate 3.9×10^{-3}. This level of agreement is considered quite satisfactory and the general increase in k with increasing axes ratio observed in the experiments and predicted by the calculations may be associated with the divergence of the mean streamlines out of the $\theta = 0°$ plane of symmetry. The situation along the $\theta = 90°$ plane, where the boundary layer is thick and the transverse curvature is large, is more complex. The measured maximum values of k are 1.5×10^{-3} for the 2:1 body and 3.5×10^{-3} for the 3:1 body while the calculations indicate 2.4×10^{-3} and 2.0×10^{-3}, respectively, i.e., a systematic decrease from the axisymmetric case. As noted earlier, the high measured value at $X/L = 0.934$ on the 3:1 body (see Fig. 45) is not consistent with the measurements further upstream. If this is disregarded, the measurements and calculations depict similar trends with respect to the maximum turbulence levels. However, the rather dramatic difference in the detailed shapes of the measured k profiles on

100

the 2:1 and 3:1 bodies (compare Figs. 57 and 45) along $\theta = 90°$ remains a mystery. The calculations do not indicate any major changes in the profile shape among the three bodies although, in all three cases, the predictions indicate greater diffusion in the outer parts of the boundary layer. The latter feature appears to be a deficiency of the turbulence model. Obviously, a much more detailed analysis of the experimental and calculated results than attempted here is required in order to gain a better insight into the performance of the turbulence model.

Thus far, we have considered the details of the flow in the planes of symmetry of the three-dimensional bodies since direct comparison is possible without any interpolation in the data or calculations. Comparisons off the symmetry planes are not as straightforward due to the quite different coordinates utilized in the experiments and calculations. An indication of the overall three-dimensionality of the flow on the 2:1 body is, however, provided by plotting the velocity vectors in several cross-sections. Since, in the present formulation, the longitudinal component (U) is parallel to the body axis, it is necessary to show only the resultant of the radial (V) and circumferential (W) components. The results of the finer-grid solutions are shown in this manner in Fig. 58. Note that these plots depict only a portion of the solution in the vicinity of the body, which is also shown to scale.

In the thin boundary layer region upto $X/L = 0.853$ (Fig. 58a,b), the velocity vectors are essentially normal to the wall, and directed towards the wall due to the longitudinal curvature of the surface. The crossflow angles are relatively small. The increasing normal velocity components predicted in the thick boundary layer region near the tail (Figs. 58c,d,e) are obviously due to the rapid changes of body shape. Although the magnitude of the secondary flow is quite small, the flow vectors indicate the development of a small zone of circumferential flow reversal or vortical flow in the tail region. This is particularly evi-

101

dent in the wake region where the radial velocity components become small also. For a better understanding of the development of this feature, the inner regions of the flow at a few stations near the tail of the body are further enlarged and shown in Fig. 59. A longitudinal vortex like structure is clearly evident in the near wake (Fig. 59c). Its size appears to grow but the strength diminishes with downstream distance. The results shown in Figs. 58 and 59 indicate that the flow on the 2:1 elliptic body is only weakly three dimensional. A similar conclusion can be drawn also for the 3:1 body.

Finally, it should be emphasized that the present calculations utilize the radial (V) and circumferential (W) components of velocity in a basic cylindrical polar coordinate system referenced to the body axis, and not the conventional boundary-layer velocity components (i.e., normal and tangential to the body surface). Therefore, the calculated V and W component velocities are, in fact, quite large and of the same order of magnitude even though the magnitude of the secondary flow in boundary-layer coordinates is relatively small. The calculations described here presented no difficulty in handling these large component velocities, and the numerical method is not restricted to small crossflows.

VI. CONCLUSIONS

A versatile new method for the calculation of the flow over the stern and in the wake of ship-like bodies has been described and several examples have been presented to demonstrate its capabilities. The method solves the partially-parabolic (or "semi-elliptic" or "parabolized") Reynolds-averaged Navier-Stokes equations. Among the distinctive features of the method are the following:

(1) Numerically-generated nonorthogonal coordinates are used to facilitate application of the method to a wide variety of body shapes.

(2) The finite-analytic scheme, which uses analytic solutions of the locally-linearized convective transport equations, enables the resolution of the flow in regions of larger velocity gradients with comparatively few grid points in the solution domain and results in an economical method.

(3) The transport equations are solved by a space- and time-marching technique, which enables future extensions to unsteady and fully-elliptic problems.

(4) The elliptic pressure field is determined by a new two-step global iteration technique which results in rapid and monotonic convergence of the entire solution. This algorithm also facilitates the future extension of the method to fully-elliptic equations.

(5) The method enables the use of a large solution domain and requires only the body geometry and initial boundary-layer information as inputs. Thus, the need for separate viscous and inviscid solutions, and

matching between them, is eliminated.

(6) For turbulent flows, the standard k-ε model has been used. However, the usual sensitivity of the solutions to the near-wall grid distribution has been greatly reduced by anchoring the solutions to the wall functions at two grid nodes adjacent to a solid wall.

All calculations presented here were performed on a Prime 750 minicomputer with computing times of less than 10 minutes for the two-dimensional and axisymmetric cases, and of the order of two hours for three-dimensional bodies. It should, therefore, be possible to use the method for practical applications.

While the overall numerical framework of the method has been established and tested, and calculations for practical hull forms are now in progress, there are several basic physical and numerical aspects of the method which require further scrutiny and development. Among these are the following:

(1) The influence of the grid distribution on the solution of the flow equations: more general grid-control functions need to be identified to provide the greater flexibility required for complex ship geometries.

(2) The influence of the initial conditions: detailed three-dimensional boundary-layer calculations may be required at the upstream station to provide more accurate initial conditions for complex three-dimensional body geometries.

(3) The influence of the choice of coordinates on the solutions: For some applications, and extensions of the method to treat separated flows, it may be necessary to use velocity components aligned with the coordinate lines. The necessary equations have been derived. These contain many more geometrical parameters which need to be either stored or recalculated.

(4) The sensitivity of the solutions to the turbulence model: the validity of the basic $k-\varepsilon$ turbulence model employed here, in general, and the limitations of the wall functions, in particular, in complex three-dimensional flows needs to be studied by more critical examination of the available experimental data and corresponding calculations.

(5) The limitations of the partially-parabolic approximations: this can be investigated by comparison with the corresponding fully-elliptic solutions.

Finally, we note that the generality of the approach presented here offers encouraging prospects for incorporating propellors and appendages in the solution domain in a more comprehensive manner than has been possible with presently available methods. Also, the structure of the solution algorithms selected is such that the method can be extended to treat fully-elliptic, unsteady, three-dimensional flows.
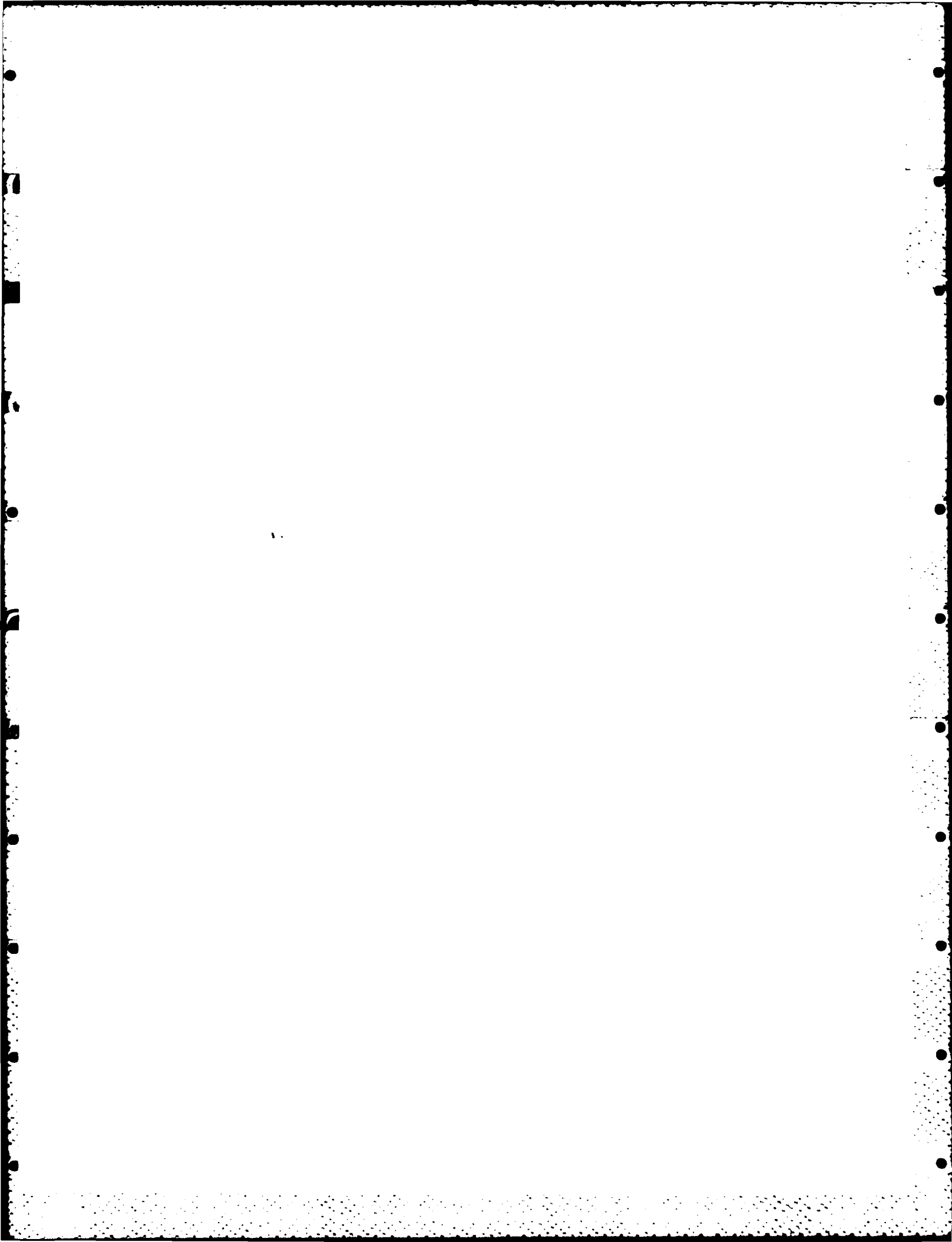
REFERENCES

ABDELMEGUID, A.M. MARKATOS, N.C., MURAOKA, K. and SPALDING, D.B.
1979 "A Comparison Between the Parabolic and Partially-Para-
bolic Solution Procedures for Three-Dimensional Turbulent
Flows Around Ship's Hulls", Appl. Math. Modelling, Vol. 3,
p. 249.

ADAIR, D., THOMPSON, B.E. and WHITELAW, J.H. 1983 "Measurements
and Calculations of a Separated Boundary Layer and the Down-
stream Wake", Proc. 2nd Sym. Numerical & Physical Aspects of
Aerodynamic Flows, Long Beach, CA.

ARIS, R. 1971 "Vectors, Tensors, and the Basic Equations of Fluid
Mechanics", Printice-Hall, Englewood Cliffs, NJ.

BALDWIN, B.S. and LOMAX, H. 1978 "Thin-Layer Approximation and
Algebraic Model for Separated Turbulent Flows", AIAA Paper
78-257.

BRADSHAW, P., KAVANAGH, M.J. and MOBBS, D. 1983 "Viscous-Inviscid
Matching Using Higher-Order Shear-Layer Equations", Proc.
2nd Sym. Numerical & Physical Aspects of Aerodynamic Flows,
Long Beach, CA.

BRILEY, W.R. and MCDONALD, H. 1977 "Solution of the Multidimen-
sional Compressible Navier-Stokes Equations by a Generalized
Implict Method", J. Comp. Phys., Vol. 24, p. 372.

CHEN, C.J. and CHEN, H.C. 1982 "Development of Finite-Analytic
Method for Unsteady Two-Dimensional Convective Transport
Equation", Proc. Int. Sym. Refined Modelling of Flows, IAHR,
Paris, Vol. 1, p. 69. Also, Iowa Inst. Hyd. Res., Report
N232-IV.

CHEN, C.J. and CHEN, H.C. 1984 "Finite-Analytic Numerical Method
for Unsteady Two-Dimensional Navier-Stokes Equations", J.
Comp. Phys., Vol. 53, pp. 210-226.

CHEN, C.J., YOON, Y.H. and YU, C.H., "The Finite Analytic
Method", Iowa Inst. Hyd. Res., Report N232-VI.

CHEN, H.C. and PATEL, V.C. 1984 "Calculation of Stern Flows by a
Time-Marching Solution of the Partially-Parabolic Equa-
tions", Proc. 15th ONR Symposium on Naval Hydrodynamics,
Hamburg, FRG.

CHENG, W.S. and PATEL, V.C. 1983 "Numerically-Generated Coordi-
nates Suitable for Ship Stern and Wake Flow Calculations",
Iowa Inst. Hydr. Res., Report No. 265, p. 33.

CHIEN, K.Y. and HSIEH, T., 1983 "Navier-Stokes Calculation for a
Body of Revolution at Incidence", Proc. 2nd Sym. Physical &
Numerical Aspects of Aerodynamic Flows, Long Beach, CA.

DAVIS, R.T. and WERLE, M. 1981 "Progress on Interacting Boundary
Layer Calculations at High Reynolds Numbers", Proc. 1st Sym.
Numerical & Physical Aspects of Aerodynamic Flows, Long
Beach, CA.

DEIWERT, G.S. 1981 "Numerical Simulation of Three-Dimensional
Boattail Afterbody Flow Field", AIAA Journal, Vol. 19, pp.
582-588.

DENNIS, S.C.R. and DUNWOODY, J. 1966 "The Steady Flow of a Viscous Fluid Past a Flat-Plate", J. Fluid Mech., Vol. 24, pp. 577-595.

DIETZ, M.S. 1980 "An Axisymmetric, Strong Interaction Procedure to Include Large, Normal Pressure Gradients", Applied Research Lab., Penn. State Univ., Tech. Memo. 80-160.

DYNE, G. 1978 "A Streamline Curvature Method for Calculating the Viscous Flow around Bodies of Revolution", Proc. Int. Sym. Ship Viscous Resistance, Goteborg, pp. 6.1-6.22.

GELLER, E.W. 1979 "Calculation of Flow in the Tail Region of a Body of Revolution", AIAA, J. Hydronautics, Vol. 13, pp. 127-129.

GROVES, N.C., BELT, G.S. and HUANG, T.T. 1982 "Stern Boundary-Layer Flow on a Three-Dimensional Body of 3:1 Elliptic Cross Section", DTNSRDC Rept. 82/022.

HAN, C. and LAKSHMINARAYANA, B. 1982 "Measurements and Prediction of Mean Velocity and Turbulence Structure in the Near Wake of an Airfoil", J. Fluid Mech., Vol. 115, pp. 251-282.

HANKEY, W.L., GRAHAM, J.E. and SHANG, J.S. 1982 "Navier-Stokes Solution of a Slender Body of Revolution at Incidence", AIAA Journal, Vol. 20, pp. 776-781.

HARLOW, F.H. and WELCH, J.E. 1965 "Numerical Calculation of Time-Dependent Viscous Incompressible Flow of Fluid with Free Surface", Phys. Fluids, Vol. 8, pp. 2182-2189.

HOFFMAN, G.H. 1980 "A Modified Displacement-Body Method for Treating the Axisymmetric Strong Interaction Problem", J. Ship Res., Vol. 24, p. 114.

HOFFMAN, G.H. 1982 "A Spline Solution of the Incompressible Para-
bolized Navier-Stokes Equations in a Sheared Coordinate
System", App. Research Lab., Penn. State Uni., Tech. Memo.
82-S1.

HOGAN, T.F. 1983 "A Calculation of the Parabolized Navier-Stokes
Equations for Turbulent Axisymmetric Flows Using Streamline
Coordinates and the $k-\varepsilon$ Turbulence Model", DTNSRDC Rept.
83/070.

HORSTMAN, C.C. 1983 "Numerical Simulation of Turbulent Trailing
Edge Flows", Proc. 2nd Numerical & Physical Aspects of
Aerodynamic Flows, Long Beach, CA.

HUANG, T.T., GROVES, N.C. and BELT, G.S. 1984 "Stern Boundary-
Layer Flow on a Three-Dimensional Body of 2:1 Elliptic Cross
Section", DTNSRDC Rept. 84/022.

HUANG, T.T., GROVES, N.C. and BELT, G.S. 1983 "Stern Boundary-
Layer Flow on Two Three-Dimensional Bodies Having Elliptic
Transverse Cross-Sections", Proc. 2nd Sym. Numerical and
Physical Aspects of Aerodynamic flows, Long Beach, CA.

HUANG, T.T., GROVES, N.C. and BELT, G. 1980 "Boundary-Layer Flow
on an Axisymmetric Body with an Inflected Stern", DTNSRDC
Rept. 80/064.

HUANG, T.T., SANTELLI, N. and BELT, G. 1979 "Stern Boundary-Layer
Flow on Axisymmetric Bodies", Proc. 12th Sym. Naval Hydrody-
namics, Nat. Acad. Sci., pp. 127-157.

HUNG, C.M. 1980 "Numerical Solution of Supersonic Laminar Flow
over an Inclined Body of Revolution", AIAA Journal, Vol. 18,
pp. 921-928.

HUNG, C.M. and CHAUSSEE, D.S. 1981 "Computation of Supersonic

    Turbulent Flows over an Inclined Ogive-Cylinder-Flare", AIAA

    Journal, Vol. 19, pp. 1139-1144.

JANSSEN, E. 1958 "Flow Past a Flat Plate at Low Reynolds

    Numbers", J. Fluid Mech., Vol. 3, pp. 329-343.

JOBE, C.E. and BURGGRAF, O.R. 1974 "The Numerical Solution of the

    Asymptotic Equations of Trailing-Edge Flow", Proc. Roy.

    Soc., Vol. A340, pp. 91-111.

KLINE, S.J., CANTWELL, B.J. and LILLEY, G.M. (Eds.) 1983 "Complex

    Turbulent Flows", Proc. 1980-81 AFOSR-HTTM-STANFORD Confer-

    ences, Vols. I, II and III.

LARSSON, L. and CHANG, M.S. 1980 "Numerical Viscous and Wake

    Resistance Calculations Including Interaction", Proc. 13th

    ONR Sym. Naval Hydrodynamics, Tokyo, Shipbuilding Res.

    Assoc. Japan, pp. 707-728.

LASS, H. 1975 "Vector and Tensor Analysis", McGraw-Hill.

LE BALLEUR, J.C. 1983 "Numerical Viscid-Inviscid Interaction in

    Steady and Unsteady Flows", Proc. 2nd Sym. Numerical &

    Physical Aspects of Aerodynamic Flows, Long Beach, CA.

LEE, Y.T. 1978 "Thick Axisymmetric Turbulent Boundary Layer and

    Wake of a Low-Drag Body", Ph.D. Thesis, The University of

    Iowa.

MARKATOS, N.C. 1984 "The Computation of Thick Axisymmetric Boun-

    dary Layers and Wakes around Bodies of Revolution", Proc.

    Inst. Mech. Engrs., London, Vol. 198 , pp. 51-62.

MARKATOS, N.C., MALIN, M.R. and TATCHELL, D.G. 1980 "Computer Analysis of Three-Dimensional Turbulent Flows Around Ship's Hulls", Proc. Inst. Mech. Engrs., London, Vol. 194, pp. 239-248.

MCDONALD, H. and BRILEY, W.R. 1983 "A Survey of Recent Work on Interacted Boundary Layer Theory for Flow with Separation", Proc. 2nd Sym. Numerical & Physical Aspects of Aerodynamic Flows, Long Beach, CA.

MELNIK, R.E. and CHOW, R. 1975 "Asymptotic Theory of Two-Dimensional Trailing Edge Flows", Grumman Research Dept., Rept RE-510J.

MESSITER, A.F. 1970 "Boundary Layer Flow Near the Trailing Edge of a Flat Plate", SIAM J. Appl. Math., Vol. 18, pp. 241-257.

MURAOKA, K. 1982 "Calculation of Viscous Flow around Ships with Parabolic and Partially Parabolic Flow Solution Procedure", Trans. West Japan Soc. Naval Arch., Vol. 63, pp. 13-29.

MURAOKA, K. 1980 "Calculation of Thick Boundary Layer and Wake of Ships by a Partially Parabolic Method", Proc. 13th ONR Sym. Naval Hydrodynamics, Tokyo, Shipbuilding Res. Assoc. Japan, pp. 601-616.

NAGAMATSU, T. 1980 "Calculation of Viscous Pressure Resistance of Ships Based on Higher Order Boundary Layer Theory", J. Soc. Naval Arch., Japan, Vol. 147. Also, SSPA-ITTC Workshop, SSPA Report 90, 1981, pp. 97-114.

NAKAYAMA, A., PATEL, V.C. and LANDWEBER, L. 1976 "Flow Interaction Near the Tail of a Body of Revolution: Parts I and II", ASME, J. Fluids Eng., Vol. 98, pp. 531-549.

NASH, J.F. and PATEL, V.C. 1972 "Three Dimensional Turbulent
  Boundary Layers", SBC Tech Books, Atlanta.

ODABASI, A.Y. and DAVIES, M.E. 1983 "Structure of the Turbulent
  Shear Flow in Ship Boundary Layers", Proc. 2nd Sym. Nu-
  merical & Physical Aspects of Aerodynamic Flows, Long Beach,
  CA.

PATANKAR, S.V. 1980 "Numerical Heat Transfer and Fluid Flow",
  McGraw-Hill.

PATANKAR, S.V. and SPALDING, D.B. 1972 "A Calculation Procedure
  for Heat, Mass and Momentum Transfer in Three-Dimensional
  Flows", Int. J. Heat Mass Transfer, Vol. 15, pp. 1787-1806.

PATEL, V.C. 1982 "Some Aspects of Thick Three-Dimensional
  Boundary Layers", Proc. 14th ONR Sym. Naval Hydrodynamics,
  Ann Arbor, MI, pp. 999-1040.

PATEL, V.C and BAEK, J.H. 1983 "Calculation of Boundary Layers
  and Separation on a Spheroid at Incidence", Proc. 2nd Sym.
  Numerical & Physical Aspects of Aerodynamic Flows, Long
  Beach, CA; Also, AIAA Journal, Vol. 23, pp. 55-63, 1985.

PATEL, V.C. and LEE, Y.T. 1977 "Thick Axisymmetric Turbulent
  Boundary Layer and Near Wake of a Low-Drag Body of Revolu-
  tion", Iowa Inst. Hyd. Research, IIHR Rept. 210.

PATEL, V.C., NAKAYAMA, A. and DAMIAN, R. 1974 "Measurements in
  the Thick Axisymmetric Turbulent Boundary Layer Near the
  Tail of a Body of Revolution", J. Fluid Mech., Vol. 63, pp.
  345-362.

PATEL, V.C., SARDA, O.P. and SHAHSHAHAN, A. 1983 "Calculation of Ship Boundary Layers", Proc. 4th Sym. Turbulent Shear Flow, Karlsruhe, p. 3.1.

PATEL, V.C. and SCHEUERER, G. 1982 "Calculation of Two-Dimensional Near and Far Wakes", AIAA Journal, Vol. 20, pp. 900-907.

POT, P.J. 1979 "Measurement in a 2D Wake Merging into a Boundary Layer", NLR, The Netherlands, Rept. TR 19063 U.

PRATAP, V.S. 1975 "Flow and Heat Transfer in Curved Ducts", Ph.D. Thesis, London University.

PRATAP, V.S. and SPALDING, D.B. 1976 "Fluid Flow and Heat Transfer in Three-Dimensional Duct Flows", Int. J. Heat & Mass Transfer, Vol. 19, pp. 1183-1188.

PULLIAM, T.H. and LOMAX, H. 1979 "Simulation of Three-Dimensional Compressible Viscous Flow on the ILLIAC IV Computer", AIAA Paper 79-0206.

PULLIAM, T.H. and STEGER, J.L. 1980 "Implicit Finite-Difference Simulations of Three-Dimensional Compressible Flow", AIAA Journal, Vol. 18, pp. 159-167.

RAMAPRIAN, B.R., PATEL, V.C. and SASTRY, M.S. 1981 "Turbulent Wake Development Behind Streamline Bodies", Iowa Inst. Hyd. Res., IIHR Rept. 231; Also, AIAA Journal, Vol. 20, pp. 1228-1235, 1982.

RUBIN, S.G. and REDDY, D.R. 1983 "Global Solution Procedures for Incompressible Laminar Flow with Strong Pressure Interaction and Separation", Proc. 2nd Sym. Numerical & Physical Aspects of Aerodynamic Flows, Long Beach, CA.

SAINT-VICTOR, X. de and COUSTEIX, J. 1984 "Methods Iteratives de
     Marche Appliquees au Calcul du Melange Tridimensionnel d'un
     Sillage et d'une Couche Limite", ONERA Rept. 61/2259 AND.

SHANG, J.S. BUNING, P.G., HANKEY, W.L. and WIRTH, M.C. 1980 "Per-
     formance of a Vectorized Three-Dimensional Navier-Stokes
     Code on the CRAY-1 Computer", AIAA Journal, Vol. 18, pp.
     1073-1079.

SHANG, J.S. and HANKEY, W.L. 1983 "Computation of Flow Past a
     Hypersonic Cruiser", Proc. 2nd Sym. Numerical & Physical
     Aspects of Aerodynamic Flows, Long Beach, CA.

SOEJIMA, S. 1983 "Calculation of Three-Dimensional Boundary
     Layers Around Ship Hull Forms", Proc. 2nd Sym. Numerical &
     Physical Aspects of Aerodynamic Flows, Long Beach, CA.

SPALDING, D.B. 1972 "A Novel Finite Difference Formulation for
     Differential Equations Involving Both First and Second
     Derivatives", Int. J. Num. Methods in Eng., Vol. 4, pp. 551-
     559.

SPALDING, D.B. 1981 "A General Purpose Computer Program for
     Multi-Dimensional One- and Two-Phase Flow", Mathematics &
     Computers in Simulation", Vol. 13, pp. 267-276.

SPRADLEY, L.W., STALNAKER, J.F. and RATLIFF, A.W. 1981 "Solution
     of the Three-Dimensional Navier-Stokes Equations on a Vector
     Processor", AIAA Journal, Vol. 19, pp. 1302-1308.

STEWARTSON, K. 1969 "On the Flow Near the Trailing Edge of a Flat
     Plate II", Mathematika, Vol. 16, pp. 106-121.

THOMPSON, J.F., WARSI, Z.U.A. and MASTIN, C.W. 1982 "Boundary-Fitted Coordinate Systems for Numerical Solution of Partial Differential Equations-A Review", J. Comp. Phys., Vol. 47, pp. 1-108.

THOMPSON, J. (Ed.) 1982 "Numerical Grid Generation", Elsevier Science Publishing Co.

TZABIRAS, G.D. 1983 "On a Method for the Calculation of Turbulent Flow at the Stern of a Double Model", Proc. 12th SMSSH Seminar, Varna, Bulgaria, p. 39-1.

TZABIRAS, G.D. and LOUKAKIS, T.A. 1983 "A Method for Predicting the Flow Around the Stern of Double Ship Hulls", Nat. Tech. Uni., Athens, Unpublished Report.

VATSA, V.N. and VERDON, J.M. 1983 "Viscous/Inviscid Interaction Analysis of Asymmetric Trailing-Edge Flows", Proc. 2nd Sym. Numerical & Physical Aspects of Aerodynamic Flows, Long Beach, CA.

VELDMAN, A.E.P. 1975 "Boundary Layer Flow Past a Finite Flat Plate", Thesis, Math. Inst., Uni. Groningen, The Netherlands.

VELDMAN, A.E.P. 1979 "A Numerical Method for the Calculation of Laminar, Incompressible Boundary Layers with Strong Viscous-Inviscid Interaction", NLR, The Netherlands, Rept. TR 79023 U.

VELDMAN, A.E.P. 1981 "New Quasi-Simultaneous Method to Calculate Interacting Boundary Layers", AIAA Journal, Vol. 19, pp. 765-785.

ZHOU, L-D. 1982 "A Streamline-Iteration Method for Calculating
Turbulent Flow Around the Stern of a Body of Revolution and
its Wake", Proc. 14th ONR Sym. Naval Hydrodynamics, Ann
Arbor, MI, pp. 1041-1069.

HORIZONTAL SECTION

VERTICAL SECTION
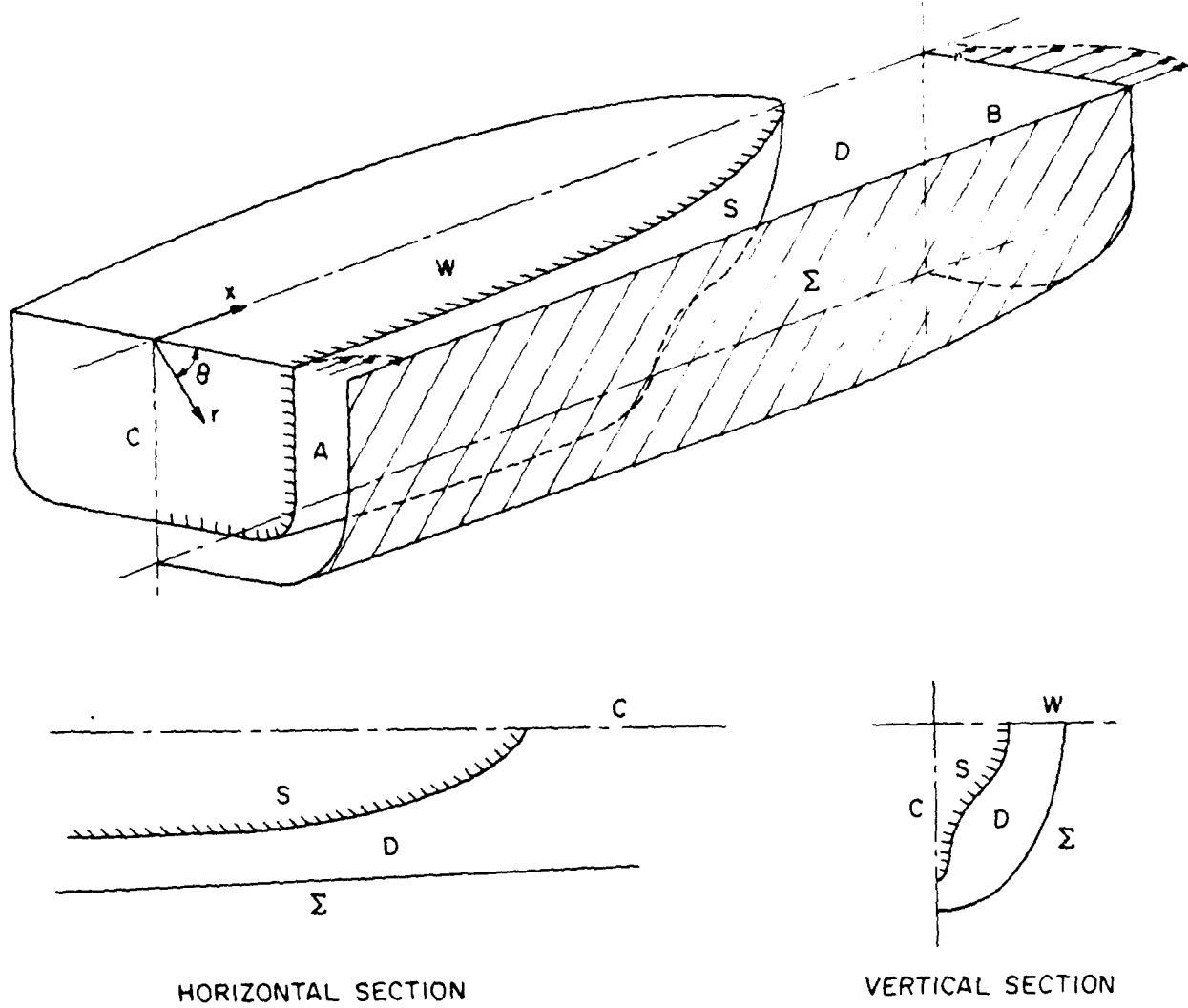
Fig. 1.   Physical Solution Domain
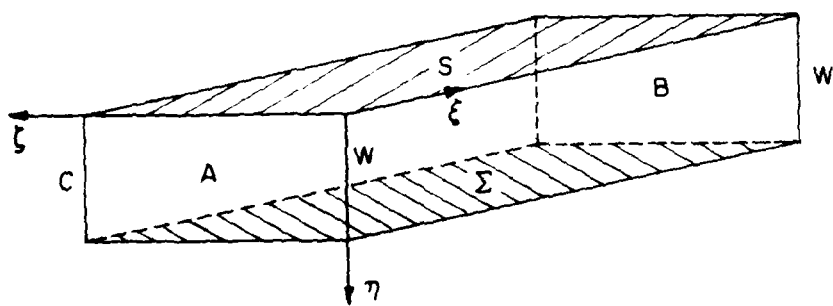
Fig. 2.   Transformed Domain
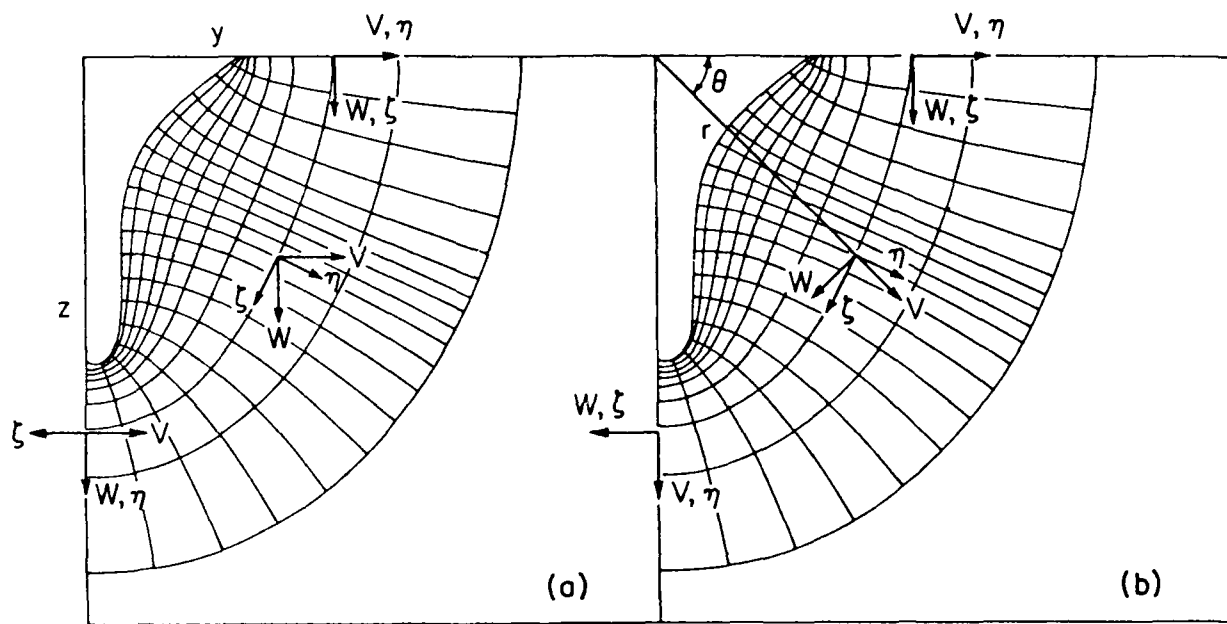
Fig. 3.   Velocity Components in (a) Cartesian,
(b) Cylindrical Coordinates

AFTERBODY5
— Exponential Scheme
--- Central-Difference Scheme
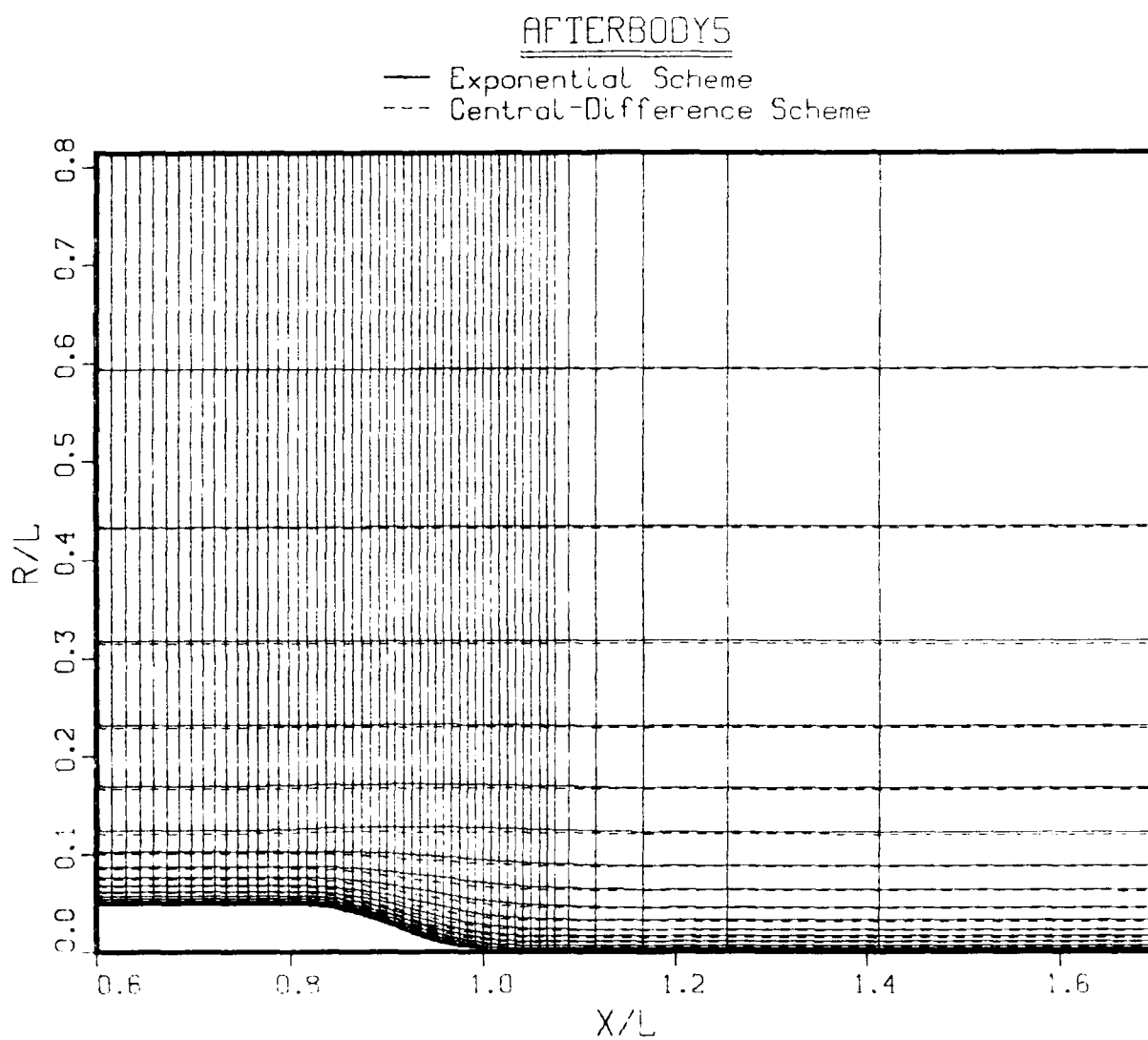
Fig. 4.   Numerical Grid for Afterbody 5 (Partial View)

3:1 BODY , θ = 0°
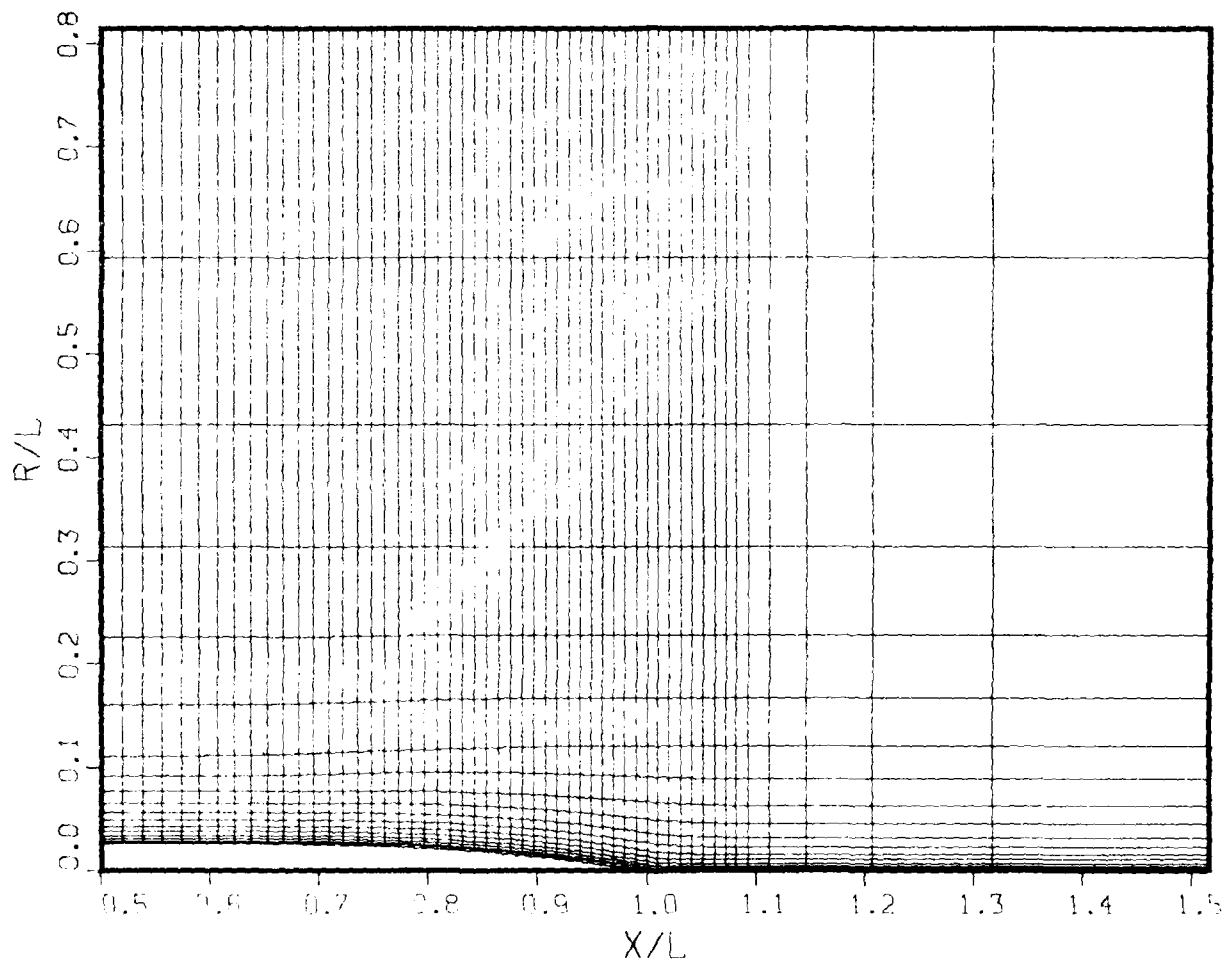
Fig. 5.   Numerical Grid for the 3:1 Elliptic Body of Huang et
           al. (1983)
           (a) Longitudinal View at θ = 90°

120

$3:1$ BODY , $\theta = 90°$
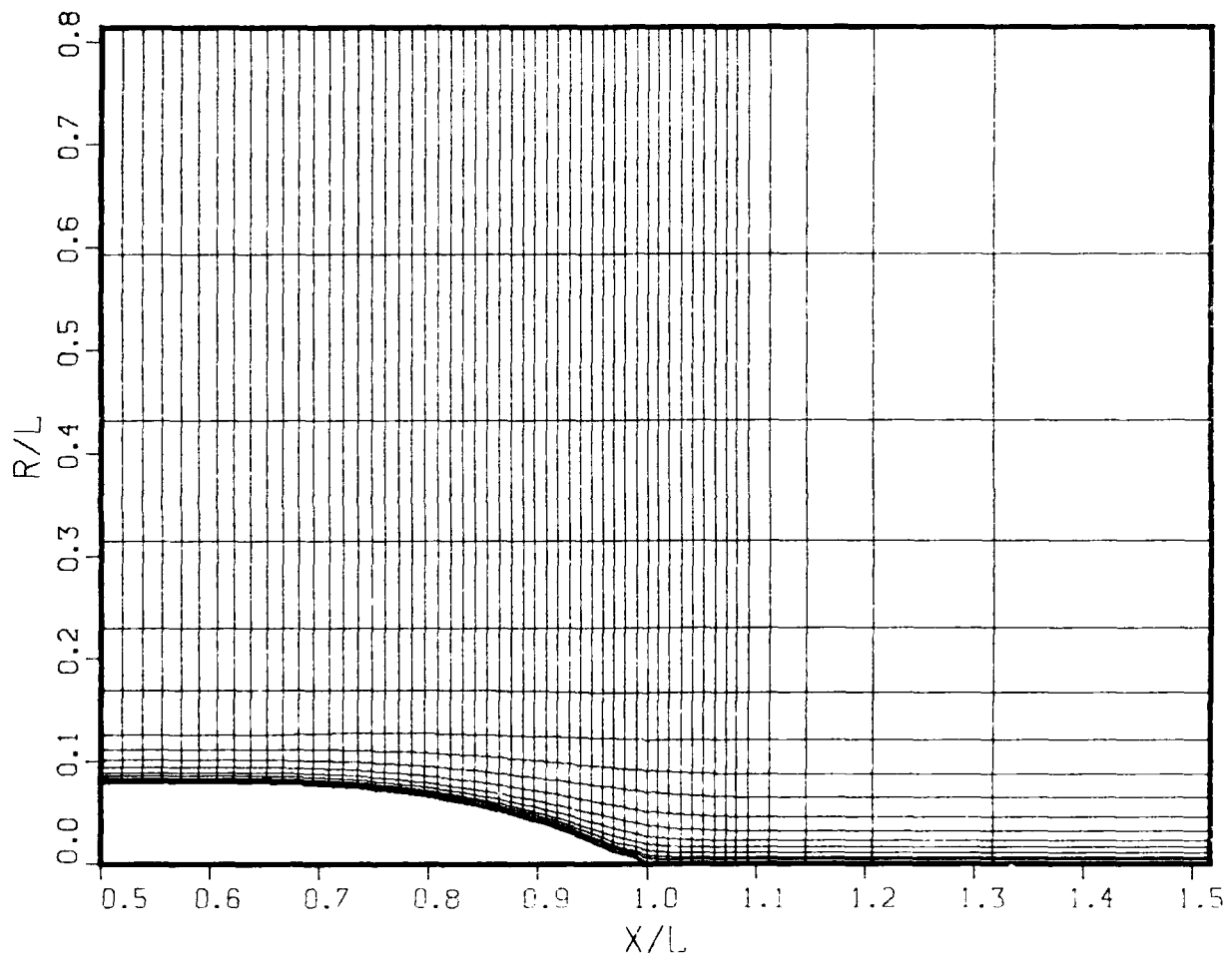
Fig. 5.   Continued
(b) Longitudinal View at $\theta = 90°$

121
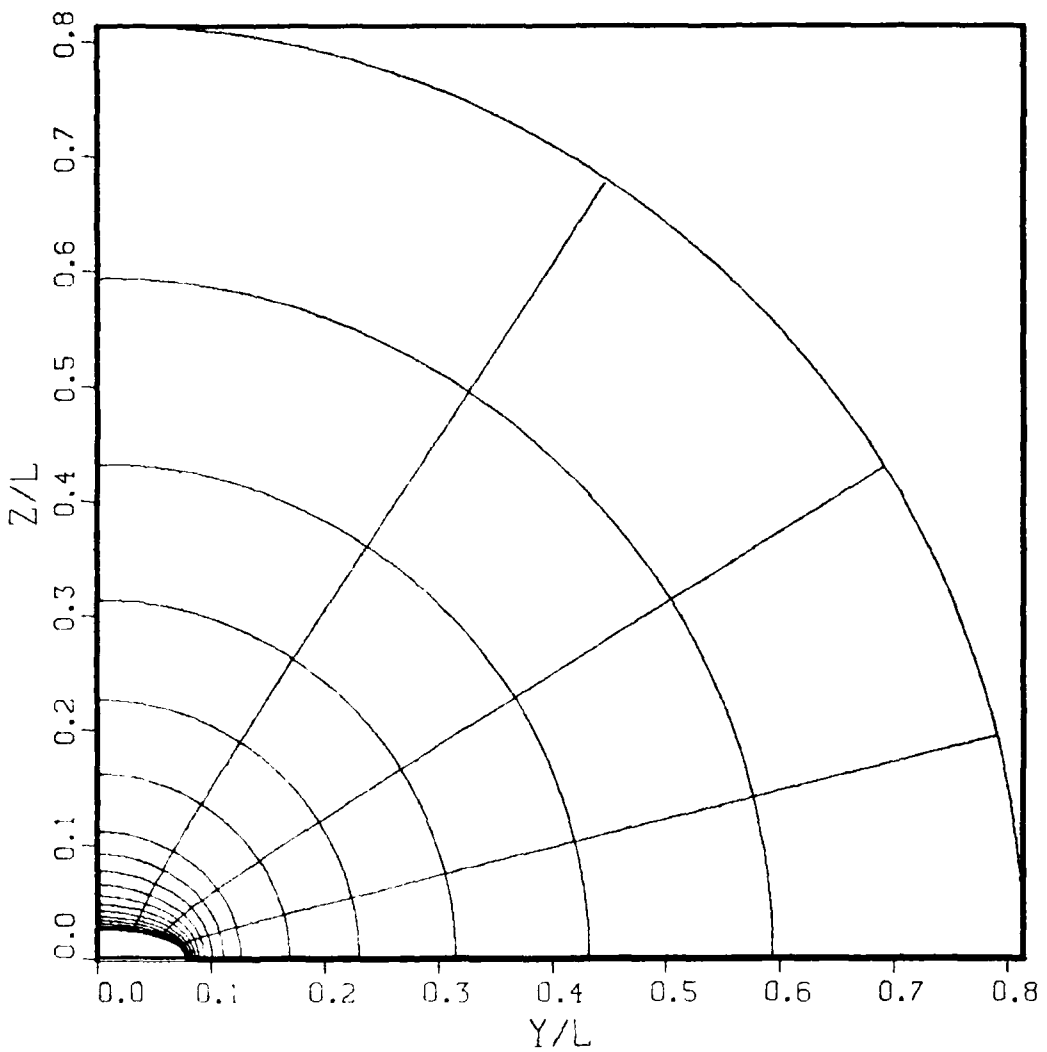
X/L=0.5900

Fig. 5. Continued
         (c) X/L = 0.5900

122
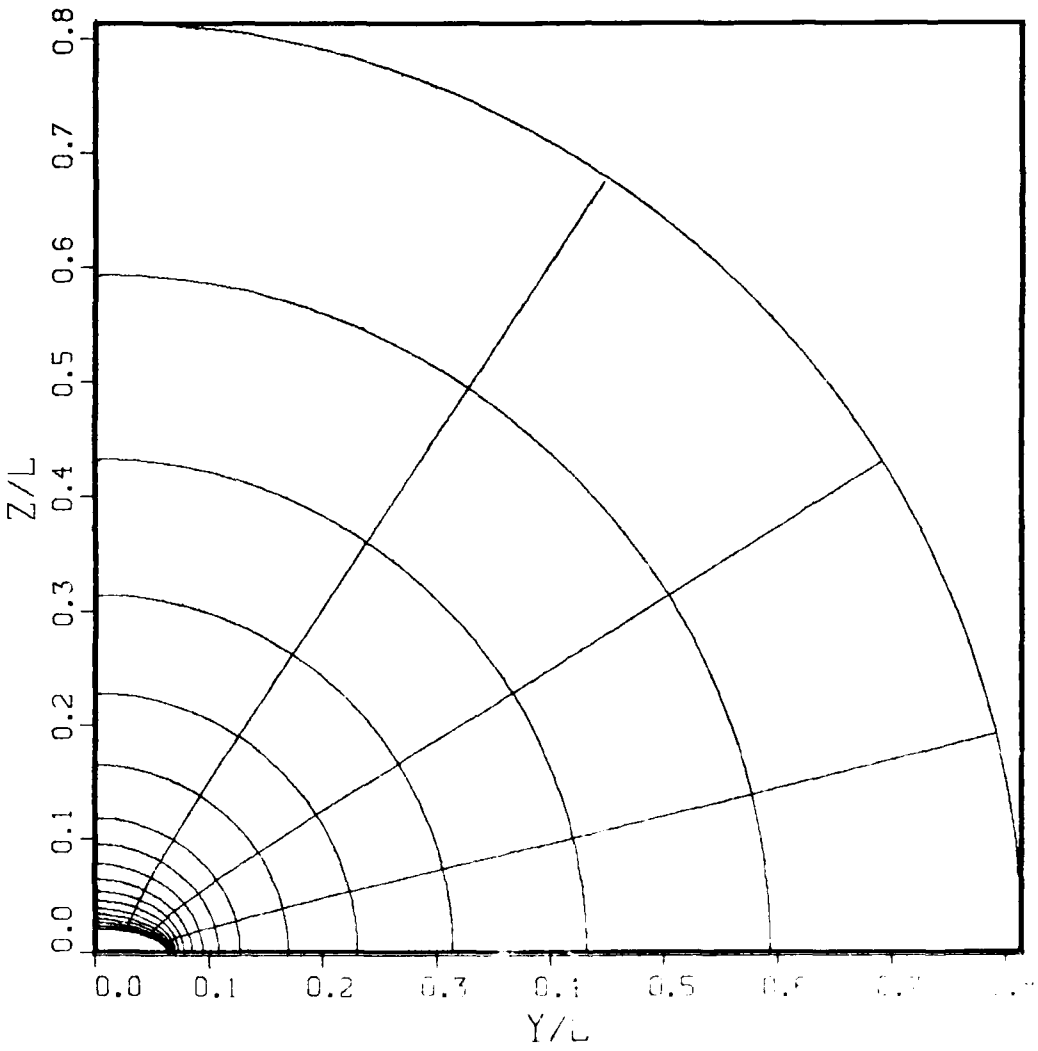
X/L=0.8082

Fig. 5.   Continued
           (d) X/L = 0.8082

X/L=0.9071
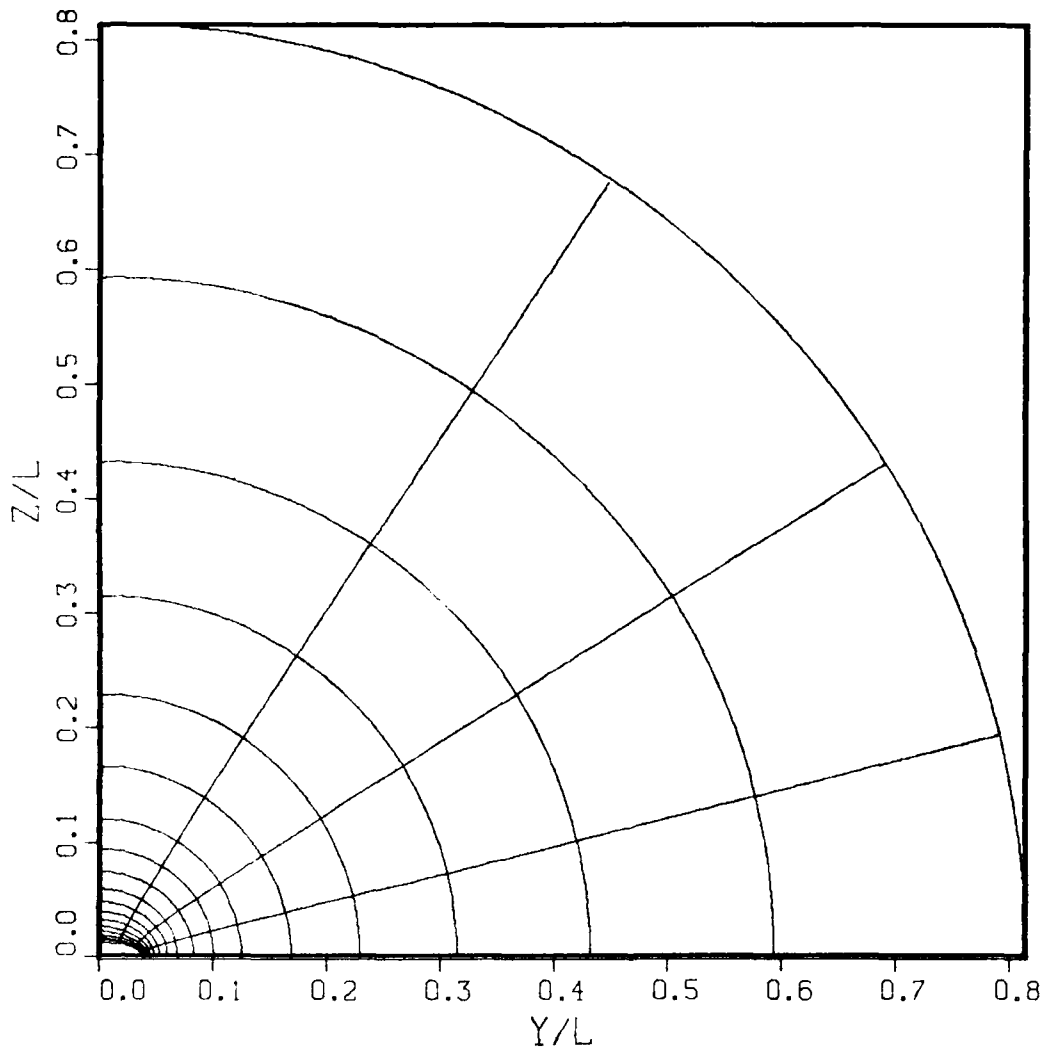
Fig. 5.   Continued
          (e) X/L = 0.9071

X/L=0.9898
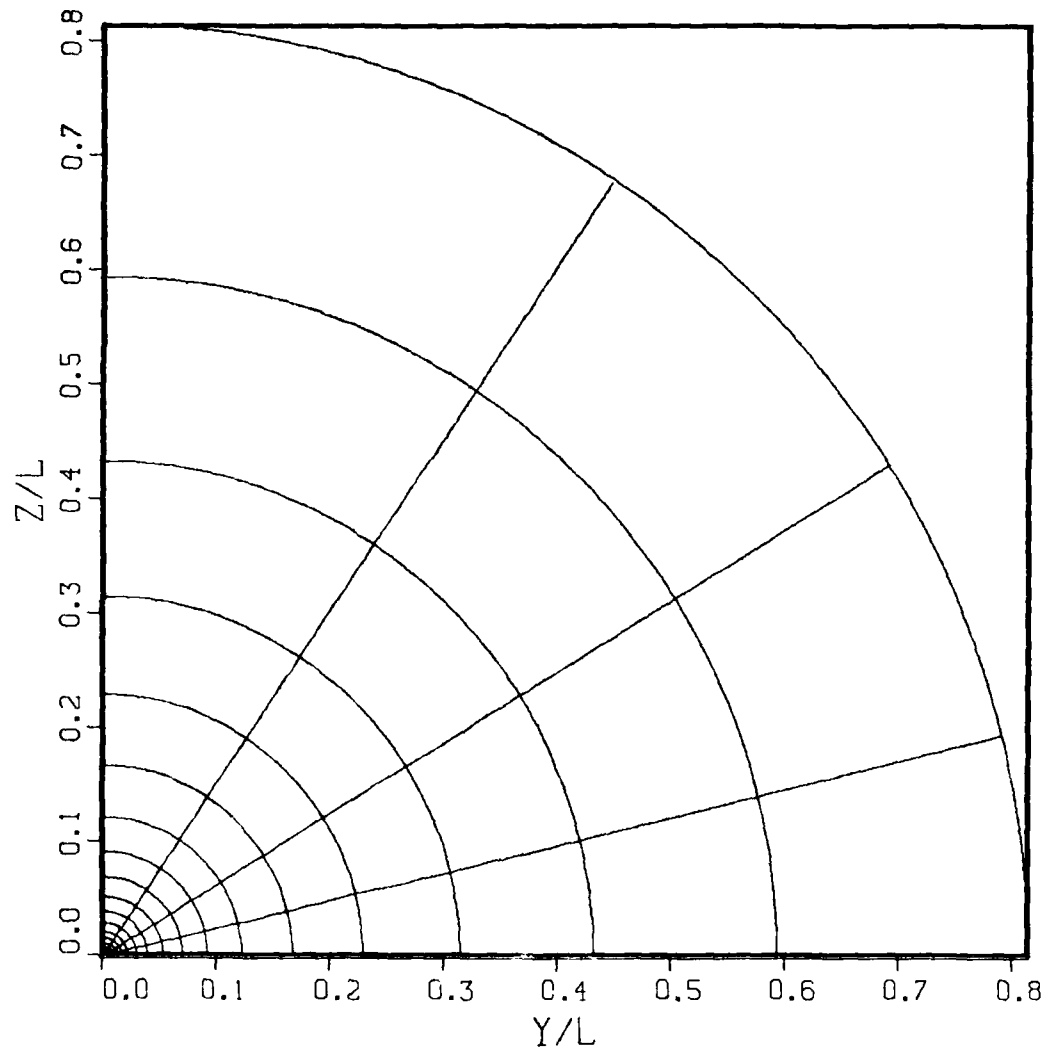
Fig. 5.   Continued
          (f) X/L = 0.9898

X/L=1.010
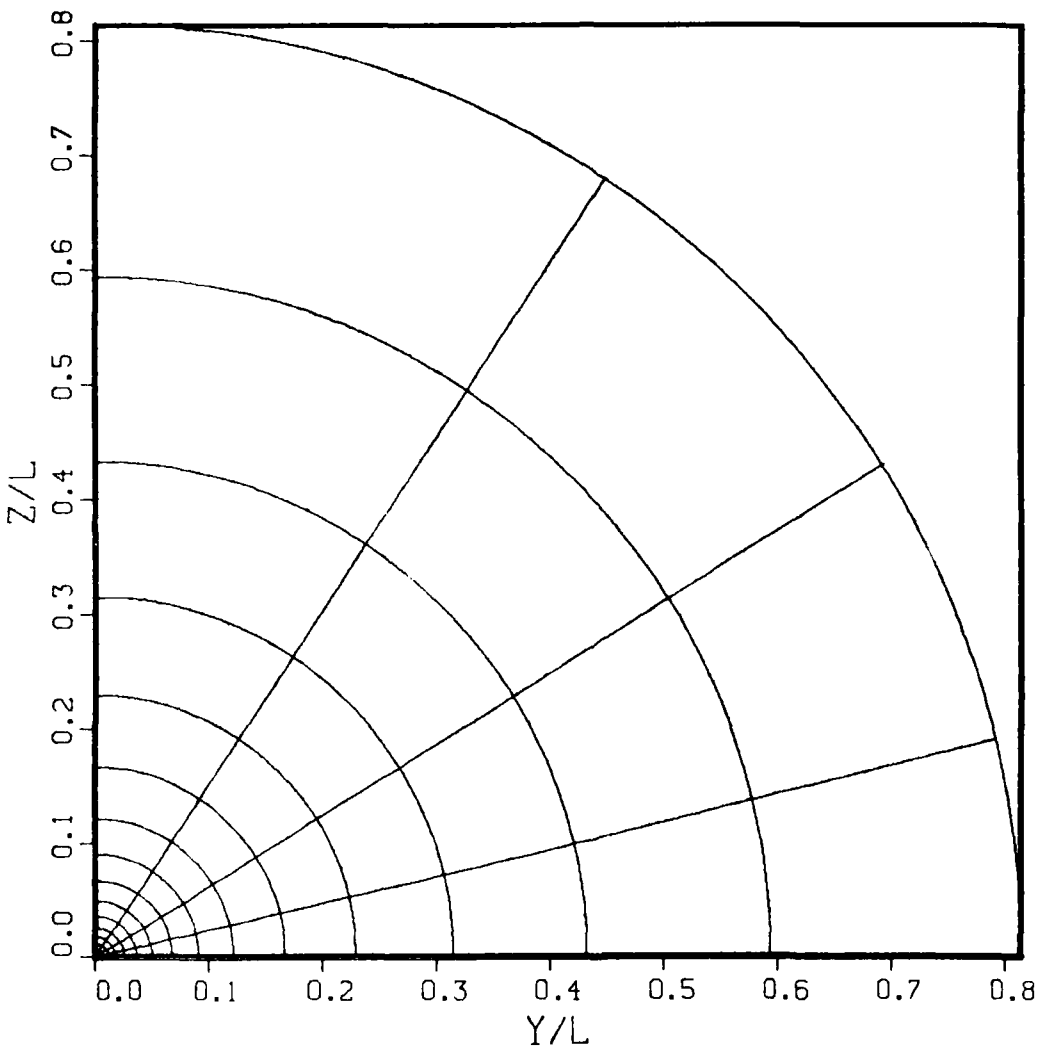
Fig. 5.   Continued
          (g) X/L = 1.010

126
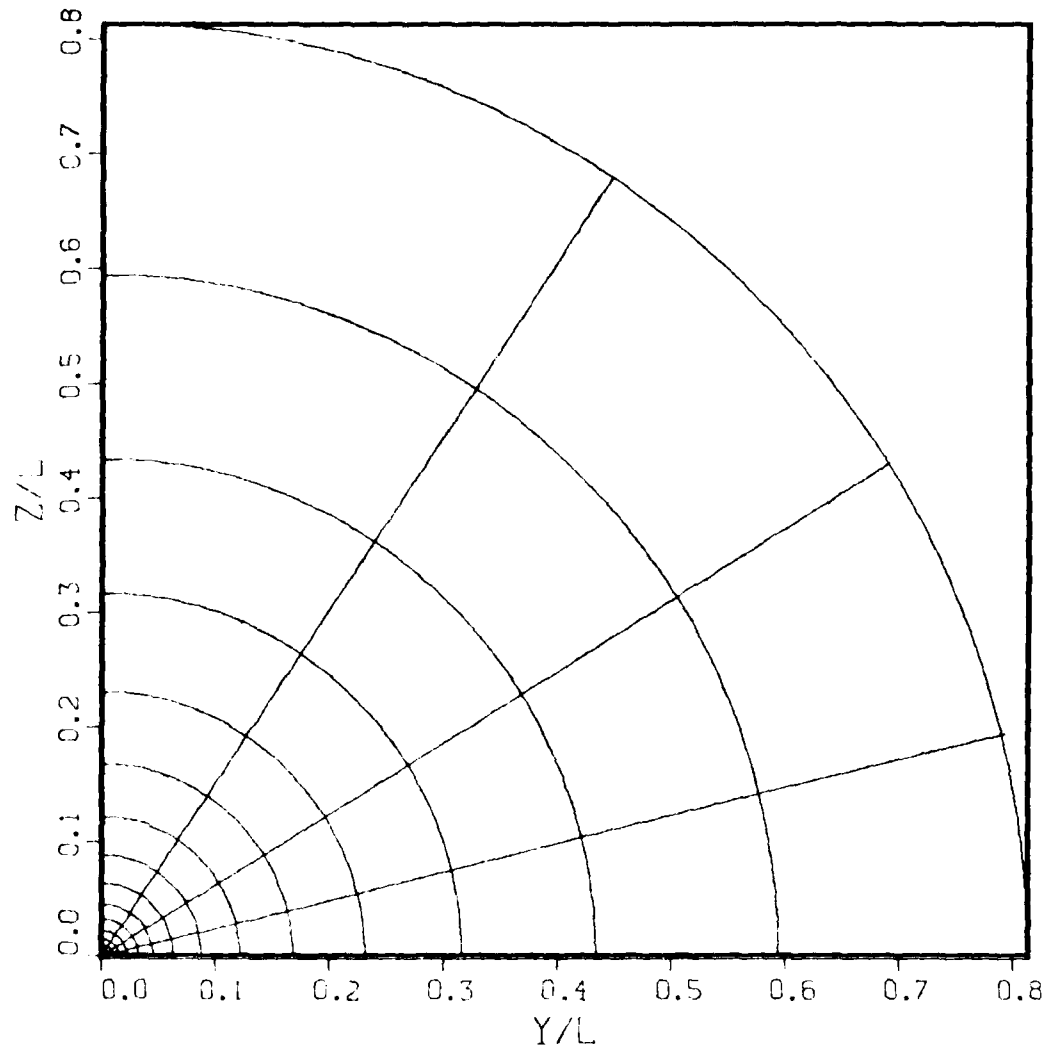
Fig. 5.   Continued
(h) X/L = 16.25

127
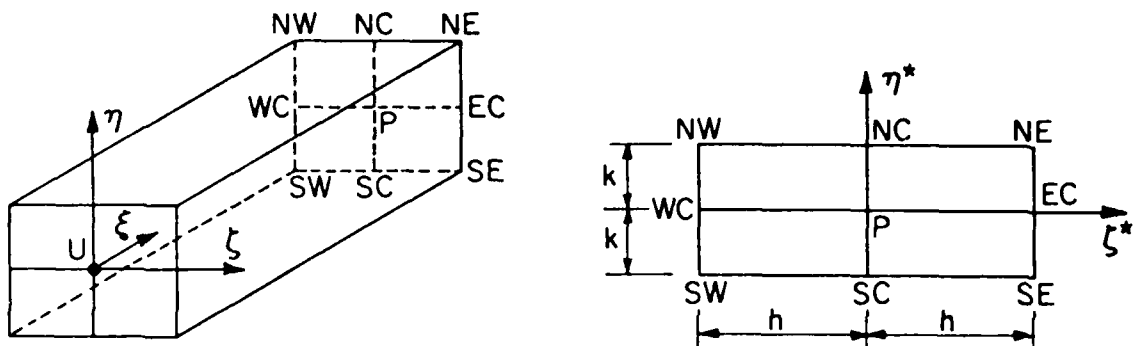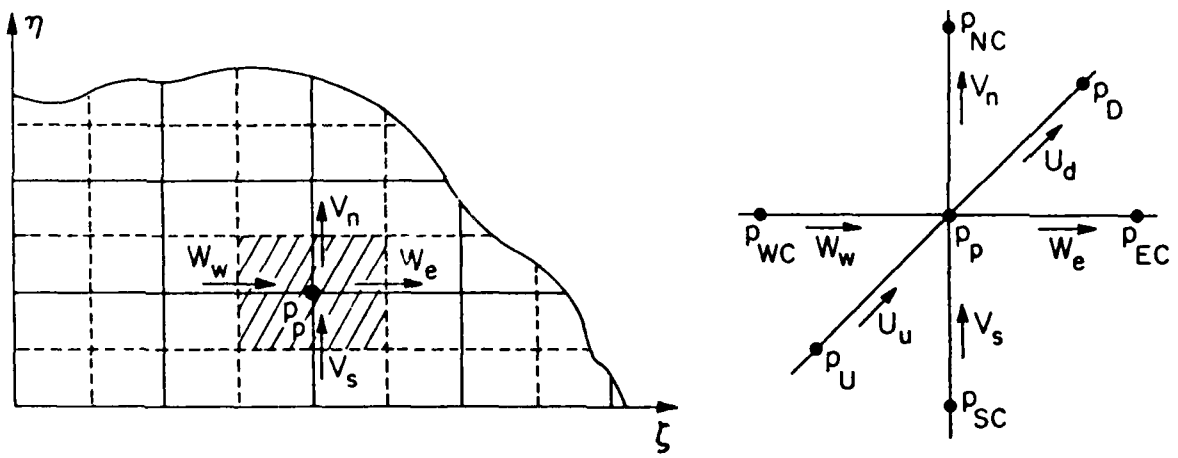
Fig. 6.   Numerical Grid and Symbols
        (a) Local Element (b) Staggered Grid

128
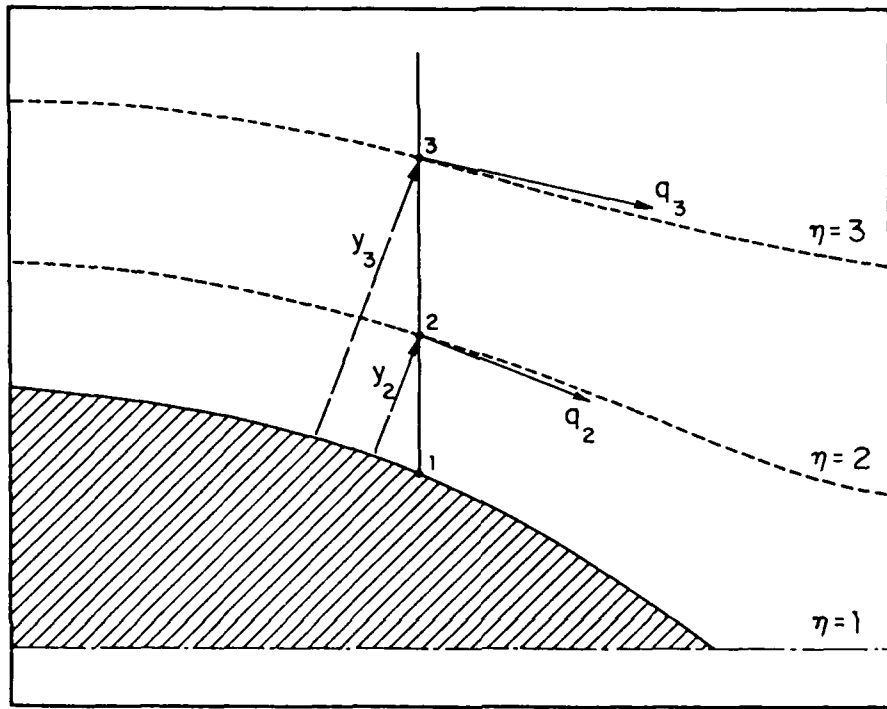
Fig. 7.   Notation for Wall Functions
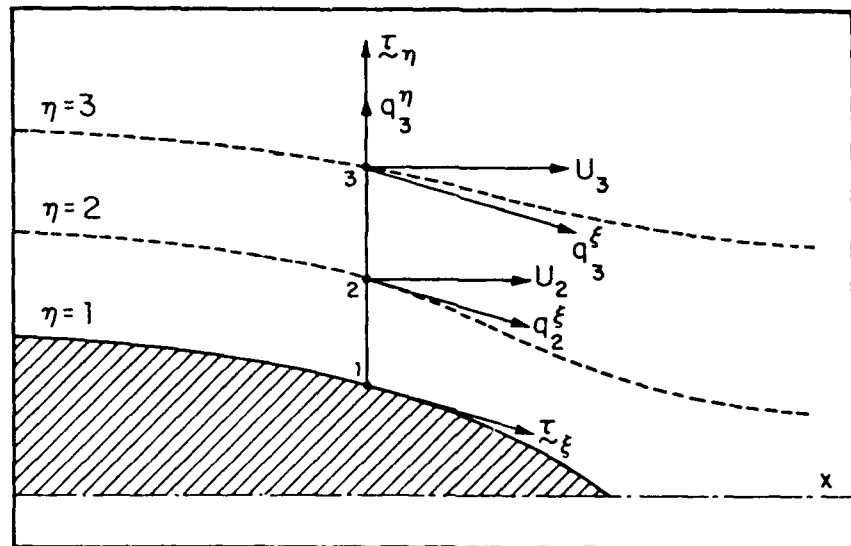
(a) Longitudinal View
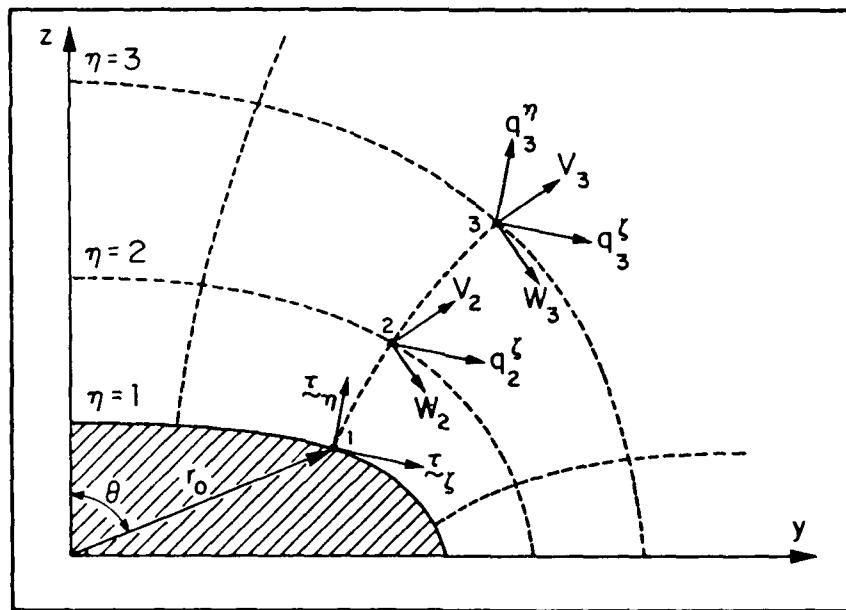
(b) Sectional View

Fig. 8.   Detailed Notation for Wall Functions

130
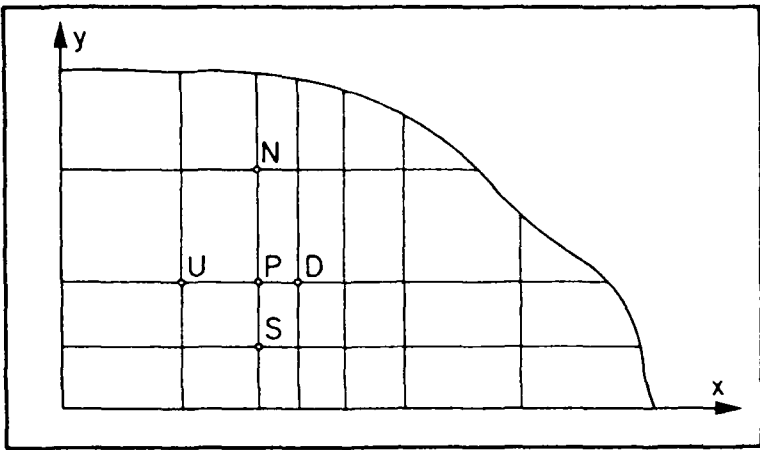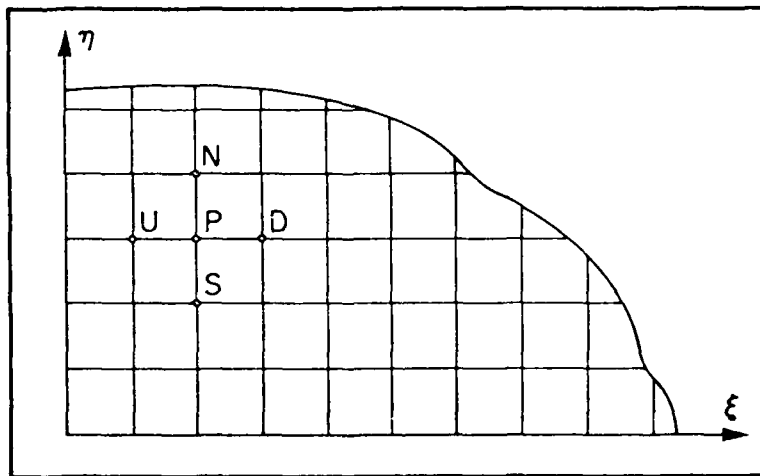
(a) Physical Plane

(b) Transformed Plane

Fig. 9.   Numerical Grid and Symbols for a Flat Plate
         (a) Physical Plane, (b) Transformed Plane

FLAT PLATE
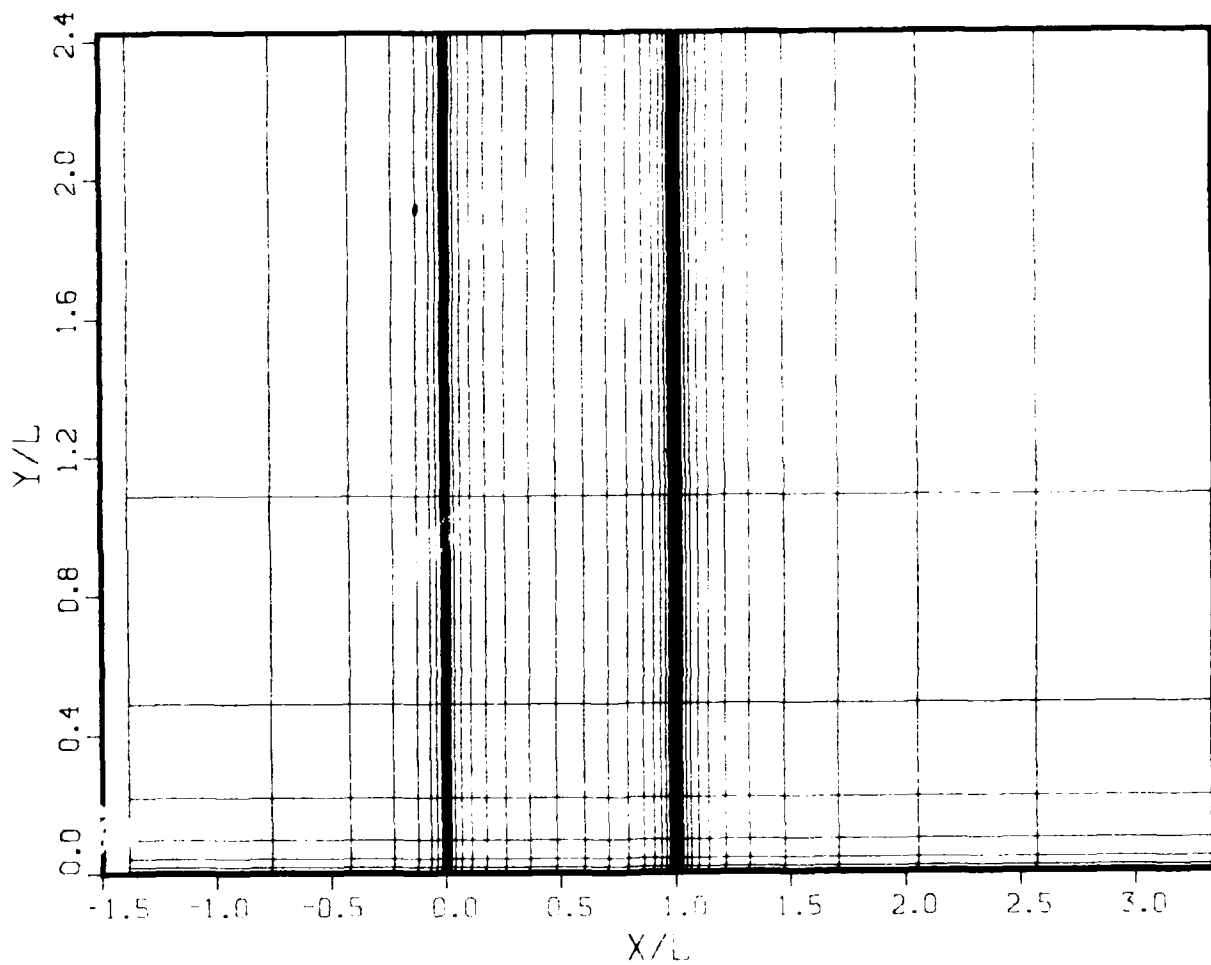
Fig. 10. A partial View of the Numerical Grid for the Flow Over
a Flat Plate (0 < X/L < 1)

132
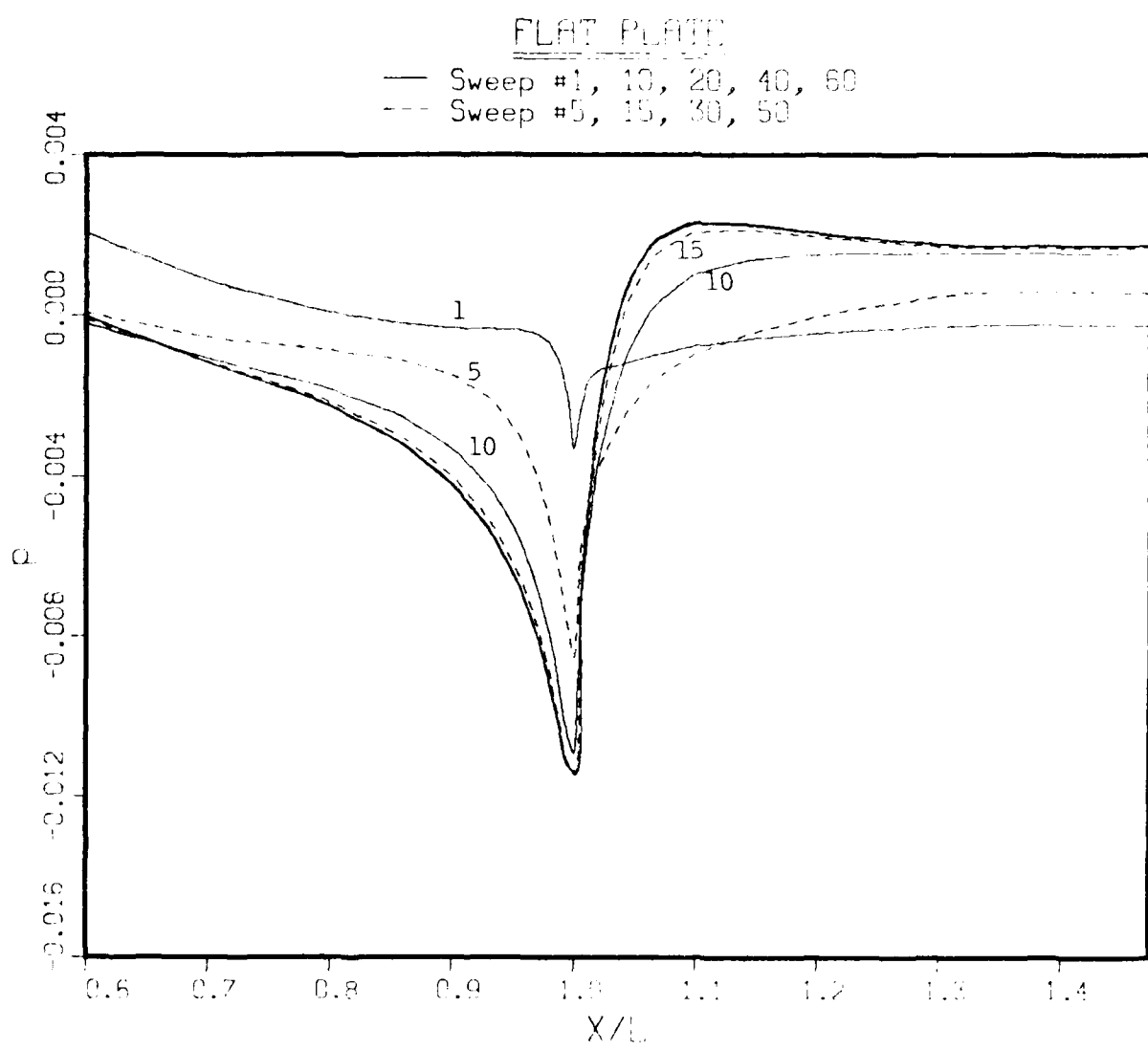
Fig. 11   Convergence History of the Pressure Distribution on the
Plate (X/L < 1) and Along the Wake Centerline (X/L > 1)

133
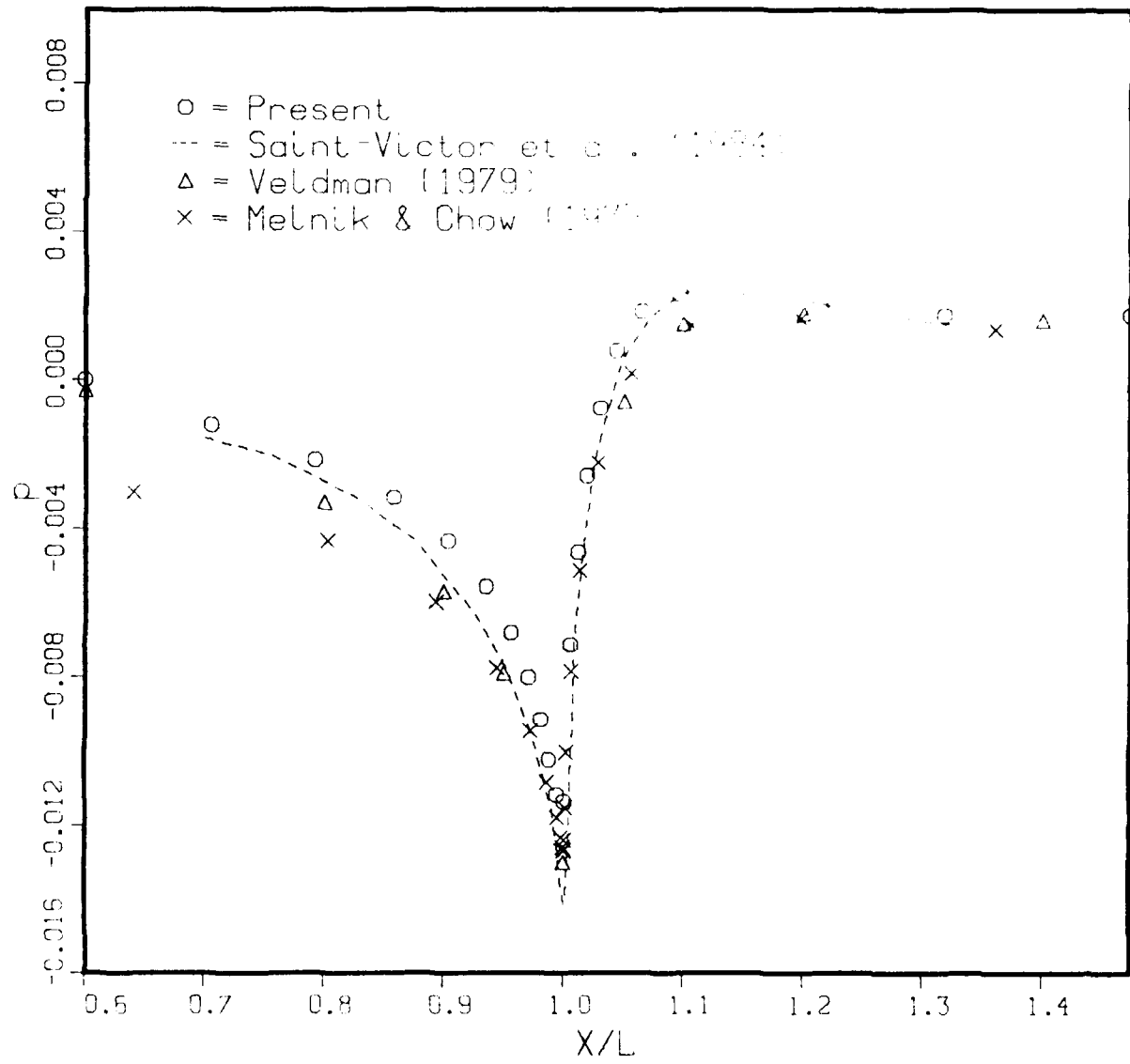
Fig. 12.   Comparison of the Pressure Distribution with Some
Previous Solutions

134
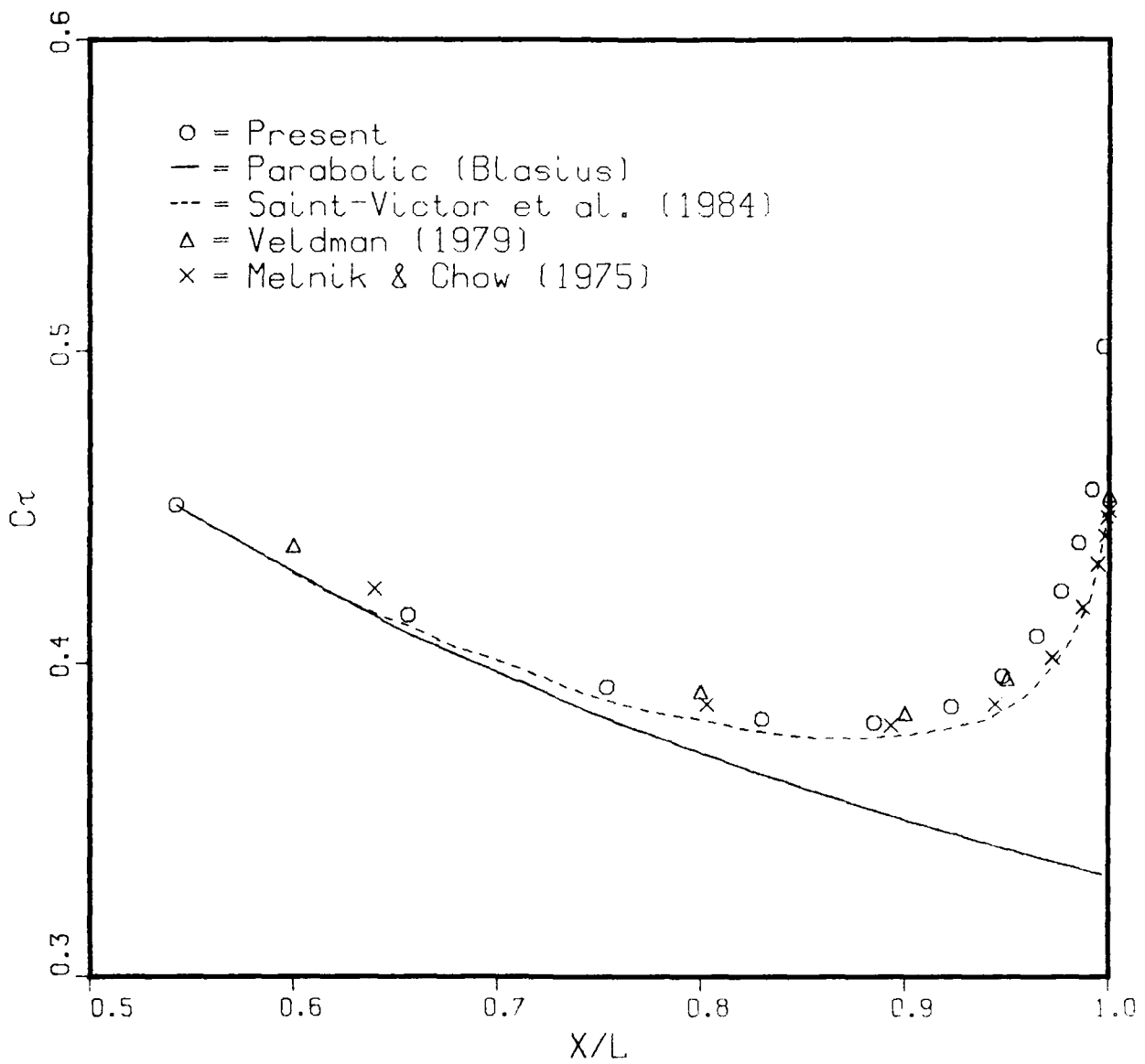
Fig. 13. Skin Friction on the Plate

Fig. 14. Wake Centerline Velocity

136

FLAT PLATE

— Sweep # 1, 20, 40, 60, 100
--- Sweep #10, 30, 50, 80
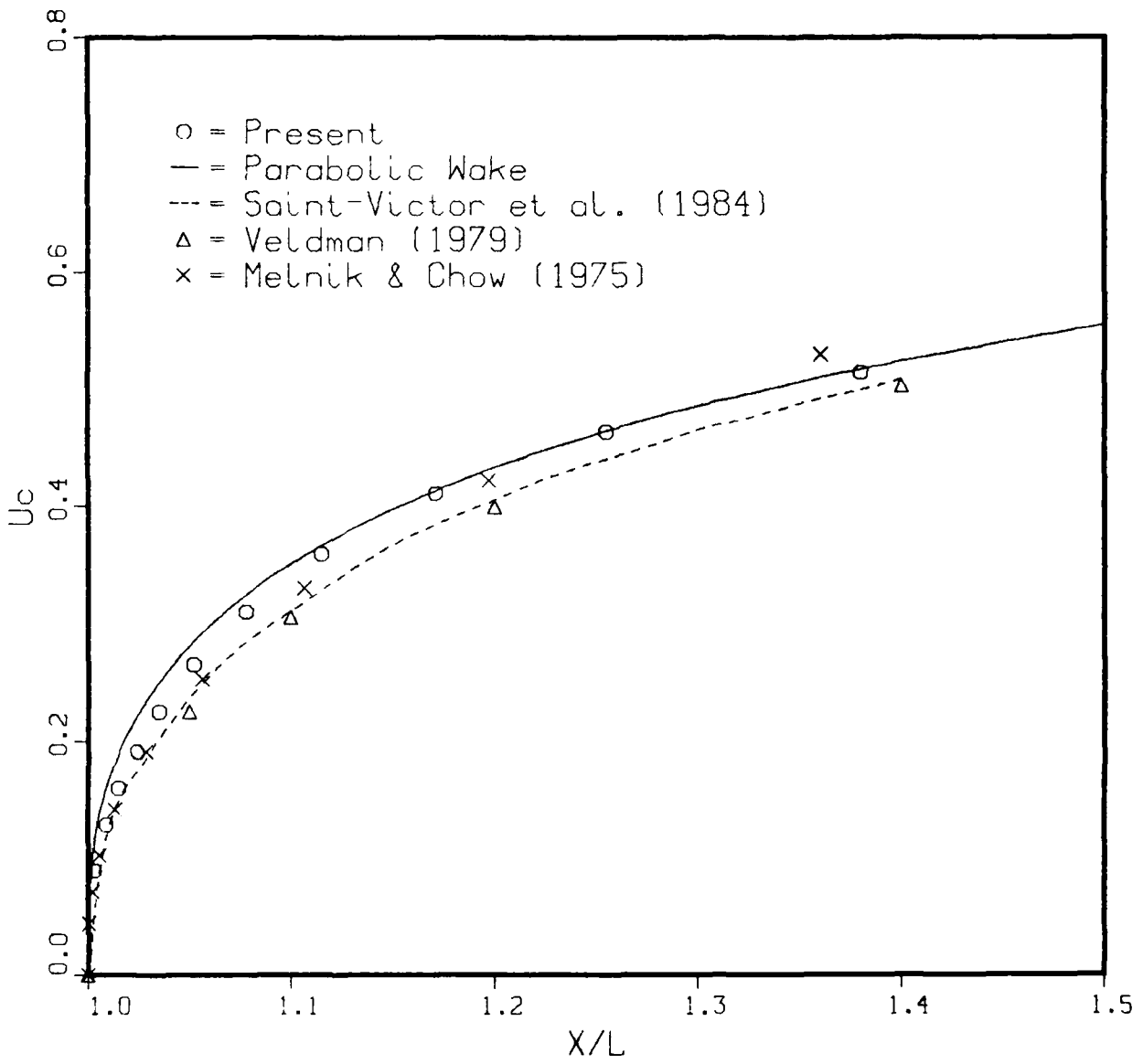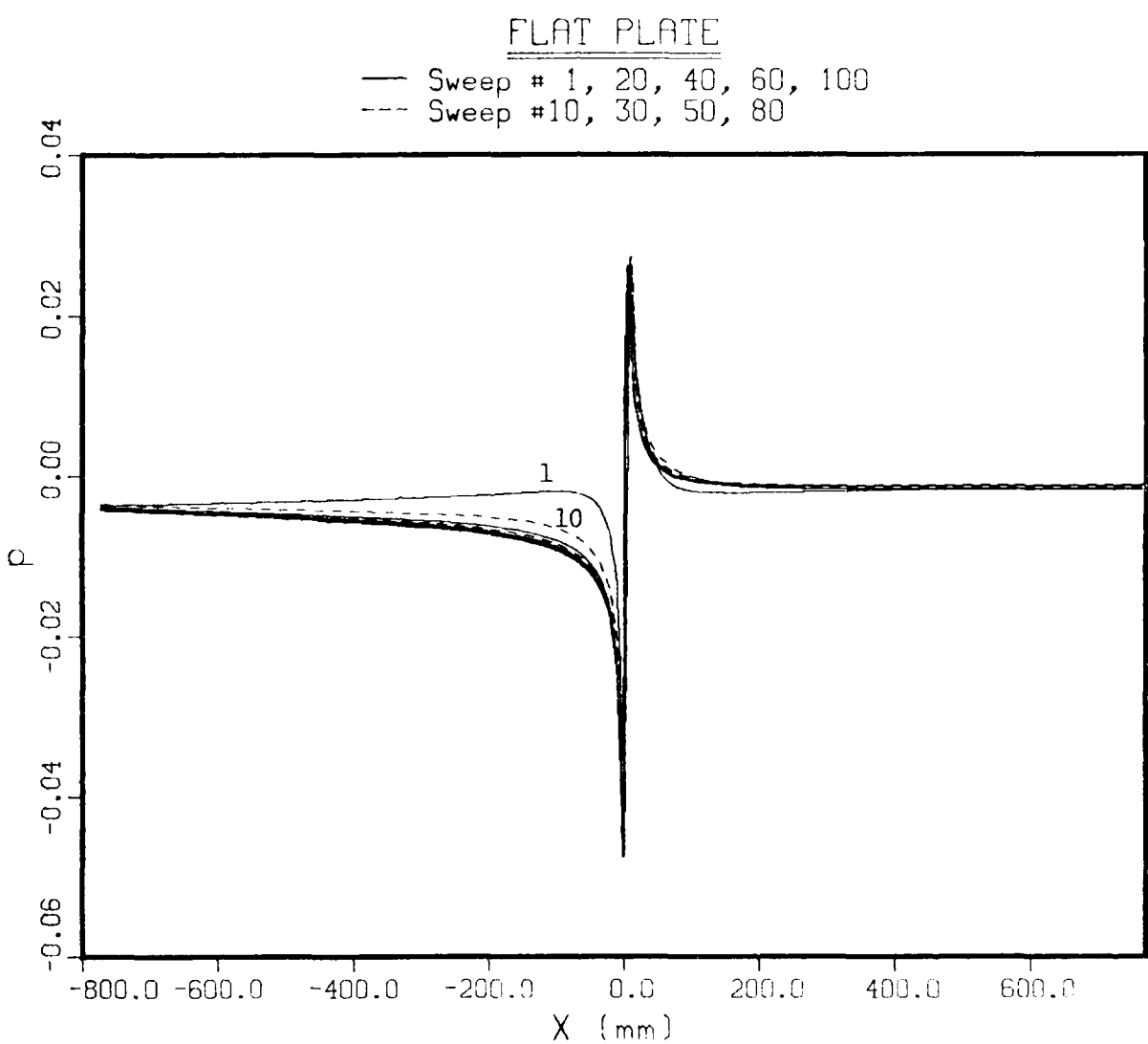
Fig. 15.   Convergence History of the Pressure on the Plate
(X < 0) and Along the Wake Centerline

137

FLAT PLATE
—— Sweep # 1, 20, 40, 60, 100
--- Sweep #10, 30, 50, 80
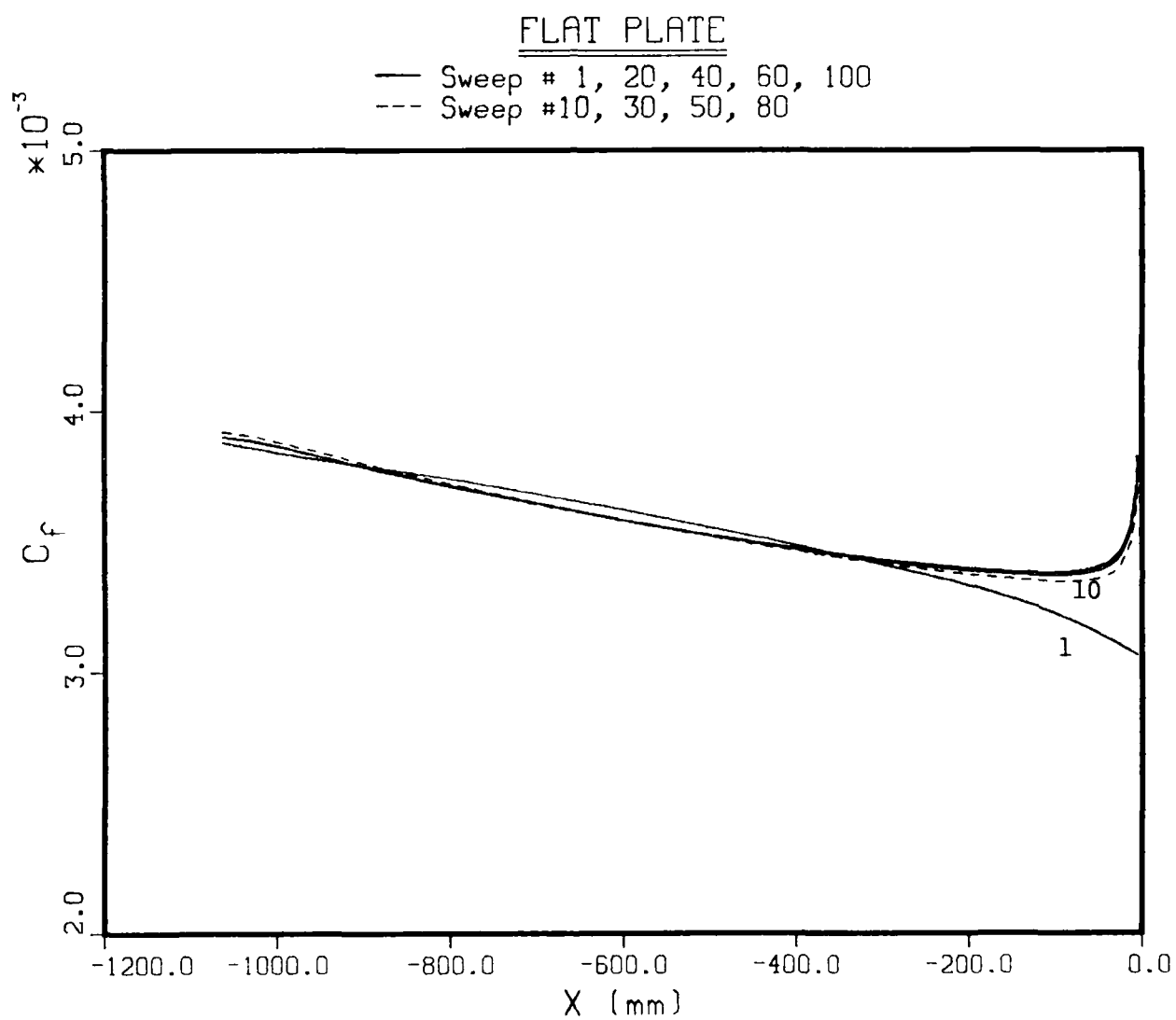
Fig. 16. Convergence of the Friction Coefficient on the Plate

FLAT PLATE
—— Sweep # 1, 20, 40, 60, 100
- - - Sweep #10, 30, 50, 80
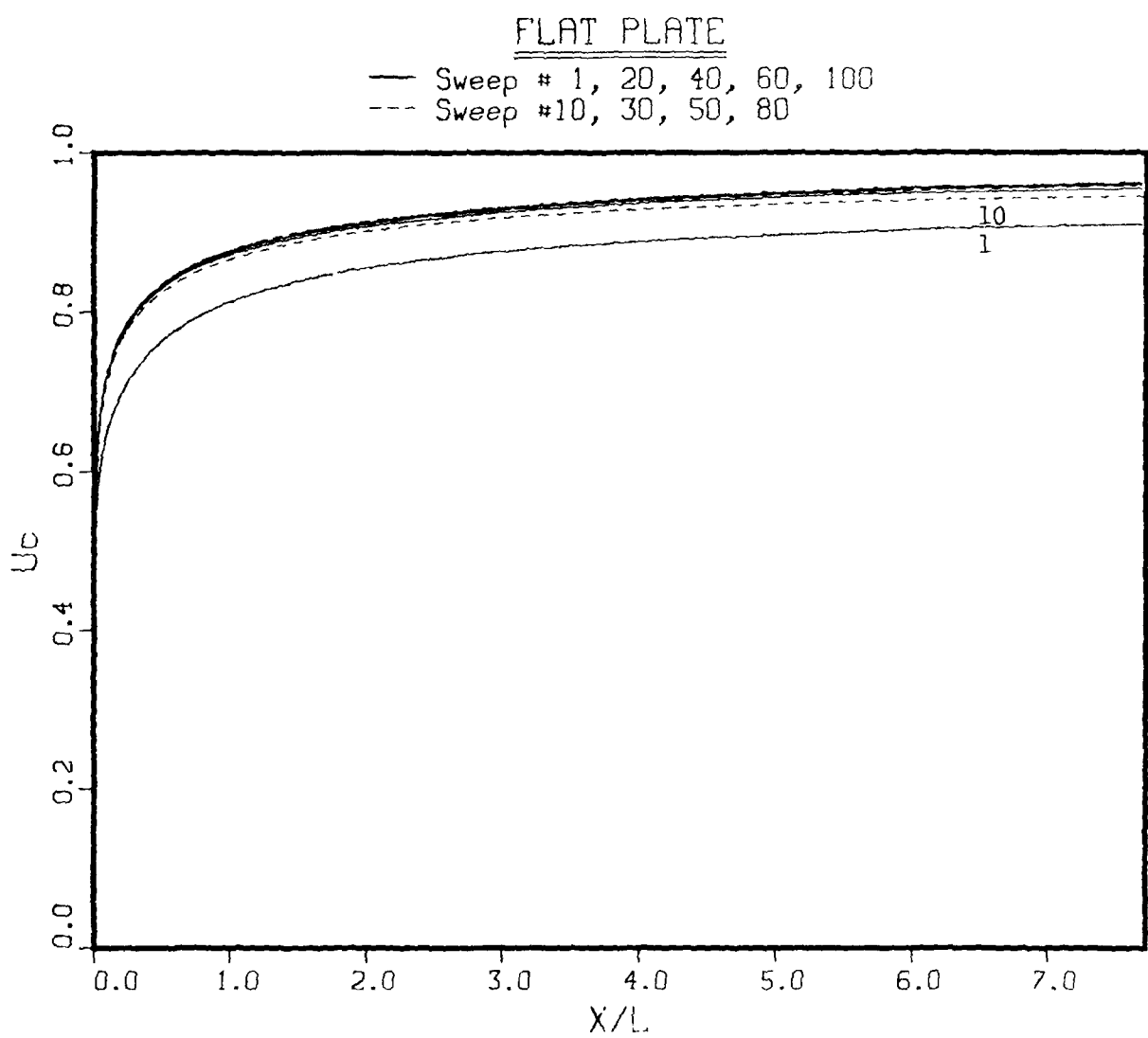
Fig. 17.   Convergence of the Wake Centerline Velocity

139

FLAT PLATE
— Sweep # 1, 20, 40, 60, 100
--- Sweep #10, 30, 50, 80
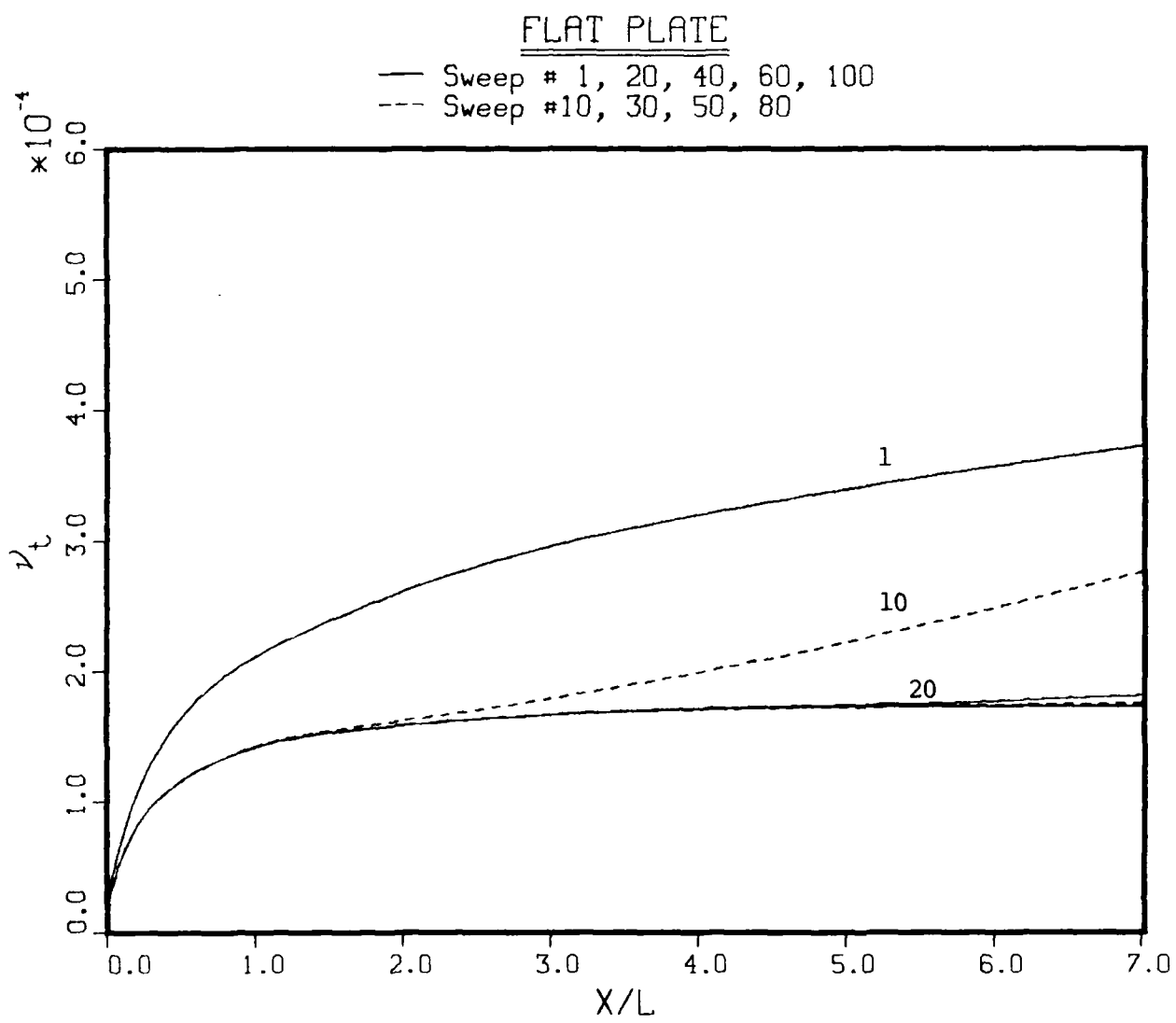
Fig. 18. Convergence of the Eddy-Viscosity Along the Wake Centerline

140

FLAT PLATE
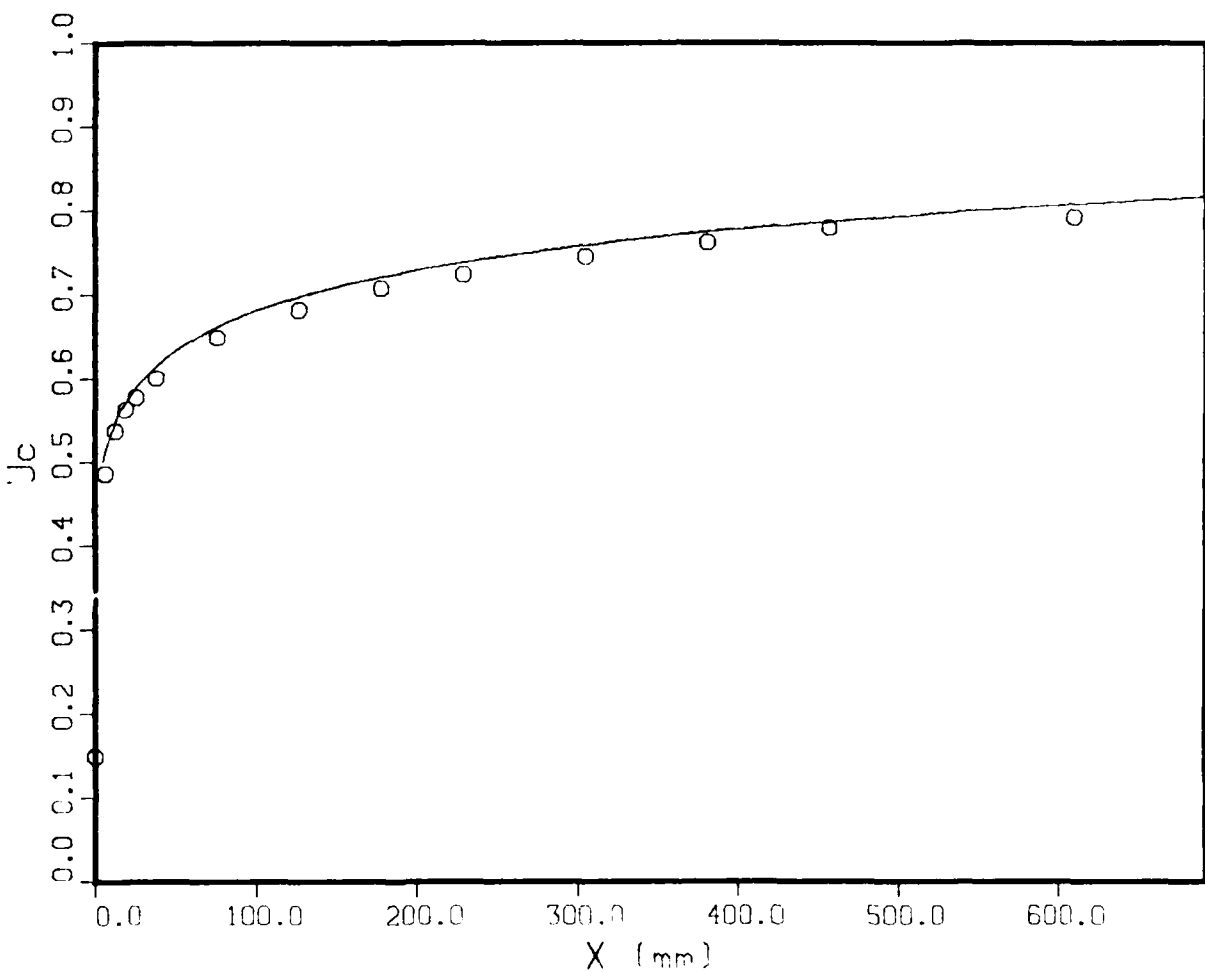
Fig. 19. Comparison of Centerline Velocity in the Near Wake with
the Data of Ramaprian, Patel and Sastry (1981)

	-76.2mm	25.4mm	76.2mm	177.8mm	304.8mm	457.2mm	X
Expt.	-9.7	3.2	9.7	22.6	38.8	58.2	X/θ
Calc.	-83.3mm	25.9mm	83.3mm	161.7mm	304.2mm	459.7mm	X
	-10.6	3.3	10.6	20.6	38.7	58.5	X/θ
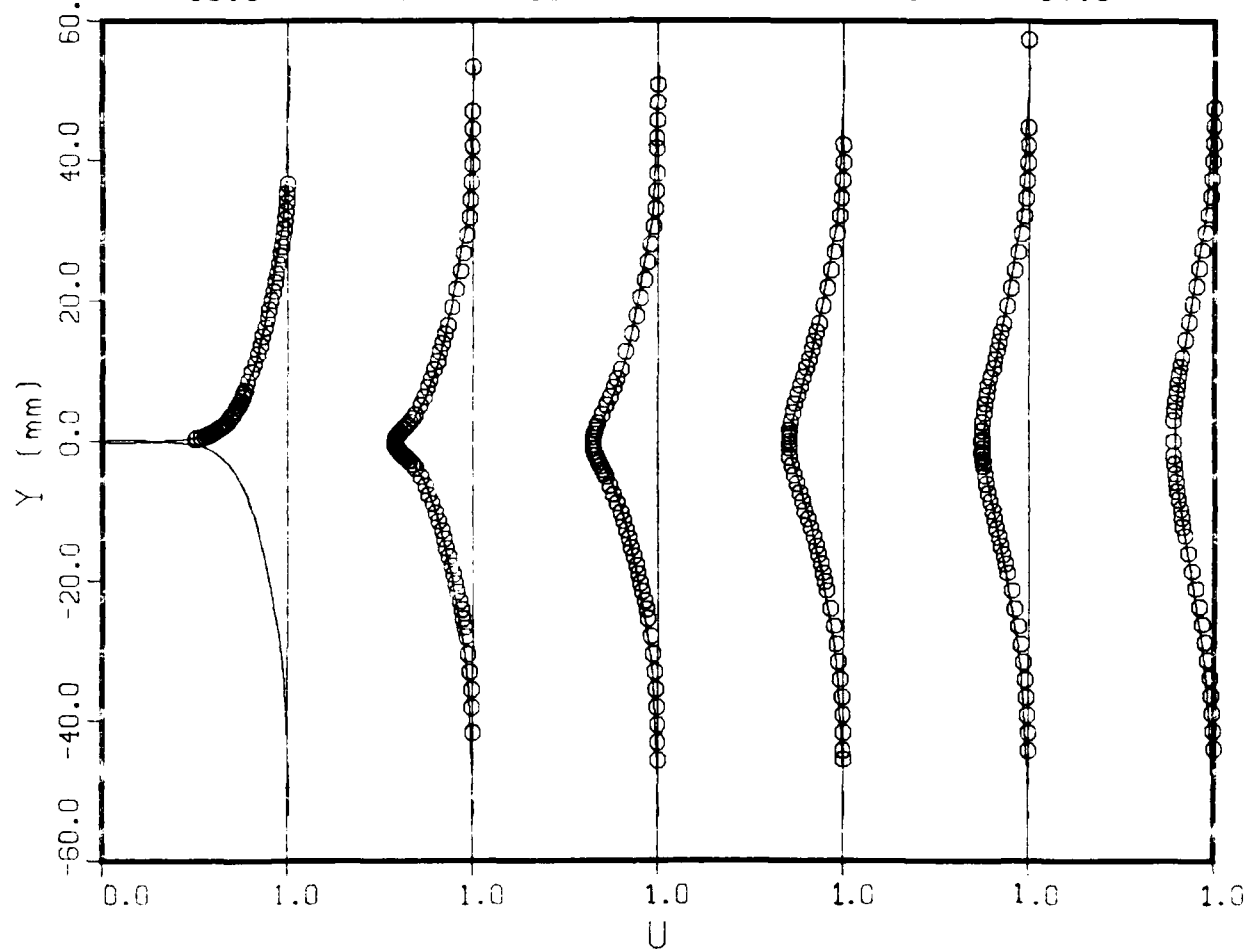
Fig. 20. Velocity Profiles in the Near Wake
o Experiment, —— Calculations

	19.1mm	127.0mm	177.8mm	381.0mm	609.6mm	X
Expt.	2.4	16.2	22.6	48.5	77.5	X/θ
Calc.	20.5mm	117.4mm	180.9mm	416.9mm	627.8mm	X
	2.6	14.9	23.0	53.0	79.9	X/θ
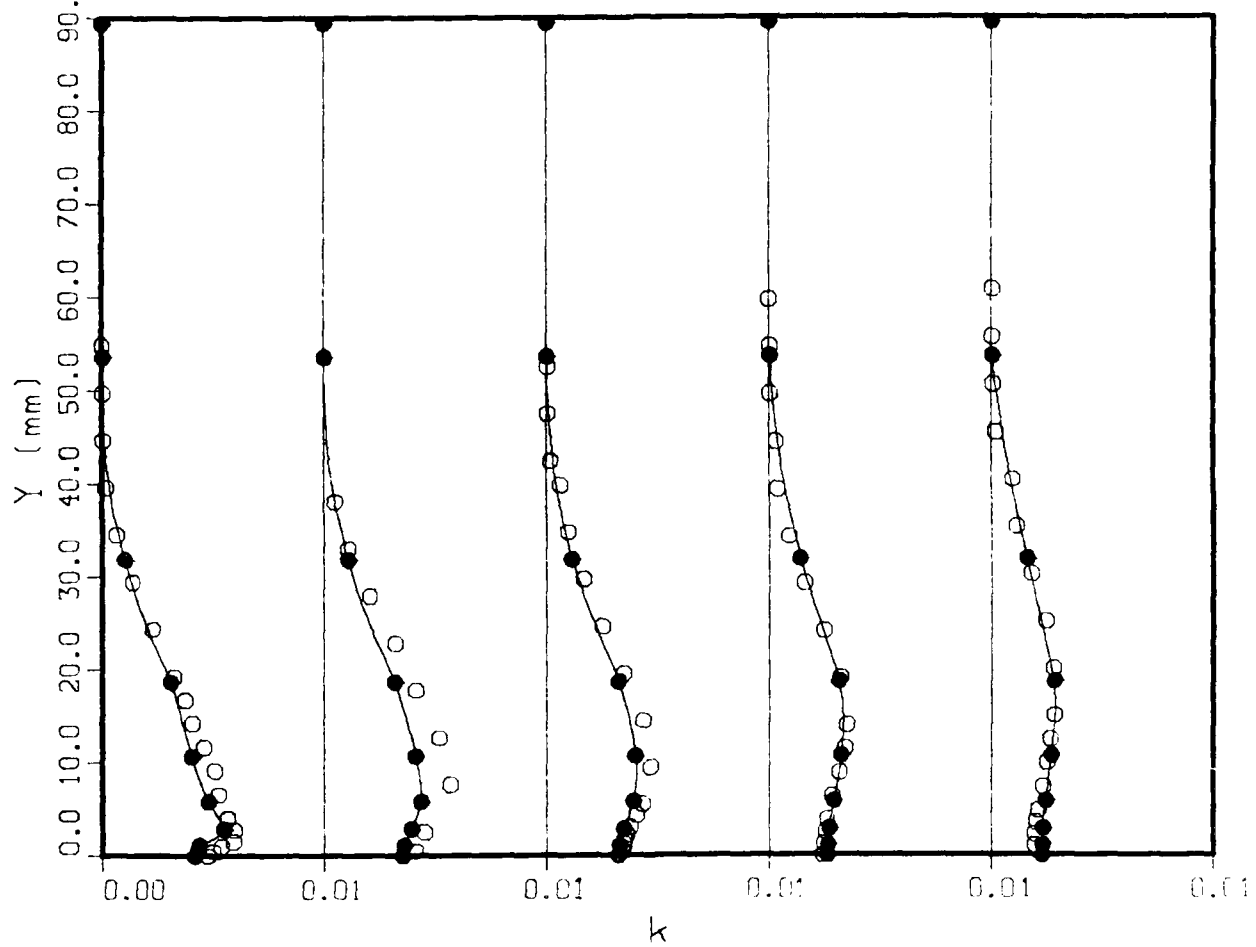
Fig. 21. Turbulent Kinetic-Energy Profiles in the Near Wake
o Experiment, ●— Calculations

Fig. 22. Alternative Definitions of Wake-Centerline (Maximum) Velocity Defect (W_o) and Half-Width (b)
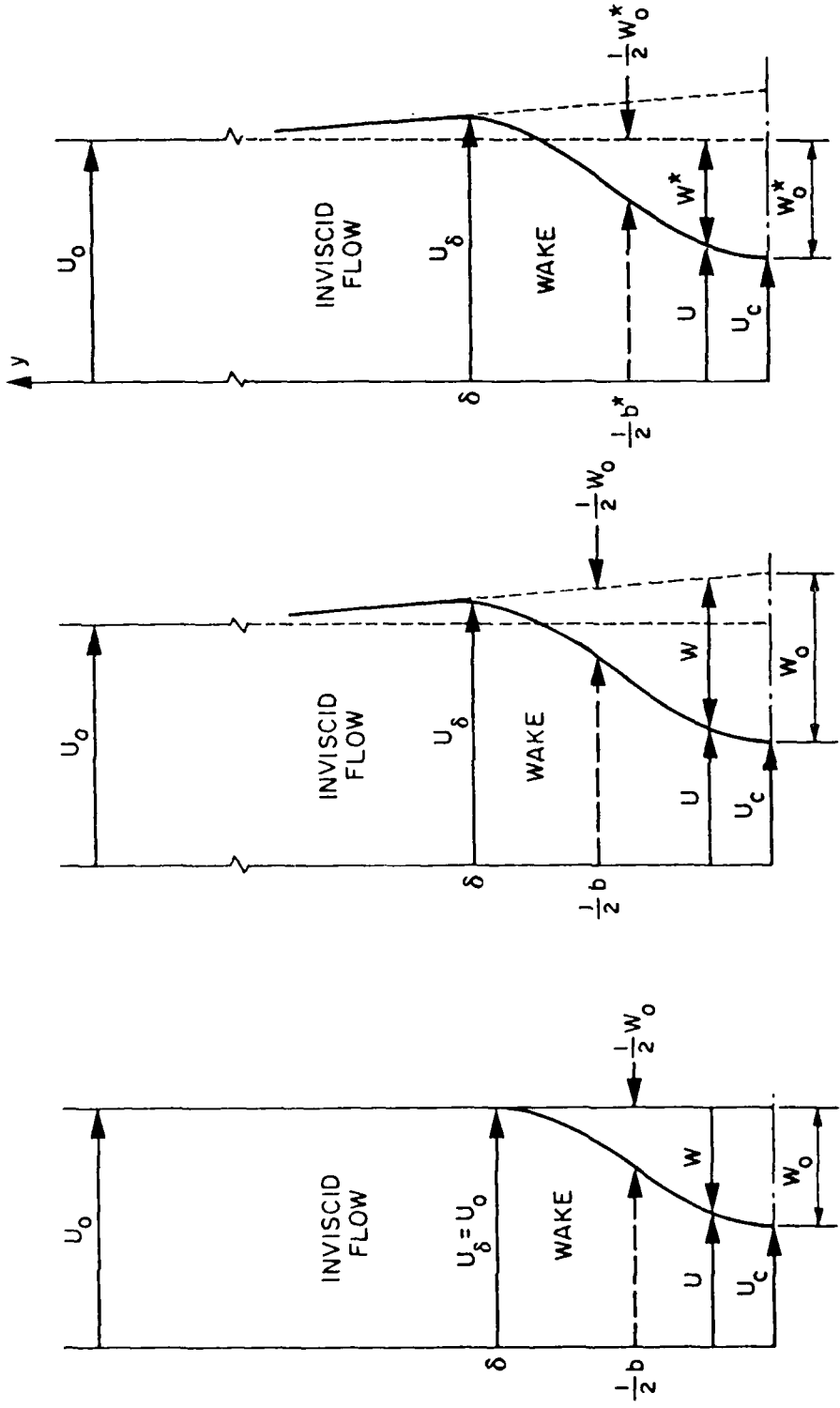
(a) Conventional (Boundary Layer) Definitions Relative to Assumed Inviscid Flow

(b) Physical Definitions Relative to Actual Inviscid Flow

(c) Definitions Adopted to Investigate Asymptotic Behavior of Present Solutions

144
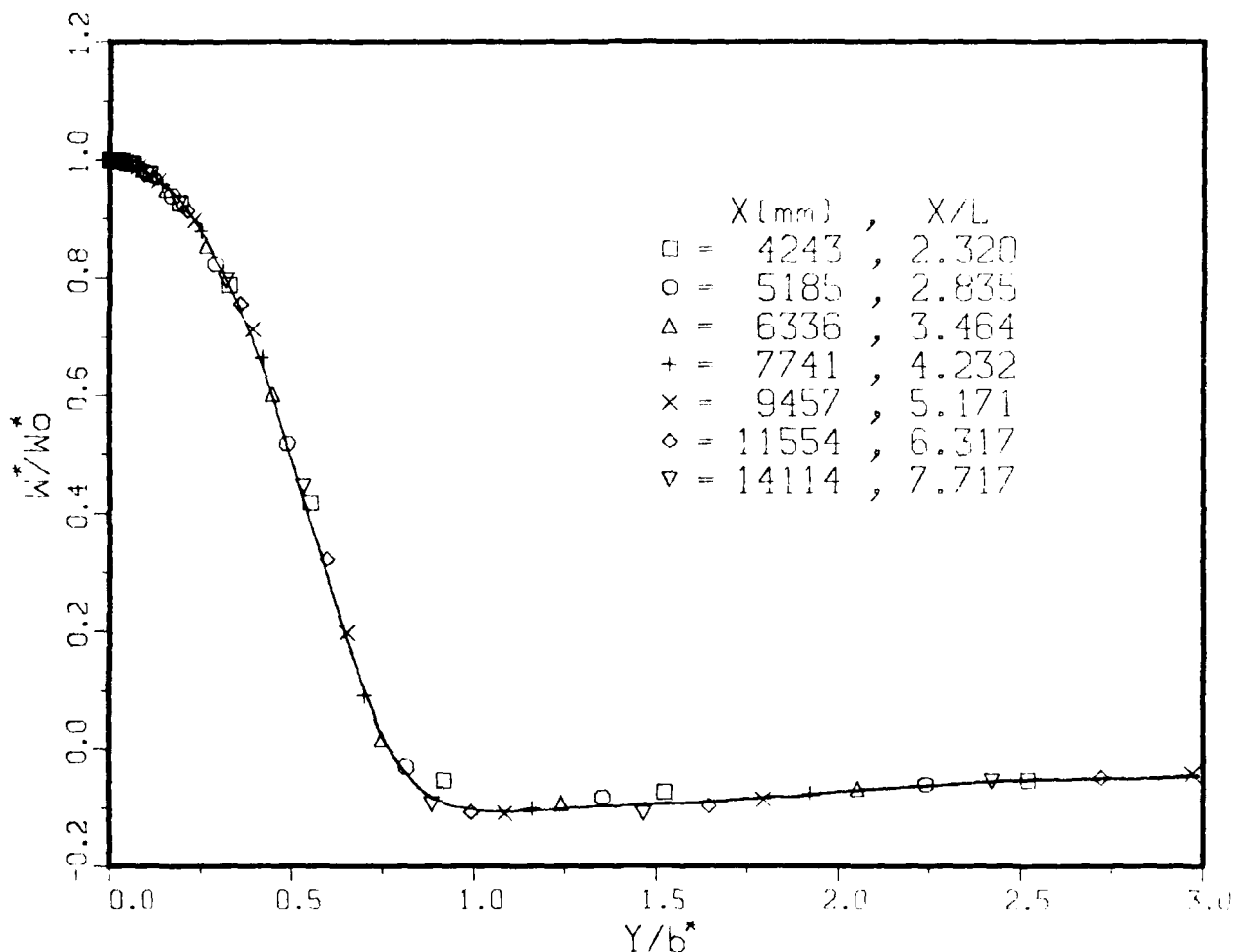
FLAT PLATE

Fig. 23. Asymptotic Velocity-Defect Profile

FLAT PLATE
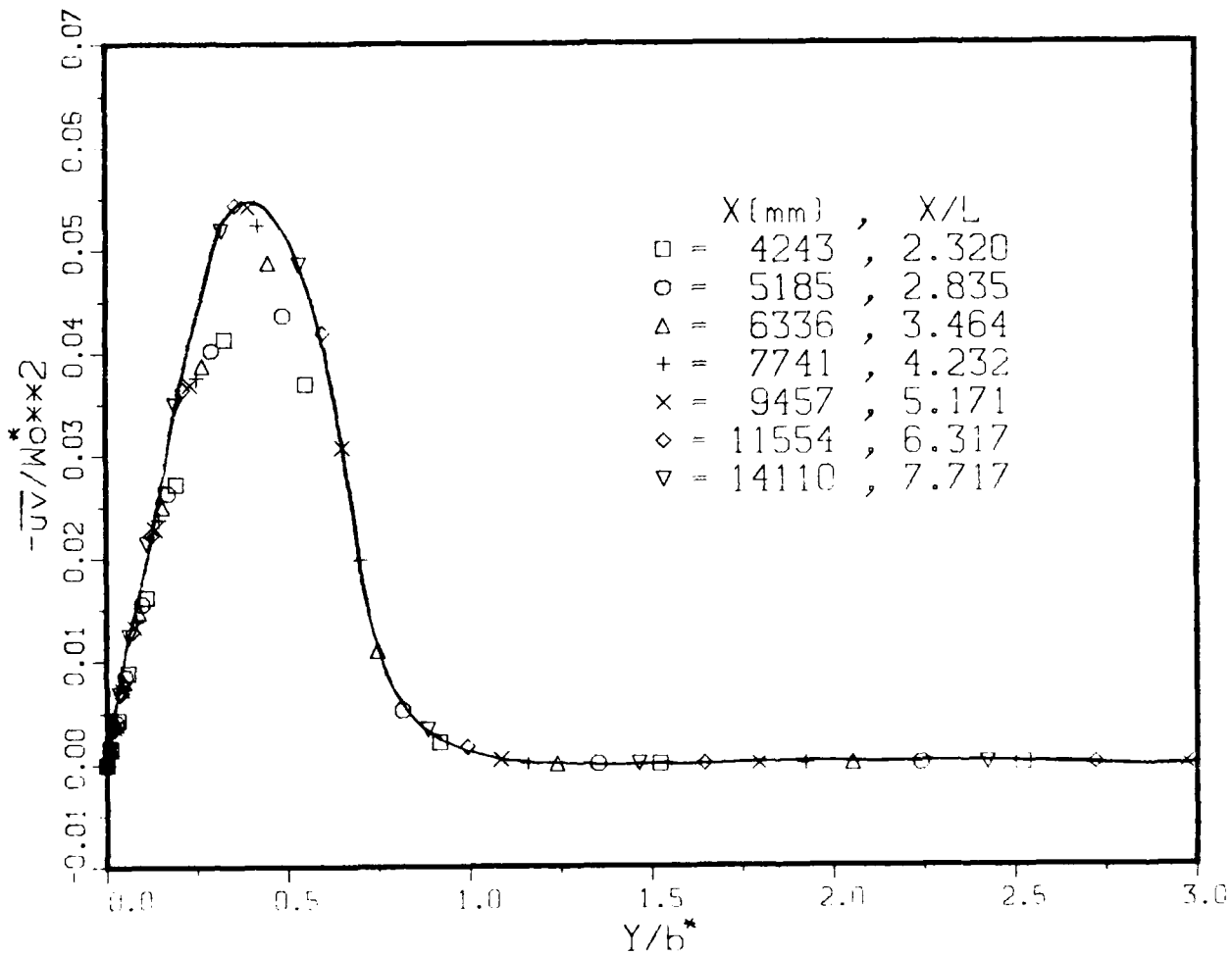
Fig. 24. Asymptotic Reynolds Shear-Stress Profile

AFTERBODY5
— Sweep #1, 10, 20, 30, 40
--- Sweep #5, 15, 25, 35
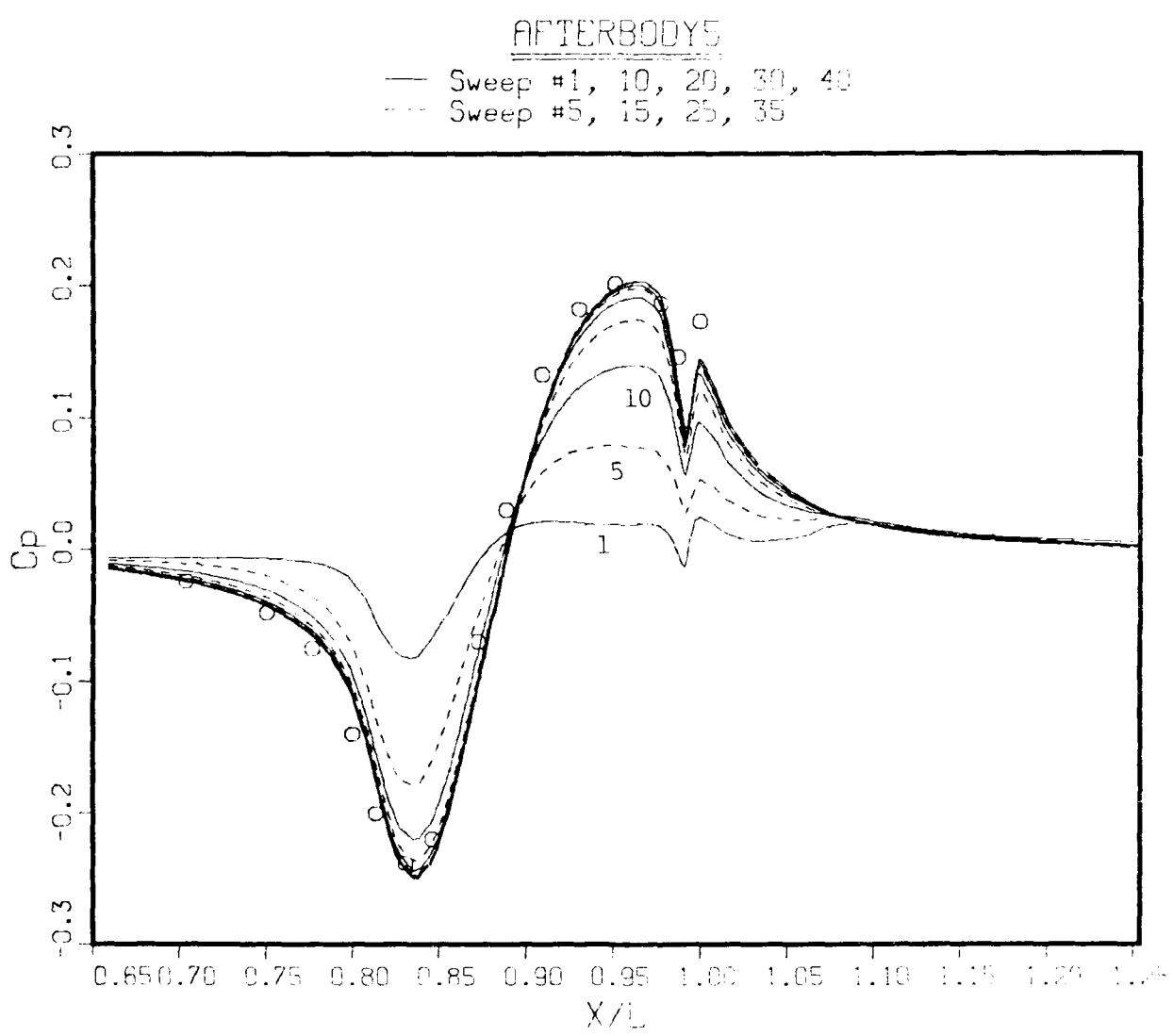
Fig. 25. Convergence History of the Pressure Distribution on the Body (X/L < 1.0) and Along the Wake Centerline (X/L > 1.0) and Comparison with Measurements on the Body; Afterbody 5

AFTERBODY5
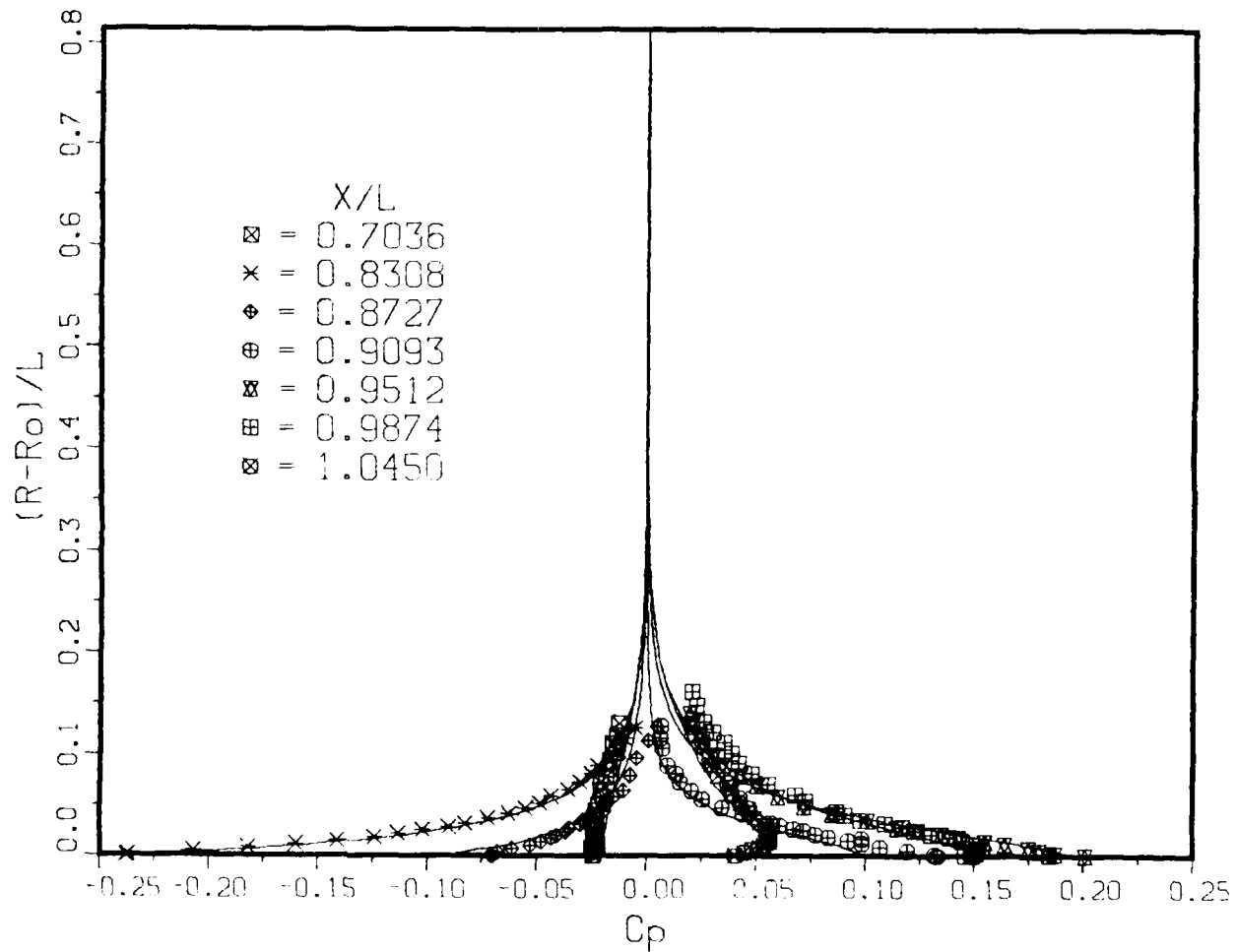
Fig. 26. Radial Variation of Pressure Coefficient Away from the
Body; Afterbody 5
Lines: Calculations, Symbols: Experiment
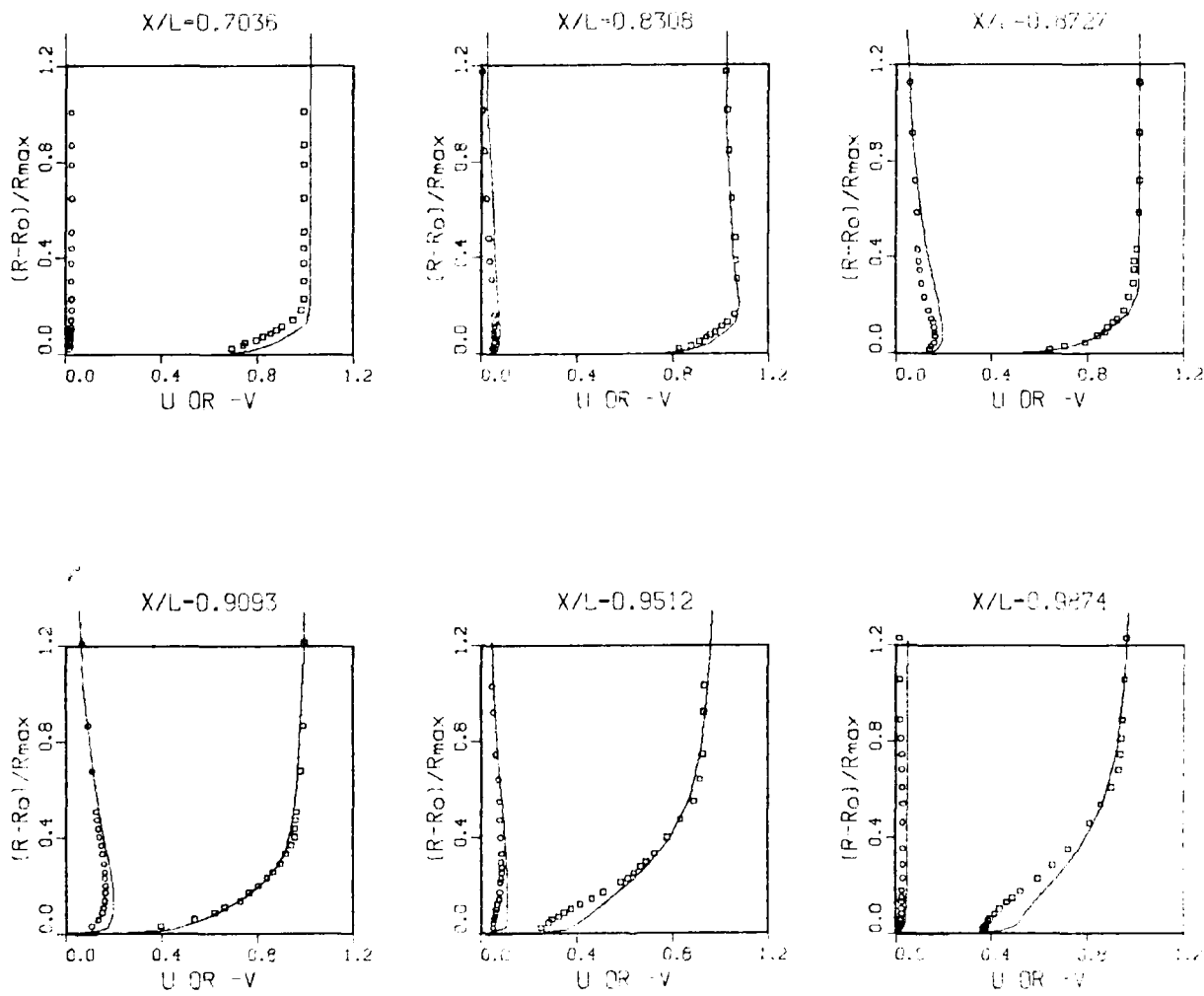
Fig. 27. Axial (U) and Radial (V) Components of Mean Velocity
Within the boundary Layer (Note: The Solution Domain
Extends to $(R-R_o)/R_{max}=16.95)$; Afterbody 5
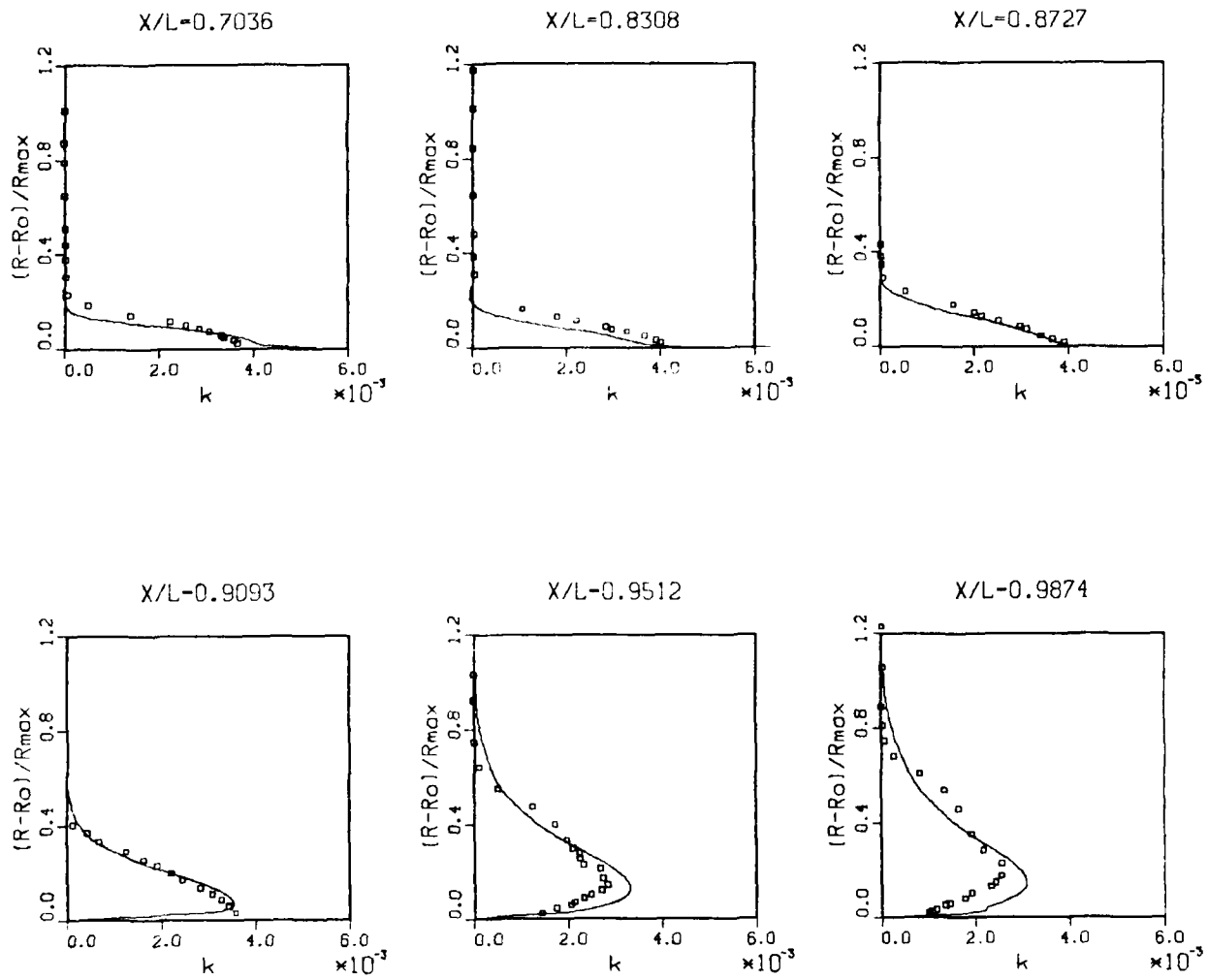
Fig. 28. Turbulent Kinetic-Energy Distributions on Afterbody 5
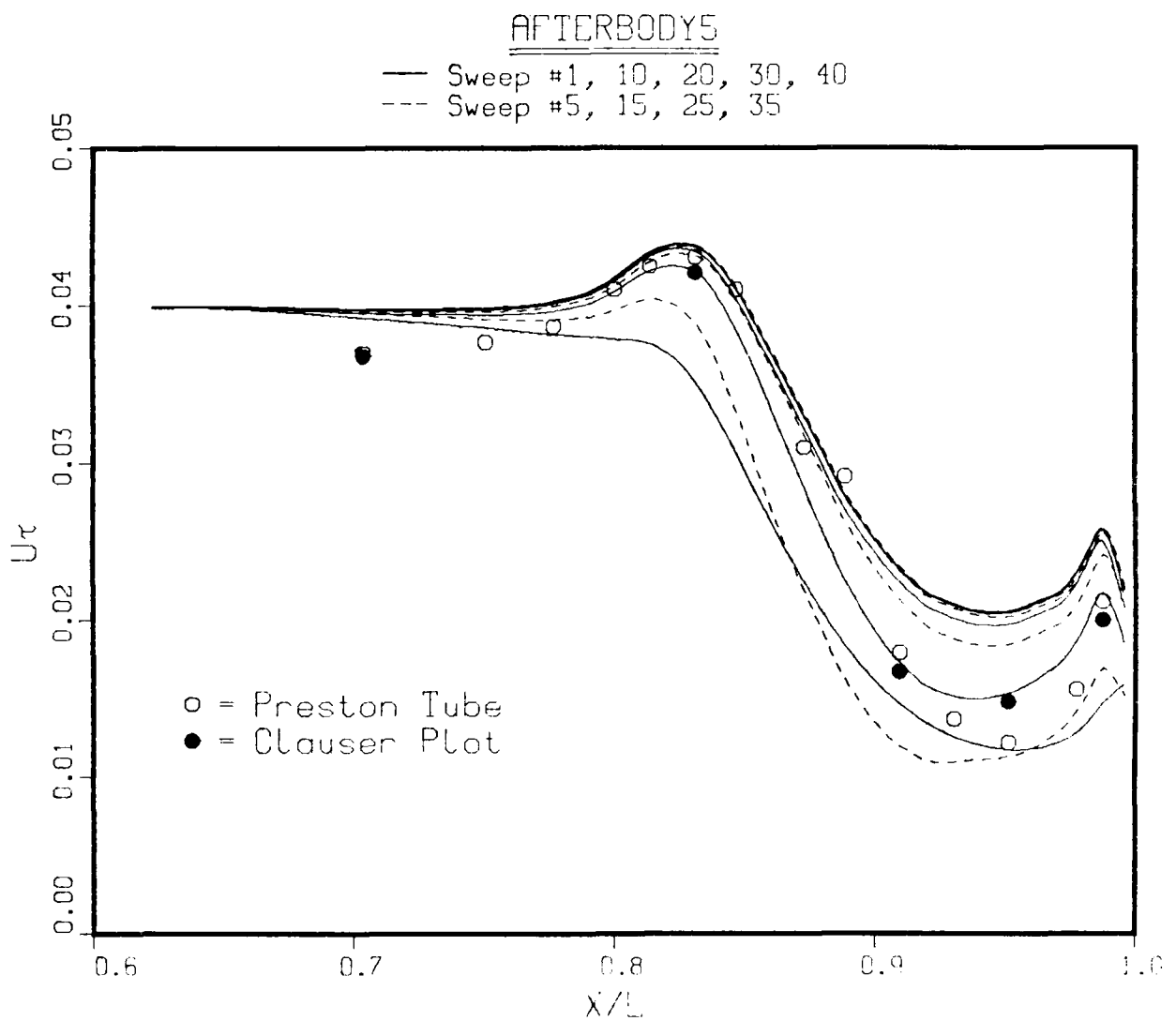
Fig. 29. Convergence History of the Wall Shear Velocity and
Comparison with Experiments; Afterbody 5
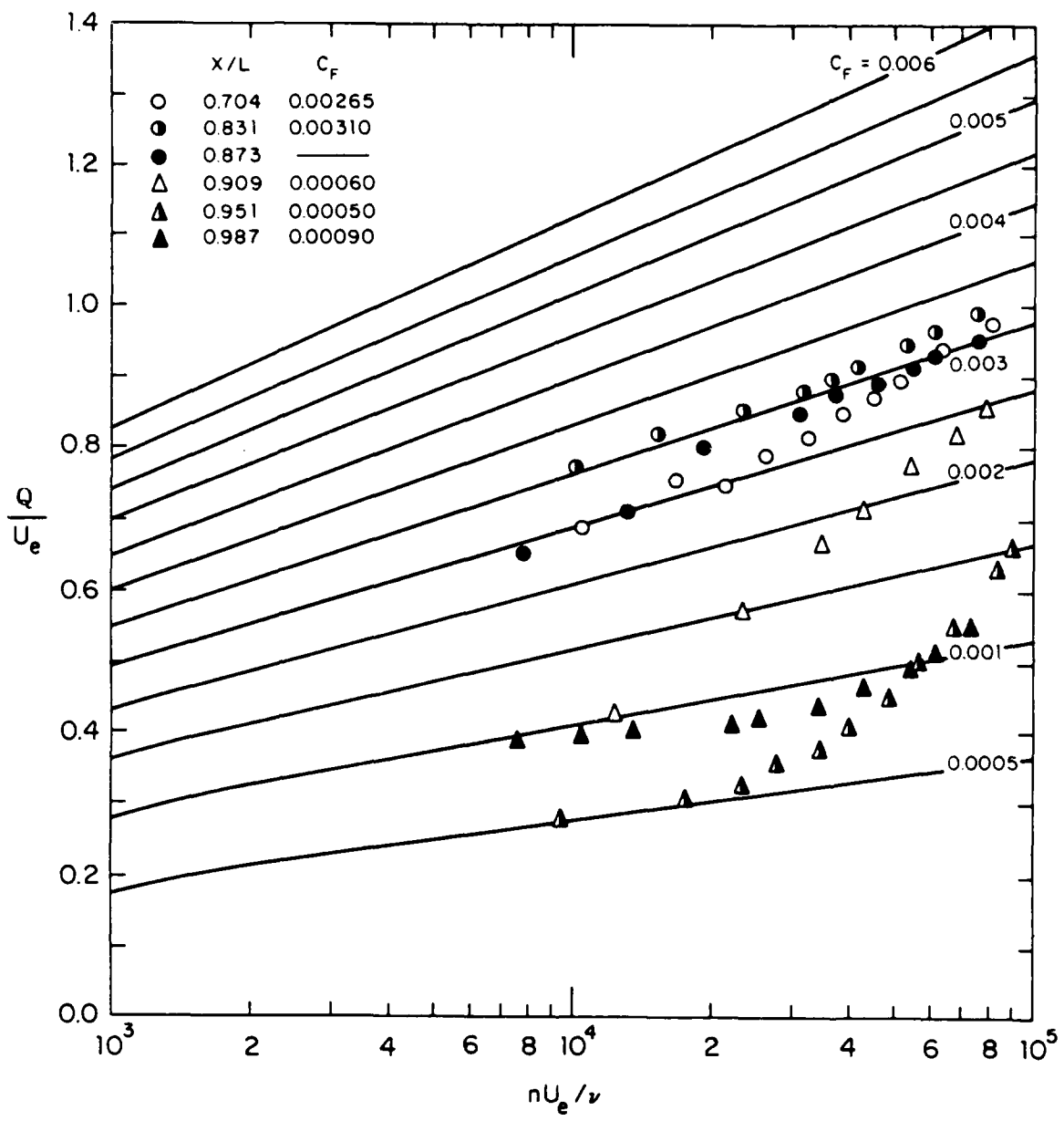
Fig. 30. Clauser Plots for Afterbody 5

152
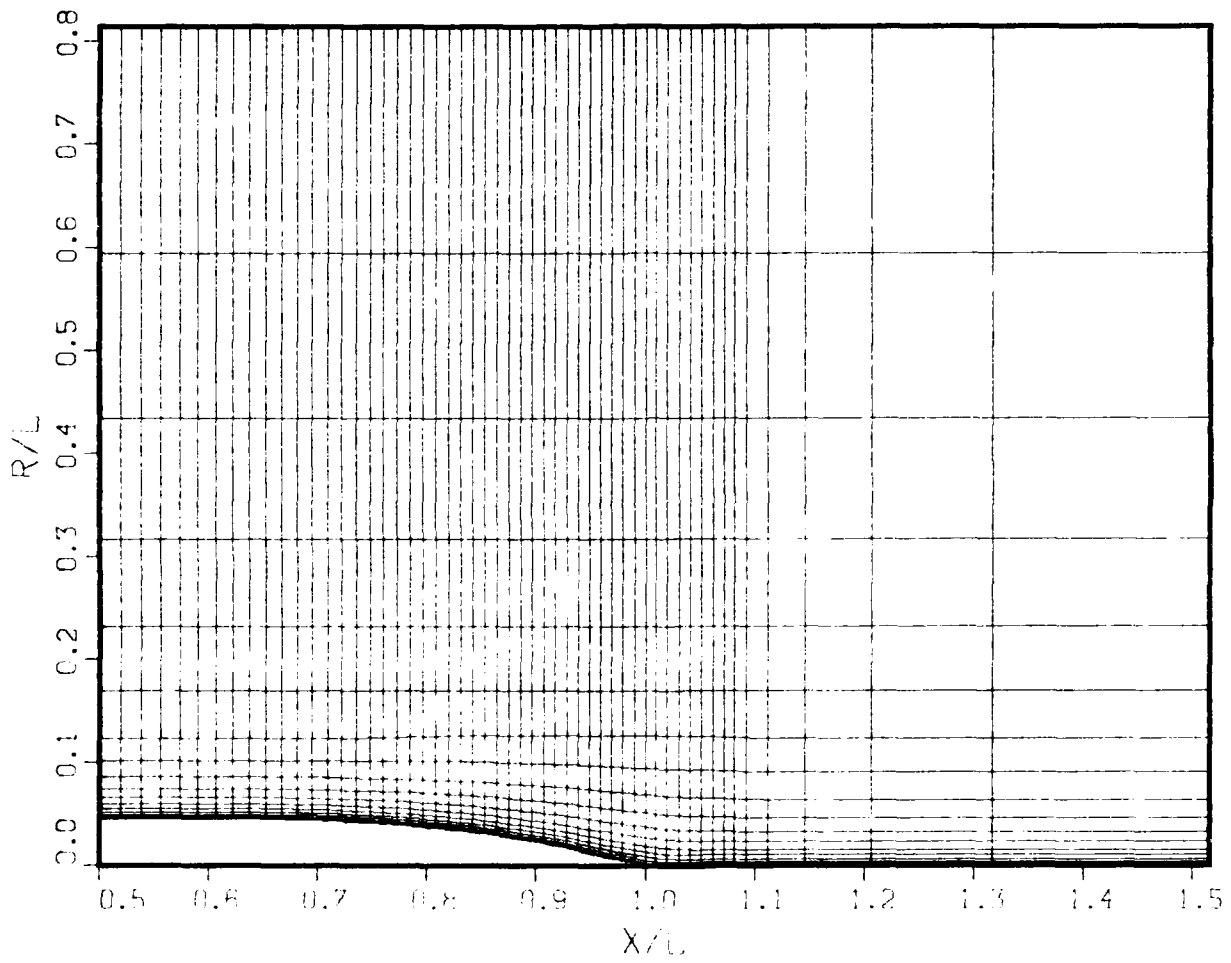
AFTERBODY1

Fig. 31. Numerical Grid for Afterbody 1 (Partial View)

AFTERBODY1
— Sweep #1, 10, 20, 30, 40
--- Sweep #5, 15, 25, 35
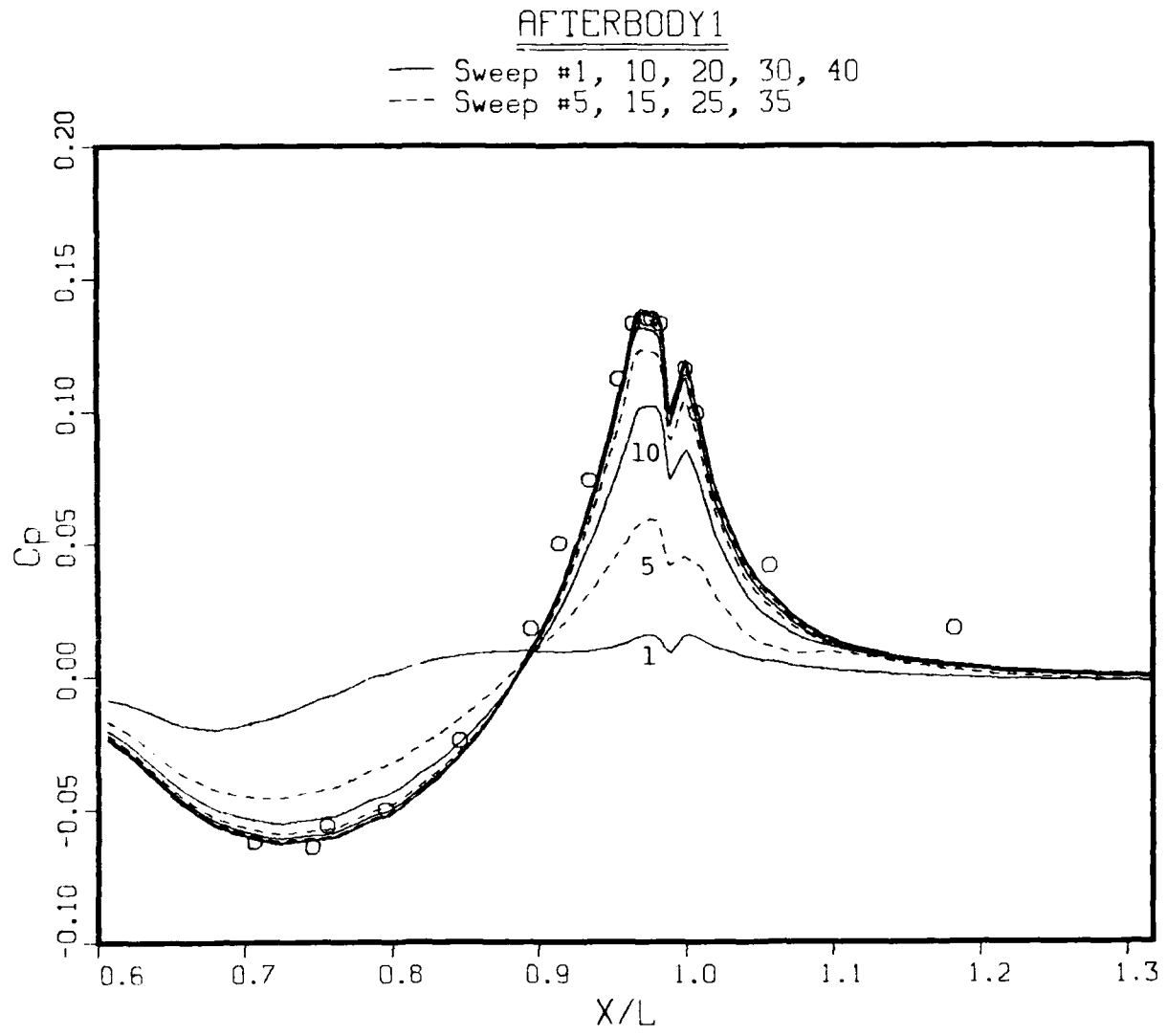
Fig. 32. Convergence History of the Pressure Distribution on the Body (X/L < 1.0) and Along the Wake Centerline (X/L > 1.0), and Comparison with Measurements, Afterbody 1

154
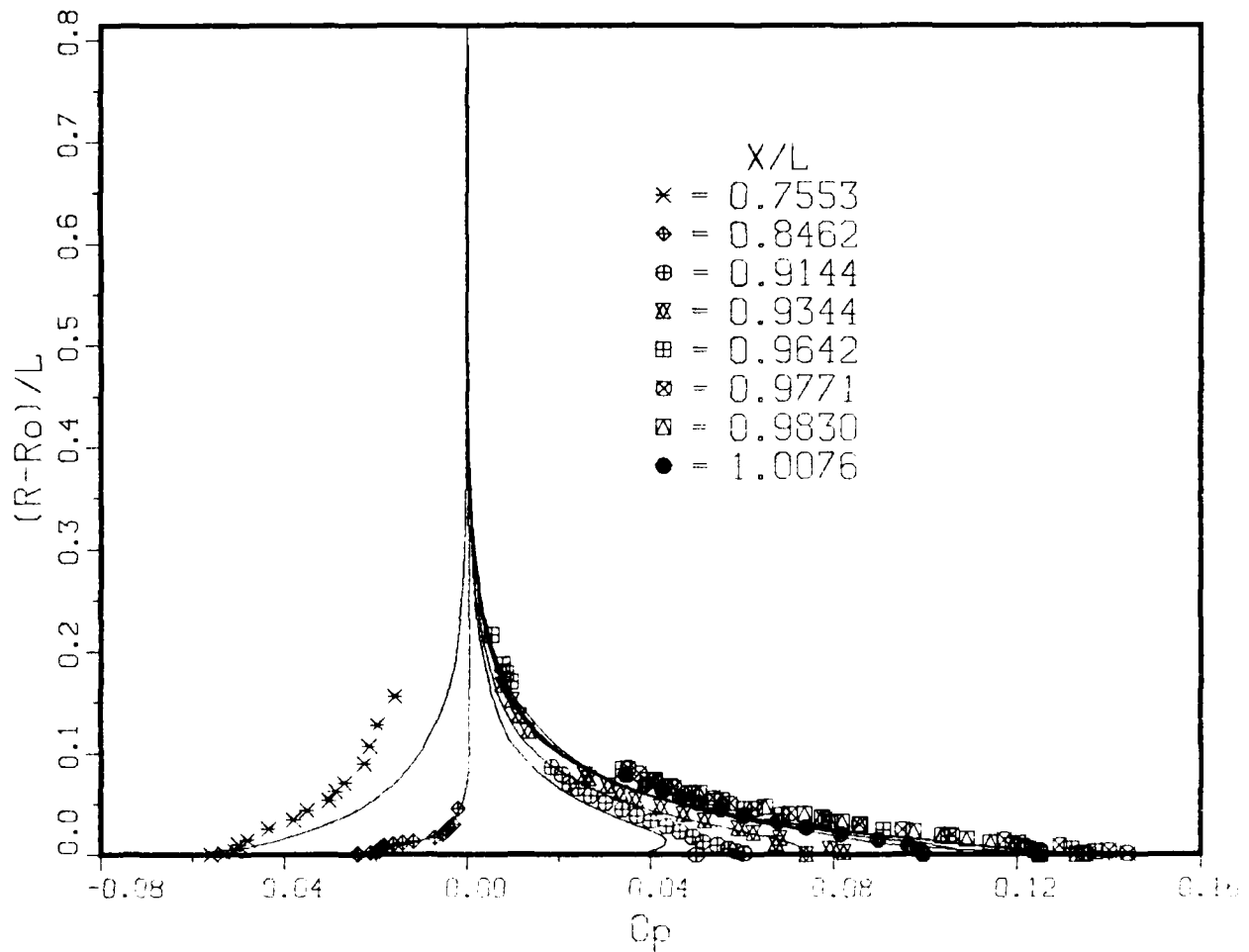
Fig. 33. Radial Variation of Pressure Coefficients Away from the
          Body; Afterbody 1
          Lines: Calculations, Symbols; Experiment
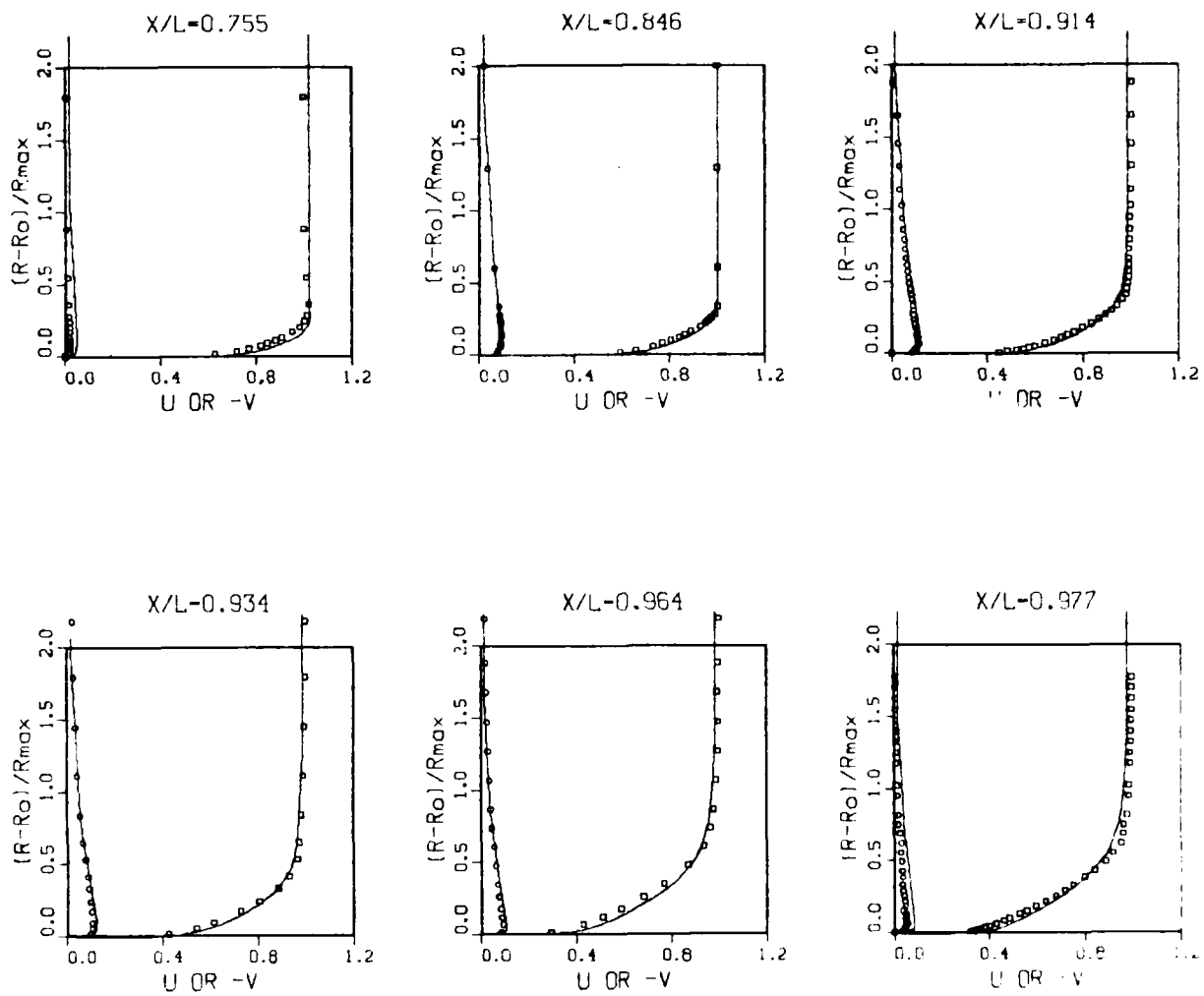
Fig. 34. Axial (U) and Radial (V) Components of Mean Velocity
Within the Boundary Layer (X/L < 1.0) and in the Wake
(X/L > 1.0); Afterbody 1

156

Fig. 34. Continued

157
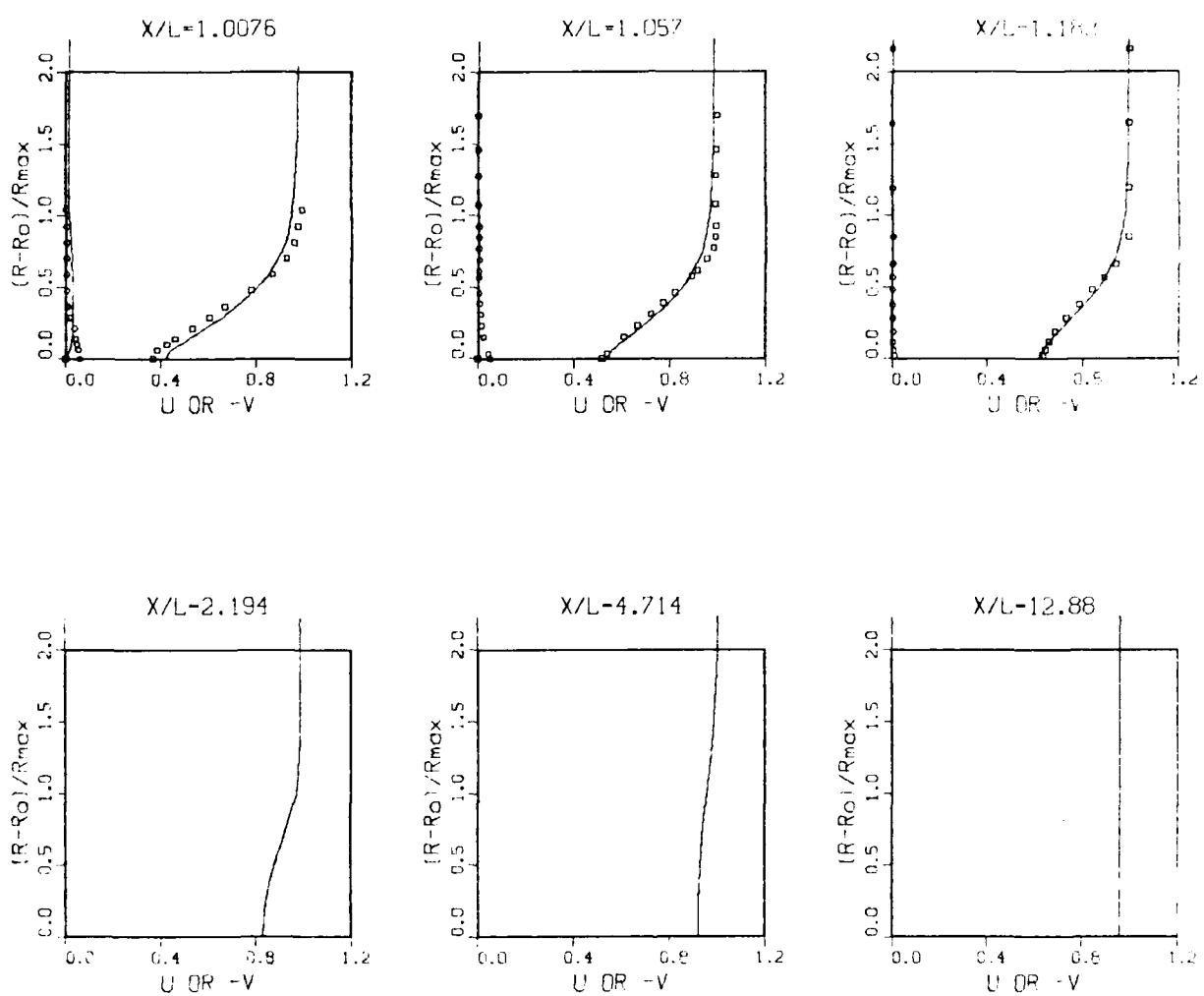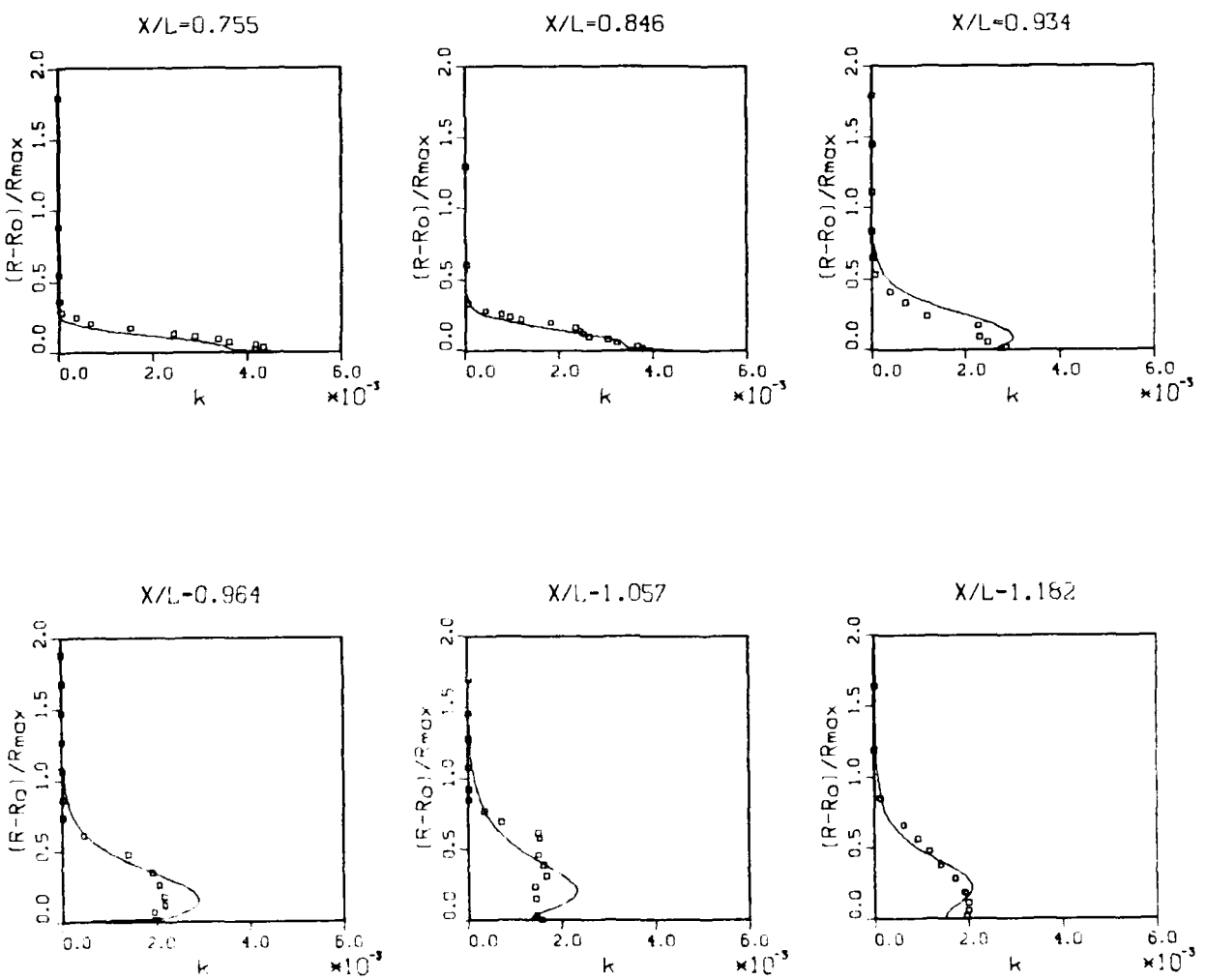
Fig. 35. Turbulent Kinetic-Energy Distribution on Afterbody 1
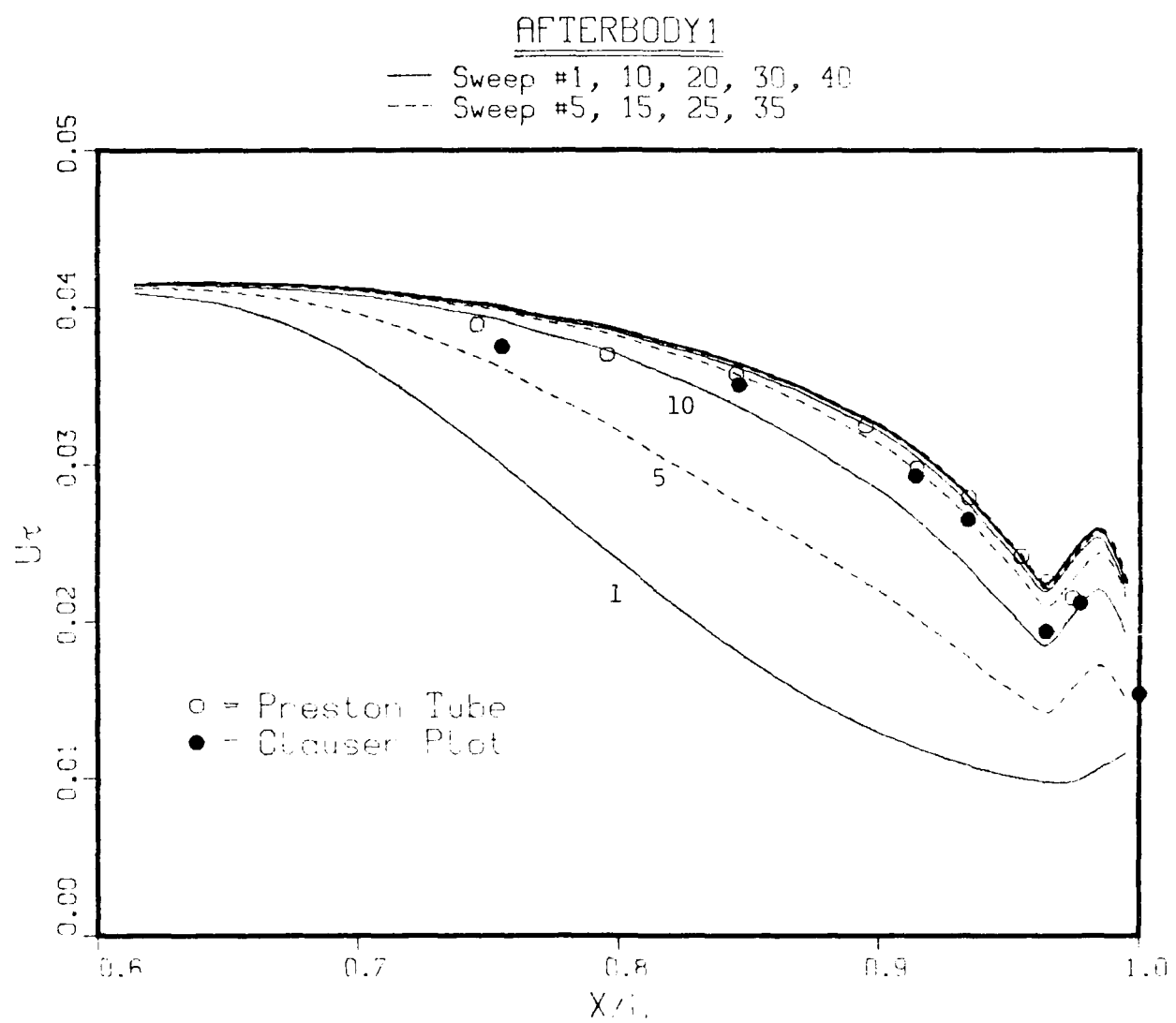
Fig. 36. Convergence History of the Wall Shear Velocity and Comparison with Experiments; Afterbody 1

159
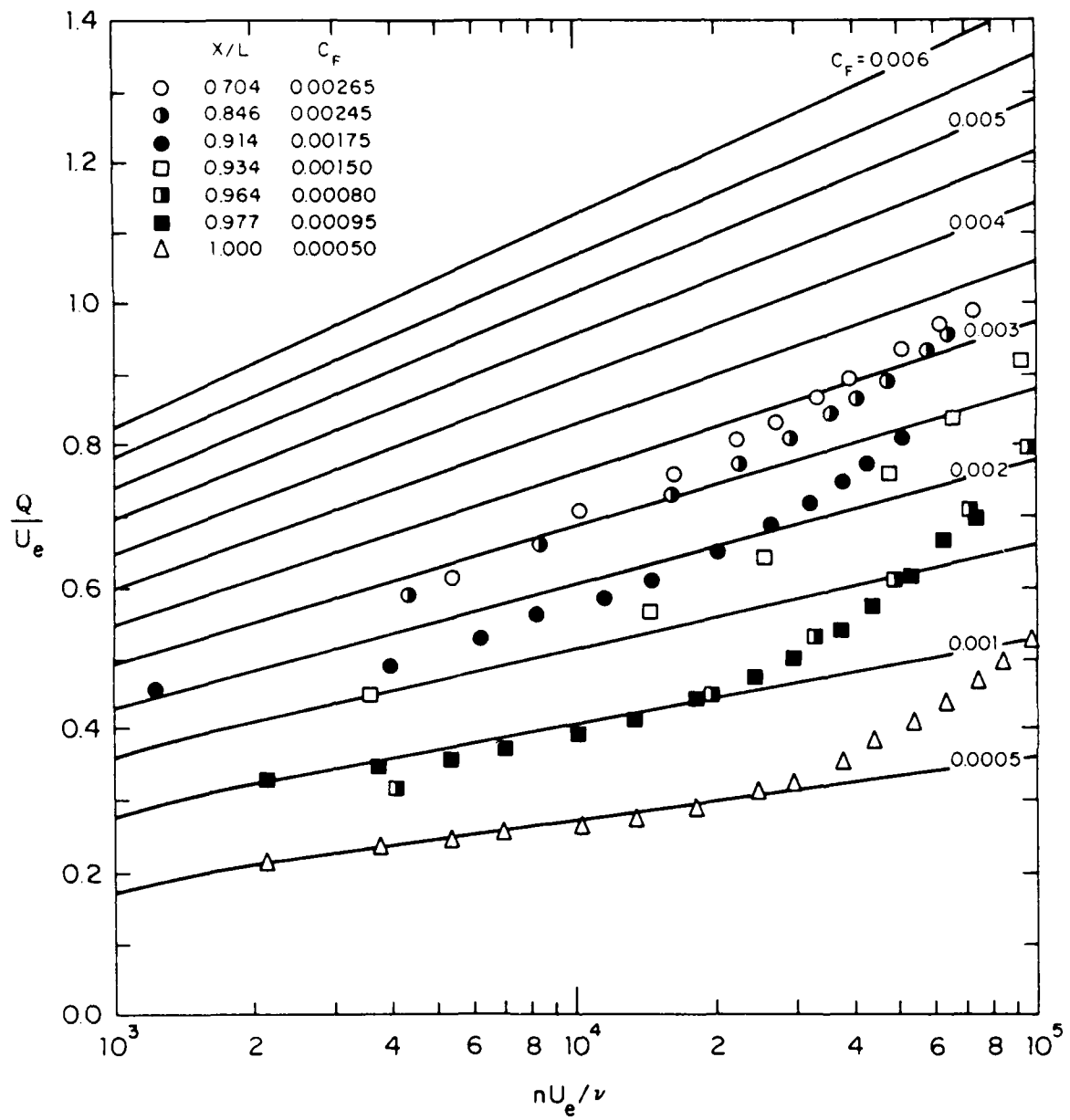
Fig. 37. Clauser Plots for Afterbody 1

160
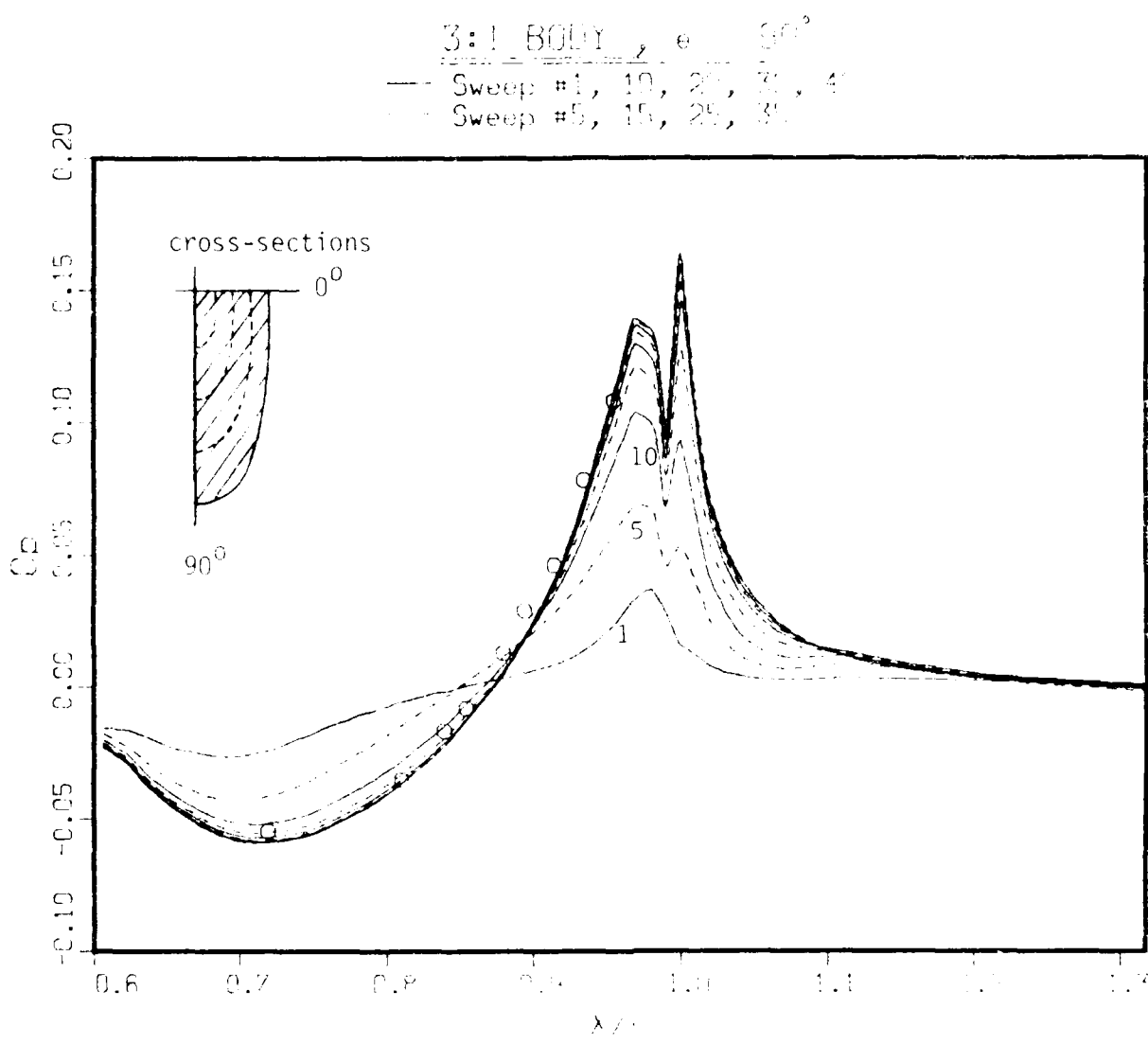
Fig. 38. Convergence of Pressure Distribution on body Surface Along $\theta = 90°$ and Wake Centerline. 3:1 Body

161
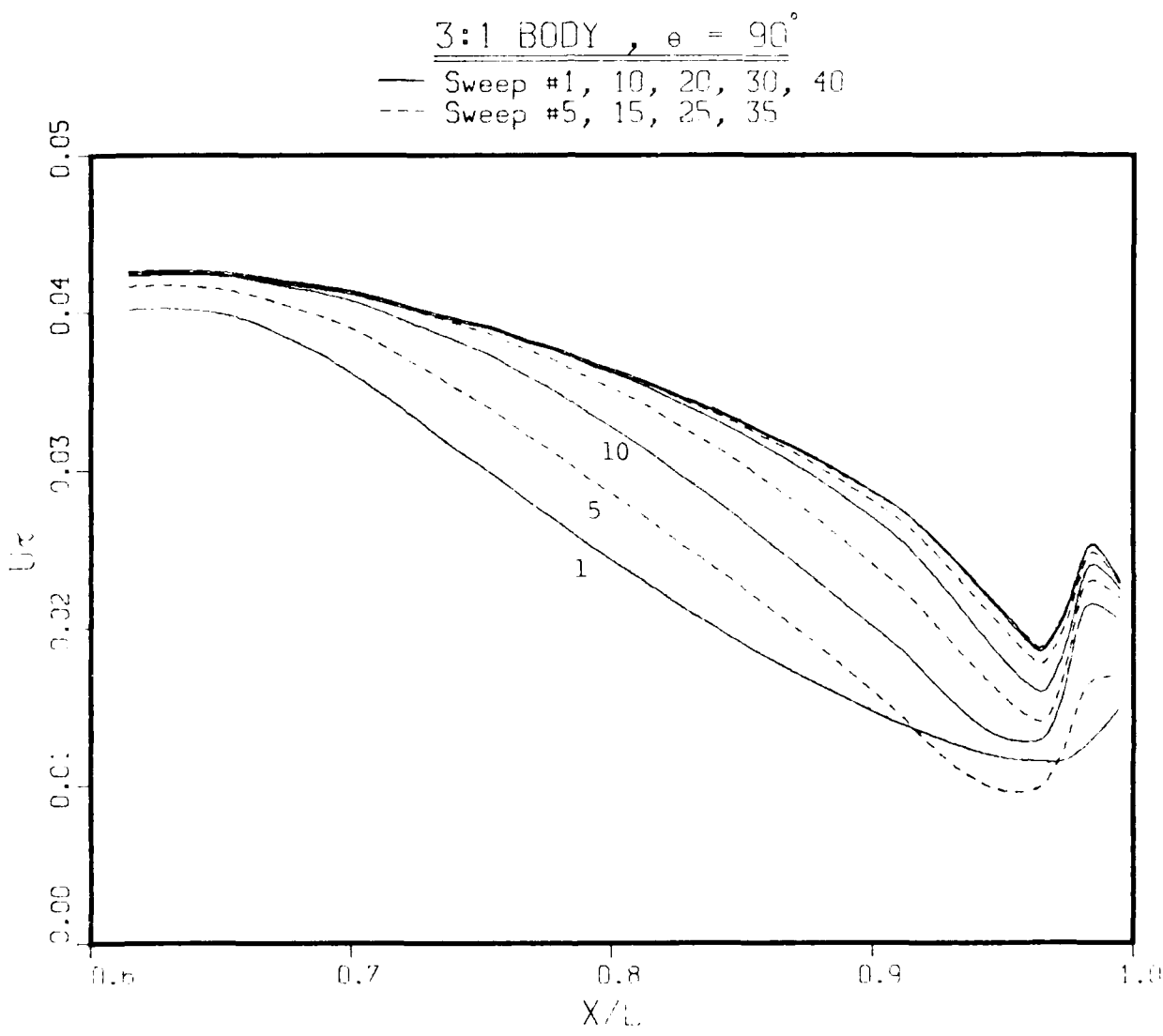
Fig. 39.   Convergence of Wall Shear Velocity Along $\theta = 90°$, 3:1 Body
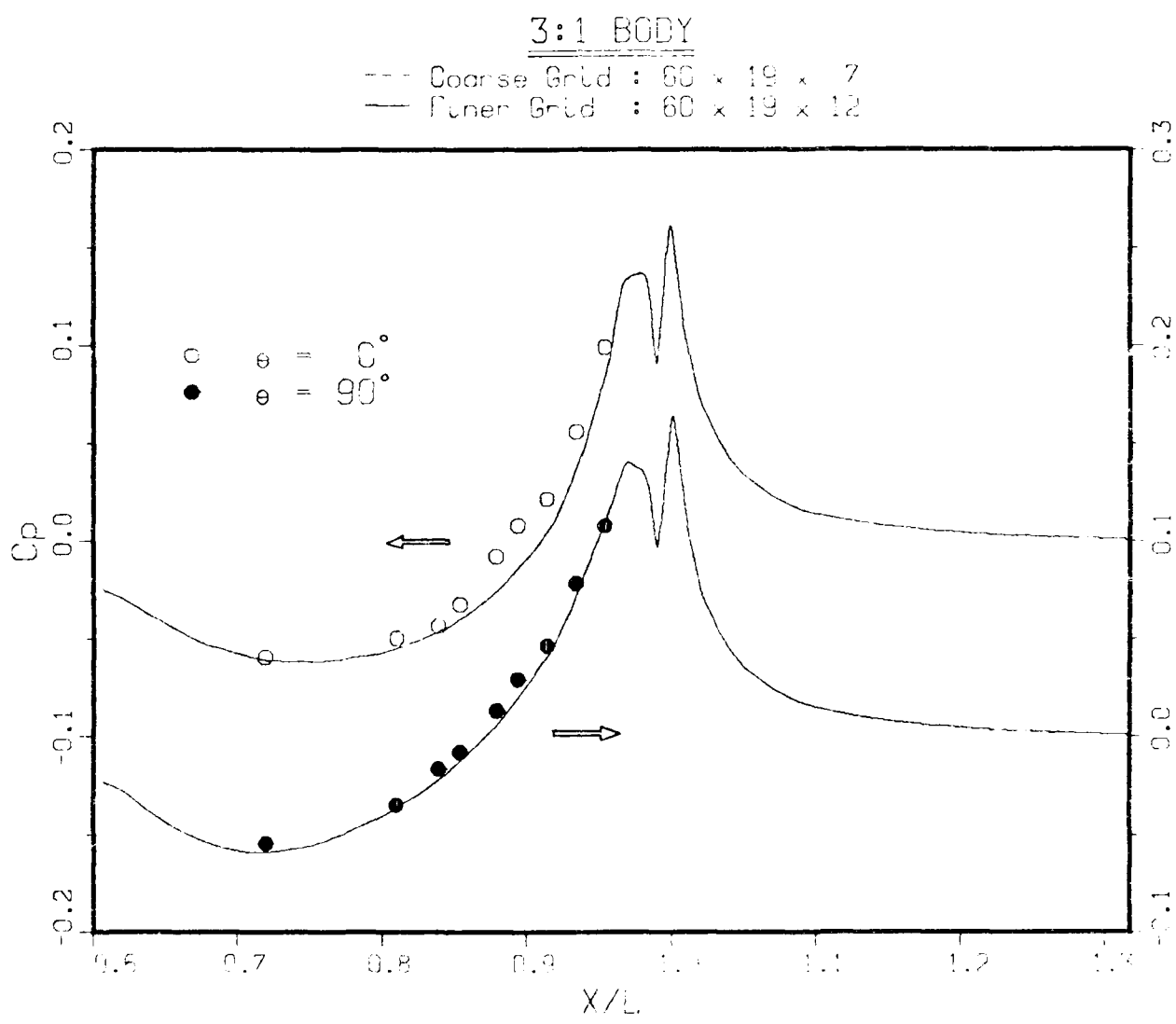
Fig. 40. Pressure Distributions Along θ = 0° and 90°, 3:1 Body

$3:1$ BODY , $\theta = 0^{\circ}$
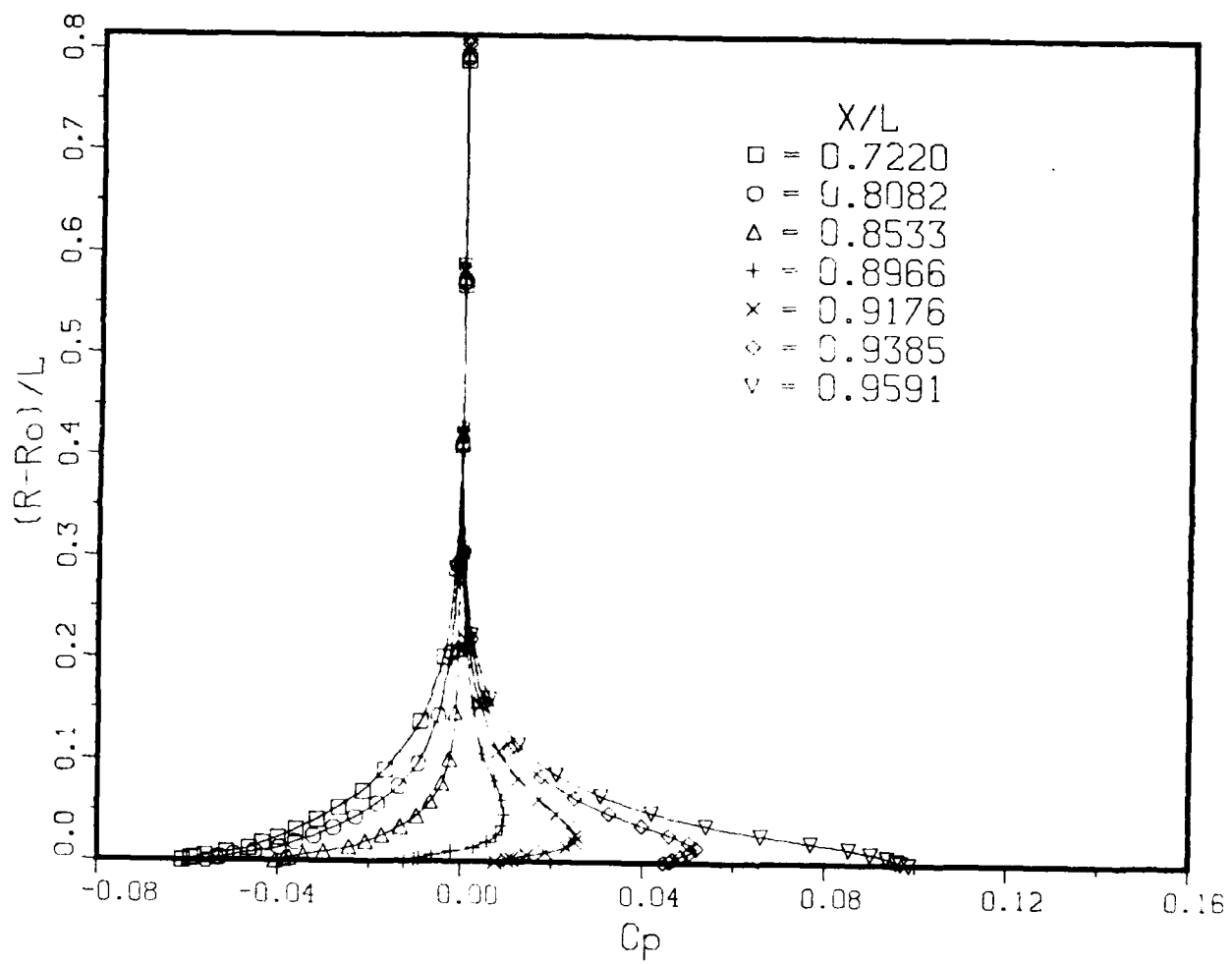
Fig. 41(a).   Radial Variation of Pressure Along $\theta = 0^{\circ}$, 3:1 Body

164

3:1 BODY , θ = 90°
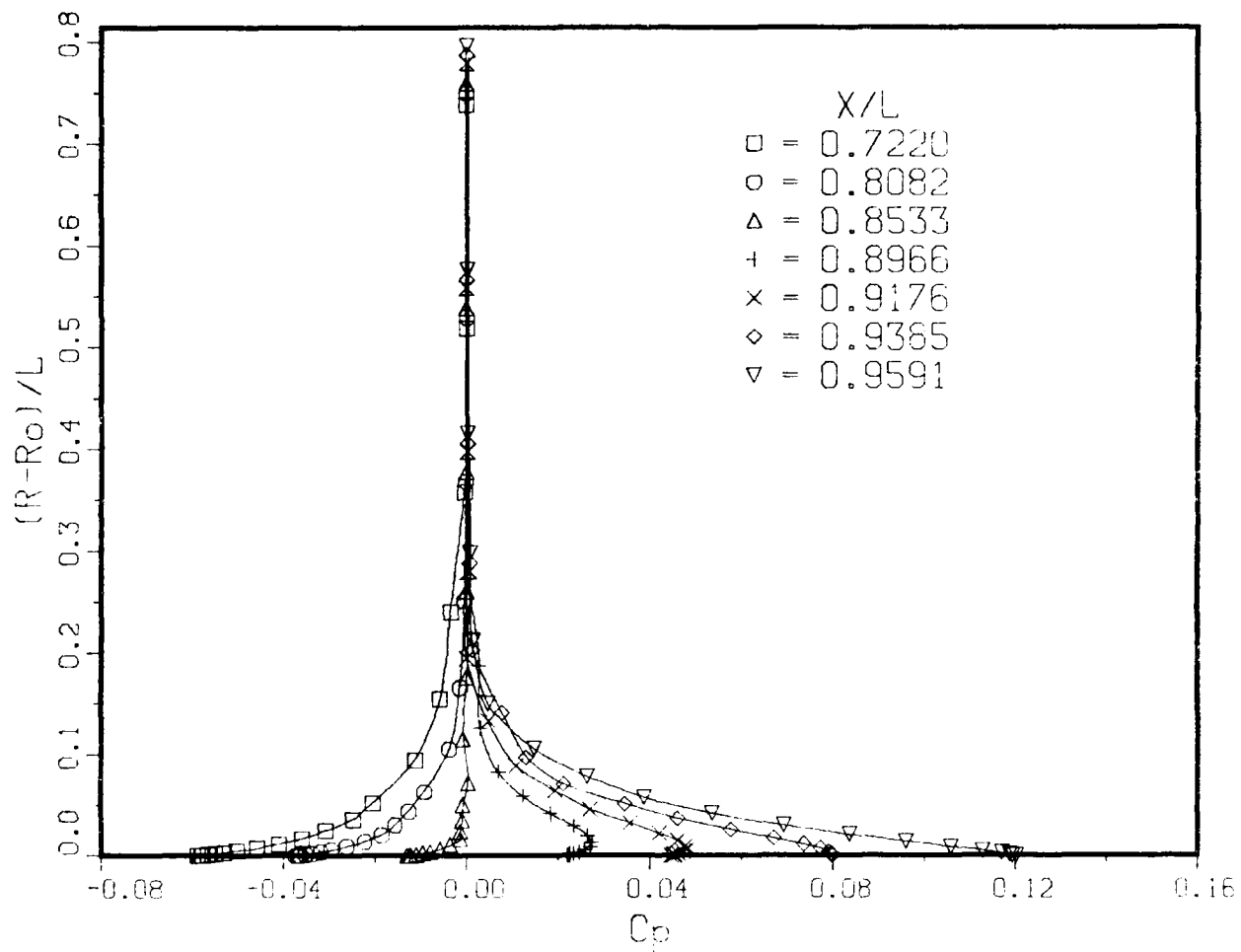
Fig. 41(b).   Radial Variation of Pressure Along θ = 90°, 3:1
        Body
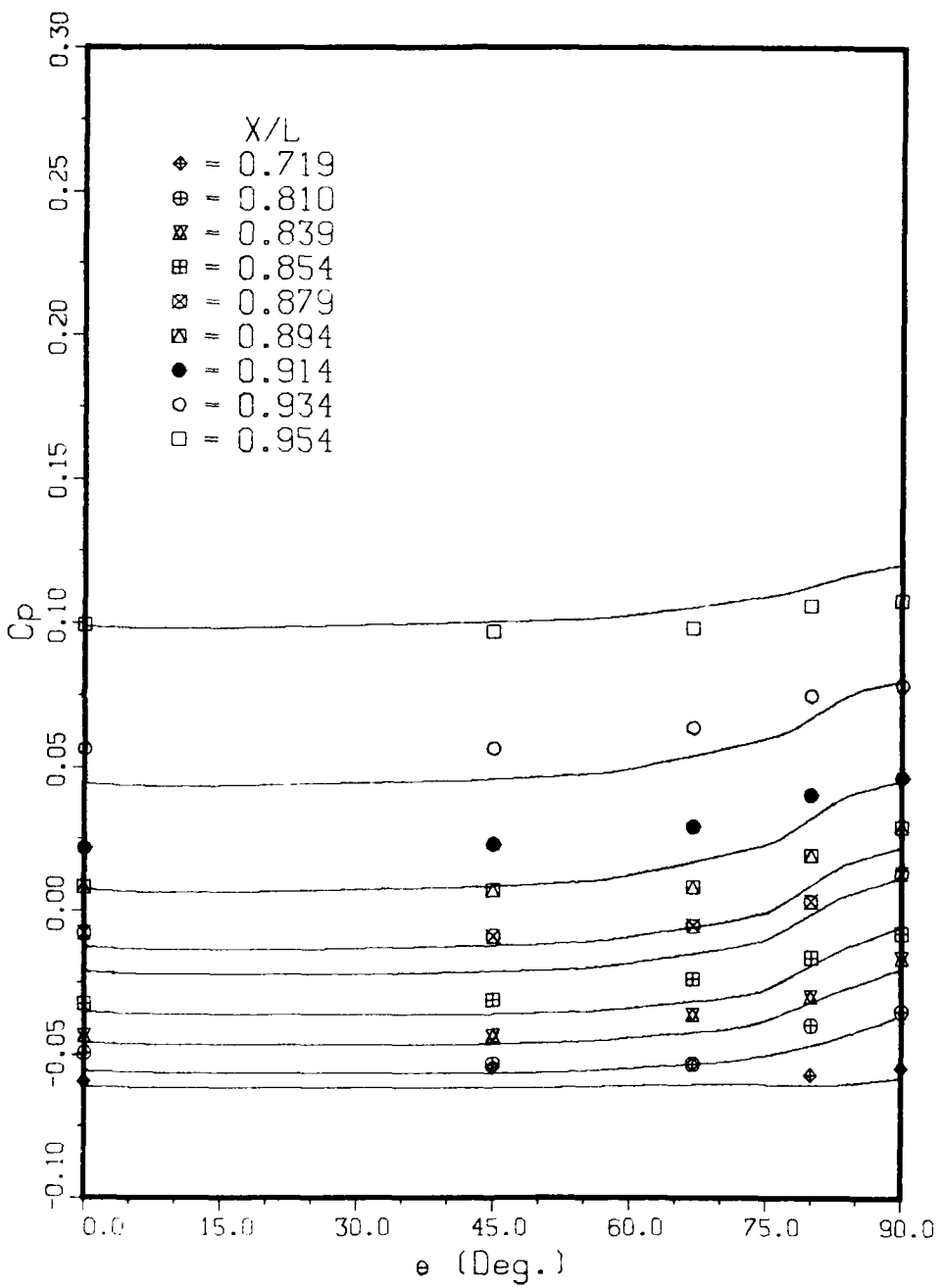
3:1 BODY

Fig. 42. Girthwise Pressure Distribution on the 3:1 Body;
Comparison with Experiments
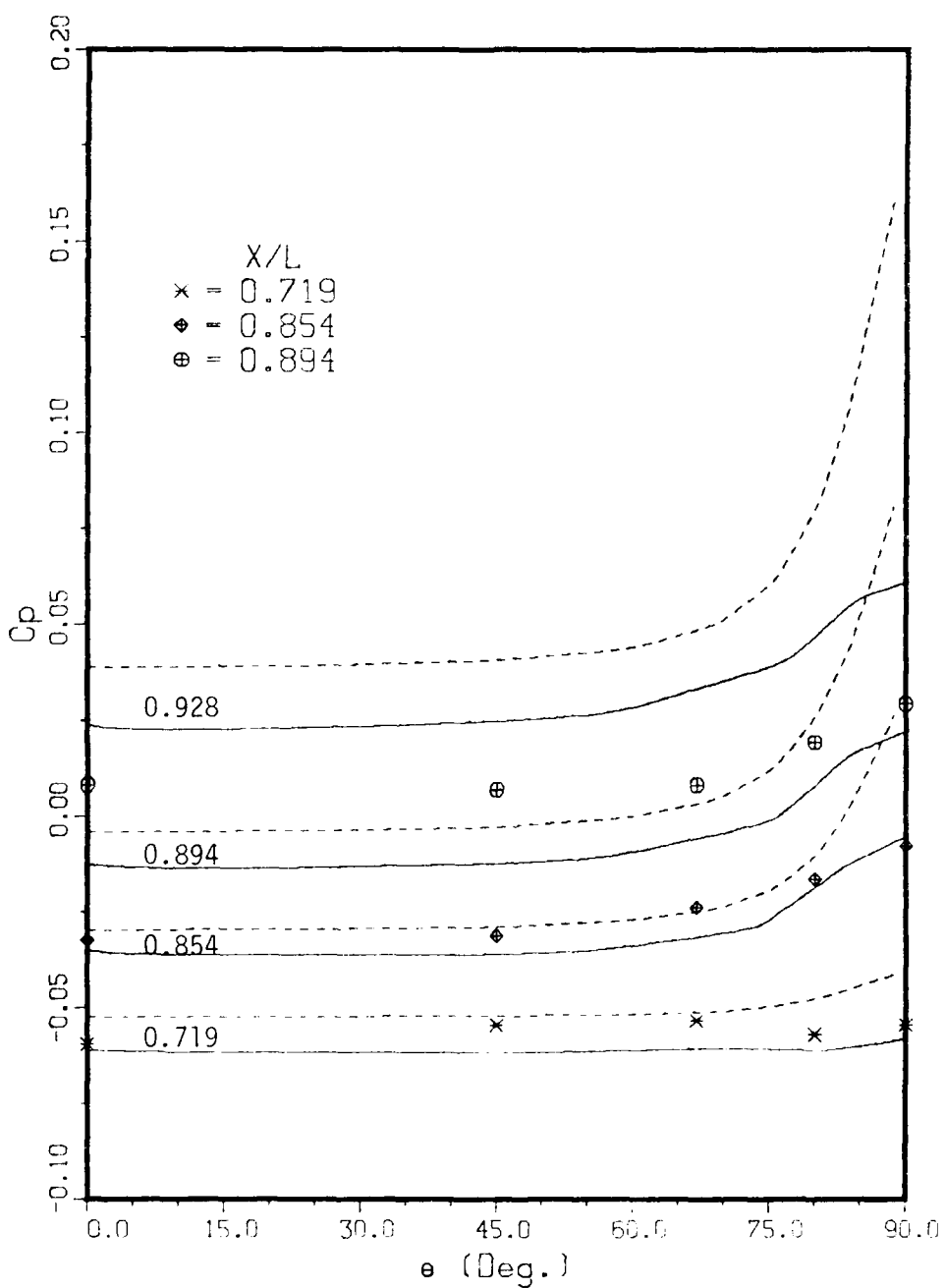
Fig. 43. Girthwise Variation of Pressure on the 3:1 Body; Comparison with Inviscid-Flow Solutions
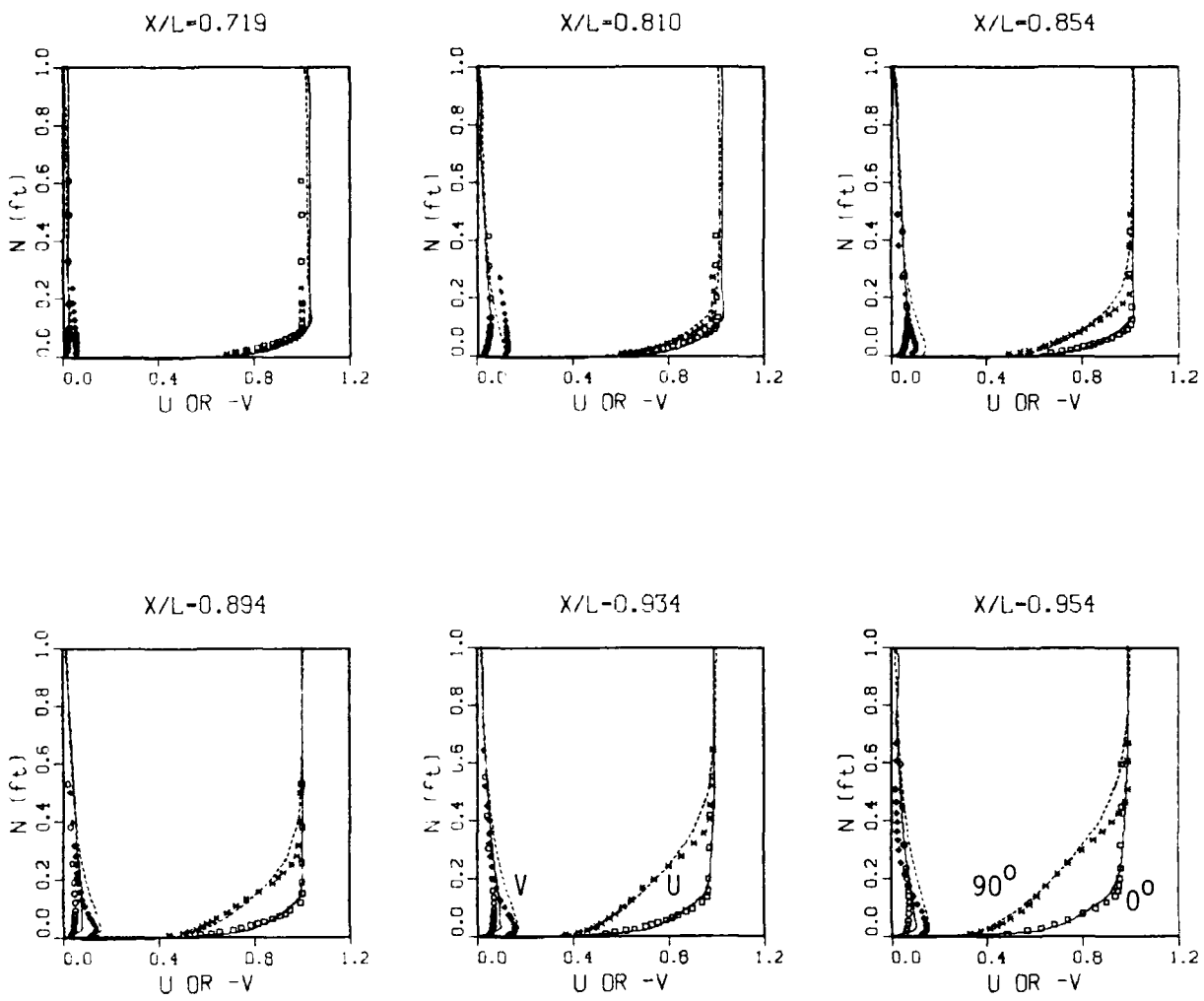
Fig. 44(a). Velocity Profiles in the Boundary Layer in the Planes of Symmetry; 3:1 Body

168
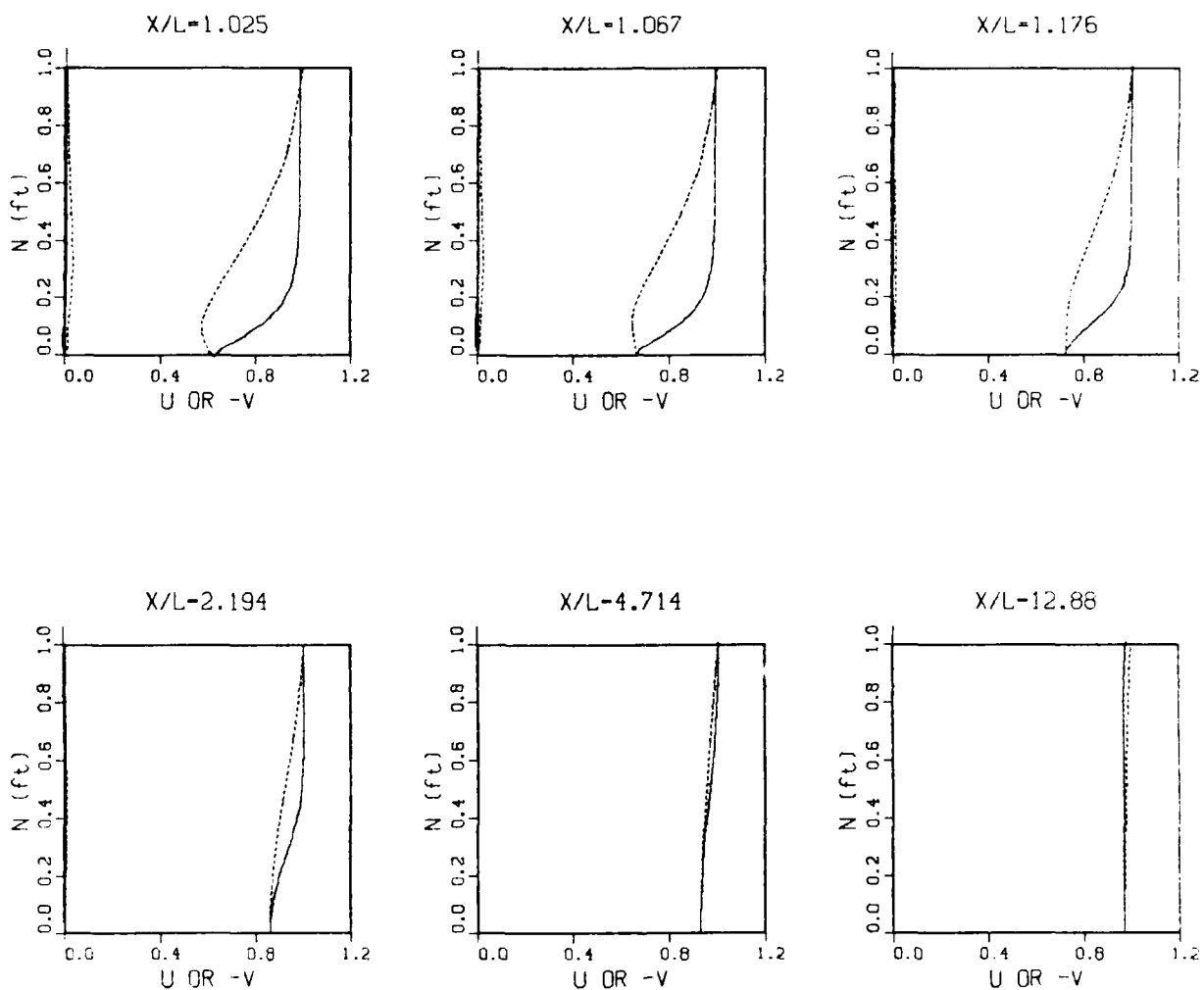
Fig. 44(b).   Velocity Profiles in the Wake in the Planes of
Symmetry; 3:1 Body

169
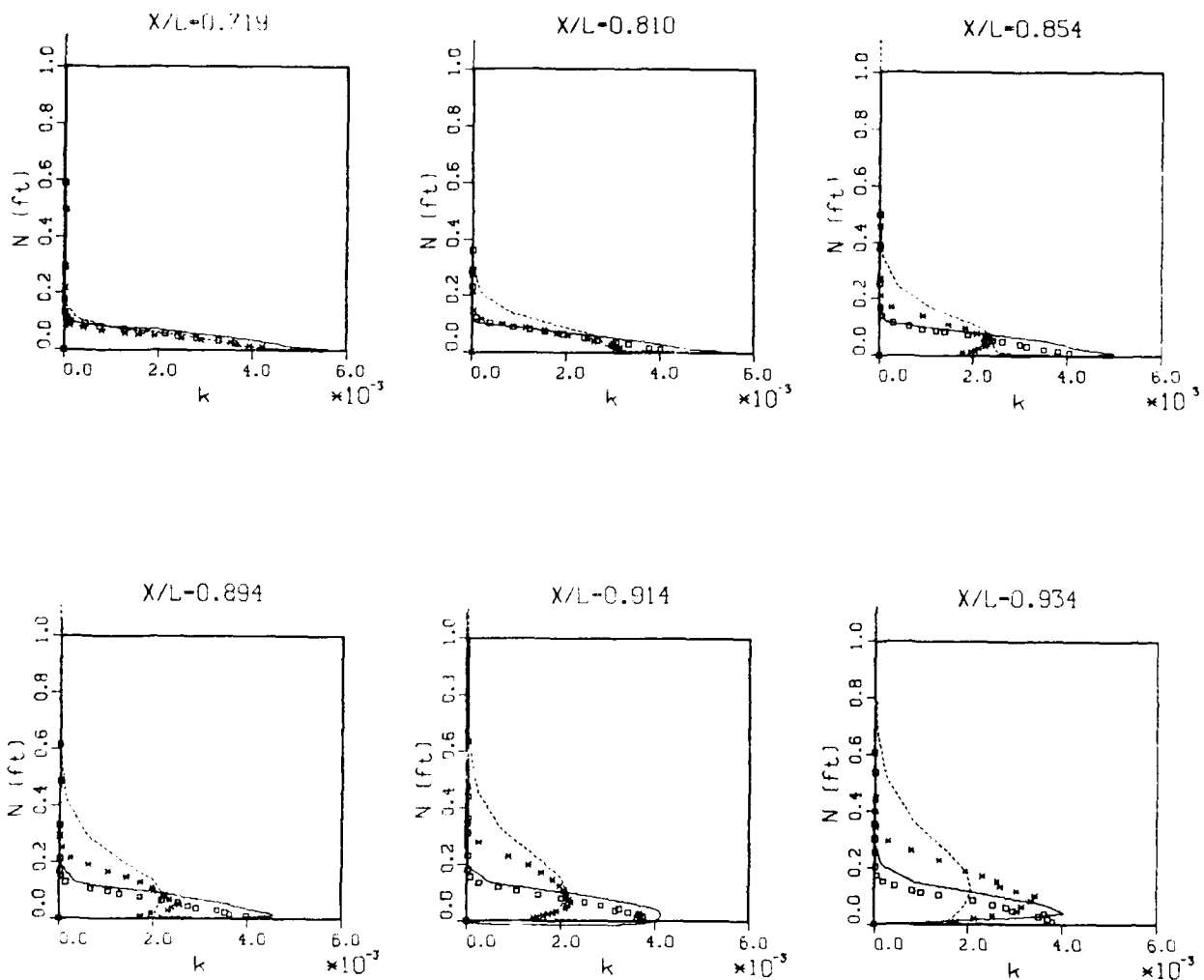
Fig. 45. Turbulent Kinetic-Energy Profiles in the Boundary Layer in the Planes of Symmetry; 3:1 Body

170
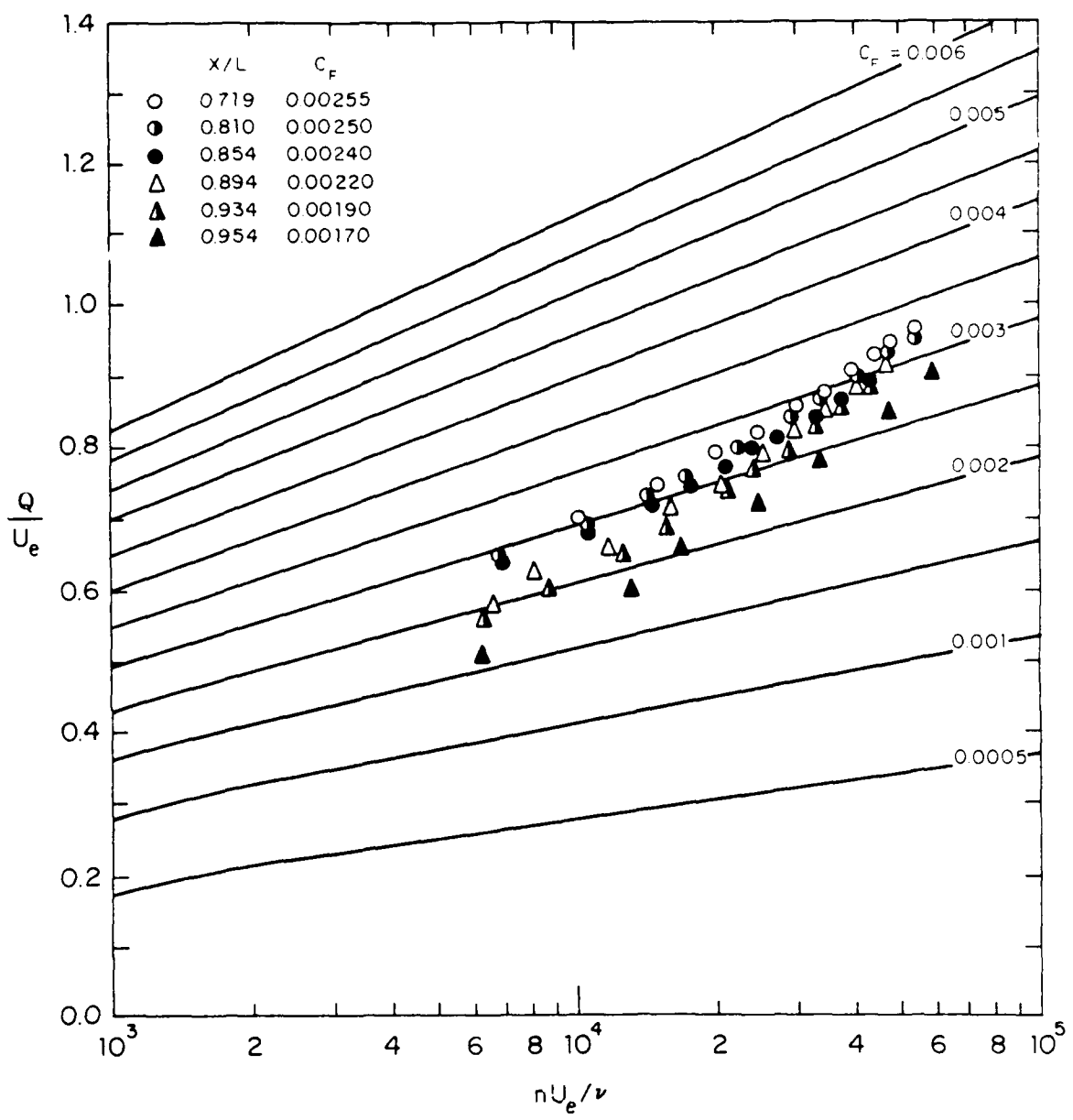
Fig. 46(a).   Clauser Plots of Measured Velocity Profiles
Along $\theta = 0°$; 3:1 Body
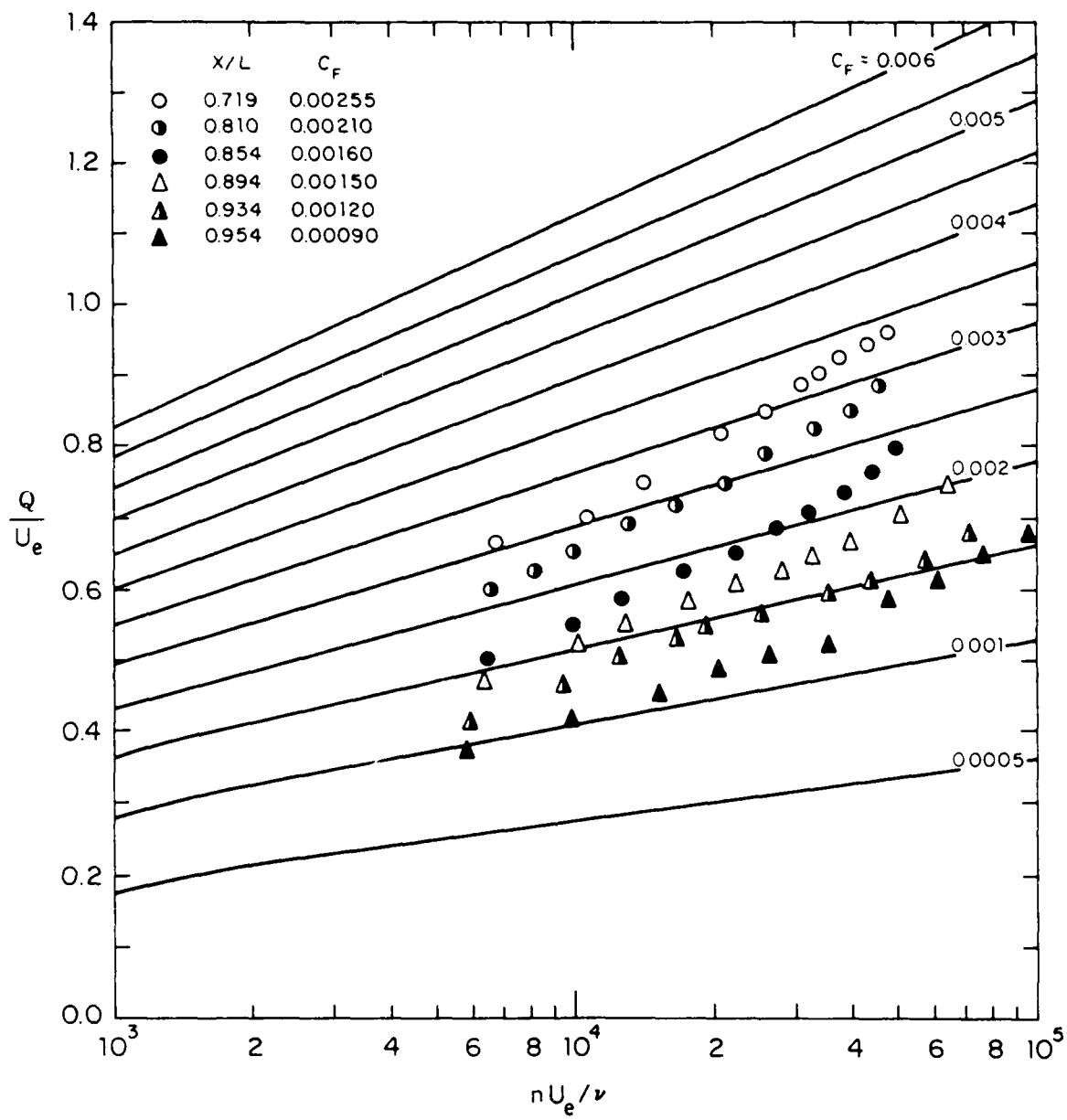
Fig. 46(b).   Clauser Plots of Measured Velocity Profiles
              Along θ = 90°; 3:1 Body

172
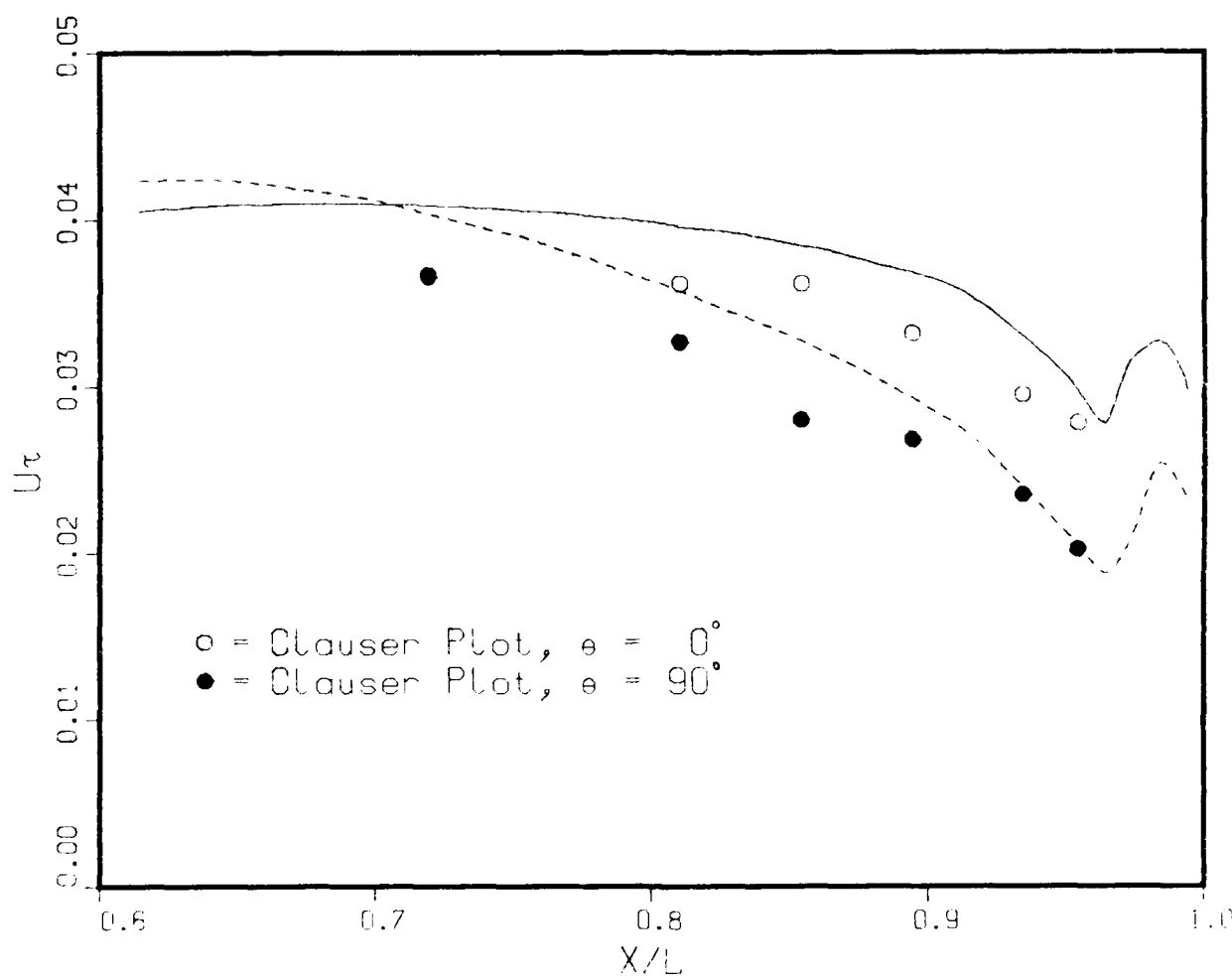
3:1 BODY

Fig. 47.   Wall Shear Velocity Along the Planes of Symmetry, 3:1
          Body
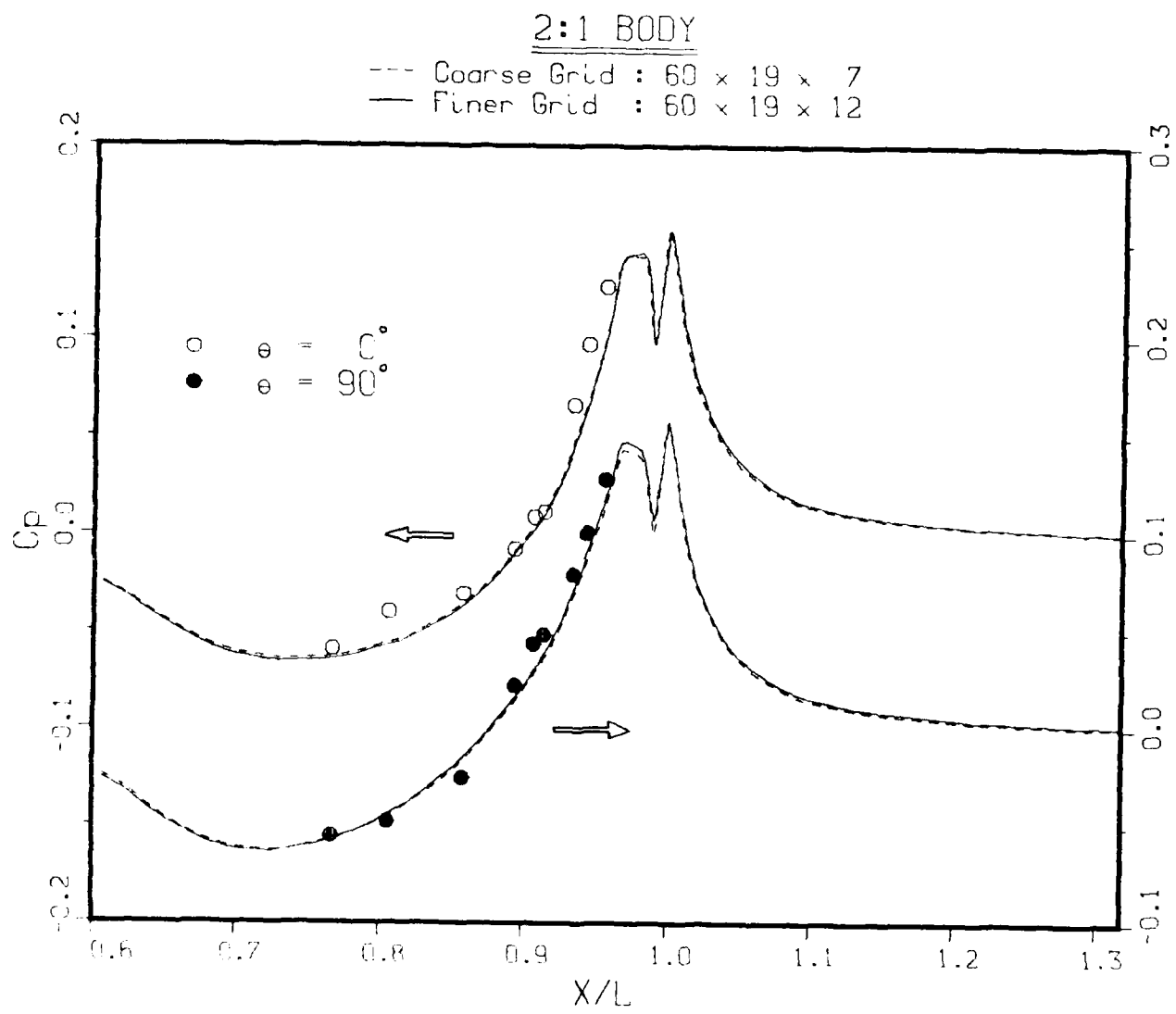
Fig. 48.   Pressure Distributions Along θ = 0° and 90°; 2:1 Body

2:1 BODY , θ = 0°
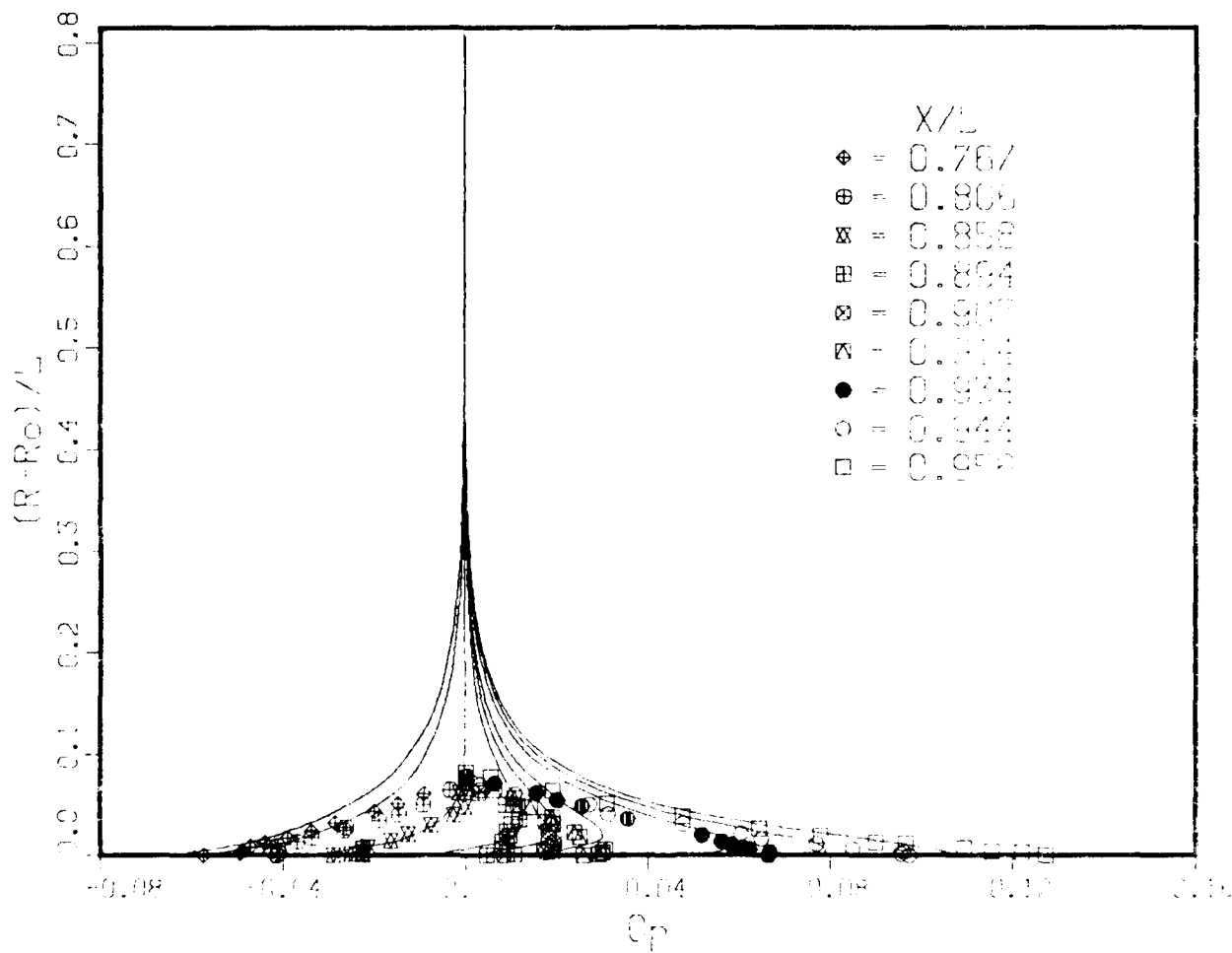
Fig. 49(a).   Radial Variation of Pressure Along θ = 0°; 2:1 Body
              Lines: Calculation; Symbols: Experiment
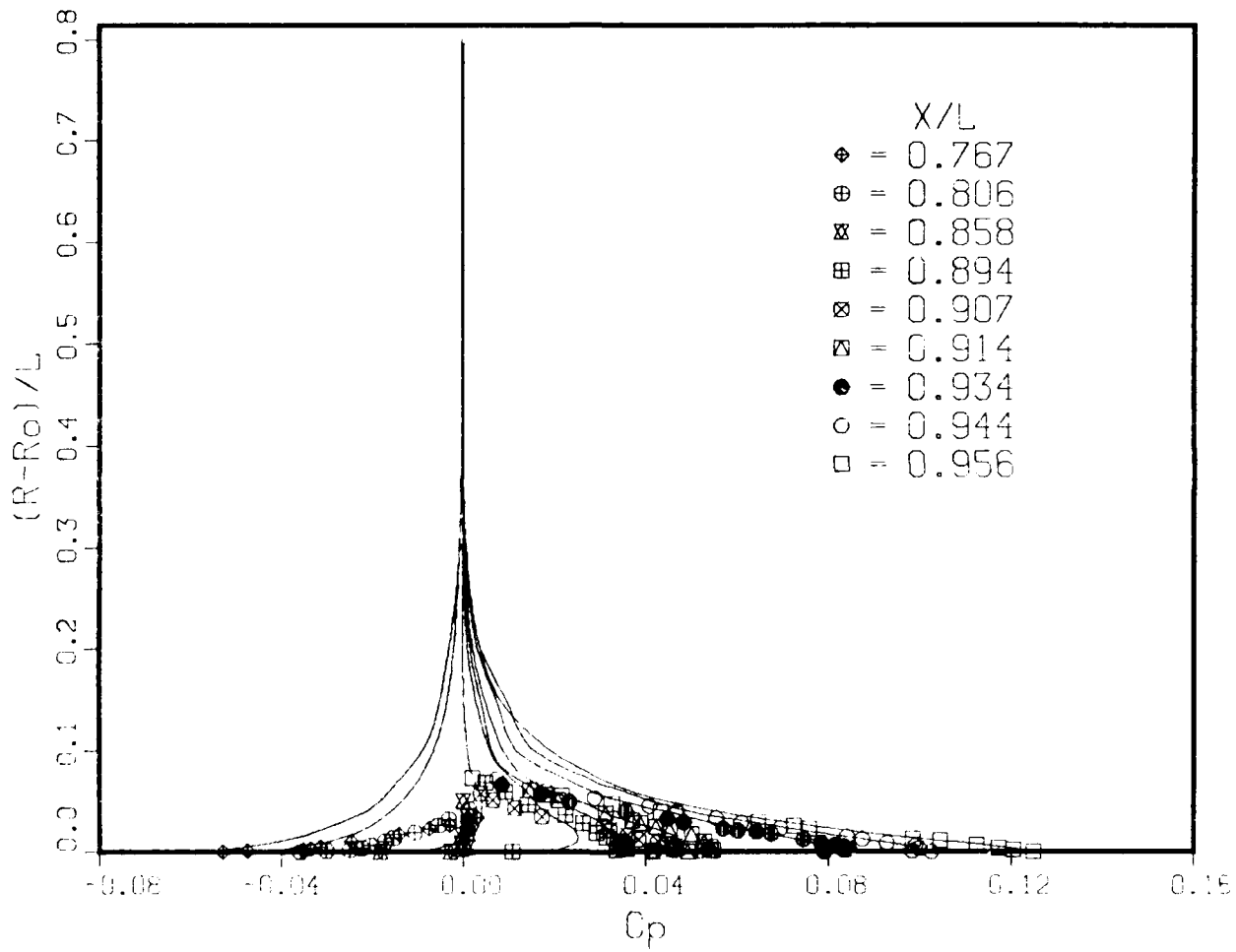
Fig. 49(b).   Radial Variation of Pressure Along θ = 90°; 2:1
Body
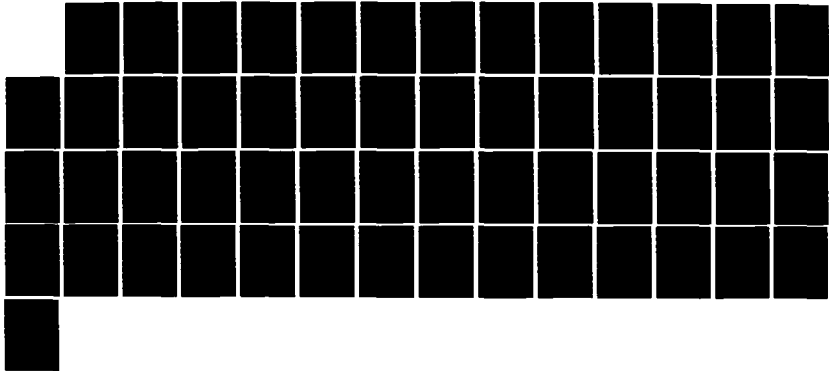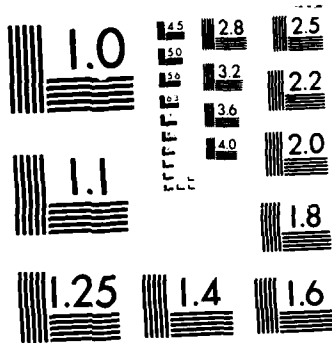
MICROCOPY RESOLUTION TEST CHART

NATIONAL BUREAU OF STANDARDS-1963-A

2:1 BODY , θ = 0°
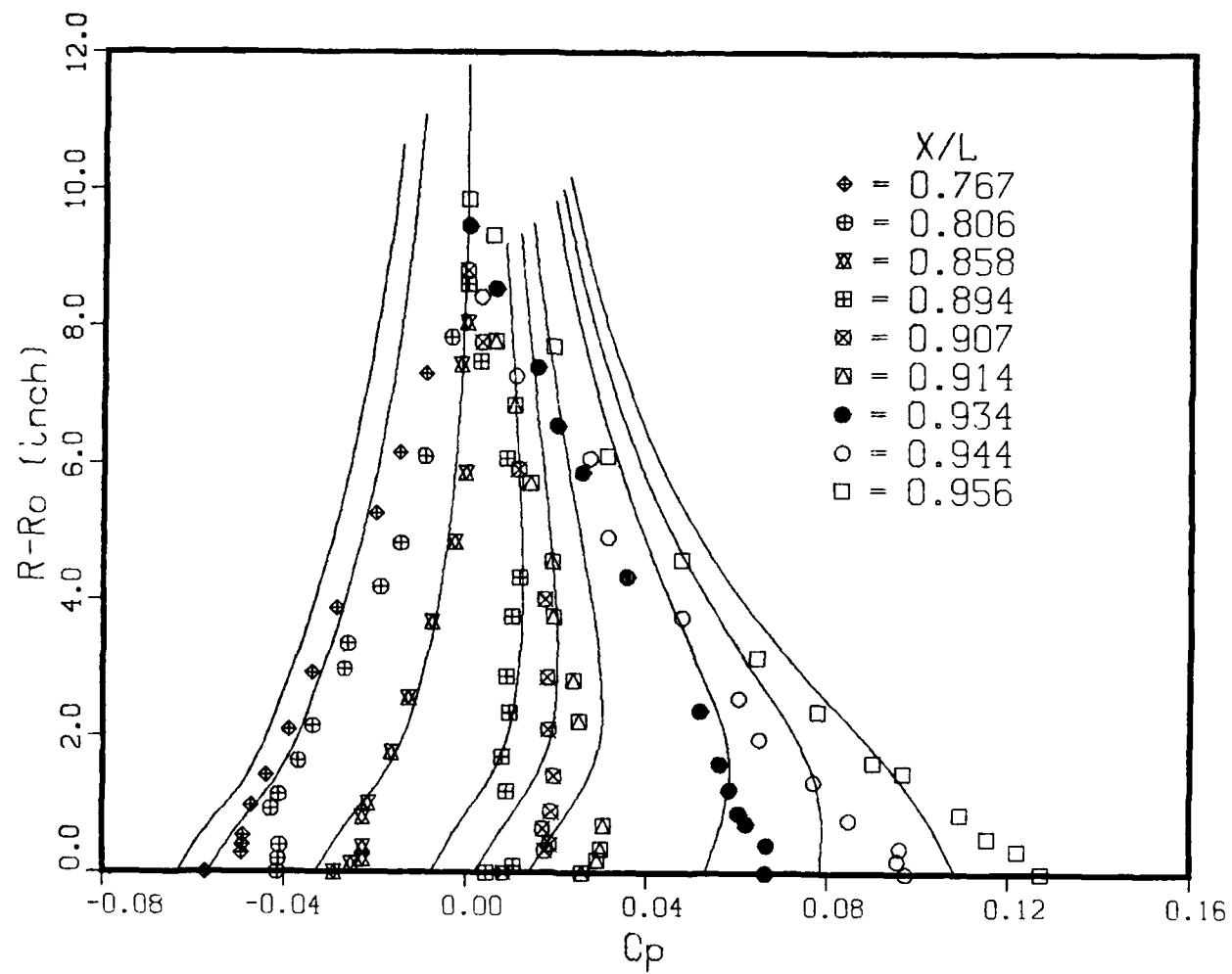
Fig. 50(a).   Details of the Radial Variation of Pressure
              Along θ = 0°

177
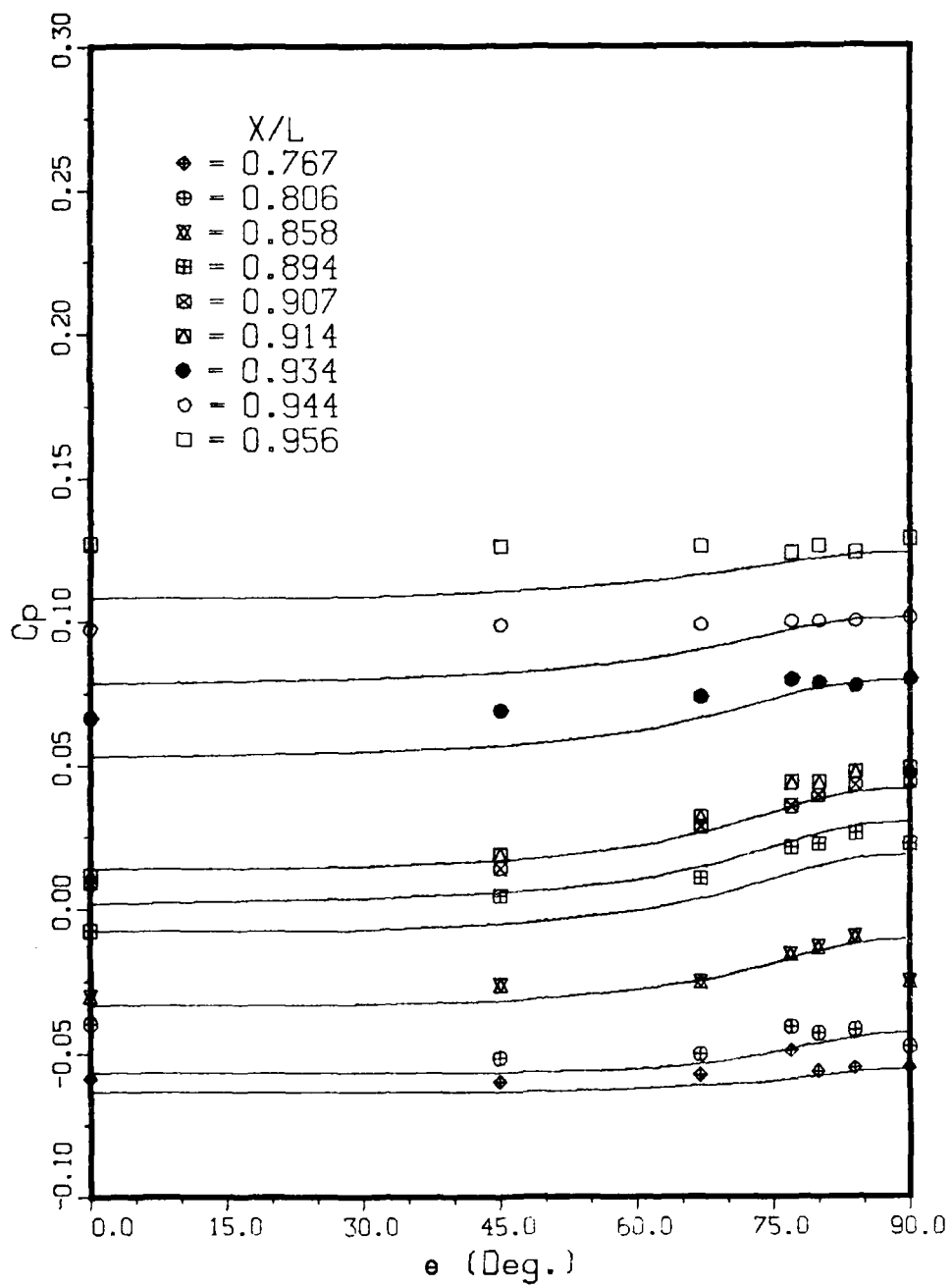
2:1 BODY

Fig. 51. Girthwise Distribution of Wall Pressure; 2:1 Body
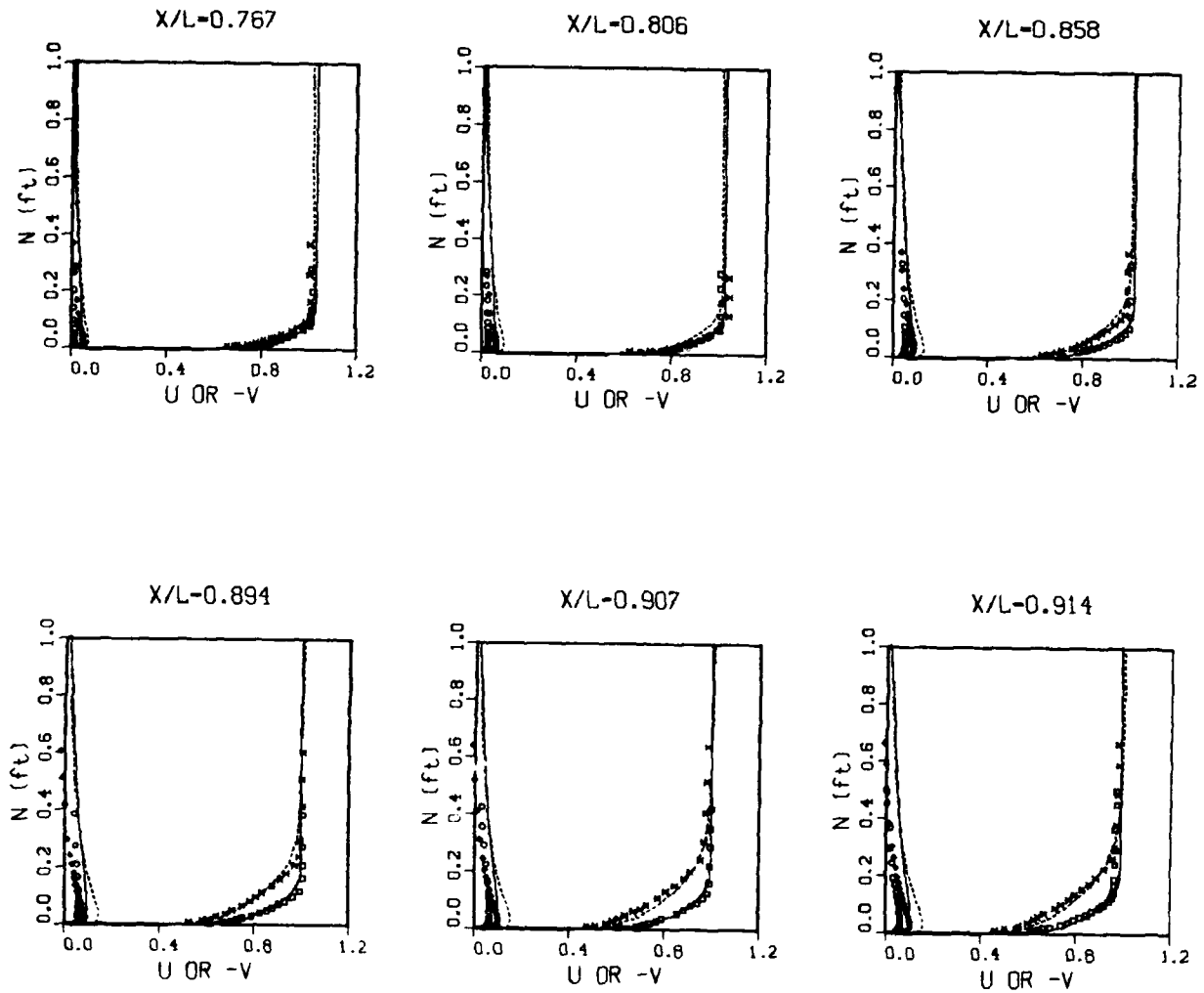
Fig. 52. Velocity Profiles in the Planes of Symmetry; 2:1 Body; Coarse Grid

180

Fig. 52. Continued

181
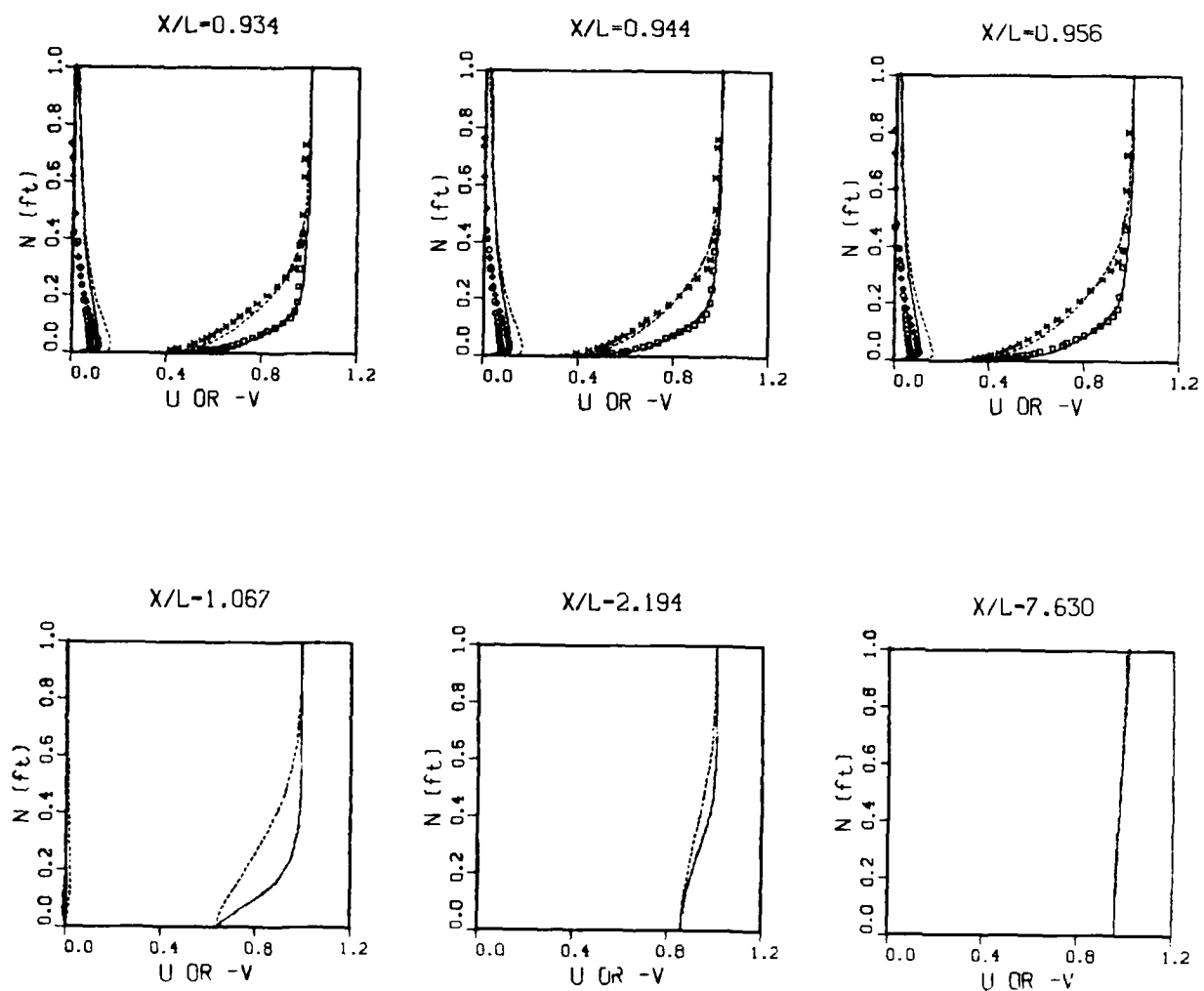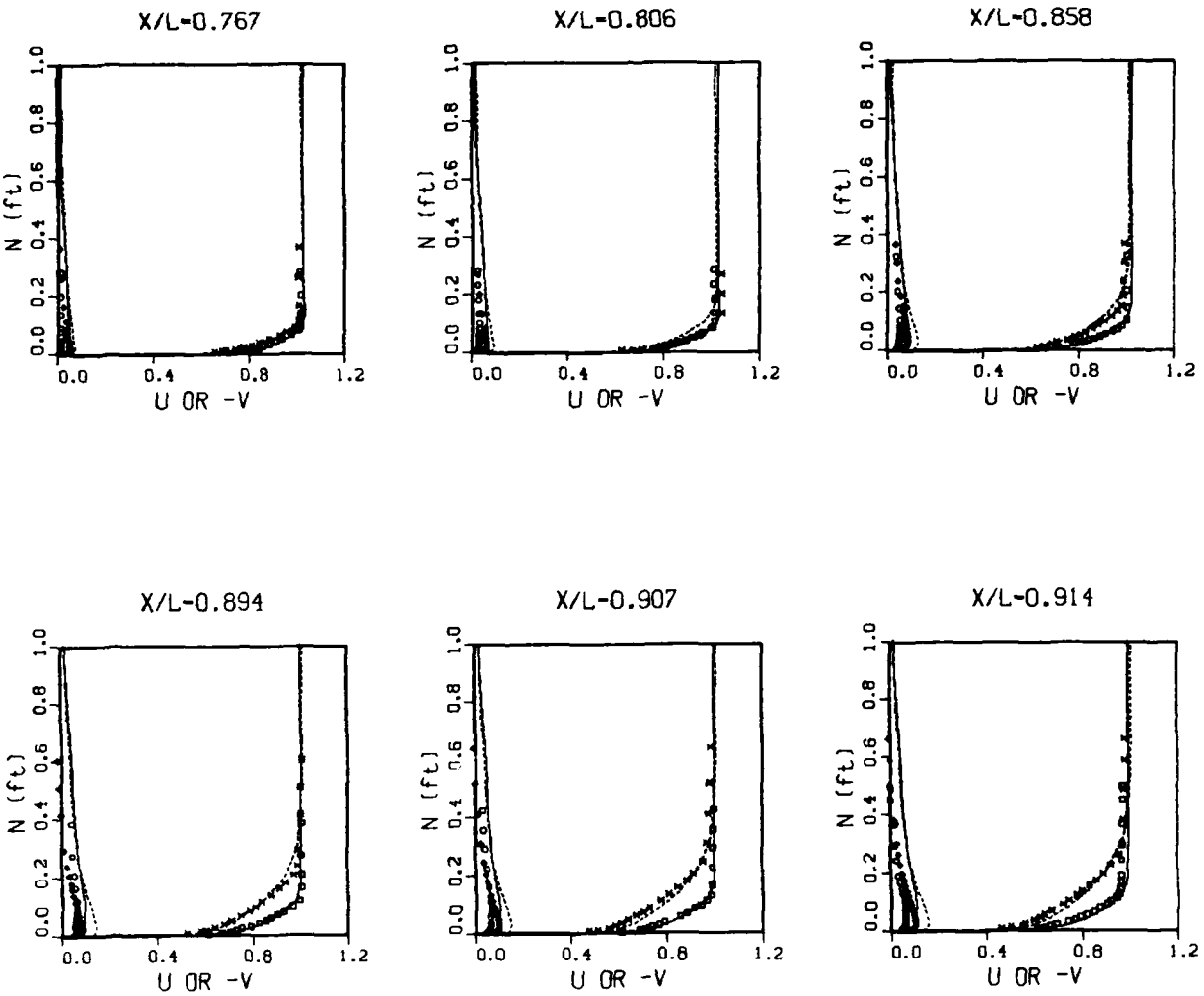
Fig. 53. Velocity Profiles in the Planes of Symmetry; 2:1 Body;
Finer Grid.

X/L=0.934   X/L=0.944   X/L=0.956

X/L-1.067   X/L-2.194   X/L-7.630
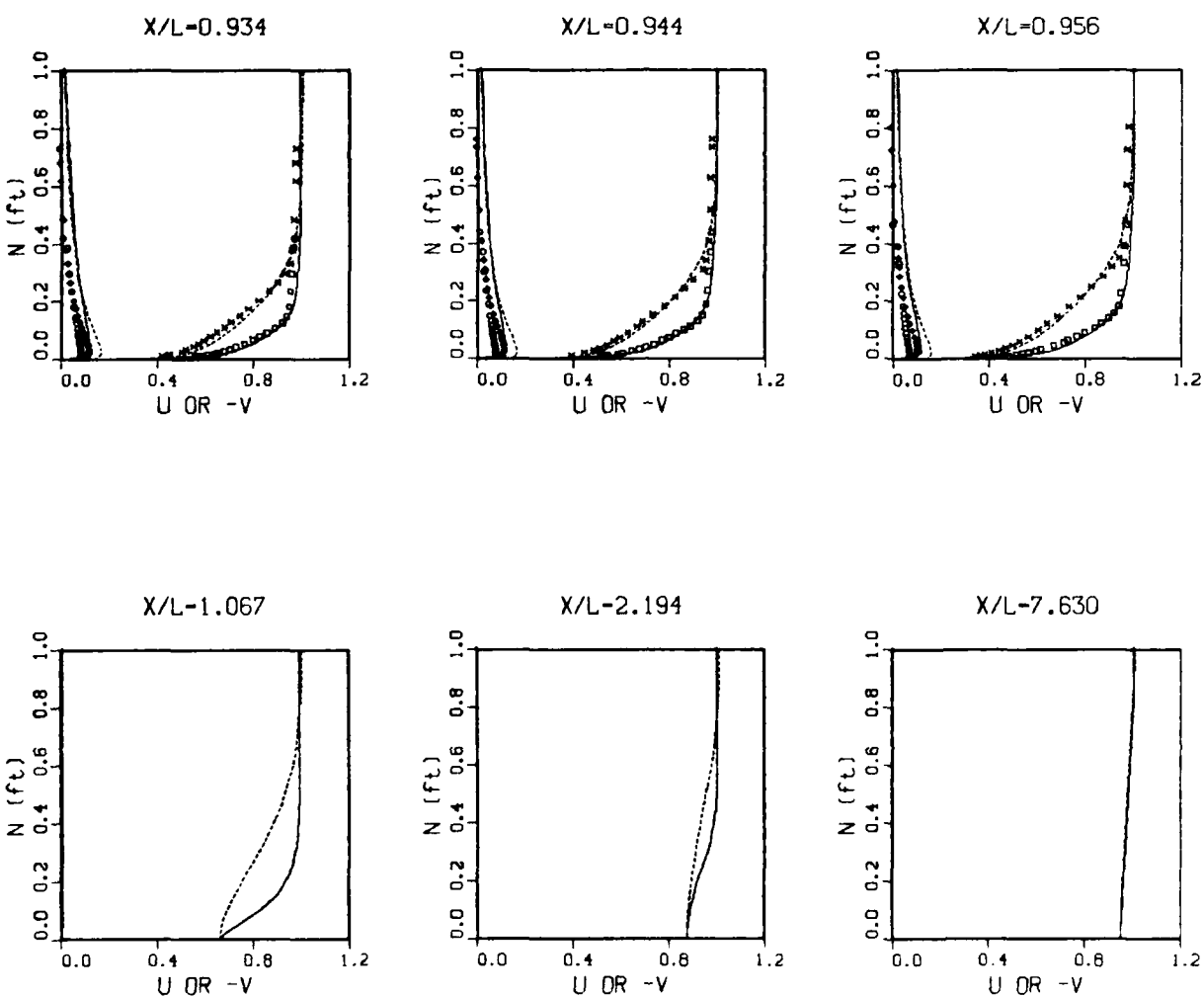
Fig. 53.   Continued
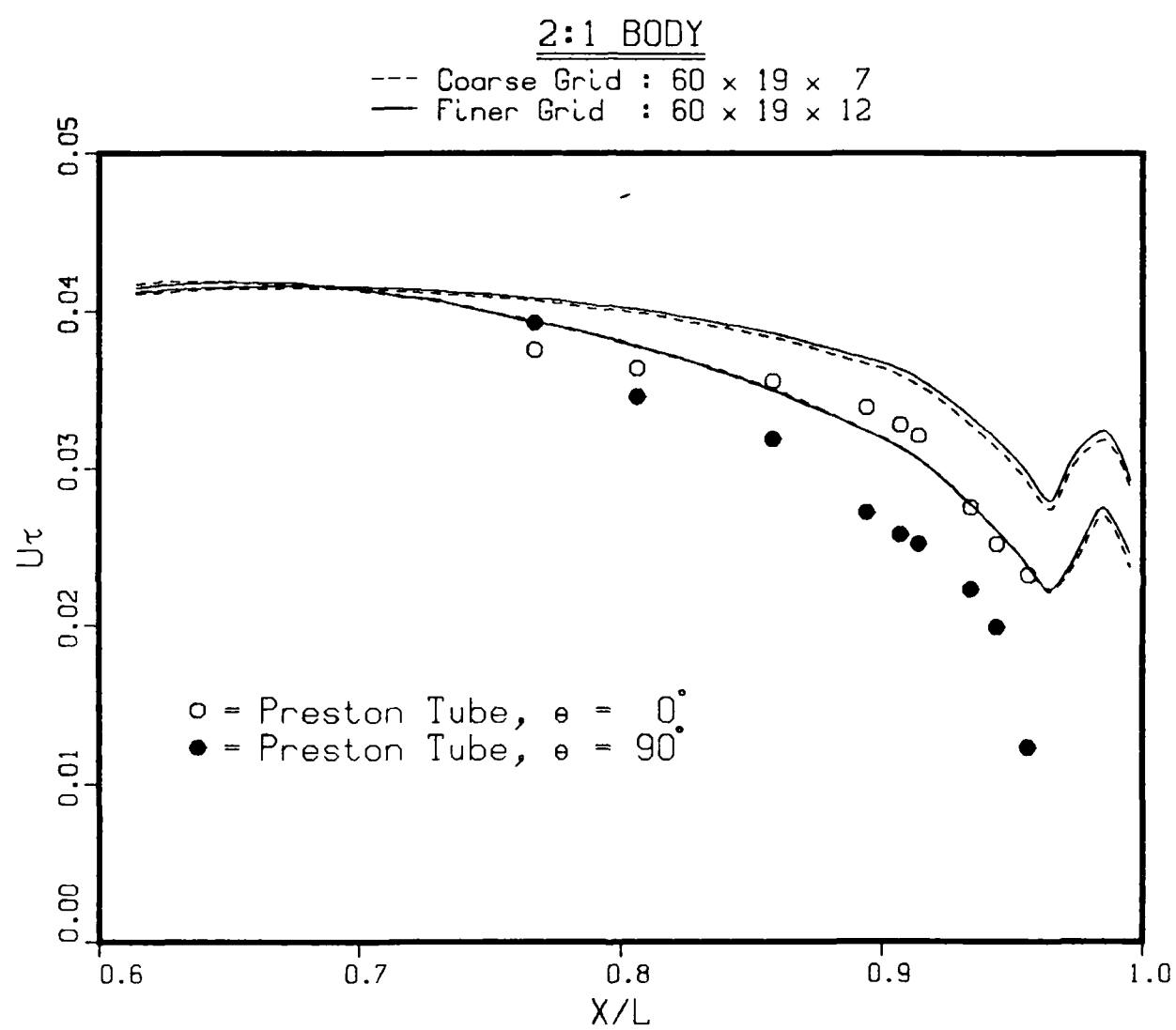
Fig. 54. **Comparison with Wall Shear Velocity Measured by Preston Tube**
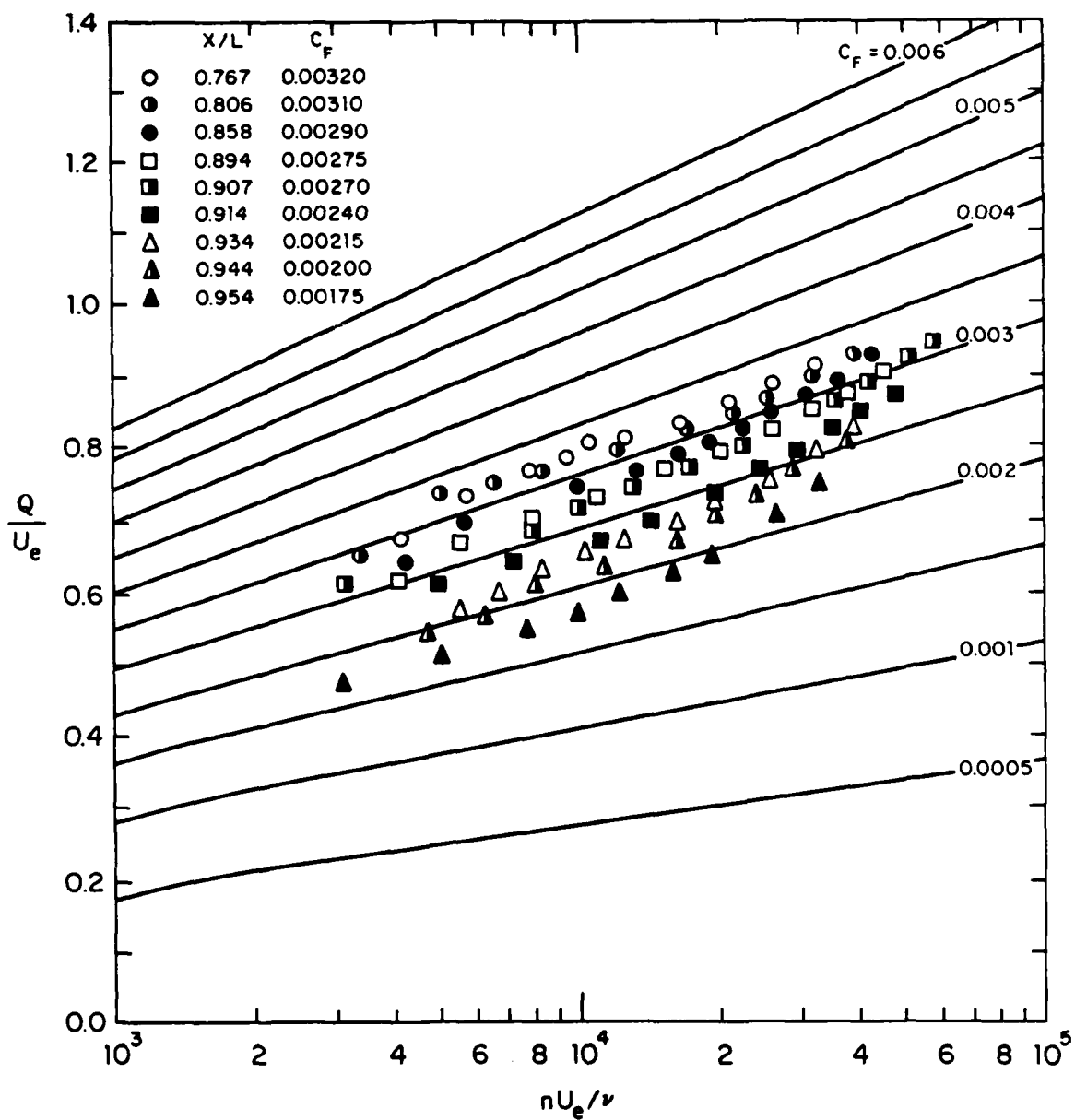
Fig. 55(a).   Clauser Plots of Measured Velocity Profiles, θ = 0°, 2:1 Body

Fig. 55(b).   Clauser Plots of Measured Velocity Profiles, θ = 90°, 2:1 Body

186
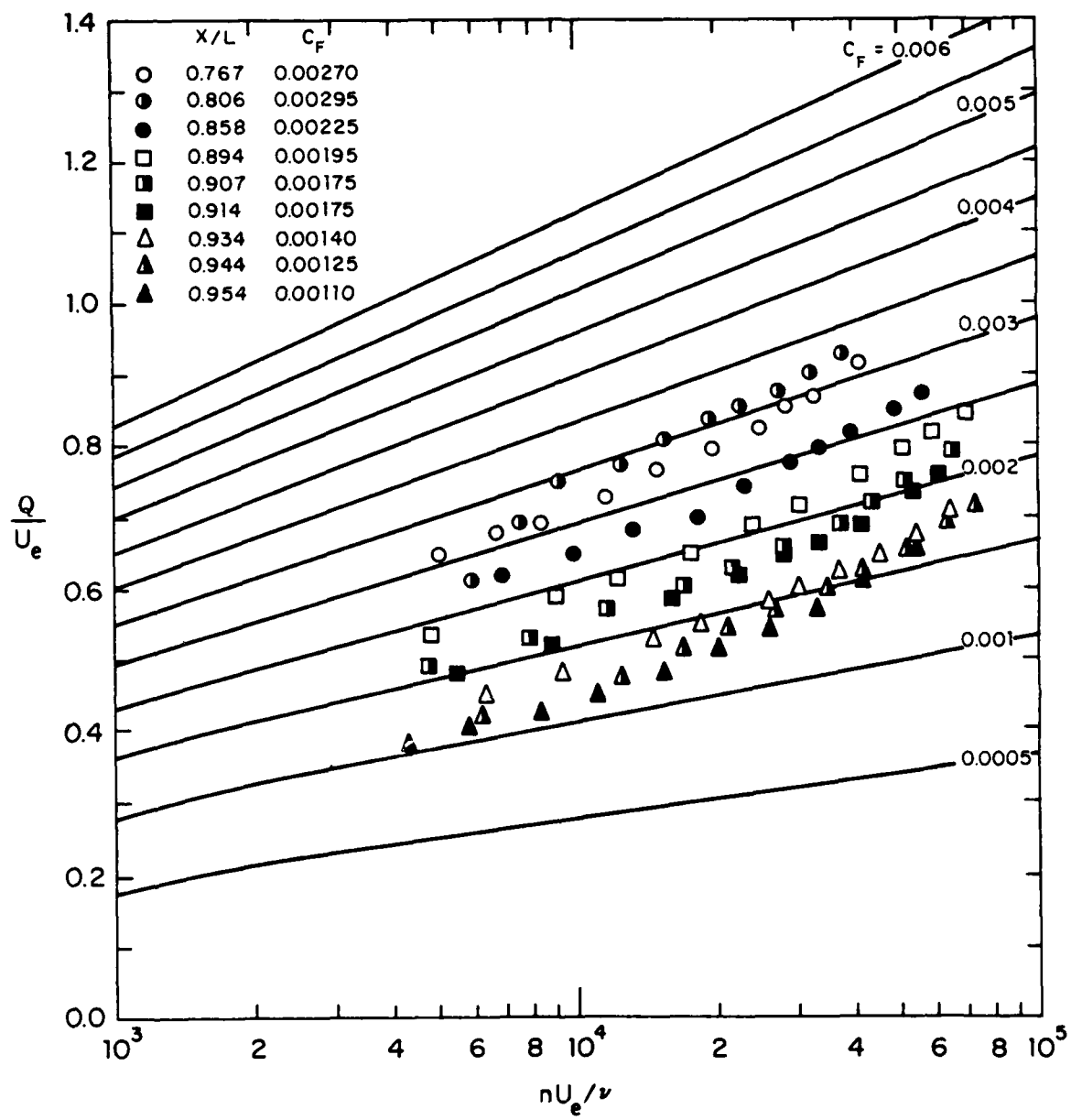
2:1 BODY
--- Coarse Grid : 60 × 19 × 7
— Finer Grid : 60 × 19 × 12

o = Clauser Plot, θ = 0°
● = Clauser Plot, θ = 90°
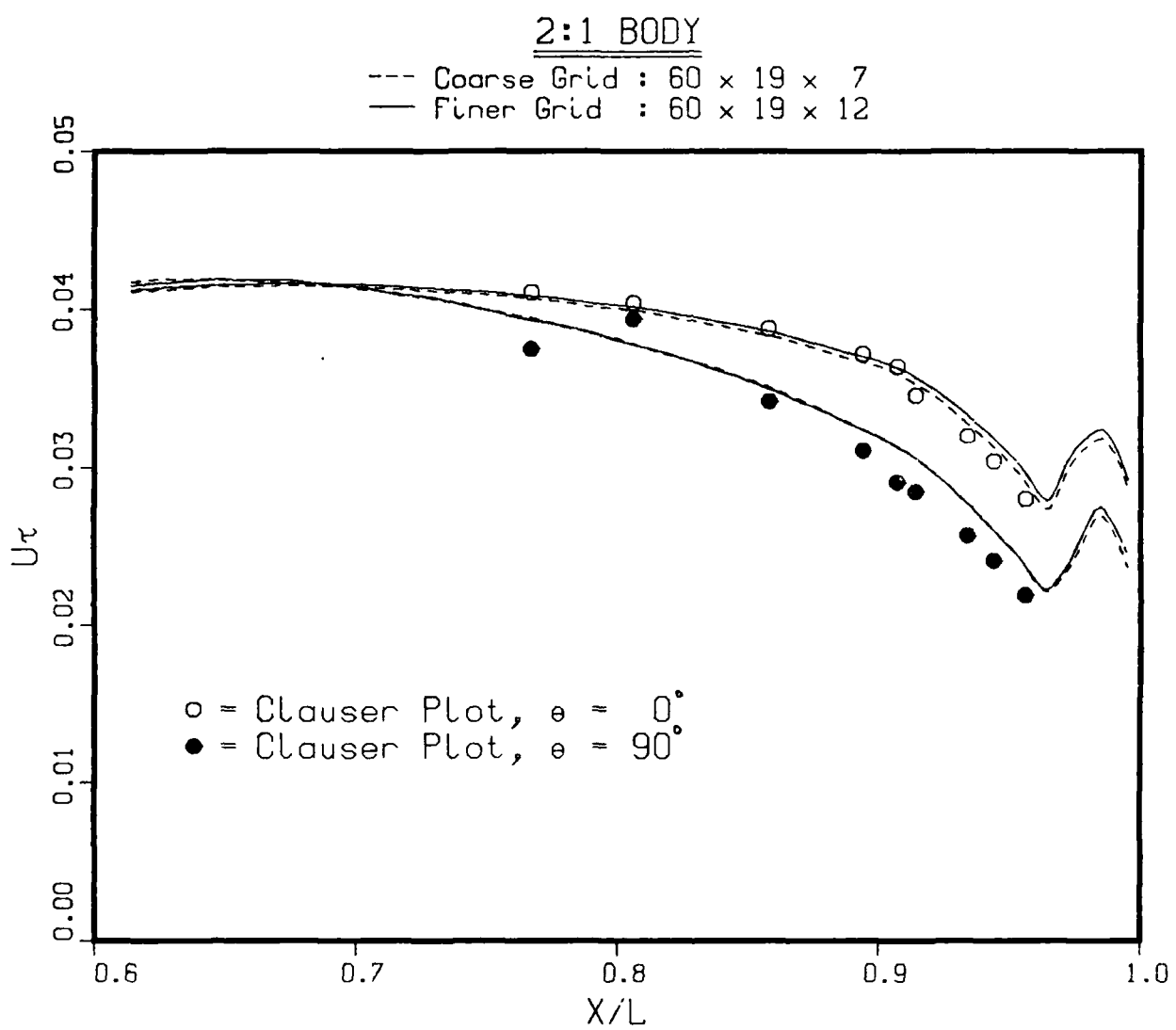
Fig. 56. Comparison with Wall Shear Velocity Evaluated from Clauser Plots

187
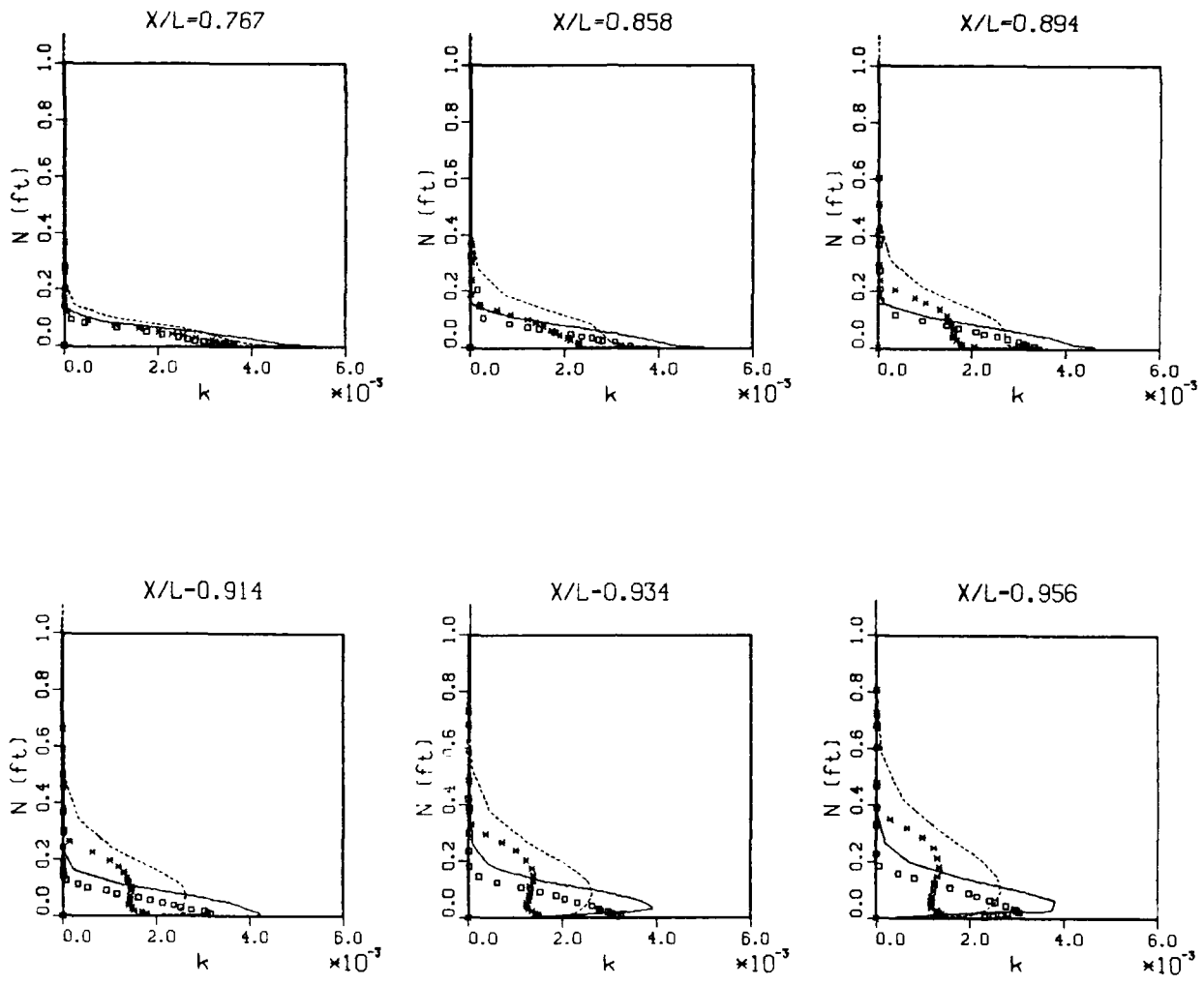
Fig. 57. Profiles of Turbulent Kinetic-Energy Along $\theta = 0°$ and $90°$; 2:1 Body

X/L=0.8082

Velocity Scale : Uo = 0.05
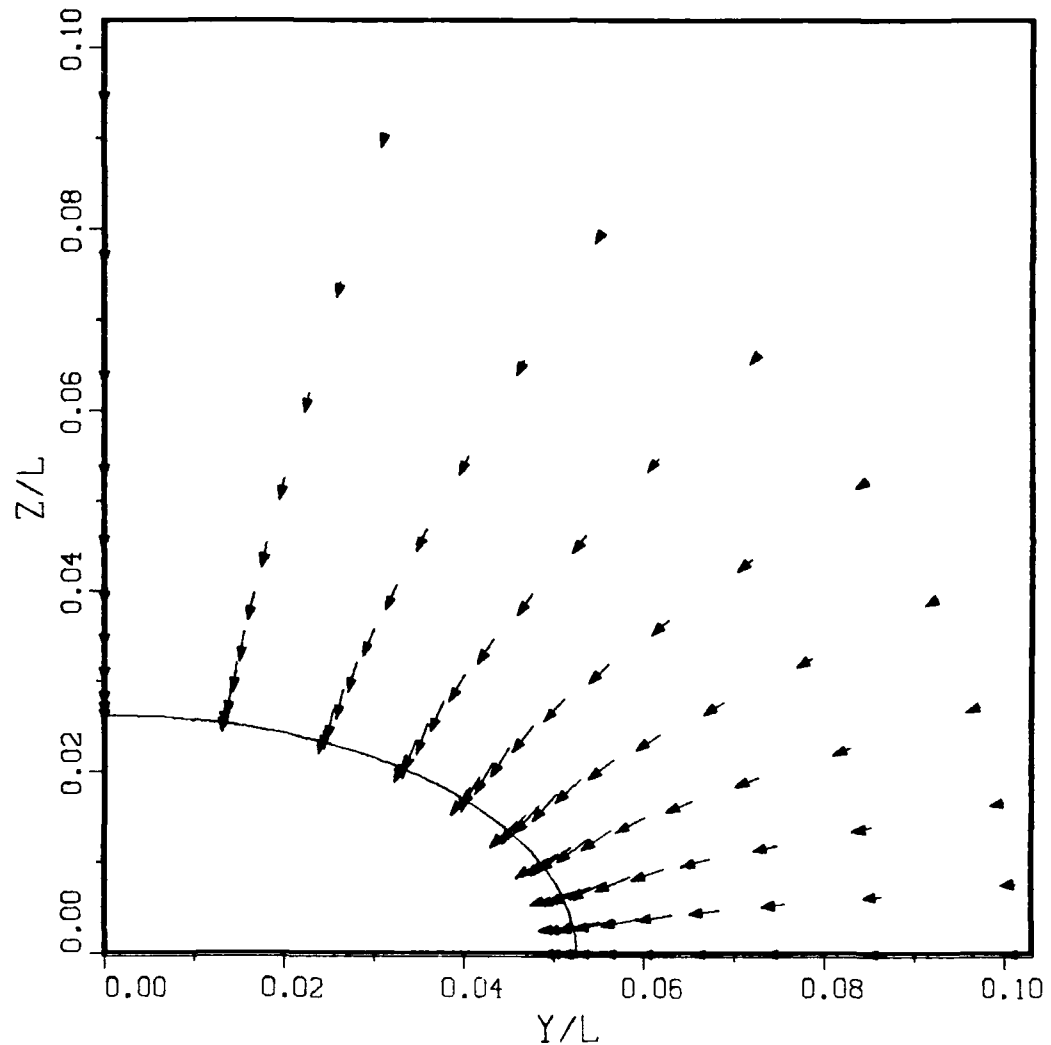
Fig. 58.   Projection of the Velocity Vectors in the Cross-
           Section; 2:1 Body
           (a) X/L = 0.8082

X/L=0.8533

Velocity Scale : Uo = 0.05
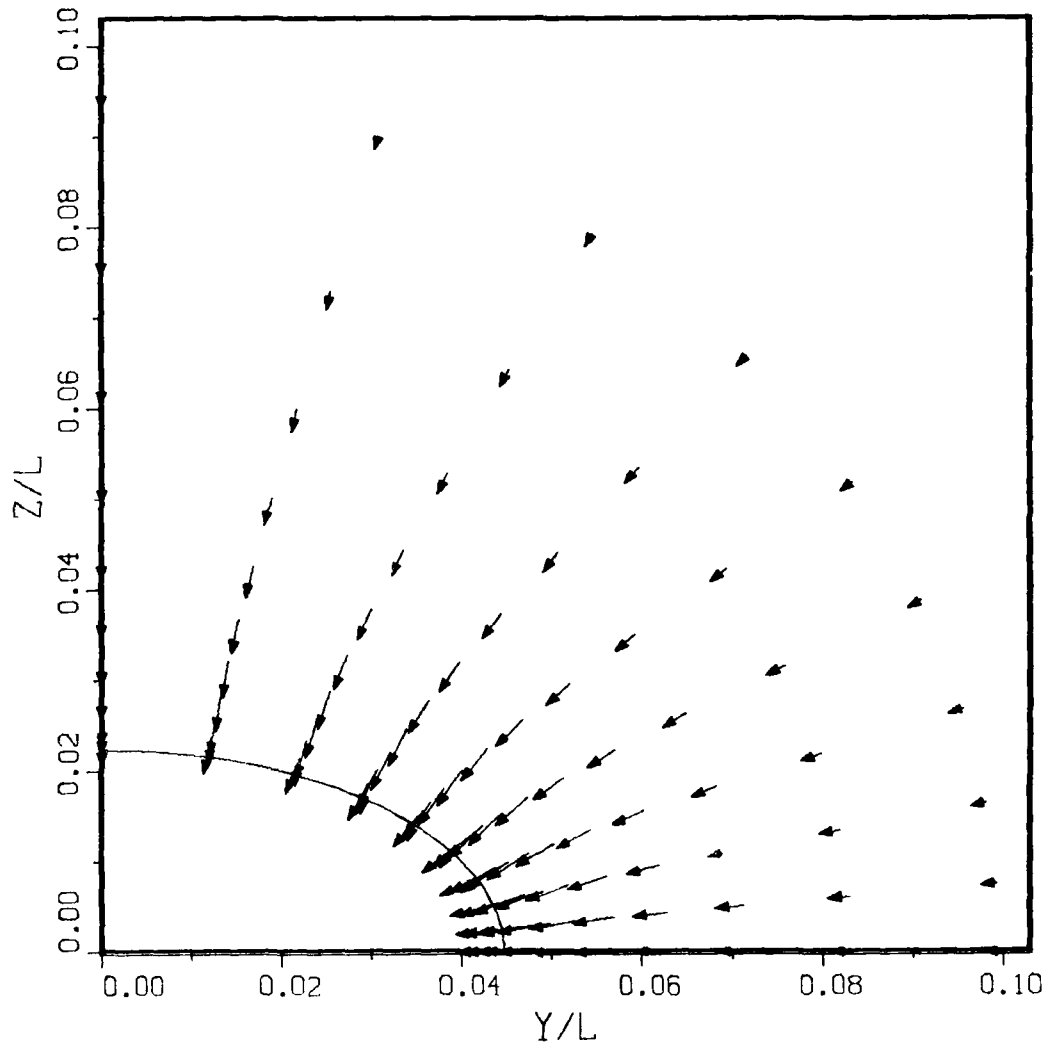
Fig. 58.   Continued
           (b)   X/L = 0.8533

X/L=0.9385

Velocity Scale : Uo - 0.05
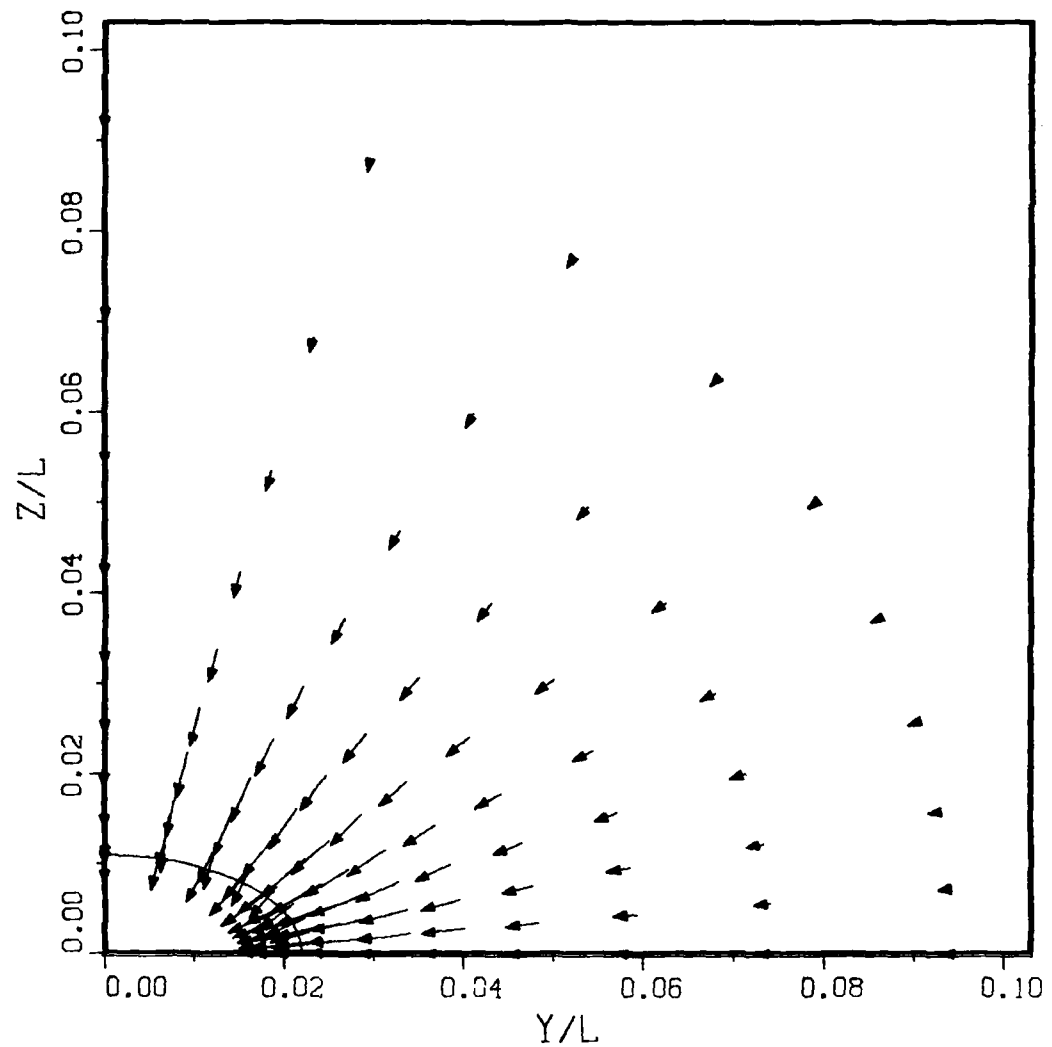
Fig. 58.   Continued
          (c)   X/L = 0.9385

191

X/L=0.9591

Velocity Scale : Uo = 0.05
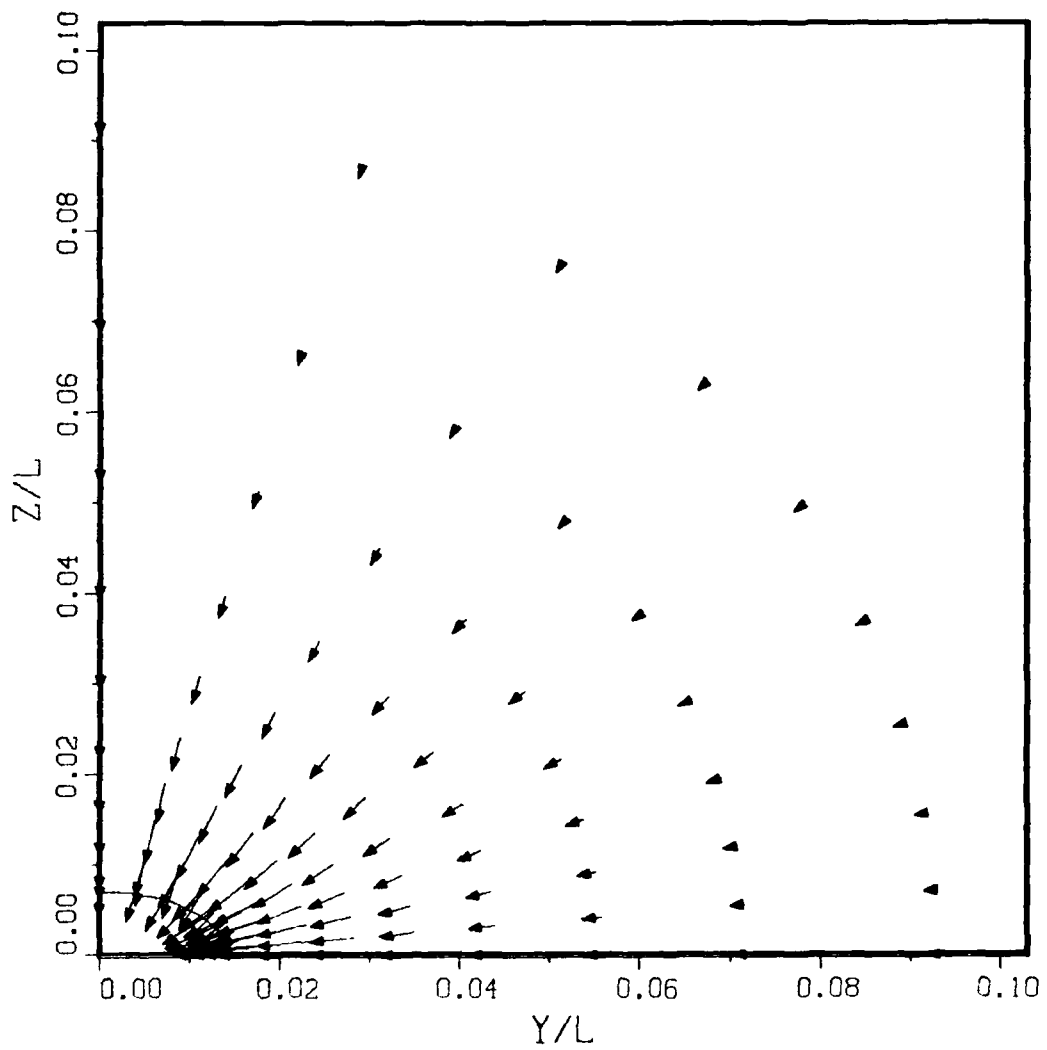
Fig. 58.   Continued
            (d)   X/L = 0.9591

192

X/L=0.9898

Velocity Scale : Uo = 0.05
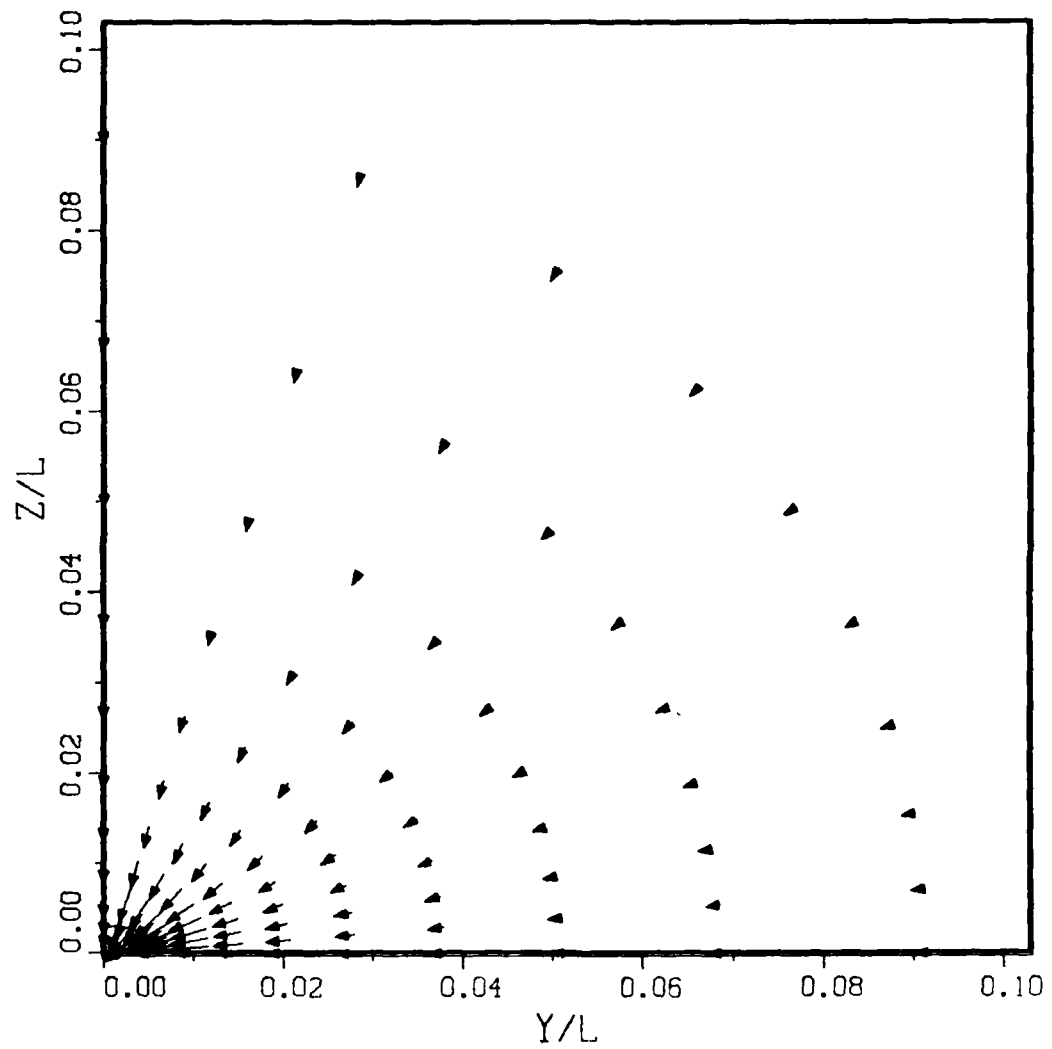
Fig. 58.   Continued
(e)   X/L = 0.9898

X/L=1.010

Velocity Scale : Uo = 0.05
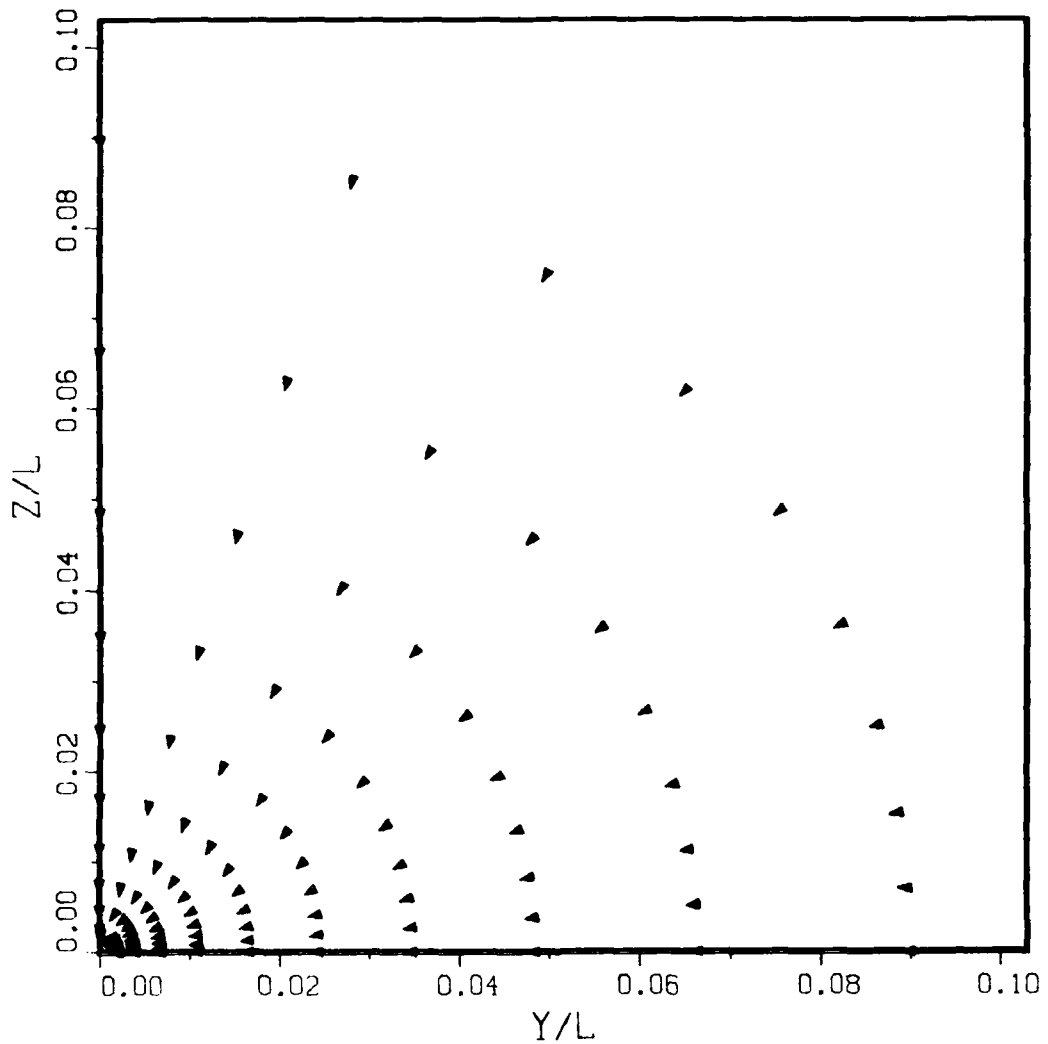
Fig. 58. Continued
         (f)   X/L = 1.010

194

X/L=1.082

Velocity Scale : Uo = 0.05
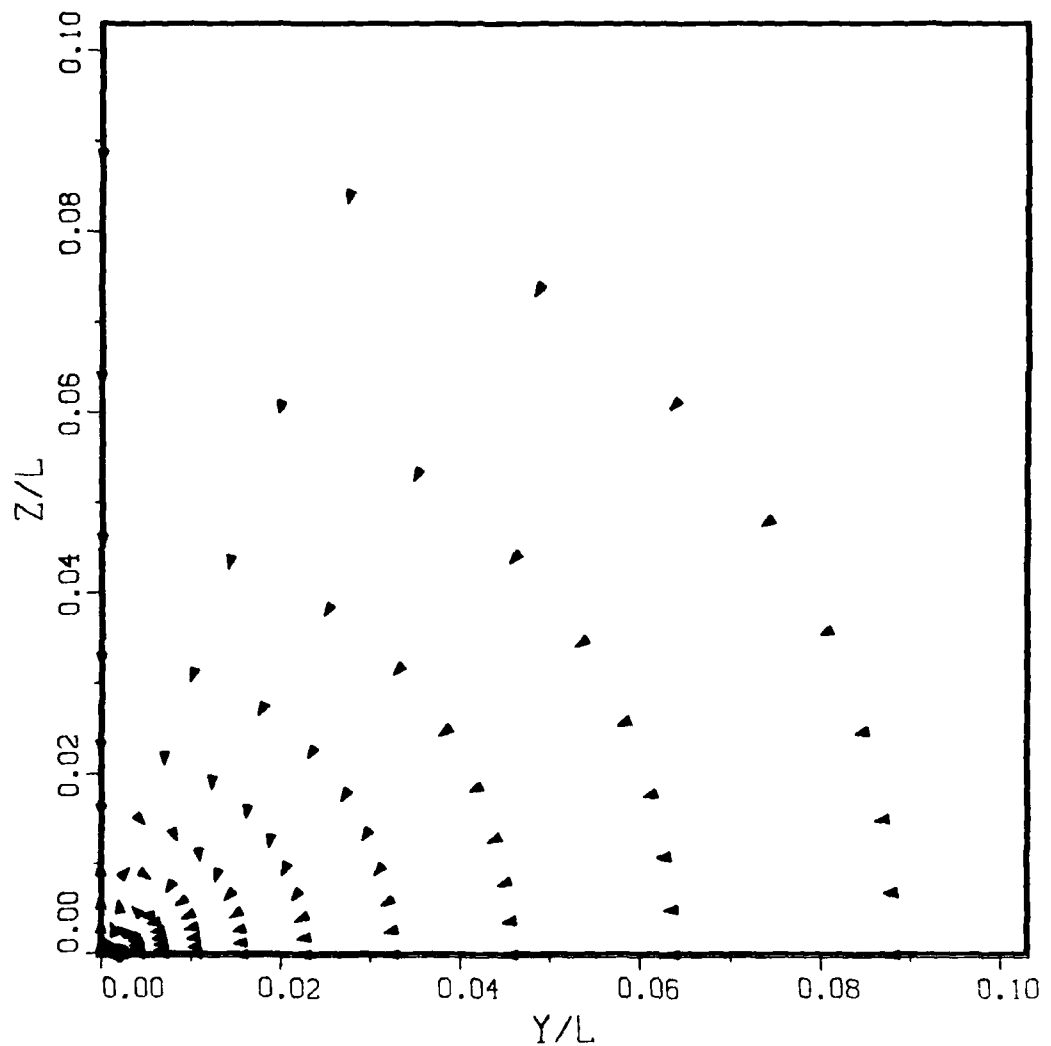
Fig. 58.   Continued
          (g)   X/L = 1.082

X/L=1.207

Velocity Scale : Uo = 0.05
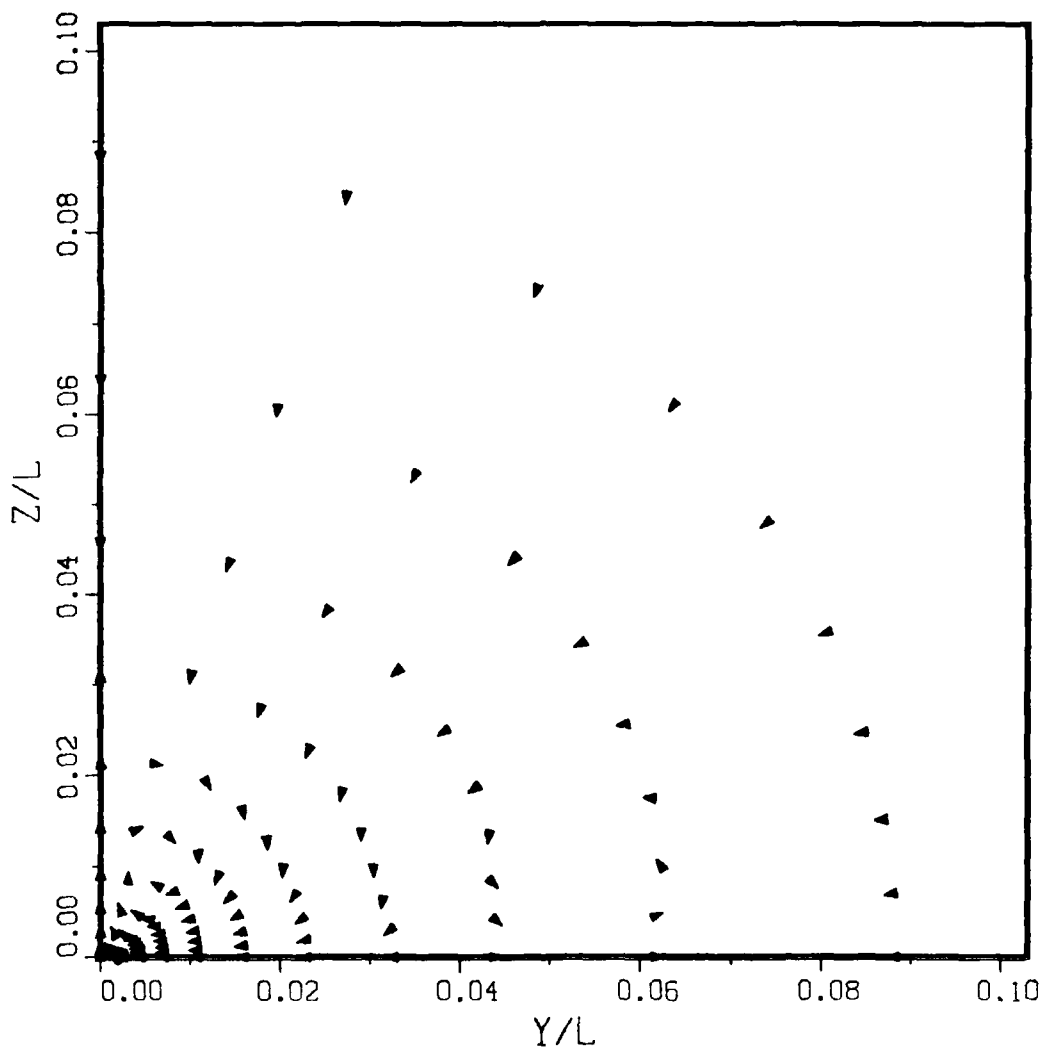
Fig. 58.   Continued
        (h)   X/L = 1.207

196

$X/L=5.756$

Velocity Scale : Uo - 0.05
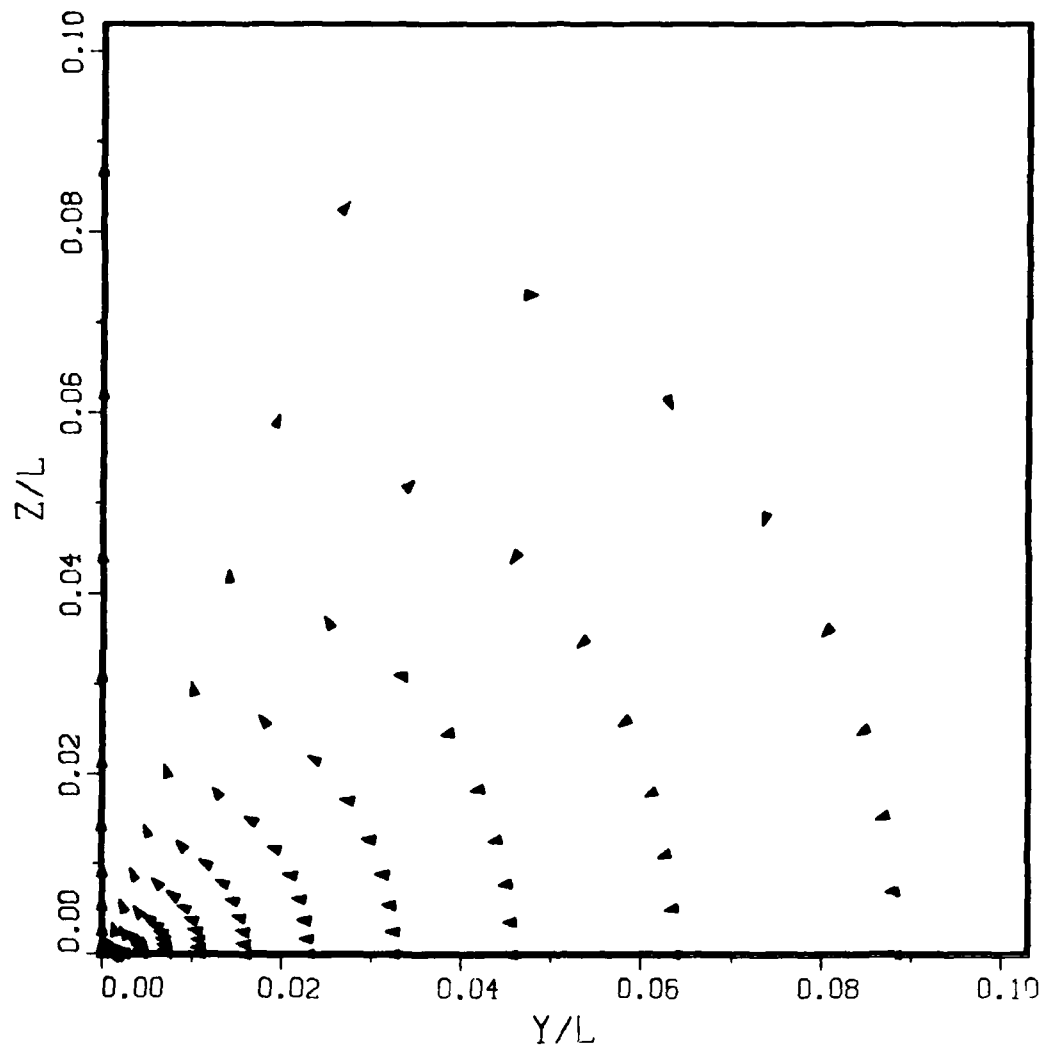
Fig. 58. Continued
(i)   X/L = 5.756

X/L=0.9591

Velocity Scale : Uo = 0.01
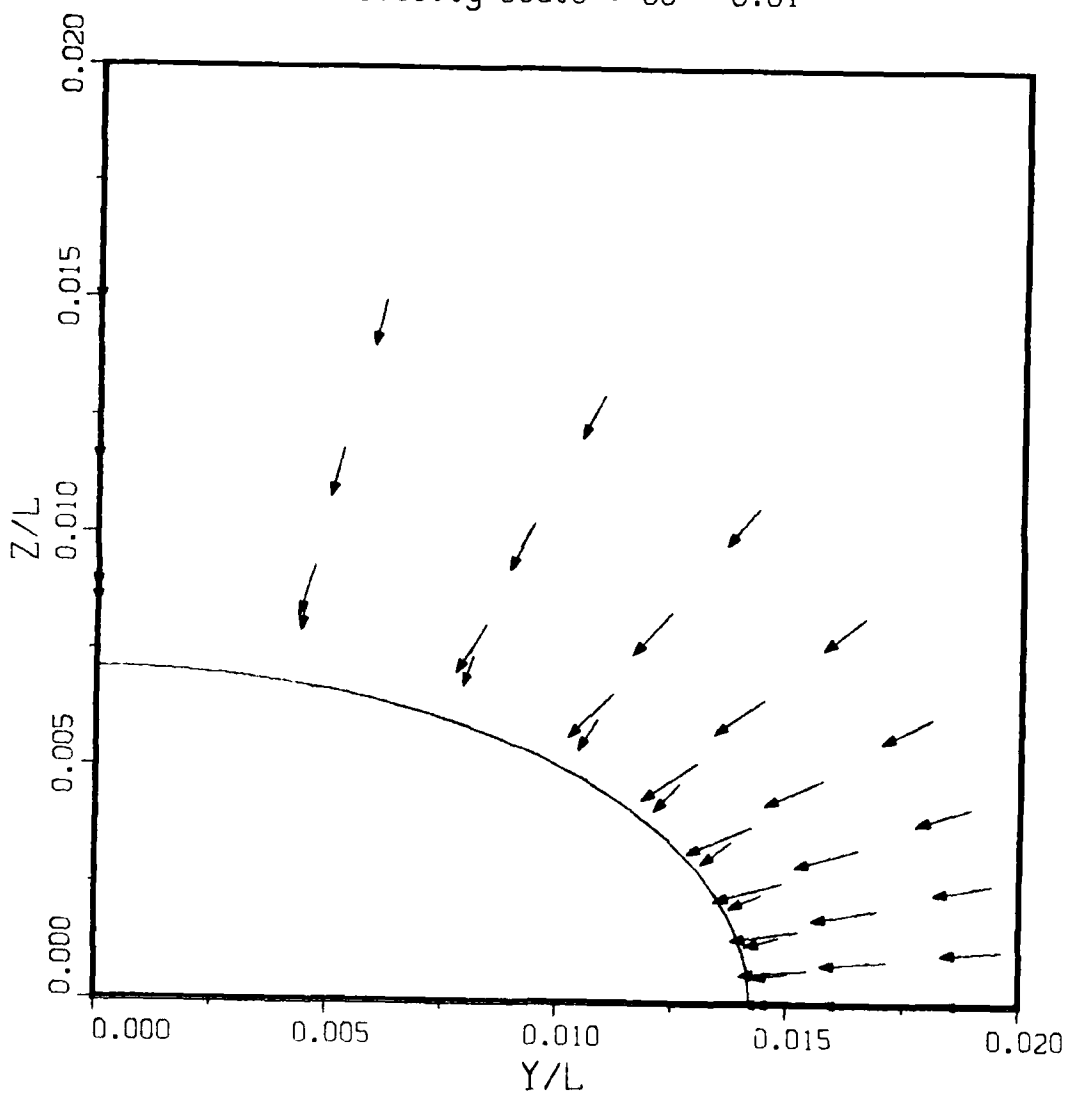
Fig. 59.   Enlarged View of Fig. 58
(a)   X/L = 0.9591

198

X/L=0.9898

Velocity Scale : Uo - 0.01
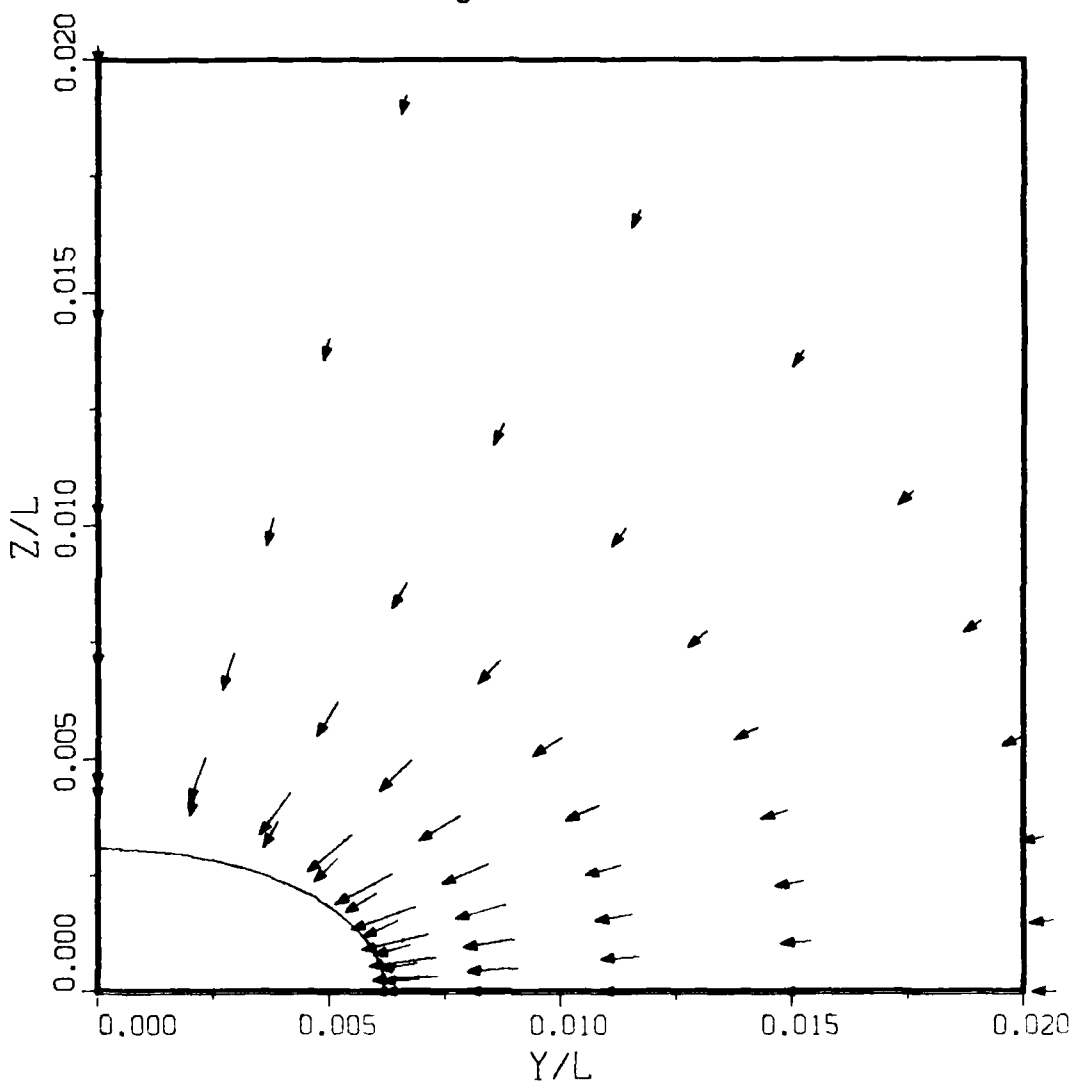
Fig. 59. Continued
(b) X/L = 0.9898

X/L=1.082

Velocity Scale : Uo ~ 0.5
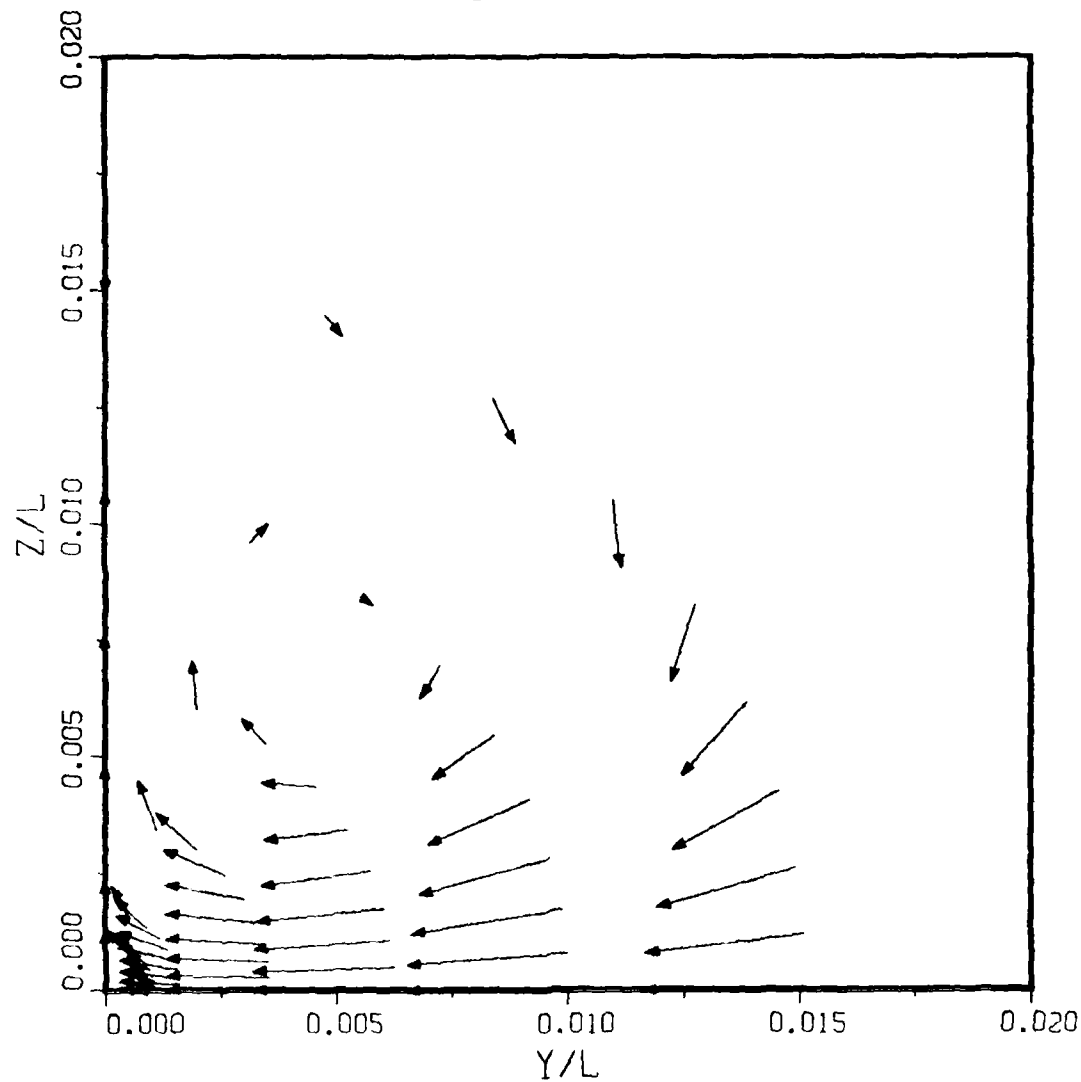
Fig. 59.   Continued
(c)   X/L = 1.082

$$X/L=1.207$$

Velocity Scale : Uo = 0.5
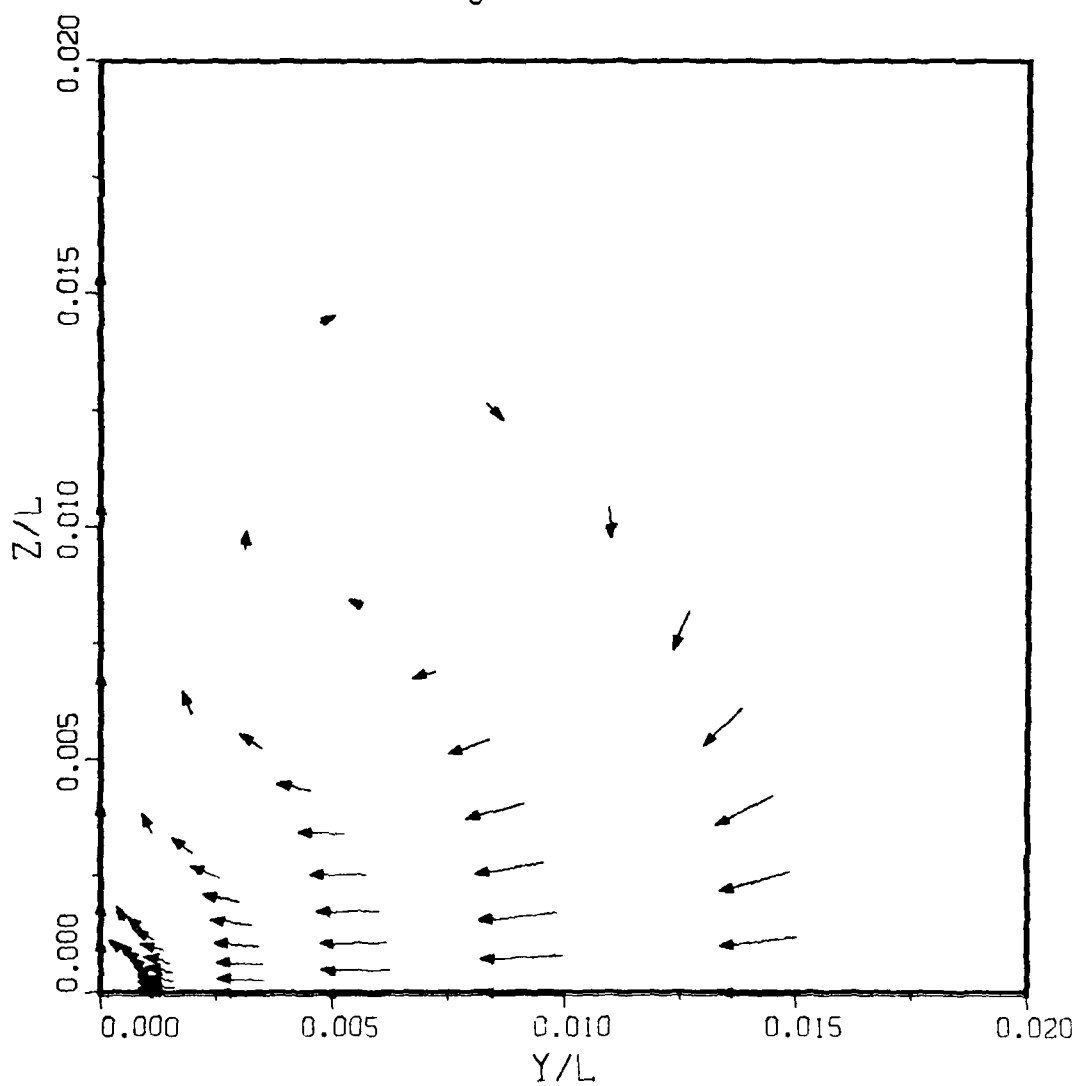
Fig. 59. Continued
(d) X/L = 1.207

201

X/L=5.756

Velocity Scale : Uo = 0.5
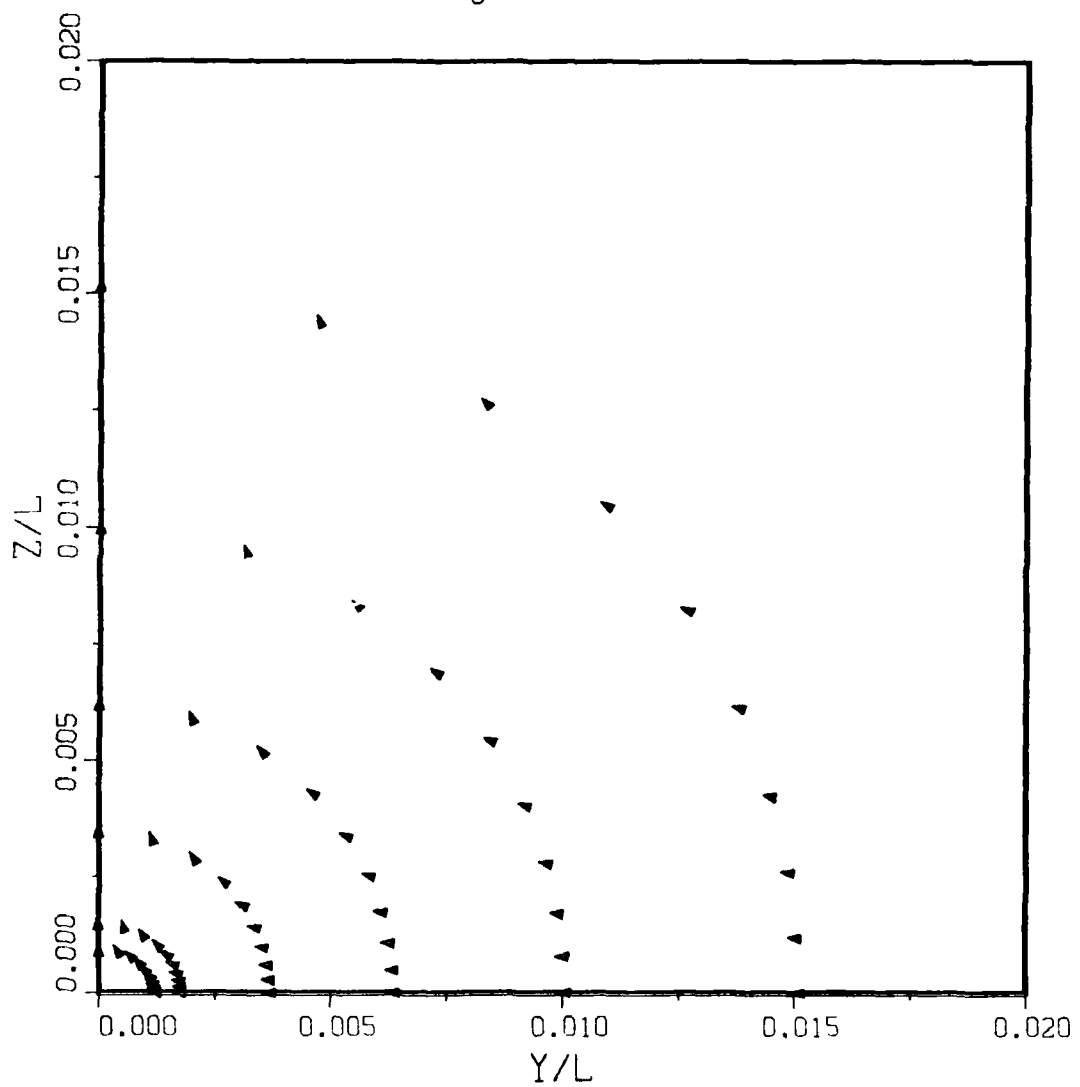
Fig. 59. Continued
(e) X/L = 5.756

APPENDIX I. COORDINATE TRANSFORMATIONS

This appendix summarizes the relationships between a basic orthogonal coordinate system x^i (x^1, x^2, x^3) and a general non-orthogonal system ξ^i (ξ^1, ξ^2, ξ^3). These relations are used in the text to invert the Poisson equations for numerical grid generation and to transform the Reynolds equations from cylindrical polar coordinates (x, r, θ) to the nonorthogonal numerical coordinates (ξ, η, ζ).

In the general coordinates ξ^i, any line element vector $d\underset{\sim}{r}$ is related to the differential change of coordinate $d\xi^i$ by

$$d\underset{\sim}{r} = \frac{\partial \underset{\sim}{r}}{\partial \xi^i} \, d\xi^i \qquad (A-1)$$

where $\underset{\sim}{r}$ is the position vector, and the expression is summed over the three values of i. It is convenient to define the derivative $\frac{\partial \underset{\sim}{r}}{\partial \xi^i}$ as a covariant base vector $\underset{\sim}{a}_i$, i.e.,

$$\underset{\sim}{a}_i = \frac{\partial \underset{\sim}{r}}{\partial \xi^i} \qquad (A-2)$$

so that the line element vector can be written

$$d\underset{\sim}{r} = d\xi^i \, \underset{\sim}{a}_i \qquad (A-3)$$

More generally, any vector $\underset{\sim}{A}$ other than a position vector $\underset{\sim}{r}$ can be decomposed in the same manner as

$$\underset{\sim}{A} = A^i \underset{\sim}{a}_i \qquad (A-4)$$

where A^i denote the contravariant components of vector $\underset{\sim}{A}$.

The reciprocal (contravariant) base vectors are defined by

$$\underset{\sim}{a}^i = \frac{\underset{\sim}{a}_j \times \underset{\sim}{a}_k}{J} \equiv \frac{1}{J} \, \varepsilon_{\ell mn} \, a_j^m \, a_k^n \qquad (A-5)$$

with i, j, k in cyclic order, so that

$$a^i \cdot a_j = a_j \cdot a^i = \delta^i_j \tag{A-6}$$

where the Kronecker delta δ^i_j is a mixed second-rank tensor defined by

$$\delta^i_j = \begin{cases} 1, & i = j \\ 0, & i \neq j \end{cases} \tag{A-7}$$

and J is the Jacobian defined by

$$J = a_i \cdot (a_j \times a_k) \tag{A-8}$$

Any vector $\underset{\sim}{A}$ can also be decomposed in terms of the contravariant base vectors a^i as

$$\underset{\sim}{A} = A_i \, a^i \tag{A-9}$$

where A_i are the covariant components of vector $\underset{\sim}{A}$. The covariant and contravariant base vectors are not usually of unit length, but a set of unit vectors tangent and normal to the coordinate lines can be defined as

$$\underset{\sim}{\tau}_i = \frac{a_i}{\left| a_i \right|} \tag{A-10a}$$

$$n^i = \frac{a^i}{\left| a^i \right|} \tag{A-10b}$$

respectively. The distance ds between any two points $\underset{\sim}{r}$ and $\underset{\sim}{r} + d\underset{\sim}{r}$ is given by

$$(ds)^2 = d\underset{\sim}{r} \cdot d\underset{\sim}{r} = (a_i \cdot a_j) \, d\xi^i d\xi^j \tag{A-11}$$

$$\equiv g_{ij} d\xi^i d\xi^j$$

where

AI-2

$$g_{ij} \equiv \underset{\sim}{a}_i \cdot \underset{\sim}{a}_j \qquad (A-12)$$

is the "metric tensor". It is clear from this definition that $g_{ij} = g_{ji}$ in any coordinate system. A conjugate (contravariant) metric tensor g^{ij} can be defined in a similar manner,

$$g^{ij} = g^{ji} \equiv \underset{\sim}{a}^i \cdot \underset{\sim}{a}^j \qquad (A-13)$$

and is related to the metric tensor g_{ij} through equation (A-6) by

$$g^{ik}g_{kj} = g_{jk}g^{ki} = \delta^i_j \qquad (A-14)$$

In other words, the components of the conjugate metric tensor g^{ij} are the inverse of those of g_{ij}. Using these equations, a covariant component A_i can be converted into a contravariant component A^i by the relation

$$A_i = g_{ij} A^j \qquad (A-15)$$

and vice versa, i.e.,

$$A^i = g^{ij} A_j \qquad (A-16)$$

Also, the contravariant base vectors $\underset{\sim}{a}^i$ are related to the covariant base vectors $\underset{\sim}{a}_i$ by

$$\underset{\sim}{a}_i = g_{ij} \underset{\sim}{a}^i \qquad (A-17)$$

and

$$\underset{\sim}{a}^i = g^{ij} \underset{\sim}{a}_j \qquad (A-18)$$

Finally, we note that neither A^i nor A_j represent the physical components of the vector $\underset{\sim}{A}$. If the physical components are denoted by A(i), they are given by

$$A(i) = (g_{ii})^{1/2} A^i = (g_{ii})^{1/2} g^{ij} A_j \qquad \text{(no sum on i)} \qquad \text{(A-19)}$$

Now, <u>in the orthogonal coordinates x^i</u>, any vector $\underset{\sim}{A}$ can be expressed as

$$\underset{\sim}{A} = E^i \underset{\sim}{e}_i = E_i \underset{\sim}{e}^i \qquad \text{(A-20)}$$

where E^i and E_i are, respectively, the contravariant and covariant components of $\underset{\sim}{A}$, $\underset{\sim}{e}_i$ are the covariant base vectors given by

$$\underset{\sim}{e}_i = \frac{\partial \underset{\sim}{r}}{\partial x^i} = (h_1 \delta_i^1, \ h_2 \delta_i^2, \ h_3 \delta_i^3) \qquad \text{(A-21)}$$

and $\underset{\sim}{e}^i$ are the contravariant (conjugate) base vectors defined by

$$\underset{\sim}{e}^i = (\frac{1}{h_1} \delta_1^i, \ \frac{1}{h_2} \delta_2^i, \ \frac{1}{h_3} \delta_3^i) \qquad \text{(A-22)}$$

such that

$$\underset{\sim}{e}^i \cdot \underset{\sim}{e}_j = \underset{\sim}{e}_j \cdot \underset{\sim}{e}^i = \delta_j^i \qquad \text{(A-23)}$$

where h_1, h_2 and h_3 are the usual metric coefficients or scale factors given by

$$(ds)^2 = (h_1 dx^1)^2 + (h_2 dx^2)^2 + (h_3 dx^3)^2 \qquad \text{(A-24)}$$

$$\equiv h_{ij} \ dx^i dx^j$$

The metric tensor h_{ij} can also be obtained from the following relation

$$h_{ij} = \underset{\sim}{e}_i \cdot \underset{\sim}{e}_j = \sum_{\ell=1}^{3} h_\ell^2 \delta_i^\ell \delta_j^\ell = h_i^2 \delta_j^i \qquad \text{(A-25)}$$

or

$$(h_{ij}) = \begin{pmatrix} h_1^2 & 0 & 0 \\ 0 & h_2^2 & 0 \\ 0 & 0 & h_3^2 \end{pmatrix} \qquad \text{(A-25a)}$$

Similarly, the conjugate metric tensor h^{ij} in the orthogonal co-ordinates is

$$h^{ij} = \underset{\sim}{e}^i \cdot \underset{\sim}{e}^j = \sum_{\ell=1}^{3} \frac{1}{h_\ell^2} \delta_\ell^i \delta_\ell^j = \frac{1}{h_j^2} \delta_j^i \qquad \text{(A-26)}$$

or

$$(h^{ij}) = \begin{pmatrix} \dfrac{1}{h_1^2} & 0 & 0 \\ 0 & \dfrac{1}{h_2^2} & 0 \\ 0 & 0 & \dfrac{1}{h_3^2} \end{pmatrix} \qquad \text{(A-26a)}$$

As before, the physical components $E(i)$ of any vector $\underset{\sim}{A}$ in the orthogonal coordinates are given by

$$E(i) = h_i E^i = \frac{1}{h_i} E_i \quad \text{(no sum on i)} \qquad \text{(A-27)}$$

Since the equations of fluid flow are usually written in orthogonal coordinate systems x^i, it is desirable to establish the transformations between the basic x^i system and the general nonorthogonal system ξ^i. From equations (A-3) and (A-20), the line element vector $d\underset{\sim}{r}$ in the two systems is given by

$$d\underset{\sim}{r} = dx^j \underset{\sim}{e}_j = d\xi^i \underset{\sim}{a}_i \qquad \text{(A-28)}$$

Since

$$dx^j = \frac{\partial x^j}{\partial \xi^i} d\zeta^i \qquad \text{(A-29)}$$

the covariant vector $\underset{\sim}{a}_i$ in ξ^i coordinates is related to $\underset{\sim}{e}_j$ (equation A-21) by

$$\underset{\sim}{a}_i = \frac{\partial x^j}{\partial \xi^i} \, \underset{\sim}{e}_j = (h_1 \, \frac{\partial x^1}{\partial \xi^i} \, , \, h_2 \, \frac{\partial x^2}{\partial \xi^i} \, , \, h_3 \, \frac{\partial x^3}{\partial \xi^i}) \qquad \text{(A-30)}$$

If the ℓth component of $\underset{\sim}{a}_i$ is denoted by a_i^ℓ, a second rank mixed tensor can be defined as

$$a_i^\ell = (\underset{\sim}{a}_i)^\ell = h_\ell \, \frac{\partial x^\ell}{\partial \xi^i} \qquad \text{(A-31)}$$

or

$$(a_i^\ell) = \begin{pmatrix} a_1^1 & a_2^1 & a_3^1 \\[2mm] a_1^2 & a_2^2 & a_3^2 \\[2mm] a_1^3 & a_2^3 & a_3^3 \end{pmatrix} = \begin{pmatrix} h_1 \, \dfrac{\partial x^1}{\partial \xi^1} & h_1 \, \dfrac{\partial x^1}{\partial \xi^2} & h_1 \, \dfrac{\partial x^1}{\partial \xi^3} \\[3mm] h_2 \, \dfrac{\partial x^2}{\partial \xi^1} & h_2 \, \dfrac{\partial x^2}{\partial \xi^2} & h_2 \, \dfrac{\partial x^2}{\partial \xi^3} \\[3mm] h_3 \, \dfrac{\partial x^3}{\partial \xi^1} & h_3 \, \dfrac{\partial x^3}{\partial \xi^2} & h_3 \, \dfrac{\partial x^3}{\partial \xi^3} \end{pmatrix} \qquad \text{(A-32)}$$

The components of the reciprocal (contravariant) base vector $\underset{\sim}{a}^i$ are given by

$$\underset{\sim}{a}^i = (\frac{1}{h_1} \, \frac{\partial \xi^i}{\partial x^1} \, , \, \frac{1}{h_2} \, \frac{\partial \xi^i}{\partial x^2} \, , \, \frac{1}{h_3} \, \frac{\partial \xi^i}{\partial x^3}) \qquad \text{(A-33)}$$

or by equation (A-5), i.e.

$$\underset{\sim}{a}^i = \frac{1}{J} \, (\underset{\sim}{a}_j \times \underset{\sim}{a}_k) = \frac{1}{J} \, \varepsilon_{\ell mn} \, a_j^m \, a_k^n$$

with (i, j, k) in cyclic order.

For convenience, we shall define

$$\underset{\sim}{b}^i = \underset{\sim}{a}_j \times \underset{\sim}{a}_k = J \, \underset{\sim}{a}^i \qquad \text{(A-34)}$$

so that b_ℓ^i, the ℓth component of $J \, \underset{\sim}{a}^i$, using equation (A-30), is

$$b_\ell^i = (\underset{\sim}{a}_j \times \underset{\sim}{a}_k)_\ell = \varepsilon_{\ell mn} \, a_j^m \, a_k^n = h_m h_n \left(\frac{\partial x^m}{\partial \xi^j} \frac{\partial x^n}{\partial \xi^k} - \frac{\partial x^n}{\partial \xi^j} \frac{\partial x^m}{\partial \xi^k} \right)$$

and, from equations (A-6) and (A-34)

$$a_j^\ell \, b_\ell^i = J \, \delta_j^i \qquad\qquad\qquad\qquad \text{(A-39)}$$

where (ℓ, m, n) are in cyclic order also.

The relationships between the metric tensors in the ξ^i and x^i coordinates can now be obtained as follows

$$g_{ij} = \underset{\sim}{a}_i \cdot \underset{\sim}{a}_j = \sum_{\ell=1}^{3} a_i^\ell \, a_j^\ell = \sum_{\ell=1}^{3} h_\ell^2 \frac{\partial x^\ell}{\partial \xi^i} \frac{\partial x^\ell}{\partial \xi^j} \qquad \text{(A-40)}$$

The conjugate (contravariant) metric tensor g^{ij} is

$$g^{ij} = \underset{\sim}{a}^i \cdot \underset{\sim}{e}^j = \frac{1}{J^2} \sum_{\ell=1}^{3} b_\ell^i b_\ell^j = \frac{1}{g} \sum_{\ell=1}^{3} b_\ell^i \, b_\ell^j \qquad \text{(A-41)}$$

where $g = J^2$ is the determinant of the metric tensor g_{ij}.

An alternative expression for g^{ij} can be obtained from equation (A-14) by recognizing that g^{ij} is the inverse of g_{ij}, i.e.,

$$g^{\ell j} = (g_{\ell j})^{-1} = \frac{1}{g} (g_{mj} \, g_{nk} - g_{mk} \, g_{nj}) \qquad \text{(A-42)}$$

with both (i, j, k) and (ℓ, m, n) in cyclic order.

It should be remarked here that the metric tensor g_{ij} and its conjugate g^{ij} follow the tensor transformation rules

$$g_{ij} = h_{\ell m} \frac{\partial x^\ell}{\partial \xi^i} \frac{\partial x^m}{\partial \xi^j} \qquad\qquad\qquad \text{(A-43a)}$$

and

$$g^{ij} = h^{\ell m} \frac{\partial \xi^i}{\partial x^\ell} \frac{\partial \xi^j}{\partial x^m} \qquad\qquad\qquad \text{(A-43b)}$$

Where $h_{\ell m}$ and $h^{\ell m}$ are the metric coefficients defined in equations (A-24) and (A-25) for the orthogonal coordinates x^i. The

AI-7

last two equations are identical with equations (A-40) and (A-41).

In addition to the above geometrical relationships, we need relationships to transform the Reynolds and continuity equations from the x^i coordinates to the ξ^i coordinates. It is therefore necessary to obtain expressions for the gradient, divergence and Laplacian operators in the general coordinates ξ^i. These operators involve the derivatives of either scalar or vector quantities with respect to ξ^i. In Cartesian coordinates, the partial derivatives always give higher order tensors. This is, however, not true for general curvilinear coordinates. For example, although $\partial\phi/\partial\xi^i$ is a covariant vector for any scalar function ϕ, the second derivative $\partial^2\phi/\partial\xi^i\partial\xi^j$ does not give a covariant second-order tensor. In this respect, the curvilinear system is not as convenient as the Cartesian system. It is important to define a derivative which preserves tensor character under coordinate transformations so that the effect of coordinate transformations on derivatives need not be considered explicitly. A derivative with the desired tensor transformation properties can be defined as follows:

$$A^{\alpha_1\alpha_2\cdots\alpha_r}_{\beta_1\beta_2\cdots\beta_s,m} = \frac{\partial}{\partial\xi^m} A^{\alpha_1\alpha_2\cdots\alpha_r}_{\beta_1\beta_2\cdots\beta_s} + \sum_{i=1}^{r} \Gamma^{\alpha_i}_{\mu_i m} A^{\alpha_1\cdots\mu_i\cdots\alpha_r}_{\beta_1\beta_2\cdots\beta_s}$$

$$- \sum_{j=1}^{s} \Gamma^{\mu_j}_{\beta_j m} A^{\alpha_1\alpha_2\cdots\alpha_r}_{\beta_1\beta_2\cdots\beta_j\cdots\beta_s} \tag{A-44}$$

This is called the "covariant derivative" of the general tensor $A^{\alpha_1\alpha_2\cdots\alpha_r}_{\beta_1\beta_2\cdots\beta_s}$, and Γ^i_{jk} is the Christoffel symbol defined by

$$\Gamma^i_{jk} = \frac{1}{2} g^{i\ell} \left(\frac{\partial g_{\ell j}}{\partial\xi^k} + \frac{\partial g_{k\ell}}{\partial\xi^j} - \frac{\partial g_{jk}}{\partial\xi^\ell}\right) \tag{A-45}$$

It is clear that the Christoffel symbol is symmetric in j and k. Furthermore, Γ^i_{ij} is related to the Jacobian J or $\sqrt{g}$ by

$$\Gamma_{ij}^{i} = \Gamma_{ji}^{i} = \frac{1}{2} \frac{\partial \log g}{\partial \xi^{i}} = \frac{1}{2g} \frac{\partial g}{\partial \xi^{i}}$$

or

$$\Gamma_{ij}^{i} = \Gamma_{ji}^{i} = \frac{1}{J} \frac{\partial J}{\partial \xi^{i}} \tag{A-46}$$

since $g = J^2$.

It is noted that both $\frac{\partial}{\partial \xi^m} A_{\beta_1 \beta_2 \ldots \beta_s}^{\alpha_1 \alpha_2 \ldots \alpha_r}$ and Γ_{jk}^{i} are not tensors; however, the covariant derivative (A-44) does preserve the tensor transformation rule under coordinate transformation and is therefore a higher order tensor. The result of equation (A-44) is that we need not consider explicitly the effect of coordinate transformations on tensor derivatives. For example, since $g_{ij},_{\ell}$ and $g^{ij},_{\ell}$ are zero in Cartesian system, they are also zero in all coordinate systems.

From equation (A-44), the covariant derivative of a covariant vector A_i with respect to ξ^i is given by

$$A_{i,j} = \frac{\partial A_i}{\partial \xi^j} - \Gamma_{ij}^{k} A_k \tag{A-47}$$

Also, the covariant derivative of a contravariant vector A^i is given by

$$A^i,_j = \frac{\partial A^i}{\partial \xi^j} + \Gamma_{kj}^{i} A^k = \frac{\partial A^i}{\partial \xi^j} + \Gamma_{jk}^{i} A^k \tag{A-48}$$

The divergence of a vector $\underset{\sim}{A}$ is a scalar quantity and is invariant under coordinate transformation. It can therefore be obtained by a covariant derivative of the contravarient component A^i and can be written in any general non-orthogonal coordinates as

$$\text{div } \underset{\sim}{A} = A^i,_i = \frac{\partial A^i}{\partial \xi^i} + \Gamma_{ij}^{i} A^j \tag{A-49}$$

AI-9

Only in Cartesian coordinates div $\underset{\sim}{A}$ reduces to $\dfrac{\partial A^i}{\partial \xi^i}$ because the Christoffel symbol Γ^i_{jk} is then zero. In other coordinates, the divergence operator is given by eq (A-46) as

$$\text{div } \underset{\sim}{A} = \frac{\partial A^i}{\partial \xi^i} + \frac{1}{J} \frac{\partial J}{\partial \xi^i} A^i = \frac{1}{J} \frac{\partial}{\partial \xi^i} (JA^i) \tag{A-50a}$$

where A^i is related to the physical components $E(\ell)$ in the orthogonal coordinates x^i by the tensor transformation rule

$$A^i = E^\ell \frac{\partial \xi^i}{\partial x^\ell} = \left(\frac{h_\ell}{J} b^i_\ell\right) E^\ell = \frac{1}{J} b^i_\ell E(\ell)$$

Thus

$$\text{div } \underset{\approx}{A} = \frac{1}{J} \frac{\partial}{\partial \xi^i} (b^i_\ell E(\ell)) \tag{A-50b}$$

In the basic orthogonal coordinate system x^i, the ith component of the gradient operator is

$$(\nabla \phi)_i = \frac{1}{h_i} \frac{\partial \phi}{\partial x^i} \tag{A-51}$$

If we apply the chain rule for differentiation, and use equations (A-33 and 34), the gradient operator in the general nonorthogonal coordinates can be written

$$(\nabla \phi)_i = \frac{1}{h_i} \left(\frac{\partial \xi^j}{\partial x^i}\right) \frac{\partial \phi}{\partial \xi^j} = \frac{1}{J} b^j_i \frac{\partial \phi}{\partial \xi^j} \tag{A-52}$$

Finally, the Laplacian $\nabla^2 \phi$ of a scalar function ϕ is defined by

$$\nabla^2 \phi = \text{div } (\nabla \phi) \tag{A-53}$$

where $\nabla \phi = \dfrac{\partial \phi}{\partial \xi^i} a_i$ and $\dfrac{\partial \phi}{\partial \xi^i}$ is the ith component of $\nabla \phi$ in general coordinates ξ^i. Since the divergence expression (A-50) applies only to the contravariant component, the associated contravariant component of $\nabla \phi$ should be used, i.e.,

$$\nabla^2 \phi = \text{div} \, (\nabla \phi)^i = \text{div} \, (g^{ij} \frac{\partial \phi}{\partial \xi^j}) = \frac{1}{J} \frac{\partial}{\partial \xi^i} (J \, g^{ij} \frac{\partial \phi}{\partial \xi^j}) \quad \text{(A-55a)}$$

or

$$\nabla^2 \phi = g^{ij} \frac{\partial^2 \phi}{\partial \xi^i \partial \xi^j} + \frac{1}{J} \frac{\partial}{\partial \xi^i} (J \, g^{ij}) \frac{\partial \phi}{\partial \xi^j} \quad \text{(A-55b)}$$

The general transformation formulas listed above have been used in the text to (a) generate the nonorthogonal numerical grid in the physical domain and (b) transform the governing equations of fluid motion from a basic orthogonal coordinate system into the nonorthogonal numerical coordinates. The procedures used to accomplish this are outlined below.

(a) Numerical grid generation

The numerical coordinates ξ^i are related to the basic orthogonal coordinates x^i by the set of Poisson equations (equation III-19 in the text)

$$\nabla^2 \xi^i = f^i \quad \text{(A-56)}$$

where ∇^2 is the Laplacian in the x^i coordinates and f^i are functions of ξ^i which control the grid spacing. Using equation (A-55b), this may be written

$$f^\ell = \nabla^2 \xi^\ell = g^{ij} \frac{\partial^2 \xi^\ell}{\partial \xi^i \partial \xi^j} + \frac{1}{J} \frac{\partial}{\partial \xi^i} (J \, g^{ij}) \frac{\partial \xi^\ell}{\partial \xi^j}$$

$$= \frac{1}{J} \frac{\partial}{\partial \xi^i} (J \, g^{i\ell}) \quad \text{(A-57)}$$

Since $J = h_1 \, h_2 \, h_3$ and $g^{i\ell} = h^{i\ell}$ in the orthogonal system, f^ℓ may be expressed in terms of the metric coefficients as

$$f^{\ell} = \frac{1}{J} \frac{\partial}{\partial x^i} (J \, h^{i\ell})$$

$$= \frac{1}{h_1 h_2 h_3} \frac{\partial}{\partial x^i} \left(\frac{h_1 h_2 h_3}{h_i^2} \delta_i^{\ell} \right)$$

$$= \frac{1}{h_1 h_2 h_3} \frac{\partial}{\partial x^{\ell}} \left(\frac{h_1 h_2 h_3}{h_{\ell}^2} \right) \quad \text{(no sum on } \ell) \quad\quad (A-58)$$

using equation (A-57), the second term on the right hand side of equation (A-55) can be expressed in terms of f^{ℓ} and the expression for the Laplacian in the numerical coordinates governed by equation (A-56) becomes

$$\nabla^2 \phi = g^{ij} \frac{\partial^2 \phi}{\partial \xi^i \partial \xi^j} + f^j \frac{\partial \phi}{\partial \xi^j} \quad\quad (A-59)$$

Thus, the inverse form of equations (A-56) which can be used for grid generation becomes

$$\nabla^2 x^i = g^{ij} \frac{\partial^2 x^i}{\partial \xi^i \partial \xi^j} + f^j \frac{\partial x^i}{\partial \xi^j}$$

$$= \frac{1}{h_1 h_2 h_3} \frac{\partial}{\partial x^i} \left(\frac{h_1 h_2 h_3}{h_i^2} \right) \quad\quad (A-60)$$

where g^{ij} is evaluated in terms of g_{ij} by equation (A-42) and f^j may be assigned appropriate values to control the grid spacing. Equations (A-60) with $i = 1, 2, 3$ are equations (III-19) in the text.

(b) Transformation of the flow equations

Consider the equations of motion in orthogonal curvilinear coordinates (x^1, x^2, x^3) for unsteady, three-dimensional, incompressible flows. The exact Reynolds-averaged equations of continuity and momentum of the mean flow (Nash and Patel (1972)) in dimensionless form are,

$$\frac{1}{h_1 h_2 h_3} \left\{ \frac{\partial}{\partial x^1} (h_2 h_3 U) + \frac{\partial}{\partial x^2} (h_1 h_3 V) + \frac{\partial}{\partial x^3} (h_1 h_2 W) \right\} = 0 \qquad (A-61)$$

$$\frac{\partial U}{\partial t} + \frac{U}{h_1} \frac{\partial U}{\partial x^1} + \frac{V}{h_2} \frac{\partial U}{\partial x^2} + \frac{W}{h_3} \frac{\partial U}{\partial x^3} + (k_{12} U - k_{21} V) V + (k_{13} U - k_{31} W) W$$

$$+ \frac{1}{h_1} \frac{\partial p}{\partial x^1} + \frac{1}{h_1} \frac{\partial}{\partial x^1} (\overline{u^2}) + \frac{1}{h_2} \frac{\partial}{\partial x^2} (\overline{uv}) + \frac{1}{h_3} \frac{\partial}{\partial x^3} (\overline{uw})$$

$$+ (2k_{12} + k_{32}) \overline{uv} + (2k_{13} + k_{23}) \overline{uw} + (k_{21} + k_{31}) \overline{u^2}$$

$$- k_{21} \overline{v^2} - k_{31} \overline{w^2} - \frac{1}{Re} \left\{ \nabla^2 U - 2k_{21} \frac{1}{h_2} \frac{\partial V}{\partial x^2} + 2k_{12} \frac{1}{h_1} \frac{\partial V}{\partial x^1} \right.$$

$$\left. - 2k_{31} \frac{1}{h_3} \frac{\partial W}{\partial x^3} + 2k_{13} \frac{1}{h_1} \frac{\partial W}{\partial x^1} + \alpha_{11} U + \alpha_{12} V + \alpha_{13} W \right\} = 0 \quad (A-62)$$

$$\frac{\partial V}{\partial t} + \frac{U}{h_1} \frac{\partial V}{\partial x^1} + \frac{V}{h_2} \frac{\partial V}{\partial x^2} + \frac{W}{h_3} \frac{\partial W}{\partial x^3} + (k_{23} V - k_{32} W) W + (k_{21} V - k_{12} U) U$$

$$+ \frac{1}{h_2} \frac{\partial p}{\partial x^2} + \frac{1}{h_1} \frac{\partial}{\partial x^1} (\overline{uv}) + \frac{1}{h_2} \frac{\partial}{\partial x^2} (\overline{v^2}) + \frac{1}{h_3} \frac{\partial}{\partial x^3} (\overline{vw})$$

$$+ (2k_{21} + k_{31}) \overline{uv} + (2k_{23} + k_{13}) \overline{vw} - k_{12} \overline{u^2} + (k_{32} + k_{12}) \overline{v^2}$$

$$- k_{32} \overline{w^2} - \frac{1}{Re} \left\{ \nabla^2 V - 2k_{32} \frac{1}{h_3} \frac{\partial W}{\partial x^3} + 2k_{23} \frac{1}{h_2} \frac{\partial W}{\partial x^2} \right.$$

$$\left. - 2k_{12} \frac{1}{h_1} \frac{\partial U}{\partial x^1} + 2k_{21} \frac{1}{h_2} \frac{\partial U}{\partial x^2} + \alpha_{21} U + \alpha_{22} V + \alpha_{23} W \right\} = 0 \quad (A-63)$$

$$\frac{\partial W}{\partial t} + \frac{U}{h_1} \frac{\partial W}{\partial x^1} + \frac{V}{h_2} \frac{\partial W}{\partial x^2} + \frac{W}{h_3} \frac{\partial W}{\partial x^3} + (k_{31} W - k_{13} U) U + (k_{32} W - k_{23} V) V$$

$$+ \frac{1}{h_3} \frac{\partial p}{\partial x^3} + \frac{1}{h_1} \frac{\partial}{\partial x^1} (\overline{uw}) + \frac{1}{h_2} \frac{\partial}{\partial x^2} (\overline{vw}) + \frac{1}{h_3} \frac{\partial}{\partial x^3} (\overline{w^2})$$

$$+ (2k_{31} + k_{21}) \overline{uw} + (2k_{32} + k_{12}) \overline{vw} - k_{13}\overline{u^2} - k_{23}\overline{v^2}$$

$$+ (k_{13} + k_{23}) \overline{w^2} - \frac{1}{Re} \{ \nabla^2 W - 2k_{13} \frac{1}{h_1} \frac{\partial U}{\partial x^1}$$

$$+ 2k_{31} \frac{1}{h_3} \frac{\partial U}{\partial x^3} - 2k_{23} \frac{1}{h_2} \frac{\partial V}{\partial x^2} + 2k_{32} \frac{1}{h_3} \frac{\partial V}{\partial x^3} + \alpha_{31}U + \alpha_{32}V$$

$$+ \alpha_{33}W \} = 0 \tag{A-64}$$

with

$$\nabla^2 = \frac{1}{h_1 h_2 h_3} \{ \frac{\partial}{\partial x^1} (\frac{h_2 h_3}{h_1} \frac{\partial}{\partial x^1}) + \frac{\partial}{\partial x^2} (\frac{h_1 h_3}{h_2} \frac{\partial}{\partial x^2}) + \frac{\partial}{\partial x^3} (\frac{h_1 h_2}{h_3} \frac{\partial}{\partial x^3}) \}$$

$$= \frac{1}{h_1^2} \frac{\partial^2}{\partial x^1 \partial x^1} + \frac{1}{h_2^2} \frac{\partial^2}{\partial x^2 \partial x^2} + \frac{1}{h_3^2} \frac{\partial^2}{\partial x^3 \partial x^3} + (- k_{11} + k_{21} + k_{31}) \frac{1}{h_1} \frac{\partial}{\partial x^1}$$

$$+ (k_{12} - k_{22} + k_{32}) \frac{1}{h_2} \frac{\partial}{\partial x^2} + (k_{13} + k_{23} - k_{33}) \frac{1}{h_3} \frac{\partial}{\partial x^3} \tag{A-65}$$

and

$$k_{ij} = \frac{1}{h_i h_j} \frac{\partial h_i}{\partial x^j} \quad \text{(no sum on i or j)}$$

are the curvature parameters. α_{11}, α_{22} etc. are functions only of the curvature parameters k_{ij} and their derivatives, and can be written

$$\alpha_{11} = - (k_{21}^2 + k_{12}^2 + k_{13}^2 + k_{31}^2)$$

$$\alpha_{22} = - (k_{32}^2 + k_{23}^2 + k_{21}^2 + k_{12}^2)$$

$$\alpha_{33} = - (k_{13}^2 + k_{31}^2 + k_{32}^2 + k_{23}^2)$$

$$\alpha_{12} = \frac{1}{h_1} \frac{\partial k_{12}}{\partial x^1} - \frac{1}{h_2} \frac{\partial k_{21}}{\partial x^2} - k_{32}(k_{31} + k_{21}) + k_{31}k_{12}$$

$$\alpha_{13} = \frac{1}{h_1} \frac{\partial k_{13}}{\partial x^1} - \frac{1}{h_3} \frac{\partial k_{31}}{\partial x^3} - k_{23}(k_{31} + k_{21}) + k_{21}k_{13}$$

$$\alpha_{21} = \frac{1}{h_2} \frac{\partial k_{21}}{\partial x^2} - \frac{1}{h_1} \frac{\partial k_{12}}{\partial x^1} - k_{31}(k_{12} + k_{32}) + k_{32}k_{21}$$

$$\alpha_{23} = \frac{1}{h_2} \frac{\partial k_{23}}{\partial x^2} - \frac{1}{h_3} \frac{\partial k_{32}}{\partial x^3} - k_{13}(k_{12} + k_{32}) + k_{12}k_{23}$$

$$\alpha_{31} = \frac{1}{h_3} \frac{\partial k_{31}}{\partial x^3} - \frac{1}{h_1} \frac{\partial k_{13}}{\partial x^1} - k_{21}(k_{23} + k_{13}) + k_{23}k_{31}$$

$$\alpha_{32} = \frac{1}{h_3} \frac{\partial k_{32}}{\partial x^3} - \frac{1}{h_2} \frac{\partial k_{23}}{\partial x^2} - k_{12}(k_{23} + k_{13}) + k_{13}k_{32}$$

The above equations can be transformed to the general cur-
vilinear coordinates ξ^i by using the expressions for divergence,
gradient and Laplacian. First, the continuity equation (A-61) is
transformed from the x^i coordinates to the ξ^i coordinates by
equation (A-50)

$$\text{div } \underset{\sim}{U} = \frac{1}{J} \frac{\partial}{\partial \xi^i} (b_\ell^i U(\ell)) = 0 \qquad\qquad (A-66)$$

where $U(\ell)$ are the physical components (U, V, W) of velocity
vector $\underset{\sim}{U}$ in the orthogonal coordinates x^i. Equation (A-66) when
written in terms of the velocity components (U, V, W) in the
cylindrical polar coordinates (x, r, θ) is equation (III-1) in
the text.

Similarly, the momentum equations (A-62) through (A-64) are
transformed to ξ^i (ξ,η,ζ) coordinates by equations (A-52) and
(A-59),

$$\frac{\partial U}{\partial t} + \frac{U}{J}(b_1^1 U_\xi + b_1^2 U_\eta + b_1^3 U_\zeta) + \frac{V}{J}(b_2^1 U_\xi + b_2^2 U_\eta + b_2^3 U_\zeta)$$

$$+ \frac{W}{J}(b_3^1 U_\xi + b_3^2 U_\eta + b_3^3 U_\zeta) + (k_{12}U - k_{21}V)V + (k_{13}U - k_{31}W)W$$

$$+ \frac{1}{J}(b_1^1 p_\xi + b_1^2 p_\eta + b_1^3 p_\zeta) + \frac{1}{J}(b_1^1 \overline{u^2}_\xi + b_1^2 \overline{u^2}_\eta + b_1^3 \overline{u^2}_\zeta)$$

$$+ \frac{1}{J}(b_2^1 \overline{uv}_\xi + b_2^2 \overline{uv}_\eta + b_2^3 \overline{uv}_\zeta) + \frac{1}{J}(b_3^1 \overline{uw}_\xi + b_3^2 \overline{uw}_\eta + b_3^3 \overline{uw}_\zeta)$$

$$+ (2k_{12} + k_{32})\overline{uv} + (2k_{13} + k_{23})\overline{uw} + (k_{21} + k_{31})\overline{u^2}$$

$$- k_{21}\overline{v^2} - k_{31}\overline{w^2} - \frac{1}{Re}\{g^{11}U_{\xi\xi} + g^{22}U_{\eta\eta} + g^{33}U_{\zeta\zeta} + 2g^{12}U_{\xi\eta}$$

$$+ 2g^{13}U_{\xi\zeta} + 2g^{23}U_{\eta\zeta} + f^1 U_\xi + f^2 U_\eta + f^3 U_\zeta - \frac{2k_{21}}{J}(b_2^1 V_\xi + b_2^2 V_\eta + b_2^3 V_\zeta)$$

$$+ \frac{2k_{12}}{J}(b_1^1 V_\xi + b_1^2 V_\eta + b_1^3 V_\zeta) - \frac{2k_{31}}{J}(b_3^1 W_\xi + b_3^2 W_\eta + b_3^3 W_\zeta)$$

$$+ \frac{2k_{13}}{J}(b_1^1 W_\xi + b_1^2 W_\eta + b_1^3 W_\zeta) + \alpha_{11}U + \alpha_{12}V + \alpha_{13}W\} = 0 \qquad \text{(A-67)}$$

$$\frac{\partial V}{\partial t} + \frac{U}{J}(b_1^1 V_\xi + b_1^2 V_\eta + b_1^3 V_\zeta) + \frac{V}{J}(b_2^1 V_\xi + b_2^2 V_\eta + b_2^3 V_\zeta)$$

$$+ \frac{W}{J}(b_3^1 V_\xi + b_3^2 V_\eta + b_3^3 V_\zeta) + (k_{23}V - k_{32}W)W + (k_{21}V - k_{12}U)U$$

$$+ \frac{1}{J}(b_2^1 p_\xi + b_2^2 p_\eta + b_2^3 p_\zeta) + \frac{1}{J}(b_1^1 \overline{uv}_\xi + b_1^2 \overline{uv}_\eta + b_1^3 \overline{uv}_\zeta)$$

$$+ \frac{1}{J}(b_2^1 \overline{v^2}_\xi + b_2^2 \overline{v^2}_\eta + b_2^3 \overline{v^2}_\zeta) + \frac{1}{J}(b_3^1 \overline{vw}_\xi + b_3^2 \overline{vw}_\eta + b_3^3 \overline{vw}_\zeta)$$

$$+ (2k_{21} + k_{31})\overline{uv} + (2k_{23} + k_{13})\overline{vw} - k_{12}\overline{u^2} + (k_{32} + k_{12})\overline{v^2}$$

$$- k_{32}\overline{w^2} - \frac{1}{Re}\{g^{11}V_{\xi\xi} + g^{22}V_{\eta\eta} + g^{33}V_{\zeta\zeta} + 2g^{12}V_{\xi\eta} + 2g^{13}V_{\xi\zeta}$$

$$+ 2g^{23}V_{\eta\zeta} + f^1 V_\xi + f^2 V_\eta + f^3 V_\zeta - \frac{2k_{32}}{J}(b_3^1 W_\xi + b_3^2 W_\eta + b_3^3 W_\zeta)$$

$$+ \frac{2k_{23}}{J}(b_2^1 W_\xi + b_2^2 W_\eta + b_2^3 W_\zeta) - \frac{2k_{12}}{J}(b_1^1 U_\xi + b_1^2 U_\eta + b_1^3 U_\zeta)$$

$$+ \frac{2k_{21}}{J} (b_2^1 U_\xi + b_2^2 U_\eta + b_2^3 U_\zeta) + \alpha_{21} U + \alpha_{22} V + \alpha_{23} W\} = 0 \quad \text{(A-68)}$$

$$\frac{\partial W}{\partial t} + \frac{U}{J} (b_1^1 W_\xi + b_1^2 W_\eta + b_1^3 W_\zeta) + \frac{V}{J} (b_2^1 W_\xi + b_2^2 W_\eta + b_2^3 W_\zeta)$$

$$+ \frac{W}{J} (b_3^1 W_\xi + b_3^2 W_\eta + b_3^3 W_\zeta) + (k_{31} W - k_{13} U) U + (k_{32} W - k_{23} V) V$$

$$+ \frac{1}{J} (b_3^1 p_\xi + b_3^2 p_\eta + b_3^3 p_\zeta) + \frac{1}{J} (b_1^1 \overline{uw}_\xi + b_1^2 \overline{uw}_\eta + b_1^3 \overline{uw}_\zeta)$$

$$+ \frac{1}{J} (b_2^1 \overline{vw}_\xi + b_2^2 \overline{vw}_\eta + b_2^3 \overline{vw}_\zeta) + \frac{1}{J} (b_3^1 \overline{w^2}_\xi + b_3^2 \overline{w^2}_\eta + b_3^3 \overline{w^2}_\zeta)$$

$$+ (2k_{31} + k_{21}) \overline{uw} + (2k_{32} + k_{12}) \overline{vw} - k_{13} \overline{u^2} - k_{23} \overline{v^2}$$

$$+ (k_{13} + k_{23}) \overline{w^2} - \frac{1}{Re} \{g^{11} W_{\xi\xi} + g^{22} W_{\eta\eta} + g^{33} W_{\zeta\zeta} + 2g^{12} W_{\xi\eta}$$

$$+ 2g^{13} W_{\xi\zeta} + 2g^{23} W_{\eta\zeta} + f^1 W_\xi + f^2 W_\eta + f^3 W_\zeta - 2 \frac{k_{13}}{J} (b_1^1 U_\xi$$

$$+ b_1^2 U_\eta + b_1^3 U_\zeta) + 2 \frac{k_{31}}{J} (b_3^1 U_\xi + b_3^2 U_\eta + b_3^3 U_\zeta) - \frac{2k_{23}}{J} (b_2^1 V_\xi$$

$$+ b_2^2 V_\eta + b_2^3 V_\zeta) + 2 \frac{k_{32}}{J} (b_3^1 V_\xi + b_3^2 V_\eta + b_3^3 V_\zeta) + \alpha_{31} U + \alpha_{32} V$$

$$+ \alpha_{33} W\} = 0 \quad \text{(A-69)}$$

In the present study, the two equation ($k - \varepsilon$) turbulence model together with the isotropic eddy-viscosity assumption is used to model the Reynolds stresses. In other words, the Reynolds stresses are assumed to be related to the mean rates of strain by means of the turbulent viscosity as follows:

$$- \overline{u^2} = \nu_t (\frac{2}{h_1} \frac{\partial U}{\partial x^1} + 2k_{12} V + 2k_{13} W) - \frac{2}{3} k$$

$$- \overline{v^2} = \nu_t (\frac{2}{h_2} \frac{\partial V}{\partial x^2} + 2k_{21} U + 2k_{23} W) - \frac{2}{3} k$$

$$- \overline{w^2} = \nu_t (\frac{2}{h_3} \frac{\partial W}{\partial x^3} + 2k_{31} U + 2k_{32} V) - \frac{2}{3} k \quad \text{(A-70)}$$

$$- \overline{uv} = \nu_t \left(\frac{1}{h_1} \frac{\partial V}{\partial x^1} + \frac{1}{h_2} \frac{\partial U}{\partial x^2} - k_{12}U - k_{21}V \right)$$

$$- \overline{uw} = \nu_t \left(\frac{1}{h_1} \frac{\partial W}{\partial x^1} + \frac{1}{h_3} \frac{\partial U}{\partial x^3} - k_{13}U - k_{31}W \right)$$

$$- \overline{vw} = \nu_t \left(\frac{1}{h_2} \frac{\partial W}{\partial x^2} + \frac{1}{h_3} \frac{\partial V}{\partial x^3} - k_{23}V - k_{32}W \right)$$

The eddy viscosity ν_t is related to the dimensionless turbulent kinetic energy k and the rate of dissipation of turbulent energy ε by

$$\nu_t = c_\mu \frac{k^2}{\varepsilon} \tag{A-71}$$

and k and ε are governed by convective transport equations of the following form

$$\frac{\partial k}{\partial t} + \frac{U}{h_1} \frac{\partial k}{\partial x^1} + \frac{V}{h_2} \frac{\partial k}{\partial x^2} + \frac{W}{h_3} \frac{\partial k}{\partial x^3} - \frac{1}{h_1 h_2 h_3} \left\{ \frac{\partial}{\partial x^1} \left(\frac{1}{\sigma_k R_{eff}} \frac{h_2 h_3}{h_1} \frac{\partial k}{\partial x^1} \right) \right.$$

$$\left. + \frac{\partial}{\partial x^2} \left(\frac{1}{\sigma_k R_{eff}} \frac{h_1 h_3}{h_2} \frac{\partial k}{\partial x^2} \right) + \frac{\partial}{\partial x^3} \left(\frac{1}{\sigma_k R_{eff}} \frac{h_1 h_2}{h_3} \frac{\partial k}{\partial x^3} \right) \right\} - G + \varepsilon = 0$$

$$\tag{A-72}$$

$$\frac{\partial \varepsilon}{\partial t} + \frac{U}{h_1} \frac{\partial \varepsilon}{\partial x^1} + \frac{V}{h_2} \frac{\partial \varepsilon}{\partial x^2} + \frac{W}{h_3} \frac{\partial \varepsilon}{\partial x^3} - \frac{1}{h_1 h_2 h_3} \left\{ \frac{\partial}{\partial x^1} \left(\frac{1}{\sigma_\varepsilon R_{eff}} \frac{h_2 h_3}{h_1} \frac{\partial \varepsilon}{\partial x^1} \right) \right.$$

$$\left. + \frac{\partial}{\partial x^2} \left(\frac{1}{\sigma_\varepsilon R_{eff}} \frac{h_1 h_3}{h_2} \frac{\partial \varepsilon}{\partial x^2} \right) + \frac{\partial}{\partial x^3} \left(\frac{1}{\sigma_\varepsilon R_{eff}} \frac{h_1 h_2}{h_3} \frac{\partial \varepsilon}{\partial x^3} \right) \right\} - c_{\varepsilon 1} \frac{\varepsilon}{k} G$$

$$+ c_{\varepsilon 2} \frac{\varepsilon^2}{k} = 0 \tag{A-73}$$

where G is the turbulent generation term

$$G = \nu_t \Big\{ 2\Big[\Big(\frac{1}{h_1}\frac{\partial U}{\partial x} + k_{12}V + k_{13}W\Big)^2 + \Big(\frac{1}{h_2}\frac{\partial V}{\partial x^2} + k_{21}U + k_{23}W\Big)^2$$

$$+ \Big(\frac{1}{h_3}\frac{\partial W}{\partial x^3} + k_{31}U + k_{32}V\Big)^2 \Big] + \Big(\frac{1}{h_1}\frac{\partial V}{\partial x^1} + \frac{1}{h_2}\frac{\partial U}{\partial x^2} - k_{12}U - k_{21}V\Big)^2$$

$$+ \Big(\frac{1}{h_1}\frac{\partial W}{\partial x^1} + \frac{1}{h_3}\frac{\partial U}{\partial x^3} - k_{13}U - k_{31}V\Big) + \Big(\frac{1}{h_2}\frac{\partial W}{\partial x^2} + \frac{1}{h_3}\frac{\partial V}{\partial x^3}$$

$$- k_{23}V - k_{32}W\Big)^2 \Big\} \tag{A-74}$$

and the effective Reynolds number is defined as

$$\frac{1}{R_{eff}} = \frac{1}{Re} + \nu_t = \frac{1}{Re} + c_\mu \frac{k^2}{\varepsilon} \tag{A-75}$$

Using equation (A-70), (A-71) and (A-75), the momentum equations (A-67) through (A-69) and the turbulence-model equations (A-72) and (A-73) are transformed to

$$\frac{\partial U}{\partial t} + \Big(U - \frac{2}{h_1}\frac{\partial \nu_t}{\partial x^1}\Big)\frac{1}{h_1}\frac{\partial U}{\partial x^1} + \Big(V - \frac{1}{h_1}\frac{\partial \nu_t}{\partial x^2}\Big)\frac{1}{h_2}\frac{\partial U}{\partial x^2} + \Big(W - \frac{1}{h_3}\frac{\partial \nu_t}{\partial x^3}\Big)$$

$$\frac{1}{h_3}\frac{\partial U}{\partial x^3} + (k_{12}U - k_{21}V)V + (k_{12}U - k_{31}W)W + \frac{1}{h_1}\frac{\partial p}{\partial x^1}$$

$$+ \frac{2}{3}\frac{1}{h_1}\frac{\partial k}{\partial x^1} - \frac{1}{h_1}\frac{\partial \nu_t}{\partial x^1}(2k_{12}V + 2k_{13}W) - \frac{1}{h_2}\frac{\partial \nu_t}{\partial x^2}\Big(\frac{1}{h_1}\frac{\partial V}{\partial x^1}$$

$$- k_{12}U - k_{21}V\Big) - \frac{1}{h_3}\frac{\partial \nu_t}{\partial x^3}\Big(\frac{1}{h_1}\frac{\partial W}{\partial x^1} - k_{13}U - k_{31}W\Big) - \frac{1}{R_{eff}}\{\nabla^2 U$$

$$- 2k_{21}\frac{1}{h_2}\frac{\partial V}{\partial x^2} + 2k_{12}\frac{1}{h_1}\frac{\partial V}{\partial x^1} - 2k_{31}\frac{1}{h_3}\frac{\partial W}{\partial x^3} + 2k_{13}\frac{1}{h_1}\frac{\partial W}{\partial x^1}$$

$$+ \alpha_{11}U + \alpha_{12}V + \alpha_{13}W\} = 0 \qquad\qquad (A-76)$$

$$\frac{\partial V}{\partial t} + (U - \frac{1}{h_1} \frac{\partial \nu_t}{\partial x^1}) \frac{1}{h_1} \frac{\partial V}{\partial x^1} + (V - \frac{2}{h_2} \frac{\partial \nu_t}{\partial x^2}) \frac{1}{h_2} \frac{\partial V}{\partial x^2} + (W - \frac{1}{h_3} \frac{\partial \nu_t}{\partial x^3})$$

$$\frac{1}{h_3} \frac{\partial V}{\partial x^3} + (k_{23}V - k_{32}W)W + (k_{21}V - k_{12}U)U + \frac{1}{h_2} \frac{\partial p}{\partial x^2}$$

$$+ \frac{2}{3} \frac{1}{h_2} \frac{\partial k}{\partial x^2} - \frac{1}{h_1} \frac{\partial \nu_t}{\partial x^1} (\frac{1}{h_2} \frac{\partial U}{\partial x^2} - k_{12}U - k_{21}V) - \frac{1}{h_2} \frac{\partial \nu_t}{\partial x^2}$$

$$(2k_{21}U + 2k_{32}W) - \frac{1}{h_3} \frac{\partial \nu_t}{\partial x^3} (\frac{1}{h_2} \frac{\partial W}{\partial x^2} - k_{23}V - k_{32}W) - \frac{1}{R_{eff}}$$

$$\{\nabla^2 V - 2k_{32} \frac{1}{h_3} \frac{\partial W}{\partial x^3} + 2k_{23} \frac{1}{h_2} \frac{\partial W}{\partial x^2} - 2k_{12} \frac{1}{h_1} \frac{\partial U}{\partial x^1}$$

$$+ 2k_{21} \frac{1}{h_2} \frac{\partial U}{\partial x^2} + \alpha_{21}U + \alpha_{22}V + \alpha_{23}W\} = 0 \qquad\qquad (A-77)$$

$$\frac{\partial W}{\partial t} + (U - \frac{1}{h_2} \frac{\partial \nu_t}{\partial x^1}) \frac{1}{h_1} \frac{\partial W}{\partial x^1} + (V - \frac{1}{h_2} \frac{\partial \nu_t}{\partial x^2}) \frac{1}{h_2} \frac{\partial W}{\partial x^2} + (W - \frac{2}{h_3} \frac{\partial \nu_t}{\partial x^3})$$

$$\frac{1}{h_3} \frac{\partial W}{\partial x^3} + (k_{31}W - k_{13}U)U + (k_{32}W - k_{23}V)V + \frac{1}{h_3} \frac{\partial p}{\partial x^3} + \frac{2}{3} \frac{1}{h_3} \frac{\partial k}{\partial x^3}$$

$$- \frac{1}{h_1} \frac{\partial \nu_t}{\partial x^1} (\frac{1}{h_3} \frac{\partial U}{\partial x^3} - k_{13}U - k_{31}W) - \frac{1}{h_2} \frac{\partial \nu_t}{\partial x^2} (\frac{1}{h_3} \frac{\partial V}{\partial x^3} - k_{23}V$$

$$- k_{32}W) - \frac{1}{h_3} \frac{\partial \nu_t}{\partial x^3} (2k_{31}U + 2k_{32}V) - \frac{1}{R_{eff}} \{\nabla^2 W - 2k_{13} \frac{1}{h_1} \frac{\partial U}{\partial x^1}$$

$$+ 2k_{31} \frac{1}{h_3} \frac{\partial U}{\partial x^3} - 2k_{23} \frac{1}{h_2} \frac{\partial V}{\partial x^2} + 2k_{32} \frac{1}{h_3} \frac{\partial V}{\partial x^3} + \alpha_{31}U + \alpha_{32}V$$

$$\{ + \alpha_{33} W \} = 0 \tag{A-78}$$

$$\frac{\partial k}{\partial t} + (U - \frac{1}{\sigma_k} \frac{1}{h_1} \frac{\partial \nu_t}{\partial x^1}) \frac{1}{h_1} \frac{\partial k}{\partial x^1} + (V - \frac{1}{\sigma_k} \frac{1}{h_2} \frac{\partial \nu_t}{\partial x^2}) \frac{1}{h_2} \frac{\partial k}{\partial x^2}$$

$$+ (W - \frac{1}{\sigma_k} \frac{1}{h_3} \frac{\partial \nu_t}{\partial x^3}) \frac{1}{h_3} \frac{\partial k}{\partial x^3} - \frac{1}{R_{eff}} \nabla^2 k - G + \varepsilon = 0 \tag{A-79}$$

$$\frac{\partial \varepsilon}{\partial t} + (U - \frac{1}{\sigma_\varepsilon} \frac{1}{h_1} \frac{\partial \nu_t}{\partial x^1}) \frac{1}{h_1} \frac{\partial \varepsilon}{\partial x^1} + (V - \frac{1}{\sigma_\varepsilon} \frac{1}{h_2} \frac{\partial \nu_t}{\partial x^2}) \frac{1}{h_2} \frac{\partial \varepsilon}{\partial x^2}$$

$$+ (W - \frac{1}{\sigma_\varepsilon} \frac{1}{h_3} \frac{\partial \nu_t}{\partial x^3}) \frac{1}{h_3} \frac{\partial \varepsilon}{\partial x^3} - \frac{1}{R_{eff}} \nabla^2 \varepsilon - c_{\varepsilon 1} \frac{\varepsilon}{k} G$$

$$+ c_{\varepsilon 2} \frac{\varepsilon^2}{k} = 0 \tag{A-80}$$

It is convenient to rewrite the governing transport equations (A-76) through (A-80) in the following general form

$$\nabla^2 \phi = R_{eff} [(a_\phi U - \frac{b_\phi}{h_1} \frac{\partial \nu_t}{\partial x^1}) \frac{1}{h_1} \frac{\partial \phi}{\partial x^1} + (a_\phi V - \frac{c_\phi}{h_2} \frac{\partial \nu_t}{\partial x^2}) \frac{1}{h_2} \frac{\partial \phi}{\partial x^2}$$

$$+ (a_\phi W - \frac{d_\phi}{h_3} \frac{\partial \nu_t}{\partial x^3}) \frac{1}{h_3} \frac{\partial \phi}{\partial x^3} + a_\phi \frac{\partial \phi}{\partial t}] + s_\phi \tag{A-81}$$

where ϕ may represent any one of the convective transport quantities U, V, W, k or ε. The cooresponding coefficients a_ϕ, b_ϕ, c_ϕ and d_ϕ are

$$
\begin{aligned}
a_U &= 1, & b_U &= 2, & c_U &= 1, & d_U &= 1 \\
a_V &= 1, & b_V &= 1, & c_V &= 2, & d_V &= 1 \\
a_W &= 1, & b_W &= 1, & c_W &= 1, & d_W &= 2 \\
a_k &= \sigma_k, & b_k &= 1, & c_k &= 1, & d_k &= 1 \\
a_\varepsilon &= \sigma_\varepsilon, & b_\varepsilon &= 1, & c_\varepsilon &= 1, & d_\varepsilon &= 1
\end{aligned}
\tag{A-82}
$$

and the source functions s_ϕ for U, V, W, k and ε are, respectively

$$s_U = R_{eff} \left[(k_{12}U - k_{21}V)V + (k_{13}U - k_{31}W)W + \frac{1}{h_1} \frac{\partial p}{\partial x^1} + \frac{2}{3} \frac{1}{h_1} \frac{\partial k}{\partial x^1} \right.$$

$$- \frac{1}{h_1} \frac{\partial \nu_t}{\partial x^1} (2k_{12}V + 2k_{13}W) - \frac{1}{h_2} \frac{\partial \nu_t}{\partial x^2} (\frac{1}{h_1} \frac{\partial V}{\partial x^1} - k_{12}U$$

$$\left. - k_{21}V) - \frac{1}{h_3} \frac{\partial \nu_t}{\partial x^3} (\frac{1}{h_1} \frac{\partial W}{\partial x^1} - k_{13}U - k_{31}W) \right] + 2k_{21} \frac{1}{h_2} \frac{\partial V}{\partial x^2}$$

$$- 2k_{12} \frac{1}{h_1} \frac{\partial V}{\partial x^1} + 2k_{31} \frac{1}{h_3} \frac{\partial W}{\partial x^3} - 2k_{13} \frac{1}{h_1} \frac{\partial W}{\partial x^1} - \alpha_{11}U - \alpha_{12}V$$

$$- \alpha_{13}W \tag{A-83a}$$

$$s_V = R_{eff} \left[(k_{23}V - k_{32}W)W + (k_{21}V - k_{12}U)U + \frac{1}{h_2} \frac{\partial p}{\partial x^2} + \frac{2}{3} \frac{1}{h_2} \frac{\partial k}{\partial x^2} \right.$$

$$- \frac{1}{h_1} \frac{\partial \nu_t}{\partial x^1} (\frac{1}{h_2} \frac{\partial U}{\partial x^2} - k_{12}U - k_{21}V) - \frac{1}{h_2} \frac{\partial \nu_t}{\partial x^2} (2k_{21}U + 2k_{23}W)$$

$$\left. - \frac{1}{h_3} \frac{\partial \nu_t}{\partial x^3} (\frac{1}{h_2} \frac{\partial W}{\partial x^2} - k_{23}V - k_{32}W) \right] + 2k_{32} \frac{1}{h_3} \frac{\partial W}{\partial x^3}$$

$$- 2k_{23} \frac{1}{h_2} \frac{\partial W}{\partial x^2} + 2k_{12} \frac{1}{h_1} \frac{\partial U}{\partial x^1} - 2k_{21} \frac{1}{h_2} \frac{\partial U}{\partial x^2} - \alpha_{21}U$$

$$- \alpha_{22}V - \alpha_{23}W \tag{A-83b}$$

$$s_W = R_{eff} \left[(k_{31}W - k_{13}U)U + (k_{32}W - k_{23}V)V + \frac{1}{h_3} \frac{\partial p}{\partial x^3} + \frac{2}{3} \frac{1}{h_3} \frac{\partial k}{\partial x^3} \right.$$

$$- \frac{1}{h_1} \frac{\partial \nu_t}{\partial x^1} \left(\frac{1}{h_3} \frac{\partial U}{\partial x^3} - k_{13}U - k_{31}W \right) - \frac{1}{h_2} \frac{\partial \nu_t}{\partial x^2} \left(\frac{1}{h_3} \frac{\partial V}{\partial x^3} - k_{23}V \right.$$

$$\left. - k_{32}W \right) - \frac{1}{h_3} \frac{\partial \nu_t}{\partial x^3} (2k_{31}U + 2k_{32}V) \right] + 2k_{13} \frac{1}{h_1} \frac{\partial U}{\partial x^1}$$

$$- 2k_{31} \frac{1}{h_3} \frac{\partial U}{\partial x^3} + 2k_{23} \frac{1}{h_2} \frac{\partial V}{\partial x^2} - 2k_{32} \frac{1}{h_3} \frac{\partial V}{\partial x^3} - \alpha_{31}U - \alpha_{32}V$$

$$- \alpha_{33}W \hspace{4cm} \text{(A-83c)}$$

$$s_k = - \sigma_k R_{eff} (G - \varepsilon) \hspace{3cm} \text{(A-83d)}$$

$$s_\varepsilon = - \sigma_\varepsilon R_{eff} \left(c_{\varepsilon 1} \frac{\varepsilon}{k} G - c_{\varepsilon 2} \frac{\varepsilon^2}{k} \right) \hspace{2cm} \text{(A-83e)}$$

The general convective transport equations (A-81) governing the transport of momentum and turbulence quantities can again be transformed from the orthogonal x^i coordinates to the general curvilinear ξ^i coordinates by using the expressions for the gradient and Laplacian, equations (A-52) and (A-59), respectively, to obtain

$$g^{11}\phi_{\xi\xi} + g^{22}\phi_{\eta\eta} + g^{33}\phi_{\zeta\zeta} + 2g^{12}\phi_{\xi\eta} + 2g^{13}\phi_{\xi\zeta} + 2g^{23}\phi_{\eta\zeta} + f^1\phi_\xi + f^2\phi_\eta$$

$$+ f^3\phi_\zeta = \frac{R_{eff}}{J} \left\{ \left[a_\phi U - \frac{b_\phi}{J} (b_1^1 \nu_{t,\xi} + b_1^2 \nu_{t,\eta} + b_1^3 \nu_{t,\zeta}) \right] (b_1^1 \phi_\xi \right.$$

$$+ b_1^2 \phi_\eta + b_1^3 \phi_\zeta) + \left[a_\phi V - \frac{c_\phi}{J} (b_2^1 \nu_{t,\xi} + b_2^2 \nu_{t,\eta} + b_2^3 \nu_{t,\zeta}) \right]$$

AI-23

$$(b_2^1 \phi_\xi + b_2^2 \phi_\eta + b_2^3 \phi_\zeta) + [a_\phi W - \frac{d_\phi}{J}(b_3^1 \nu_{t,\xi} + b_3^2 \nu_{t,\eta}$$

$$+ b_3^3 \nu_{t,\zeta})](b_3^1 \phi_\xi + b_3^2 \phi_\eta + b_3^3 \phi_\zeta)\} + a_\phi R_{eff} \phi_t + s_\phi \qquad (A\text{-}84)$$

where

$$s_U = R_{eff}\{(k_{12}U - k_{21}V)V + (k_{13}U - k_{31}W)W + \frac{1}{J}(b_1^1 p_\xi + b_1^2 p_\eta + b_1^3 p_\zeta)$$

$$+ \frac{2}{3J}(b_1^1 k_\xi + b_1^2 k_\eta + b_1^3 k_\zeta) - \frac{1}{J}(b_1^1 \nu_{t,\xi} + b_1^2 \nu_{t,\eta} + b_1^3 \nu_{t,\zeta})$$

$$(2k_{12}V + 2k_{13}W) - \frac{1}{J}(b_2^1 \nu_{t,\xi} + b_2^2 \nu_{t,\eta} + b_2^3 \nu_{t,\zeta})[\frac{1}{J}(b_1^1 V_\xi$$

$$+ b_1^2 V_\eta + b_1^3 V_\zeta - k_{12}U - k_{21}V) - \frac{1}{J}(b_3^1 \nu_{t,\xi} + b_3^2 \nu_{t,\eta} + b_3^3 \nu_{t,\zeta})$$

$$[\frac{1}{J}(b_1^1 W_\xi + b_1^2 W_\eta + b_1^3 W_\zeta) - k_{13}U - k_{31}W)]\} + 2\frac{k_{21}}{J}(b_2^1 V_\xi$$

$$+ b_2^2 V_\eta + b_2^3 V_\zeta) - 2\frac{k_{12}}{J}(b_1^1 V_\xi + b_1^2 V_\eta + b_1^3 V_\zeta) + 2\frac{k_{31}}{J}$$

$$(b_3^1 W_\xi + b_3^2 W_\eta + b_3^3 W_\zeta) - 2\frac{k_{13}}{J}(b_1^1 W_\xi + b_1^2 W_\eta + b_1^3 W_\zeta)$$

$$- \alpha_{11}U - \alpha_{12}V - \alpha_{13}W \qquad (A\text{-}85a)$$

$$s_V = R_{eff}\{(k_{23}V - k_{32}W)W + (k_{21}V - k_{12}U)U + \frac{1}{J}(b_2^1 p_\xi + b_2^2 p_\eta + b_2^3 p_\zeta)$$

$$+ \frac{2}{3J}(b_2^1 k_\xi + b_2^2 k_\eta + b_2^3 k_\zeta) - \frac{1}{J}(b_1^1 \nu_{t,\xi} + b_1^2 \nu_{t,\eta} + b_1^3 \nu_{t,\zeta})$$

$$[\frac{1}{J}(b_2^1 U_\xi + b_2^2 U_\eta + b_2^3 U_\zeta) - k_{12}U - k_{21}V] - \frac{1}{J}(b_2^1 \nu_{t,\xi} + b_2^2 \nu_{t,\eta}$$

$$+ b_2^3 \nu_{t,\zeta})(2k_{21}U + 2k_{23}W) - \frac{1}{J}(b_3^1 \nu_{t,\xi} + b_3^2 \nu_{t,\eta} + b_3^3 \nu_{t,\zeta})$$

$$[\frac{1}{J}(b_2^1 W_\xi + b_2^2 W_\eta + b_2^3 W_{\smile}) - k_{23}V - k_{32}W]\} + 2\frac{k_{32}}{J}(b_3^1 W_\xi + b_3^2 W_\eta$$

$$+ b_3^3 W_\zeta) - 2\frac{k_{23}}{J}(b_2^1 W_\xi + b_2^2 W_\eta + b_2^3 W_\zeta) + 2\frac{k_{12}}{J}(b_1^1 U_\xi + b_1^2 U_\eta$$

$$+ \; b_1^3 U_\zeta) \; - \; 2 \; \frac{k_{21}}{J} \; (b_2^1 U_\xi + \; b_2^2 U_\eta + \; b_2^3 U_\zeta) \; - \; \alpha_{21} U \; - \; \alpha_{22} V$$

$$- \; \alpha_{23} W \tag{A-85b}$$

$$s_W = R_{eff} \{ (k_{31}W - k_{13}U)U + (k_{32}W - k_{23}V) \; V + \frac{1}{J} \; (b_3^1 p_\xi + b_3^2 p_\eta + b_3^3 p_\zeta)$$

$$+ \; \frac{2}{3J} \; (b_3^1 k_\xi + b_3^2 k_\eta + b_3^3 k_\zeta) \; - \; \frac{1}{J} \; (b_1^1 \nu_{t,\xi} + b_1^2 \nu_{t,\eta} + b_1^3 \nu_{t,\zeta})$$

$$[\frac{1}{J} \; (b_3^1 U_\xi + b_3^2 U_\eta + b_3^3 U_\zeta) \; - \; k_{13}U - k_{31}W) \; - \; \frac{1}{J} \; (b_2^1 \nu_{t,\xi} + b_2^2 \nu_{t,\eta}$$

$$+ \; b_2^3 \nu_{t,\zeta}) \; [\frac{1}{J} \; (b_3^1 V_\xi + b_3^2 V_\eta + b_3^3 V_\zeta) \; - \; k_{23}V - k_{32}W]$$

$$- \; \frac{1}{J} \; (b_3^1 \nu_{t,\xi} + b_3^2 \nu_{t,\eta} + b_3^3 \nu_{t,\zeta})(2k_{31}U + 2k_{32}V)]\}$$

$$+ \; 2 \; \frac{k_{13}}{J} \; (b_1^1 U_\xi + b_1^2 U_\eta + b_1^3 U_\zeta) \; - \; 2 \; \frac{k_{31}}{J} \; (b_3^1 U_\xi + b_3^2 U_\eta + b_3^3 U_\zeta)$$

$$2 \; \frac{k_{23}}{J} \; (b_2^1 V_\xi + b_2^2 V_\eta + b_2^3 V_\zeta) \; - \; 2 \; \frac{k_{32}}{J} \; (b_3^1 V_\xi + b_3^2 V_\eta + b_3^3 V_\zeta)$$

$$- \; \alpha_{31} U \; - \; \alpha_{32} V \; - \; \alpha_{33} W \tag{A-85c}$$

$$s_k = - \; \sigma_k R_{eff} (G - \epsilon) \tag{A-85d}$$

$$s_\epsilon = - \; \sigma_\epsilon R_{eff} \; (c_{\epsilon 1} \; \frac{\epsilon}{k} \; G - c_{\epsilon 2} \; \frac{\epsilon^2}{k}) \tag{A-85e}$$

with

$$G = \nu_t \{ 2 [\frac{1}{J} \; (b_1^1 U_\xi + b_1^2 U_\eta + b_1^3 U_\zeta) \; + \; k_{12}V + k_{13}W]^2 + 2[\frac{1}{J} \; (b_2^1 V_\xi + b_2^2 V_\eta$$

$$+ \; b_2^3 V_\zeta) \; + \; k_{21}U + k_{23}W]^2 + 2[\frac{1}{J} \; (b_3^1 W_\xi + b_3^2 W_\eta + b_3^3 W_\zeta) \; + \; k_{31}U$$

$$+ k_{32}V]^2 + [\frac{1}{J} (b_1^1 V_\xi + b_1^2 V_\eta + b_1^3 V_\zeta + b_2^1 U_\xi + b_2^2 U_\eta + b_2^3 U_\zeta) - k_{12}U$$

$$- k_{21}V]^2 + [\frac{1}{J} (b_1^1 W_\xi + b_1^2 W_\eta + b_1^3 W_\zeta + b_3^1 U_\xi + b_3^2 U_\eta + b_3^3 U_\zeta) - k_{13}U$$

$$- k_{31}V]^2 + [\frac{1}{J} (b_2^1 W_\xi + b_2^2 W_\eta + b_2^3 W_\zeta + b_3^1 V_\xi + b_3^2 V_\eta + b_3^3 V_\zeta) - k_{23}V$$

$$- k_{32}W]^2 \} \qquad\qquad (A-85f)$$

It is noted that equations (A-84) depend upon g^{ij}, b_i^j, k_{ij}, α_{ij} and the Jacobian. All these quantities are functions of coordinates only. When an analytic transformation is used to generate the coordinates, the geometrical coefficients are known analytically without additional approximation. On the other hand, if equations (A-60) are solved numerically for the coordinate values $x^i = x^i (\xi,\eta,\zeta)$, then the coefficients g^{ij}, b_i^j and the Jacobian J must be evaluated numerically. In the present study, conventional finite-difference techniques are employed for the numerical grid generation and also the evaluation of the coefficients.

U.S. DISTRIBUTION LIST

U.S. Naval Academy
Annapolis, MD 21402
ATTN: Technical Library

Naval Postgraduate School
Monterey, CA 93940
ATTN: Library (2124)

Study Center
National Maritime Research Center
U.S. Merchant Marine Academy
Kings Point, LI, New York 11024

The Pennsylvania State University
Applied Research Laboratory (Library)
P.O. Box 30
State College, PA 16801

Dr. B. Parkin, Director
Garfield Thomas Water Tunnel
Applied Research Laboratory
P.O. Box 30
State College, PA 16801

Bolt, Beranek & Newman (Library)
50 Moulton Street
Cambridge, MA 02138

Cambridge Acoustical Associates, Inc.
54 Rindge Ave Extension
Cambridge, MA 02140

R & D Manager
Electric Boat Division
General Dynamics Corporation
Groton, Conn 06340

Gibbs & Cox, Inc. (Tech. Info. Control)
21 West Street
New York, NY 10006

Tracor Hydronautics, Inc. (Library)
Pindell School Rd.
Laurel, MD 20810

Newport New Shipbuilding and
   Dry Dock Co. (Tech. Library)
4101 Washington Ave.
Newport News, VA 23607

Society of Naval Architects and
Marine Engineers (Tech. Library)
One World Trade Center, Suite 1369
New York, NY 10048

Sperry Systems Management Division
Sperry Rand Corporation (Library)
Great Neck, NY 10020

Stanford Research Institute
Menlo Park, CA 94025
ATTN: Library

Southwest Research Institute
P.O. Drawer 28510
San Antonio, TX 78284
ATTN: Dr. H. Abramson

Mr. Robert Taggart
9411 Lee Highway, Suite P
Fairfax, VA 22031

Ocean Engr. Department
Woods Hole Oceanographic Inc.
Woods Hole, Mass 02543

Worcester Polytechnic Inst.
Alden Research Lab (Tech Library)
Worcester, MA 01609

Applied Physics Laboratory
University of Washington (Tech. Library)
1013 N. E. 40th Street
Seattle, WA 98105

University of California
Naval Architecture Department
Berkeley, CA 94720
ATTN: Profs. Webster, Paulling,
Wehausen & Library

California Institute of Technology
Pasadena, CA 91109
ATTN: Library

Engineering Research Center
   Reading Room
Colorado State University
Foothills Campus
Fort Collins, CO 80521

Florida Atlantic University
Ocean Engineering Department
Boca Raton, Florida 33432
ATTN: Technical Library

END

FILMED

8-85

DTIC